



Dipl.-Ing. Daniel Markl, BSc

Optical Coherence Tomography
for Non-Destructive
In-line Tablet Coating Analysis

DOCTORAL THESIS

to achieve the university degree of
Doktor der technischen Wissenschaften
submitted to

Graz University of Technology

Supervisor

Univ.-Prof. Dr. Johannes G. Khinast

Institute for Process and Particle Engineering
Graz University of Technology

AFFIDAVIT

I declare that I have authored this thesis independently, that I have not used other than the declared sources/resources, and that I have explicitly indicated all material which has been quoted either literally or by content from the sources used. The text document uploaded to TUGRAZonline is identical to the present doctoral thesis.

Date

Signature

Daniel Markl
Optical coherence tomography
for non-destructive
in-line tablet coating analysis
Dissertation

First assessor

Univ.-Prof. Dr. Johannes G. Khinast
Institute for Process and Particle Engineering
Graz University of Technology, and
Research Center Pharmaceutical Engineering GmbH

Second assessor

Assoc.-Prof. Dr. David Stifter
Center for Surface- and Nanoanalytics
Christian Doppler Laboratory for Microscopic and Spectroscopic Material
Characterization
Johannes Kepler University Linz

Kurzfassung

Durch unterschiedlichste Ansätze, unter anderem Quality by Design (QbD) und Process Analytical Technology (PAT), versuchen die zuständigen Behörden, die pharmazeutische Industrie dazu zu bewegen, das Verständnis ihrer Prozesse und Produkte zu erhöhen. Die Implementierung einer geeigneten Kontrollstrategie ist für das Prozess- und Produktverständnis sowie für die Prozessoptimierung und Qualitätssicherung unerlässlich. Dies betrifft im Speziellen die Verwendung von In-Prozesskontrollen. Diese Arbeit zeigt eine neue in-line Technologie zur Überwachung des Coatingwachstums während der Beschichtung einer festen Darreichungsform. Das Coating hat in der pharmazeutischen Industrie eine lange Tradition – zu Beginn waren es einfache Formulierungen, die die Tablette schützen oder sogar erst die Form gaben. Heute werden jedoch bereits zunehmend kompliziertere Polymersysteme mit maßgeschneiderter Funktionalität verwendet. Insbesondere bei solchen funktionalen Coatings ist die Dicke und Gleichförmigkeit der Schicht entscheidend für die Wirksamkeit des Medikaments. Die in-line Überwachung der Coatingschicht wird mittels optischer Kohärenztomographie (OCT) durchgeführt. OCT ermöglicht die zerstörungsfreie und berührungslose Erstellung von Querschnittsbildern der Beschichtung. Die Dicke der Beschichtung kann somit direkt aus den OCT Bildern bestimmt werden; im Gegensatz zu der Schichtdickenbestimmung mittels Nahinfrarot- oder Raman-Spektroskopie sind keine chemometrischen Kalibrierungsmodelle notwendig. Um jedoch das volle Potenzial der OCT Technologie ausschöpfen zu können, ist eine automatische Auswertung der Messdaten notwendig. Die Geschwindigkeit der Auswertung ist sehr kritisch, da die Daten kontinuierlich generiert und in Echtzeit verarbeitet werden sollten. Daher wird in der vorliegenden Arbeit eine effiziente Vorgehensweise vorgestellt, die zukünftig eine Verwendung der Grafikkarte (engl. graphical processing unit, GPU) ermöglicht. Die automatische Auswertung liefert hochgenaue Ergebnisse, unabhängig von der Tablettenlage und Schichtdicke. Solch ein Algorithmus bildet die Basis für die Anwendung von OCT in einem Beschichtungsverfahren. Es wird eine In-Prozesskontrolle eines pharmazeutischen Trommel- und Wirbelschichtcoaters während der Beschichtung von Tabletten und Pellets mittels OCT durchgeführt. Dabei zeigen die in-line und off-line Resultaten eine hohe Übereinstimmung. Des Weiteren ermöglicht diese Technik eine direkte Schichtdickenmessung an mehreren, unterschiedlichen Positionen auf einzelnen Pellets/Tabletten während des Beschichtungs Vorgangs. Diese Daten liefern

wesentlich mehr Informationen über die Qualität der Beschichtung als Standardverfahren. Im Speziellen bedeutet das, dass Abweichungen auf einzelnen Pellets/Tabletten ("*intra-tablet coating variability*") und zwischen Pellets/Tabletten ("*inter-tablet coating variability*") analysiert werden können. Die Informationen zu diesen Parametern unterstreichen die Fähigkeit von OCT das Prozess- und Produktverständnis verbessern zu können.

Abstract

Authorities made several approaches, including quality by design (QbD) and process analytical technology (PAT), in order to encourage the pharmaceutical industry, to become more concerned with an in-depth understanding of process and product characteristics. Implementing a suitable control strategy based on proper in-line monitoring techniques is essential for process improvement, optimization and quality assurance. This work demonstrates a new in-line measurement technique for monitoring the coating growth during coating of a solid dosage form. Coating is a traditional and widely applied unit operation in the pharmaceutical industry. It is frequently used to mask the taste of a solid dosage form or to control the release of the active pharmaceutical ingredient (API). For functional coatings in particular, thickness and uniformity of the coating layer are crucial for efficacy as well as for compliance. Process monitoring is performed by an optical coherence tomography (OCT) sensor providing cross-section images of film coatings in a non-destructive and contactless manner. The coating thickness can be determined directly from these OCT images without the need of chemometric calibration models. However, to utilize the full potential of the OCT technology an automatic evaluation of the OCT measurements is essential. The main requirements on such an algorithm are to be fast and efficient as well as to provide reliable and accurate results. The speed of the evaluation is very critical, as the data is acquired continuously and has to be processed in real-time. Therefore, this work presents an efficient approach allowing the use of a graphical processing unit (GPU) in future. The automated evaluation algorithm provides highly accurate results independent of tablet orientation and coating thickness. In-line quality control of a pharmaceutical pan coater and of a fluid-bed coating process is presented by means of OCT. The in-line results of both fluid-bed and pan coating are consistent with off-line measurements. Moreover, this technique enables a multiple direct measurement of the coating thickness on individual pellets/tablets rather than providing the average coating thickness of a large number of samples. This gives substantially more information about the coating quality, i.e. *intra-* and *inter-*particle coating variability, than standard quality control methods. The information about those parameters specifically emphasizes the high capability of the OCT technology to improve process understanding and to assure a high product quality.

Acknowledgement

Foremost and first I offer my sincerest gratitude to my supervisor **Prof. Johannes Khinast**, who has supported me throughout my thesis with his patience and knowledge, whilst allowing me the room to work in my own way.

I would like to thank **Prof. David Stifter** for accepting the role as second assessor for this thesis; and for short, but interesting and valuable discussions with him.

This thesis would not have been possible without **Daniel Koller** and **Michael Leitner** performing the first OCT measurements of film-coated tablets and publishing a paper, presenting their findings. On the grounds of this collaboration, they initiated a new project, in the context of which I wrote my dissertation. The finalization of the cooperation agreement between RCPE and RECENDT was carried out by **Stephan Sacher**, who encouraged myself to take part in this project. Special thanks goes to **Stephan** for the excellent support throughout the work at RCPE.

I am grateful to all (current and some former) members of the **RCPE**. In particular, I would like to express my thanks to my colleagues from the PAT group/QbD-PAT group/CoProQuaCo group, **Roland Hohl**, **Otto Scheibelhofer**, **Elena Stocker**, **Diana Dujmovics**, **Patrick Wahl**, **Gregor Hauseder**, **Manuel Zettl** and **Daniel Wiegele** for the great collaboration, the constructive, animated, instructive discussions, and especially for all the fun we have had in the last years. I am also indebted to many other colleagues who have supported me over the last few years: **Eva Faulhammer**, **Verena Wahl**, **Maximilian Besenhard**, **Georg Neubauer**, **Diogo Lopes**, **Marcos Llusa** and **Gregor Toschkoff**.

I would like to acknowledge the support of the laboratory team. I would particularly like to thank **Willibald Stumptner**, **Michael Piller**, **Mario Hainschitz** and **Paul Rinner** for assisting me in the lab and for your kind and helpful answers to all of my questions.

I also want to thank the students I had the chance to work with: **Manuel Zettl**, **Theresa Hörmann** and **Jakob Ziegler**.

I owe a debt of gratitude to all members of the **IPPT**. Especially, I want to thank **Michaela Cibulka**, **Daniel Treffer**, **Andreas Eitzlmayr** and **Johann Grubbauer**.

Furthermore, I want to thank all the people from **RECENDT** for their great cooperation and support during my stays in Linz. I would like to express my special appreciation and thanks to **Günther Hanneschläger**, **Michael Leitner** and **Andreas Buchsbaum** for their valuable technical and scientific support.

Furthermore I thank **ProCepT nv**, **G.L. Pharma GmbH** and **L.B. Bohle GmbH** for the support and for allowing me access to their equipment.

Finally, I would like to express my thanks to **Margot** and the whole family, **Reinhilde**, **Georg**, **Julia**, **Anita**, **Wolfgang**, **Lisa** and **Christoph**, for supporting me throughout my studies. Without them all this would not have been possible. Your support was essential for the completion of this dissertation.

Thank you all!

Daniel Markl

Content

LIST OF FIGURES.....	XIV
LIST OF TABLES.....	XVIII
ABBREVIATIONS	XIX
1 INTRODUCTION.....	1
1.1 PHARMACEUTICAL FILM COATING	1
1.1.1 Pan Coating.....	4
1.1.2 Fluid-Bed Coating	5
1.2 COATING PROCESS MONITORING	6
1.3 OBJECTIVE AND CONTENT OF THE THESIS.....	12
1.3.1 Objective.....	12
1.3.2 Content	13
1.4 REFERENCES.....	14
2 OPTICAL COHERENCE TOMOGRAPHY	21
2.1 THEORY.....	22
2.2 SPECTRAL-DOMAIN OCT.....	25
2.3 INTEGRATION OF OCT SENSOR IN COATING PROCESS	28
2.4 OCT SYSTEM DESIGN	32
2.4.1 Design Parameters.....	32
2.4.2 OCT System Requirements	34
2.4.3 Developed OCT System.....	37
2.5 ANALYSIS OF COATING THICKNESS	40
2.6 REAL-TIME OCT IMAGING	42
2.7 REFERENCES.....	45
3 IN-LINE QUALITY CONTROL OF MOVING OBJECTS BY MEANS OF SPECTRAL-DOMAIN OCT.....	51
3.1 INTRODUCTION.....	52
3.2 MATERIALS AND METHODS.....	54
3.2.1 Theory: Resolution in OCT.....	54
3.2.2 Theory: Transverse Motion Effects	55
3.2.3 Broadening of Beam Displacement.....	56
3.2.4 Broadening of Transverse Resolution.....	58
3.2.5 Blurring of the Sample Area of a B-scan	59
3.3 EXPERIMENTS.....	60
3.3.1 OCT system.....	60
3.3.2 3-Axis positioning stage.....	62
3.3.3 Samples	63
3.4 RESULTS AND DISCUSSION	64
3.4.1 Theoretical Results of Transverse Motion Effects	64
3.4.2 Experimental Results of Transverse Motion Effects	68
3.5 CONCLUSION.....	72

3.6	REFERENCES.....	73
4	OPTICAL COHERENCE TOMOGRAPHY AS A NOVEL TOOL FOR IN-LINE MONITORING OF A PHARMACEUTICAL FILM-COATING PROCESS	77
4.1	INTRODUCTION.....	78
4.2	MATERIALS AND METHODS	81
4.2.1	Optical Coherence Tomography.....	81
4.2.2	OCT Systems.....	83
4.2.3	Used Tablets.....	85
4.2.4	In-line Analysis.....	86
4.3	RESULTS	91
4.3.1	Off-Line Measurements	91
4.3.2	Experimental Results of the In-Line Feasibility Study.....	93
4.4	CONCLUSION.....	98
4.5	REFERENCES.....	99
5	CALIBRATION-FREE IN-LINE MONITORING OF PELLET COATING PROCESSES VIA OPTICAL COHERENCE TOMOGRAPHY	105
5.1	INTRODUCTION.....	106
5.2	MATERIALS AND METHODS	108
5.2.1	Pellet Preparation	108
5.2.2	Pellet Coating.....	109
5.2.3	Methods.....	109
5.2.4	Post-Processing and Data Analysis	113
5.3	RESULTS AND DISCUSSION.....	117
5.3.1	Coating Thickness	117
5.3.2	Coating Uniformity	120
5.3.3	Coating Distribution.....	123
5.4	CONCLUSION.....	124
5.5	REFERENCES.....	125
6	AUTOMATED PHARMACEUTICAL TABLET COATING LAYER EVALUATION OF OPTICAL COHERENCE TOMOGRAPHY IMAGES.....	131
6.1	INTRODUCTION.....	132
6.2	MATERIALS AND METHODS	134
6.2.1	Materials.....	134
6.2.2	Optical Coherence Tomography.....	135
6.2.3	Experimental Setup.....	136
6.2.4	Methods.....	137
6.3	RESULTS	146
6.3.1	Evaluation of Variable Coating Thicknesses	147
6.3.2	Evaluation of Different Tablet Orientations and Varying Beam Displacements.....	149
6.4	CONCLUSION.....	154
6.5	REFERENCES.....	154
7	REAL-TIME DATA PROCESSING FOR IN-LINE MONITORING OF A	

PHARMACEUTICAL COATING PROCESS BY OPTICAL COHERENCE TOMOGRAPHY	159
7.1 INTRODUCTION	160
7.2 MATERIALS AND METHODS.....	161
7.2.1 Optical Coherence Tomography	161
7.2.2 Experimental Setup	163
7.2.3 Tablets and Coating	164
7.2.4 Automatic Coating Thickness Evaluation Algorithm.....	164
7.3 RESULTS AND DISCUSSION	170
7.4 CONCLUSION.....	174
7.5 REFERENCES.....	174
8 IN-LINE MONITORING OF A PHARMACEUTICAL PAN COATING PROCESS BY OPTICAL COHERENCE TOMOGRAPHY	179
8.1 INTRODUCTION	180
8.2 MATERIALS AND METHODS.....	182
8.2.1 Tablet Core and Coating Material	182
8.2.2 Tablet Coating.....	183
8.2.3 Optical Coherence Tomography	184
8.2.4 Experimental Setup	186
8.2.5 Automatic Thickness Evaluation Algorithm	188
8.3 RESULTS	193
8.4 CONCLUSION.....	201
8.5 REFERENCES.....	202
9 CONCLUSION AND OUTLOOK.....	207
9.1 CONCLUSIVE FINDINGS	207
9.2 OUTLOOK.....	209
9.3 REFERENCES.....	213
PUBLICATIONS	215
PEER-REFEREED JOURNALS	215
CONFERENCE PROCEEDINGS	216
PATENT APPLICATIONS.....	216
MAGAZINE ARTICLE.....	216
TALKS	217
POSTER	217
APPENDICES.....	219
APPENDIX A NU-FFT FOR SD-OCT	219
A.1 NU-FFT	219
A.2 References.....	221
APPENDIX B GAUSSIAN OPTICS	222
B.1 Gaussian Optics	222
B.2 References.....	223
APPENDIX C PROPAGATION OF UNCERTAINTY FOR FILM-COATED TABLETS OF DIFFERENT DIMENSIONS AND SHAPES	224

C.1	Volume of a Film-coated Tablet.....	224
C.2	Propagation of Uncertainty.....	225
C.3	References	227

List of Figures

Figure 1.1: Types of pharmaceutical coatings.....	2
Figure 1.2: Function of modified-release film coatings. Adapted from (“Gastrointestinal Complications (PDQ®),” 2015).....	3
Figure 1.3: Cross-section model of a typical pan coater.....	5
Figure 1.4: Cross-section model of a bottom-spray fluid-bed coater.....	6
Figure 1.5: Schematic of film-coated tablets explaining inter- and intra-particle coating variability.	9
Figure 2.1: Simplified block diagram of a low-coherence interferometry system..	23
Figure 2.2: Different variants of OCT systems.	25
Figure 2.3: The transformation of the OCT data from frequency-domain to time- domain.	26
Figure 2.4: OCT data of film-coated tablets. Each B-scan is synthesized by several hundred A-scans.....	28
Figure 2.5: Mounting position of the OCT sensor head (highlighted in dark blue) in a pan coater.	29
Figure 2.6: Illustration of transverse resolution, beam waist radius and the confocal parameter.	33
Figure 2.7: Schematic of an SD-OCT system. Schematic of the experimental design.....	38
Figure 2.8: Picture of the developed OCT system.	39
Figure 2.9: Reconstruction of a film-coated tablet from 3-D OCT data.....	40
Figure 2.10: Off-line investigation of film-coated tablets (periodically sampled from a pan coating process) using a colored modified-release coating solution.	41
Figure 2.11: CPU-GPU architecture. A linear interpolation for the wavelength (λ)to wavenumber (k) resampling is currently implemented.	44
Figure 2.12: Screenshots of the OCT software for real-time process monitoring.	45
Figure 3.1: Trajectory of B-scans considering the sensor head moves at a speed across a stationary sample.....	56
Figure 3.2: Schematic of the experimental design.	62
Figure 3.3: Schematic of the 3-axis positioning system.	62
Figure 3.4: Effective field profile depending on the speed difference.	64
Figure 3.5: Theoretical analysis of broadening effects.....	65
Figure 3.6: Simulations of the 2-D normalized effective beam profile for different	

speeds of the 1-D and 2-D sensor heads.	66
Figure 3.7: The efficiencies for the 1-D sensor head and for the 2-D sensor head in dependence on the sensor heads velocity.	67
Figure 3.8: Cross-section OCT images of the variable frequency resolution target	69
Figure 3.9: B-scans of the tablets for five different velocities of the 1-D (left images) and the 2-D (right images) sensor head.....	71
Figure 3.10: Experimental analysis of efficiency of an A-scan for the 1-D sensor head.....	72
Figure 4.1: An A-scan is a single-depth scan.	83
Figure 4.2: Schematic of the experimental design.....	85
Figure 4.3: Trajectory of B-scans considering the sensor head moves at a certain speed.....	88
Figure 4.4: The transverse resolution δx is proportional to the ratio of the focal length f and the beam diameter d at lens L1 (Figure 4.2).	90
Figure 4.5: Schematic of the 3-axis positioning system.....	91
Figure 4.6: OCT images of Diclofenac®, Tromcardin®, Glucophage®, Zurcal®, Pantoloc®, Voltaren® and Thrombo ASS®.....	92
Figure 4.7: B-scans of the tablets at 10 velocities of (a) the 1-D and (b) the 2-D sensor head.	94
Figure 4.8: Coating thickness for the (a) 1-D and (b) 2-D sensor heads.	96
Figure 4.9: Standard deviation for the (a) 1-D and (b) 2-D sensor heads showing the intra-tablet coating uniformity.....	97
Figure 4.10: OCT images of tablets at four velocities of the 2-D sensor head.....	97
Figure 5.1: Schematic of the fluid-bed coater, the OCT system and data processing.	111
Figure 5.2: (a) Surface model of a pellet.....	114
Figure 5.3: Schematic of the post-processing of coating thickness measurements.	116
Figure 5.4: OCT images of film-coated pellets at different process times (in minutes).....	118
Figure 5.5: Off-line OCT images of film-coated pellets sampled at different process times (in minutes).....	118
Figure 5.6: The mean coating thickness of B02 depending on the process time for a time interval T of 20 seconds.	119
Figure 5.7: Coating thickness of all three replication experiments as a function of	

process time and for a time interval T of 20 seconds.....	120
Figure 5.8: Coating uniformity as a function of process time for B01.....	121
Figure 5.9: Examples of coating thickness distribution (frequency) from B02....	123
Figure 5.10: Number weighted frequency distribution of the particle size of uncoated and fully coated pellets determined by the Qicpic particle size analyzer.	124
Figure 6.1: Front view of an uncoated round and bi-convex tablet model.	135
Figure 6.2: Schematic of the rotation stage.	136
Figure 6.3: OCT images (each 200 x 200 pixels) of film-coated tablets sampled at two different process times T (resulting in different coating thicknesses) and three different displacements Δx between successive A-scans.	137
Figure 6.4: Overview of coating thickness evaluation algorithm.	139
Figure 6.5: Definition of the region of interests (ROI) of the air/coating (AC) and coating/tablet core (CT) interfaces.	141
Figure 6.6: Example image and graph representation.....	142
Figure 6.7: Cross-section model of a bi-convex tablet.....	143
Figure 6.8: OCT images at different steps of the thickness evaluation algorithm.	146
Figure 6.9: Corrected OCT images from different stages of a coating process. ..	147
Figure 6.10: Comparison of manual (red squares) and automatic (black asterisks) determined coating thickness measurements.	149
Figure 6.11: Corrected OCT images for different angles of rotation α (rows) and beam displacements Δx (columns).....	150
Figure 6.12: Thickness measurements as a function of rotation angle for a beam displacement of 4.02 μm	151
Figure 7.1: Schematic of the OCT system.	162
Figure 7.2: (a) Schematic of the experimental setup.....	164
Figure 7.3: Overview of the coating thickness evaluation algorithm.	165
Figure 7.4: OCT images of different tablets acquired at a sensor head speed of 0.2 m/s.	166
Figure 7.5: Results of the different steps of the automatic coating thickness algorithm.	171
Figure 7.6: Selected OCT images of tablets sampled at four different process times.	172
Figure 7.7: Comparison of manual and automatic coating thickness measurements.	173

Figure 8.1: Schematic of OCT system. DC – directional coupler, FF – fiber focuser, BS – beamsplitter, M – mirror, FC – fiber coupler, DG – diffraction grating, L – lens, CCD – charged coupled device.	184
Figure 8.2: Schematic of the experimental setup.	187
Figure 8.3: Pictures of the experimental setup.	187
Figure 8.4: Overview of the coating thickness evaluation algorithm.	188
Figure 8.5: OCT images of different tablets acquired during the coating process.	189
Figure 8.6: Schematic of the extracted features used for the classification.....	190
Figure 8.7: Results of the different steps of the automatic coating thickness algorithm.	193
Figure 8.8: OCT images acquired in-line at different process times (in minutes) from B01.....	196
Figure 8.9: Coating thickness and coating mass as a function of process time...197	
Figure 8.10: RSD of coating thickness measurements per tablet of batch B01...198	
Figure 8.11: Coating thickness analysis of B01.....	199
Figure 8.12: Comparison of the results of three replication experiments (B01- B03).....	200
Figure 9.1: OCT images of capsules.	210
Figure 9.2: Monitoring of suspensions by means of OCT.....	212
Figure 9.3: En-face OCT images of a tablet produced by compressing pellets. ...	212

List of Tables

Table 2.1: Minimum required acquisition rate calculated from given pan coater specifications.....	31
Table 2.2: Requirements on the OCT system derived from the quality attributes of a film-coated tablet.....	36
Table 2.3: Specifications of the OCT system.....	39
Table 2.4: Specifications of the 1-D and 3-D sensor head.....	40
Table 3.1: Experimental results for the displacement angle α and the transverse beam displacements as a function of the sensor head velocity.....	68
Table 4.1: Tablets investigated during the off-line studies.....	86
Table 4.2: Composition of the enteric film coating suspension.....	86
Table 4.3: Transverse image size for the 1-D and 2-D sensor heads as a function of the sensor head speed.....	95
Table 5.1: Summary of the results for all three batches.....	122
Table 6.1: Coating thickness results determined automatically through application of the algorithm presented in this study.....	152
Table 6.2: Coating thickness results determined automatically through application of the algorithm presented in this study.....	153
Table 7.1: Listing of the used features.....	167
Table 8.1: Composition of the enteric coating suspension.....	183
Table 8.2: List of used features.....	191
Table 8.3: Classification error for LG and LG-HMM.....	194
Table 8.4: Counts of transitions between different classes and between the same class for all A-scans of the validation data.....	195
Table 8.5: Results of all three batches.....	201

Abbreviations

1-D	One-dimensional
2-D	Two-dimensional
3-D	Three-dimensional
AFM	Atomic force microscopy
API	Active pharmaceutical ingredient
ASA	Acetylsalicylic acid
CaSt	Calcium stearate
CCD	Charge-coupled device
CLSM	Confocal laser scanning microscopy
CMOS	Complementary metal-oxide-semiconductor
CPU	Central processing unit
CQA	Critical quality attribute
CUDA	Compute unified device architecture
DC	Direct current
DFT	Discrete Fourier transform
DP	Dynamic programming
EDX	Energy dispersive X-ray
FDA	Food and drug administration
FFT	Fast Fourier transform
FPGA	Field-programmable gate array
FWHM	Full-width at half maximum
GMP	Good manufacturing practice
GPGPU	General purpose graphics processing unit
GPU	Graphics processing unit
GSM	Glycerol monostearate
GUI	Graphical user interface
HMM	Hidden Markov model
IFFT	Inverse fast Fourier transform
IR	Infrared
LCI	Low-coherence interferometry
LG	Logistic regression
LM	Lactose monohydrate
LUS	Laser ultrasound

MCC	Microcrystalline cellulose
MRI	Magnetic resonance imaging
MVDA	Multivariate data analysis
NA	Numerical aperture
NDE	Non-destructive evaluation
NDT	Non-destructive testing
NIR	Near-infrared
NMR	Nuclear magnetic resonance
NU-FFT	Non-uniform fast Fourier transform
PAI	Photo-acoustic imaging
PAT	Process analytical technology
QbD	Quality by design
RAM	Random access memory
RECENDT	Research Center for Non-Destructive Testing
RSD	Relative standard deviation
SD	Standard deviation
SD-OCT	Spectral-domain optical coherence tomography
SEM	Scanning electron microscopy
SiO ₂	Silicone dioxide
SLD	Superluminescent diode
SNR	Signal to noise ratio
SVM	Support vector machine
TD-OCT	Time-domain optical coherence tomography
TPI	Terahertz pulse imaging
X _μ CT	X-ray computed microtomography

1

Introduction

Over the years, in pharmaceutical manufacturing numerous quality tests have been introduced to guarantee the quality and safe use of pharmaceutical products. Authorities encouraged the pharmaceutical industry to improve quality testing in general by implementing different measures to define the characteristics of a product, including concepts such as quality by design (QbD) and process analytical technology (PAT). The aim was to raise their interest in an in-depth understanding of processes and product characteristics. Implementing a suitable control strategy based on proper in-line monitoring techniques is essential in order to streamline processes, optimize production stages and assure quality. In particular, this applies to pharmaceutical coating processes. This chapter gives insight into pharmaceutical film coating, the monitoring of coaters and further presents the objective and content of this thesis.

1.1 Pharmaceutical Film Coating

Film coating represents a traditional and widely used unit operation in the pharmaceutical industry for solid dosage forms. In film coating, a thin continuous layer of solid is applied onto the surface of a tablet or a granule containing active

pharmaceutical ingredients (APIs) (Porter et al., 2009). Different methods can be deployed to obtain film coating. These include spraying liquid, dipping into liquid, precipitating from supercritical fluids or depositing a powder using an electrostatic technique, with spraying liquid being the most widely used method. As a rule, this process includes three basic steps: (1) An atomized liquid is sprayed on the target surface which is in continuous movement, (2) heated air flow is applied to maintain a controlled balance between spray and evaporation and, (3) the process continues until the desired amount of coating has been applied. The formulation of the film coating depends on the application. Film coatings are applied to pharmaceutical oral solid dosage forms for a number of purposes. At least three different coating categories can be distinguished by its function, namely immediate-release, modified-release and active coatings (as given in **Figure 1.1**). Immediate-release coating is primarily used for aesthetic purposes but may also be deployed to improve the product stability, to facilitate product identification and to achieve an improvement in product organoleptic characteristic (such as taste and odor). The main functionality of modified-release coating is to attain a change of the initial drug release kinetics that depends on the pH of the environment (see **Figure 1.2**). In addition, coatings are applied to realize fixed dose combinations using active coatings. An active coating contains an API in the coat to prevent interactions of different drugs and to combine different release behaviors in one single dosage form (Knop and Kleinebudde, 2013).

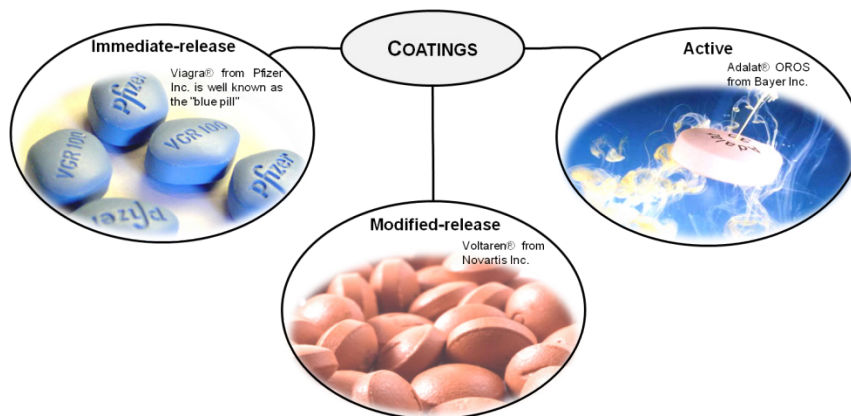


Figure 1.1: Types of pharmaceutical coatings.

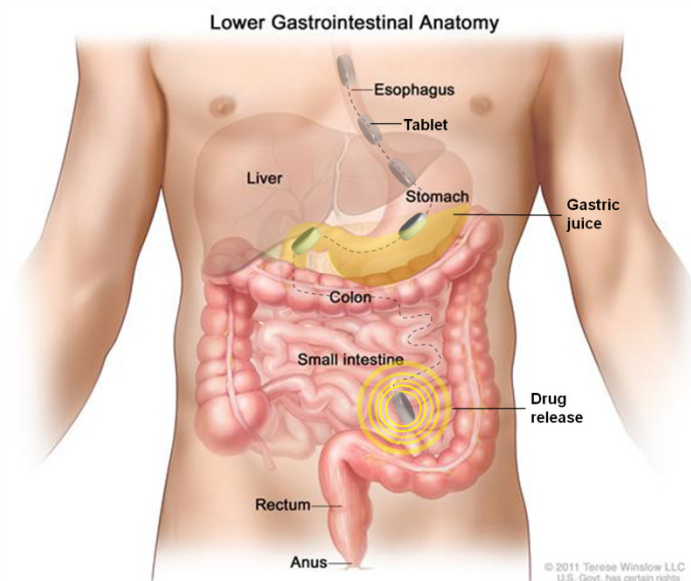


Figure 1.2: Function of modified-release film coatings. Adapted from (“Gastrointestinal Complications (PDQ®),” 2015).

The liquid coating system typically has the form of (1) polymers applied as organic solvent-based solution (e.g., modified-release film coating), (2) polymers applied as aqueous solution (e.g., immediate-release applications), (3) polymers applied as aqueous dispersion (e.g., modified-release film coating) or (4) various materials applied as hot/melts (e.g., modified-release and taste-masking applications). One of the main challenges of film coating is to apply the spray droplets uniformly and to dry at a proper evaporate rate. As there is a lack of understanding of how material and operating parameters impact product quality there are still serious problems. The most common tablet coating defects are: (1) overwetting/picking (i.e., part of the film coating is pulled off one tablet and is deposited on another), (2) twinning (i.e., two or more of the tablet cores stuck together), (3) orange peel (i.e., roughened film due to spray drying), (4) bridging (i.e., film coating lifts up out of the tablet logo), (5) cracking (i.e., internal stresses in the film), (6) coating thickness variations (i.e., within a batch due to poor process and equipment design) (6) coating inhomogeneity (i.e., either a visible variation in color from tablet to tablet or an unacceptable release profile for tablets), (7) tablet attrition/erosion (i.e., some portion of the product substrate exhibits a high level of friability), (8) core erosion (i.e., attrition due to overwetting of the tablet), (9) peeling (i.e., large pieces or flakes of the film coating fall off the tablet core), (10) loss of logo definition (i.e., tablet logo is no longer clearly legible), (11) core stability issues (i.e.,

discoloration of the core or degradation of the core active), and (12) tablet marking (i.e., black marking on the face of the tablets) (Porter et al., 2009).

As aforementioned, in a modern coating system usually the coating suspension is sprayed onto the product, with fluid-bed systems and pan coaters being the most widely applied coating processes. The decision whether to use the coating pan or the fluid-bed coating underlies the size of the product substrate and the batch size. Nowadays, the batch size of modern production-scale pan coaters ranges from 0.5 kg to 2000 kg. As a rule of thumb, if the product diameter is approximately 6 mm or less (e.g. pellets) the fluid-bed coater should be preferred. Most tablets are coated in a pan coater, though. The following sub-chapter gives insight into this specific method.

1.1.1 Pan Coating

A modern pan coating system has a cylindrical container rotating on a horizontal axis while a coating material will be sprayed onto the surface of a moving bed of the solid dosage form (see **Figure 1.3**). Usually a spray gun is used as a dispersion device which is mounted on an arm inside the pan and is directed towards the tablet bed. Basically, the coating process can be divided in three phases, i.e. spraying, wetting and drying (Muliadi and Sojka, 2014; Porter et al., 2009). The tablet stays only a split second inside the spraying zone, while the tablet bed is in constant motion. In this short timeframe the droplets are supposed to land on the moving tablet. The liquid from the coating suspension will rapidly evaporate due to the high temperature of the tablets; thus, only the dried solids will be left on the tablet. This process can be encouraged by (re)-directing the drying air towards the surface of the tablet bed to guarantee a good heat and mass transfer. There are different designs that picture various ways of the exhaust air exiting the pan, i.e., through side opening, from inside the tablet bed (through an immersion tube system) or through a perforated rotary pan. However, using a perforated pan is particularly advantageous, as it allows the drying air to flow through the tablet bed in co-flow with the injected spray, leading to a more efficient coating process (Suzzi et al., 2010).

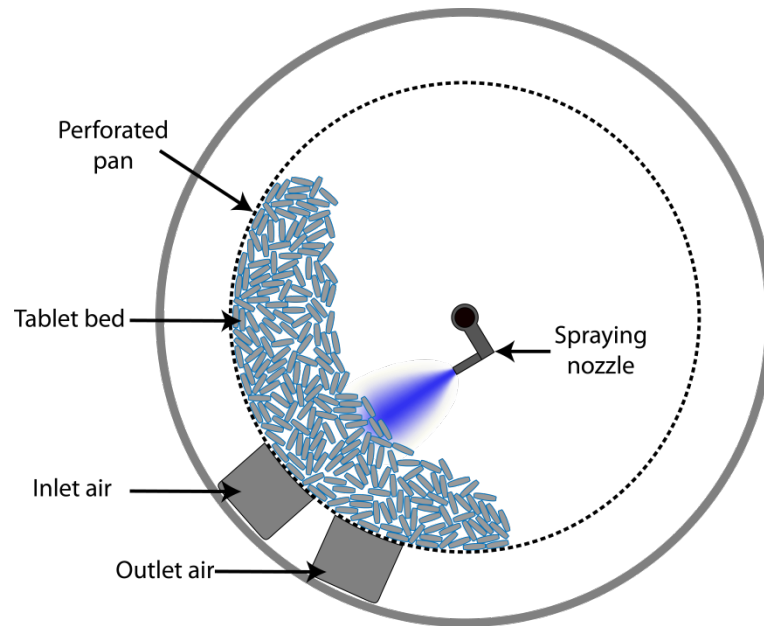


Figure 1.3: Cross-section model of a typical pan coater.

1.1.2 Fluid-Bed Coating

In a fluidized bed process particles are inserted into the product container and fluidized by an air current, as schematically shown in **Figure 1.4**. The brought in fluid will pass up through the holes between the solid particles. The state of the fluid bed depends on the air velocity and the powder properties, as described by Geldart, 1986; Kunii and Levenspiel, 1991. With low velocity, the bed remains in a solid state, as the drag force is insufficient to match the gravitational force of the particles. With increasing velocities the drag force moves the particles further away from each other and thereby increases the volume of the bed. At a certain point, when the drag force and the gravitational force are balanced, the bed becomes fluidized. The velocity required to obtain this state is called the minimal fluidization velocity. As the velocity increases the bed becomes more and more turbulent and increases in volume, until the air flow is too strong and starts to drag the particles (Kraume, 2012; Kumpugdee-Vollrath and Krause, 2011).

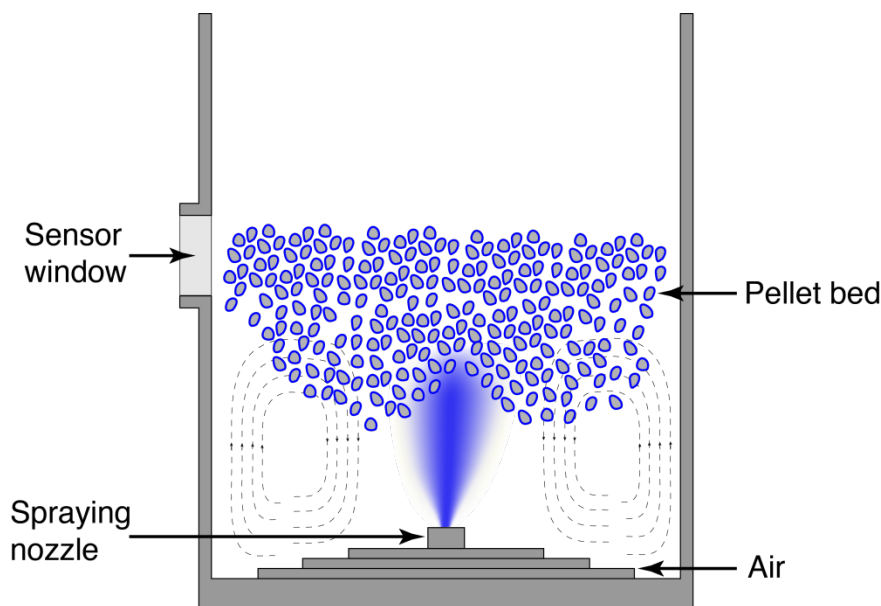


Figure 1.4: Cross-section model of a bottom-spray fluid-bed coater.

This process shows a good performance in terms of mixture and fluctuation of the particles, and can thus be used for coating. The coating suspension is pumped to a nozzle and sprayed on the particles to form a homogeneous coating layer. There are several methods to realize coating in a fluidized bed, differing by the position of the spraying nozzle (top-, bottom-, or tangential-spray) or the geometrical properties within the reactor (e.g., Wurster tube). The quality of the coating highly depends on the fluid velocity, which is influenced by the volumetric flow, the temperature of the solid material, the fluid and the coating substance, the spray pressure and the spray rate (Kraume, 2012; Kumpugdee-Vollrath and Krause, 2011). To guarantee a high quality outcome, each process needs to be closely monitored.

1.2 Coating Process Monitoring

Slight changes of the coating equipment and process parameters may impact the physicochemical properties of the film and may consequently affect the coating quality, especially when it comes to modified-release and active coatings. Thus, monitoring the coating process is of paramount importance to prevent output risks including batch reprocessing, batch reject and product recall. Characterizing coating properties such as coating thickness and uniformity is therefore of great

interest for the purpose of quality control and quality assurance.

The following traditional parameters, among others, have been used as benchmarks during the dosage form and coating development process for a long time:

- spatial dimensions,
- hardness,
- mass,
- content uniformity,
- porosity,
- friability,
- tensile strength,
- moisture content,
- disintegration time,
- dissolution profile, and
- weight gain.

However, fundamental properties of film-coated dosage forms, i.e., coating thickness and its uniformity, must be investigated to facilitate full understanding of the processing steps and the final product. These properties cannot be easily monitored without the help of a process analytical tool. PAT is described by the U.S. Food and Drug Administration (FDA) as

“a system for designing, analyzing, and controlling manufacturing through timely measurements (i.e., during processing) of critical quality and performance attributes of raw and in-process materials and processes, with the goal of ensuring final product quality” (FDA, 2004).

In general these sensors can be classified into four groups, according to their integration into the process stream (Bakeev, 2010):

- in-line: sample is not removed from the process and analyzed in the process.
- on-line: sample is diverted from the process, analyzed and returned.
- at-line: sample is removed and analyzed close to the process.
- off-line: sample is removed and analyzed away from the process in the lab.

In-line or on-line measurements usually provide the fastest results, whereas at-line and off-line are more time-consuming. Moreover, a tool for quality control of pharmaceutical coatings needs to be

- non-destructive,

Chapter 1: Introduction

- contactless,
- fast (in terms of data acquisition and data processing),
- robust,
- easy deployable,
- allow a calibration-free quantitative analysis of
 - mean coating thickness of single particles,
 - *intra*-particle coating variability: variation of coating thickness on a single particle; it is usually quantified by the standard deviation (SD) of several coating thickness measurements at different positions on one single particle (see **Figure 1.5(a)**), and
 - *inter*-particle coating variability; variation of mean coating thickness between particles within one batch; this is usually quantified by the SD of several mean coating thicknesses of different particles (see **Figure 1.5(b)**).

Numerous measurement techniques, recently reviewed by Knop and Kleinebudde, in 2013, have been applied to assure coating quality. Off-line and at-line analysis of film-coated particles were performed by several different analytical methods including confocal laser scanning microscopy (CLSM) (Laksmana et al., 2009; Ruotsalainen et al., 2003), atomic force microscopy (AFM) (Ringqvist et al., 2003), nuclear magnetic resonance (NMR) (Ensslin et al., 2008; Fyfe and Blazek-Welsh, 2000), scanning electron microscopy (SEM) (Koller et al., 2011; Liu et al., 2009), energy dispersive X-ray (EDX) (Liu et al., 2009), fluorescence microscopy (Andersson et al., 2000b) and acoustic microscopy (Bikiaris et al., 2012). Yet, these methods are currently not suitable for in- or on-line applications.

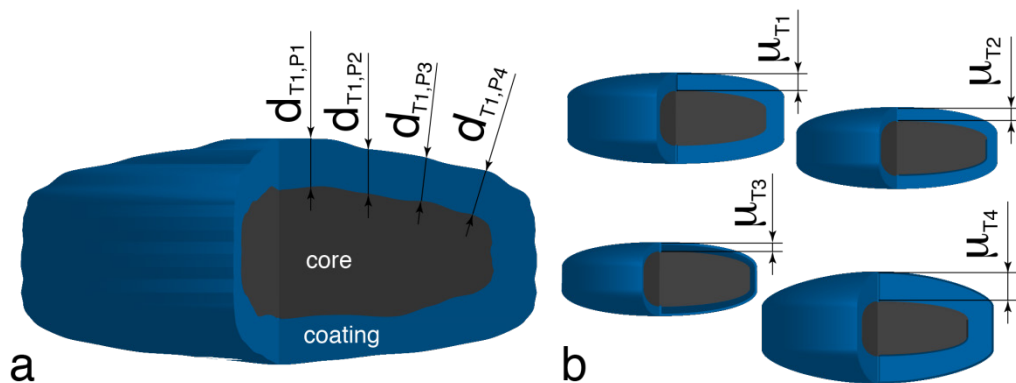


Figure 1.5: Schematic of film-coated tablets explaining inter- and intra-particle coating variability. (a) Intra-particle coating variability. d_{P1} to d_{P4} correspond to the coating thicknesses at position 1 ($P1$) to position 4 ($P4$), respectively. (b) Inter-particle coating variability. μ_{T1} to μ_{T4} correspond to the mean coating thicknesses of tablet 1 ($T1$) to tablet 4 ($T4$), respectively. These mean values are calculated from N_{Tj} (with $j = 1, \dots, M$; M is the number of analyzed tablets) thickness measurements $d_{Tj, Pi}$ (with $i = 1, \dots, N_{Tj}$)

In-line quality control of tablet coating processes has been investigated considerably more extensively than coating of pellets or granules. Most in-line measurements in pan coaters and fluid-bed coaters were performed via Raman or NIR spectroscopy. In combination with multivariate data analysis (MVDA), these methods allow real-time non-invasive and quantitative process monitoring. Such an MVDA model is developed by correlating reference measurements (using aforementioned off-line or at-line methods) from samples with the attenuation of the spectral features of one of the mutually exclusive constituents found either in the product substrate or in the coating formulation. The development of such multivariate calibration models that link the spectral information to a key parameter is tedious and even slight variations in the process conditions or in raw material properties may invalidate the model.

Several studies show the in-line characterization via NIR and Raman of weight gain (Andersson et al., 1999; Gendre et al., 2011b), coating thickness (Andersson et al., 2000a; Gendre et al., 2011b; Kirsch and Drennen, 1995; Lee et al., 2011; Möltgen et al., 2013; Müller et al., 2012; Pérez-Ramos et al., 2005; Römer et al., 2008; Romero-Torres et al., 2006) or release rate (Gendre et al., 2011a; Müller et al., 2012) for pellet and tablet coating. Particularly for tablet coating, Pérez-Ramos et al., 2005, noted that the dynamic motion of the tablets in a tumbling pan must

be taken into account when monitoring the process. They compared the tablet face film growth and the tablet band film growth on a bi-convex tablet and concluded that a larger face spends more time on average toward the spray gun relative to the band or edge. The difference in coating thickness between tablet face and band is thus statistically significant. This strengthens the assumption that the tablets have a preferred orientation when they pass the spray gun. Therefore, it is highly interesting to investigate the *intra*-particle coating variability. Beside the fact that NIR and Raman are in general not calibration-free, they only provide measurements representing the temporal and spatial average over a large number of particles. Therefore, these techniques cannot provide any information about single particles and local coating properties.

In the past years very few scientific papers dealt with a non-destructive calibration-free analysis of local coating properties by applying tomographic approaches. Tomographic methods provide spatially (transversally and axially) resolved information of a sample. Zeitler and Gladden, 2009 reviewed four tomographic techniques: X-ray computed microtomography (X μ CT), magnetic resonance imaging (MRI), terahertz pulse imaging (TPI) and optical coherence tomography (OCT). These techniques non-destructively resolve the three-dimensional structure of a dosage form. However, only TPI and OCT fulfill the requirements of an in-line sensor.

The characterization of pharmaceuticals have served as one of the core fields of development of TPI (Ho et al., 2009a, 2009b, 2008, 2007; Zeitler et al., 2007) TPI is highly suitable for the investigation of pharmaceuticals, since terahertz radiation easily penetrates the excipients typically used. The change in the refractive index of interfaces from different coating layers and the tablet core or substructures within the tablet leads to a contrast in the images. Shen and Taday, 2008, addressed TPI for the non-destructive inspection of pharmaceutical tablets. Analysis of the coating based on terahertz waveforms were used to determine the refractive index of the tablet surface, the coating thickness and the interface index. The interface index were related to a change in physical and chemical composition at the interface. It was emphasized that the measured time-domain terahertz signal is a coupling mixture of both structural and chemical features.

TPI's high potential as an in-line sensor was demonstrated by May et al., 2010. They successfully applied an in-line sensor for terahertz measurements of the film coating ranging from 40 μ m to 1 mm. However, the transversal and axial spatial

resolutions in TPI are limited to 50 μm and 40 μm , respectively. Since the coating thickness of most commercially-available pharmaceutical tablets ranges from 5 μm to 200 μm , a better axial resolution would be preferable. Moreover, TPI is limited in terms of acquisition speed to determine several thickness measurements per particle as required for the analysis of the *intra*-particle coating variability.

These problems may be avoided by using OCT, which is easily deployable and has a high data acquisition rate, a good transversal resolution and an extremely high axial resolution. OCT is a contactless non-destructive high resolution imaging technique that originates from the field of biomedicine with the main applications in ophthalmology (Sakata et al., 2009), cardiology (Bezerra et al., 2009), dermatology (Welzel, 2001), gastroenterology and endoscopy (Adler et al., 2009). Over the last years, the number of OCT applications in non-destructive testing and evaluation (NDT, NDE) of non-biological materials has substantially increased (Stifter, 2007).

Mauritz et al., 2010, discussed the imaging of pharmaceutical tables with OCT. They compared the detection of the coating thickness of cosmetic and modified-release coating using two different light sources. The applied light sources had a central wavelength of 930 nm and 1325 nm and a bandwidth of 100 nm and 130 nm, respectively. In addition, they addressed the absorption of near-infrared light. An exponential decay of the signal intensity in respect to the imaging depth can be observed, which corresponds to the Beer-Lambert law of absorption:

$$I_{\theta,l}(d) = I_0 e^{-\mu_{\theta,l}d}, \quad (1.1)$$

where $I_{\theta,l}$ is the attenuated intensity at angle θ and horizontal offset from the axis of rotation l , I_0 is the source intensity, μ is the absorption coefficient and d is the thickness of the object. Any additional losses (e.g., scattering) are omitted for simplicity (Zeitler and Gladden, 2009).

Moreover, they stated that the air/cosmetic coating interface has a very weak refractive index change along the surface and, thus, determining the coating thickness was rarely possible. In contrast, the thickness of the modified-release coating was identified due to two large refractive index changes. Mauritz et al., 2010, noticed that the resolution using the light source with a center wavelength at 930 nm is greater as expected by theory, but the imaging depth did not increase using a longer center wavelength.

Therefore, OCT offers an approach to directly measure the coating thickness and

could be a suitable alternative technology to monitor coating processes in-line. OCT allows the acquisition of one-, two- and three dimensional depth resolved image data of coatings (Wojtkowski, 2010). Such data facilitates the calculation of complete coating thickness maps of samples. Due to its high acquisition rate, it further allows the analysis of coating thickness variations on single particles (*intra*-particle variation) and between particles (*inter*-particle variation) during processing and in real-time.

1.3 Objective and Content of the Thesis

1.3.1 Objective

The focus of this thesis is put on

1. the development of an OCT system for in-line quality control of film-coated solid dosage forms, and
2. the application of an OCT system for monitoring coating processes.

Both points are performed in close collaboration with the Research Center for Non-Destructive Testing (RECENDT) GmbH (Linz, Austria). RECENDT currently deals with the technological fields of OCT, infrared spectroscopy (IR), THz technology (THz), laser ultrasound (LUS), and photoacoustic imaging (PAI). Within the context of this project RECENDT is responsible for the development of an OCT prototype suited for industrial needs. A prerequisite for the development of a prototype is a clear definition of the requirements. Therefore, the first part of the research aims to define the requirements for an OCT system used for in-line monitoring coating processes. This encompasses the declaration of a suitable mounting position of the OCT sensor in a coater, as this directly affects the requirements.

The main goal of this research is to demonstrate for the first time an OCT sensor for in-line monitoring of a coating process of randomly moving tablets and pellets in a pan coater and a fluid-bed coater, respectively. The main focus in this research is put on pan coaters and the coating of tablets, since this type of coater and this solid dosage form are mostly applied and used in the pharmaceutical industry. Yet, applying OCT as an in-line quality control tool requires not only a suitable mounting position in a coater, but also an automatic evaluation algorithm. The

purpose of such algorithm is to detect the samples and to determine the coating thickness in real-time. Its implementation is a significant challenge, but it is essential to make OCT workable for in-process applications. Apart from the development of an OCT system suitable for pharmaceutical application, the thesis is focused towards the development of algorithms suitable to compute representative parameters in real time.

1.3.2 Content

Initially, pharmaceutical film coating and the monitoring of such coating processes is introduced in chapter 1. This chapter further provides a motivation for the application of OCT as an in-line quality control tool. The concept of OCT is presented in chapter 2, which focuses on spectral-domain (SD-)OCT. SD-OCT is one of several variants of OCT - in this thesis only such systems are employed. In addition, chapter 2 introduces the concept of the OCT sensor head integration in a pan coating process, the definition of the requirements and the real-time OCT imaging. Several studies are performed to ascertain the needs and limitations of such an in-line quality control tool. These studies (as presented in chapter 3 and 4) in particular focus on motion effects that can arise in SD-OCT systems.

Chapter 5 outlines for the first time in-line monitoring of a pellet coating process by means of OCT. The direct integration of the OCT sensor head into a fluid-bed coating system allowed continuous monitoring of the coating growth. The coating thickness was then manually extracted from in-line OCT measurements.

An in-line monitoring tool requires an automated determination of the parameter of interest. Therefore, chapter 6 presents an algorithm for automated pharmaceutical tablet coating layer evaluation. Beside the segmentation of the coating layer, optical distortions due to refraction of the beam by the air/coating interface are corrected.

Before this algorithm can be applied on in-line measurements, tablets must be detected in an in-line OCT image. This is carried out by a classification of each depth measurement (i.e., A-scan) as shown in chapter 7. The algorithm is tested on OCT data acquired by moving the sensor head of the OCT system across a static tablet bed.

Chapter 8 demonstrates OCT for monitoring the coating growth of randomly moving tablets in a pan coating process. The OCT images are analyzed by a fully

automated algorithm (classification and coating layer evaluation). This fully automated algorithm is based on the developments from chapters 6 and 7.

A general conclusion about the application of OCT in the pharmaceutical industry is provided in chapter 9. This chapter further gives an outlook to future activities which should be undertaken to utilize the full potential of OCT in the pharmaceutical industry.

1.4 References

- Adler, D.C., Zhou, C., Tsai, T.-H., Schmitt, J., Huang, Q., Mashimo, H., Fujimoto, J.G., 2009. Three-dimensional endomicroscopy of the human colon using optical coherence tomography. *Opt. Express* 17, 784–796.
- Andersson, M., Folestad, S., Gottfries, J., Johansson, M.O., Josefson, M., Wahlund, K.G., 2000a. Quantitative analysis of film coating in a fluidized bed process by in-line NIR spectrometry and multivariate batch calibration. *Anal. Chem.* 72, 2099–108.
- Andersson, M., Holmquist, B., Lindquist, J., Nilsson, O., Wahlund, K.G., 2000b. Analysis of film coating thickness and surface area of pharmaceutical pellets using fluorescence microscopy and image analysis. *J. Pharm. Biomed. Anal.* 22, 325–39.
- Andersson, M., Josefson, M., Langkilde, F.W., Wahlund, K.G., 1999. Monitoring of a film coating process for tablets using near infrared reflectance spectrometry. *J. Pharm. Biomed. Anal.* 20, 27–37.
- Bakeev, K.A. (Ed.), 2010. *Process Analytical Technology: Spectroscopic Tools and Implementation Strategies for the Chemical and Pharmaceutical Industries*, Second Edi. ed. John Wiley & Sons, Ltd.
- Bezerra, H.G., Costa, M. a, Guagliumi, G., Rollins, A.M., Simon, D.I., 2009. Intracoronary optical coherence tomography: a comprehensive review clinical and research applications. *JACC Cardiovasc. Interv.* 2, 1035–1046.
- Bikiaris, D., Koutri, I., Alexiadis, D., Damtsios, a, Karagiannis, G., 2012. Real time and non-destructive analysis of tablet coating thickness using acoustic microscopy and infrared diffuse reflectance spectroscopy. *Int. J. Pharm.* 438, 33–44.

- Ensslin, S., Moll, K.P., Paulus, K., Mäder, K., 2008. New insight into modified release pellets - Internal structure and drug release mechanism. *J. Control. Release* 128, 149–56.
- FDA, 2004. Guidance for Industry. PAT - a framework for innovative pharmaceutical development, manufacturing, and quality assurance, Quality Assurance. US Department of Health, Rockville, MD.
- Fyfe, C., Blazek-Welsh, a. ., 2000. Quantitative NMR imaging study of the mechanism of drug release from swelling hydroxypropylmethylcellulose tablets. *J. Control. Release* 68, 313–333.
- Gastrointestinal Complications (PDQ®) [WWW Document], 2015. . Univ. Chichago. URL <http://www.uchospitals.edu/online-library/content=CDR62834> (accessed 2015/01/14).
- Geldart, D., 1986. Gas fluidization technology. Wiley, New York.
- Gendre, C., Boiret, M., Genty, M., Chaminade, P., Pean, J.M., 2011a. Real-time predictions of drug release and end point detection of a coating operation by in-line near infrared measurements. *Int. J. Pharm.* 421, 237–43.
- Gendre, C., Genty, M., Boiret, M., Julien, M., Meunier, L., Lecoq, O., Baron, M., Chaminade, P., Péan, J.M., 2011b. Development of a Process Analytical Technology (PAT) for in-line monitoring of film thickness and mass of coating materials during a pan coating operation. *Eur. J. Pharm. Sci.* 43, 244–250.
- Ho, L., Müller, R., Gordon, K.C., Kleinebudde, P., Pepper, M., Rades, T., Shen, Y., Taday, P.F., Zeitler, J.A., 2008. Applications of terahertz pulsed imaging to sustained-release tablet film coating quality assessment and dissolution performance. *J. Control. Release* 127, 79–87.
- Ho, L., Müller, R., Gordon, K.C., Kleinebudde, P., Pepper, M., Rades, T., Shen, Y., Taday, P.F., Zeitler, J.A., 2009a. Terahertz pulsed imaging as an analytical tool for sustained-release tablet film coating. *Eur. J. Pharm. Biopharm.* 71, 117–23.
- Ho, L., Müller, R., Gordon, K.C., Kleinebudde, P., Pepper, M., Rades, T., Shen, Y., Taday, P.F., Zeitler, J.A., 2009b. Monitoring the Film Coating Unit Operation and Predicting Drug Dissolution Using Terahertz Pulsed Imaging. *J. Pharm. Sci.* 98, 4866–4876.

- Ho, L., Müller, R., Römer, M., Gordon, K.C., Heinämäki, J., Kleinebudde, P., Pepper, M., Rades, T., Shen, Y.C., Strachan, C.J., Taday, P.F., Zeitler, J. a, 2007. Analysis of sustained-release tablet film coats using terahertz pulsed imaging. *J. Control. Release* 119, 253–61.
- Kirsch, J.D., Drennen, J.K., 1995. Determination of film-coated tablet parameters by near-infrared spectroscopy. *J. Pharm. Biomed. Anal.* 13, 1273–1281.
- Knop, K., Kleinebudde, P., 2013. PAT-tools for process control in pharmaceutical film coating applications. *Int. J. Pharm.* 457, 527–536.
- Koller, D.M., Hanneschläger, G., Leitner, M., Khinast, J.G., 2011. Non-destructive analysis of tablet coatings with optical coherence tomography. *Eur. J. Pharm. Sci.* 44, 142–148.
- Kraume, M., 2012. *Transportvorgänge in der Verfahrenstechnik: Grundlagen und apparative Umsetzungen.* Springer Berlin Heidelberg.
- Kumpugdee-Vollrath, M., Krause, J.-P., 2011. *Easy Coating, Studienbücher Chemie.* Vieweg + Teubner.
- Kunii, D., Levenspiel, O., 1991. *Fluidization Engineering,* Butterworth-Heinemann series in chemical engineering. Butterworth-Heinemann.
- Laksmana, F.L., Van Vliet, L.J., Hartman Kok, P.J. a, Vromans, H., Frijlink, H.W., Van der Voort Maarschalk, K., 2009. Quantitative image analysis for evaluating the coating thickness and pore distribution in coated small particles. *Pharm. Res.* 26, 965–76.
- Lee, M.-J., Seo, D.-Y., Lee, H.-E., Wang, I.-C., Kim, W.-S., Jeong, M.-Y., Choi, G.J., 2011. In line NIR quantification of film thickness on pharmaceutical pellets during a fluid bed coating process. *Int. J. Pharm.* 403, 66–72.
- Liu, F., Lizio, R., Schneider, U.J., Petereit, H.-U., Blakey, P., Basit, A.W., 2009. SEM/EDX and confocal microscopy analysis of novel and conventional enteric-coated systems. *Int. J. Pharm.* 369, 72–8.
- Mauritz, J.M.A., Morrisby, R.S., Hutton, R.S., Legge, C.H., Kaminski, C.F., 2010. Imaging Pharmaceutical Tablets with Optical Coherence Tomography. *J. Pharm. Sci.* 99, 385–391.
- May, R.K., Evans, M.J., Zhong, S., Warr, I., Gladden, L.F., Shen, Y., Zeitler, J.A., 2010. Terahertz in-line sensor for direct coating thickness measurement of

- individual tablets during film coating in real-time. *J. Pharm. Sci.* 100, 1535–1544.
- Möltgen, C.-V., Herdling, T., Reich, G., 2013. A novel multivariate approach using science-based calibration for direct coating thickness determination in real-time NIR process monitoring. *Eur. J. Pharm. Biopharm.* 85, 1056–63.
- Muliadi, A.R., Sojka, P.E., 2014. A review of pharmaceutical tablet spray coating. *At. Sprays* 20, 611–638.
- Müller, J., Brock, D., Knop, K., Axel Zeitler, J., Kleinebudde, P., 2012. Prediction of dissolution time and coating thickness of sustained release formulations using Raman spectroscopy and terahertz pulsed imaging. *Eur. J. Pharm. Biopharm.* 80, 690–697.
- Pérez-Ramos, J.D., Findlay, W.P., Peck, G., Morris, K.R., 2005. Quantitative analysis of film coating in a pan coater based on in-line sensor measurements. *AAPS PharmSciTech* 6, 127–136.
- Porter, S., Sackett, G., Liu, L., 2009. Chapter 33 - Development, Optimization, and Scale-up of Process Parameters: Pan Coating. In: Qiu, Y., Chen, Y., Zhang, G.G.Z., Liu, L., Porter, W.R. (Eds.), *Developing Solid Oral Dosage Forms*. Academic Press, San Diego, pp. 761–805.
- Ringqvist, A., Taylor, L.S., Ekelund, K., Ragnarsson, G., Engström, S., Axelsson, A., 2003. Atomic force microscopy analysis and confocal Raman microimaging of coated pellets. *Int. J. Pharm.* 267, 35–47.
- Römer, M., Heinämäki, J., Strachan, C., Sandler, N., Yliruusi, J., 2008. Prediction of tablet film-coating thickness using a rotating plate coating system and NIR spectroscopy. *AAPS PharmSciTech* 9, 1047–1053.
- Romero-Torres, S., Pérez-Ramos, J.D., Morris, K.R., Grant, E.R., 2006. Raman spectroscopy for tablet coating thickness quantification and coating characterization in the presence of strong fluorescent interference. *J. Pharm. Biomed. Anal.* 41, 811–819.
- Ruotsalainen, M., Heinämäki, J., Guo, H., Laitinen, N., Yliruusi, J., 2003. A novel technique for imaging film coating defects in the film-core interface and surface of coated tablets. *Eur. J. Pharm. Biopharm.* 56, 381–388.

- Sakata, L.M., Deleon-Ortega, J., Sakata, V., Girkin, C.A., 2009. Optical coherence tomography of the retina and optic nerve - a review. *Clin. Exp. Ophthalmol.* 37, 90–99.
- Shen, Y.-C., Taday, P.F., 2008. Development and Application of Terahertz Pulsed Imaging for Nondestructive Inspection of Pharmaceutical Tablet. *IEEE J. Sel. Top. Quantum Electron.* 14, 407–415.
- Stifter, D., 2007. Beyond biomedicine: a review of alternative applications and developments for optical coherence tomography. *Appl. Phys. B* 88, 337–357.
- Suzzi, D., Radl, S., Khinast, J.G., 2010. Local analysis of the tablet coating process: Impact of operation conditions on film quality. *Chem. Eng. Sci.* 65, 5699–5715.
- Welzel, J., 2001. Optical coherence tomography in dermatology: a review. *Ski. Res. Technol.* 7, 1–9.
- Wojtkowski, M., 2010. High-speed optical coherence tomography: basics and applications. *Appl. Opt.* 49, 30–61.
- Zeitler, J.A., Gladden, L.F., 2009. In-vitro tomography and non-destructive imaging at depth of pharmaceutical solid dosage forms. *Eur. J. Pharm. Biopharm.* 71, 2–22.
- Zeitler, J.A., Shen, Y., Baker, C., Taday, P.F., Pepper, M., Rades, T., 2007. Analysis of Coating Structures and Interfaces in Solid Oral Dosage Forms by Three Dimensional Terahertz Pulsed Imaging. *J. Pharm. Sci.* 96, 330–340

2

Optical Coherence Tomography¹

Optical coherence tomography is an emerging, non-invasive and contactless optical imaging modality, which enables cross-sectional tomographic visualization of the internal microstructure of (semi-) transparent and turbid materials. Since its invention in the late 1980s and early 1990s, the first applications were related to the evaluation of biological tissue, i.e. the real-time, *in vitro* imaging of retinal structure as well as of an arterial wall with fatty-calcified plaque regions (Huang et al., 1991). The biomedical field pushed the development of OCT towards *in vivo* diagnostics with the main applications in ophthalmology (Sakata et al., 2009), cardiology (Bezerra et al., 2009), dermatology (Welzel, 2001) gastroenterology (Testoni and Mangiavillano, 2008) and endoscopy (Adler et al., 2009) Not surprisingly, in the last twenty years OCT was primarily applied in the biomedicine. However, the unique characteristics of OCT, namely to provide high resolution depth-resolved information also in strongly scattering media,

¹ This chapter is partly based on Markl, D., Sacher, S., Khinast, J.G., 2015. Optical Coherence Tomography: An alternative methodology to monitor pharmaceutical coating processes. G.I.T. Lab. J. Eur. 7-8 17–19., and on Markl, D., Hanneschläger, G., Sacher, S., Buchsbaum, A., Pescod, R., Baele, T., Khinast, J.G., 2015. In-line Characterization of Pharmaceutical Coatings by Means of Optical Coherence Tomography. Pharm. Technol. *to be submitted*

make it an attractive method for a broad spectrum of research topics and applications beyond biomedicine (Stifter, 2007). These applications include off-line characterization of paper (Prykäri et al., 2010), silicon integrated-circuits (Serrels et al., 2010), food (Verboven et al., 2013), fiber composites (Stifter et al., 2008) and pharmaceutical tablets (D M Koller et al., 2011). Moreover, OCT was recently demonstrated as an in-line quality control tool for monitoring printed electronics (Alarousu et al., 2013) and in-line characterization of multi-layered foils (Hanneschläger et al., 2011). These publications reveal the immense potential of OCT. This chapter starts with providing a general theoretical description of OCT. Furthermore, the requirements for an OCT system for the in-line application and the design parameters are described. In addition, this chapter presents the newly developed system together with a general analysis of the coating layer and the real-time implementation of the OCT image reconstruction process.

2.1 Theory

Cross-sectional or three-dimensional (3-D) reconstruction of the investigated material is obtained by measuring the echo time delay and magnitude of backscattered light. Due to the high speed of light, a direct measurement of “optical echoes” is impossible. An interferometric technique with ultrashort light pulses or partially coherent light is therefore used to generate depth scans with a resolution of several micrometers.

In OCT an optical beam emitted by a broadband light source (i.e., high spatial but low temporal coherence) is focused onto the surface of the sample as schematically illustrated in **Figure 2.1**. The amplitude of the electromagnetic radiation in the Michelson interferometer (Michelson and Morley, 1887) is divided into a reference and a sample beam by a beamsplitter. The main part of the sample light beam is directly reflected by the surface of the sample. A substantial fraction of the light penetrates into the sample structure (i.e., coating) and is then reflected back by subsequent interfaces separating two media with different index of refraction, e.g. coating and core material. The light wave returning from the object is thus a superposition of waves arriving with different delays $\tau = z/c$ (c is the speed of light in vacuum). The electric fields returning from the object ($E_S(t)$) and the reference arm ($E_R(t)$) superimpose and yield

$$E(t) = E_R(t) + \sum_n E_S(t + \tau_{S_n}). \quad (2.1)$$

In the experiment one could measure the light intensity $I(t) = \langle E^*(t)E(t) \rangle$ at the output of the interferometer. This intensity may be expressed in terms of the depth z as

$$\begin{aligned} I(z) = \frac{\rho}{8} \gamma(z) & \left(R_R + \sum_n R_{S_n} \right) \\ & + \frac{\rho}{8} \sum_{m \neq n} \sqrt{R_{S_n} R_{S_m}} (\gamma[2(z_{S_n} - z_{S_m})] \\ & + \gamma[-2(z_{S_n} - z_{S_m})]) \\ & + \frac{\rho}{4} \sum_{m \neq n} \sqrt{R_R R_{S_n}} (\gamma[2(z_R - z_{S_n})] + \gamma[-2(z_R - z_{S_n})]) \end{aligned} \quad (2.2)$$

where ρ is the responsivity of the detector (in Ampere/Watt), R_R and R_{S_n} are the reflectivity of the reference mirror and of the n th layer of the sample, respectively. The goal of OCT is the reconstruction of the function $\sqrt{R_S(z_s)}$ from the interferometric measurements. z_R and z_{S_n} are the pathlength variables respectively in the reference and in the sample arm measured from the beamsplitter (Izatt and Choma, 2008). $\gamma(z)$ is the complex degree of coherence. Low-coherence light as used in OCT systems can be characterized by the coherence length l_c , which is the average length interval in which the light wave oscillates in a predictable way. The coherence length is inversely proportional to the frequency bandwidth of the light. Using a low-coherence light, interference is only observed when the path lengths of the reference and sample arms coincide within the coherence length of the light.

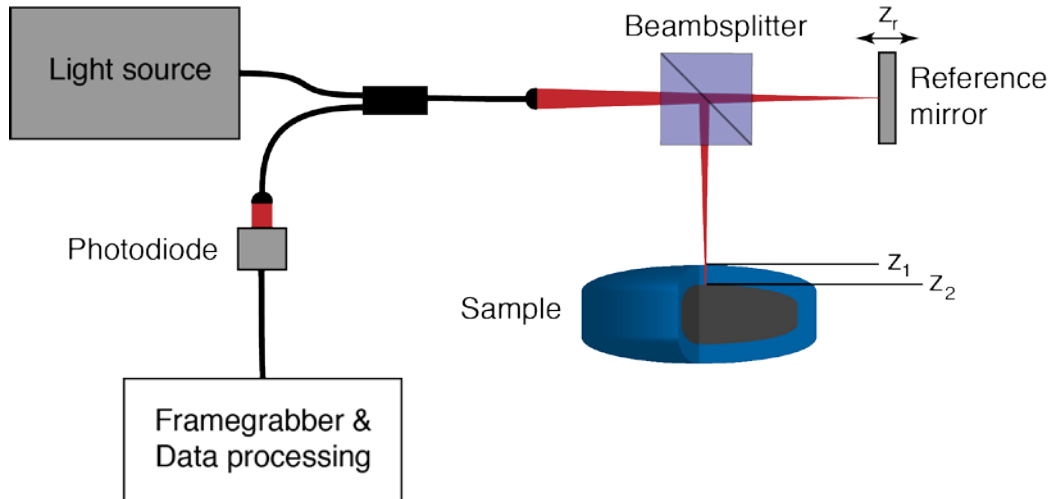


Figure 2.1: Simplified block diagram of a low-coherence interferometry system.

Usually a Gaussian-shaped light source spectrum is assumed as it approximates the shape of actual light sources and also has useful properties for the analysis and processing of the signals. In particular, a normalized Gaussian-shaped spectrum and its Fourier transform yielding the coherence function is defined as

$$S(k) = \frac{1}{\Delta k \sqrt{\pi}} e^{-\left[\frac{(k-k_c)}{\Delta k}\right]^2} \xleftrightarrow{\mathcal{F}} \gamma(z) = e^{-z^2 \Delta k^2}, \quad (2.3)$$

where k_c and Δk represent the central wavenumber and the spectral bandwidth of the light source spectrum, respectively. Δk corresponds to the half-width of the spectrum at $1/e$ of its maximum. The coherence function $\gamma(z)$ dominates the point spread function (PSF) in OCT imaging systems and is typically characterized by its full width at half maximum (FWHM) value, which is the definition of the coherence length l_c of the light source. For such a Gaussian-shaped spectrum, the coherence length is defined in wavelength terms as

$$l_c = \frac{4 \ln(2)}{\pi} \frac{\lambda_c^2}{\Delta \lambda}, \quad (2.4)$$

with $\lambda_c = 2\pi/k_c$ and $\Delta \lambda$ as the central wavelength and the spectral bandwidth of the light source spectrum, respectively. The coherence length determines the axial resolution of an OCT system. Considering that the light travels back and forth in an interferometer, the axial resolution is expressed by the formula

$$\delta z = \frac{l_c}{2} = \frac{2 \ln(2)}{\pi} \frac{\lambda_c^2}{\Delta \lambda}. \quad (2.5)$$

One has to note that in a dispersive medium the coherence time (and the axial resolution) needs to be divided by the group refractive index n_g of the medium to obtain the actual value. More details about the theory of OCT can be found in (Bouma et al., 2008; de Boer, 2008; Fercher, 2010; Fercher et al., 2003; Fujimoto and Drexler, 2008; Fujimoto, 2003; Hu and Rollins, 2008; Leitgeb et al., 2004; Tomlins and Wang, 2005; Wojtkowski et al., 2005; Wojtkowski, 2010)

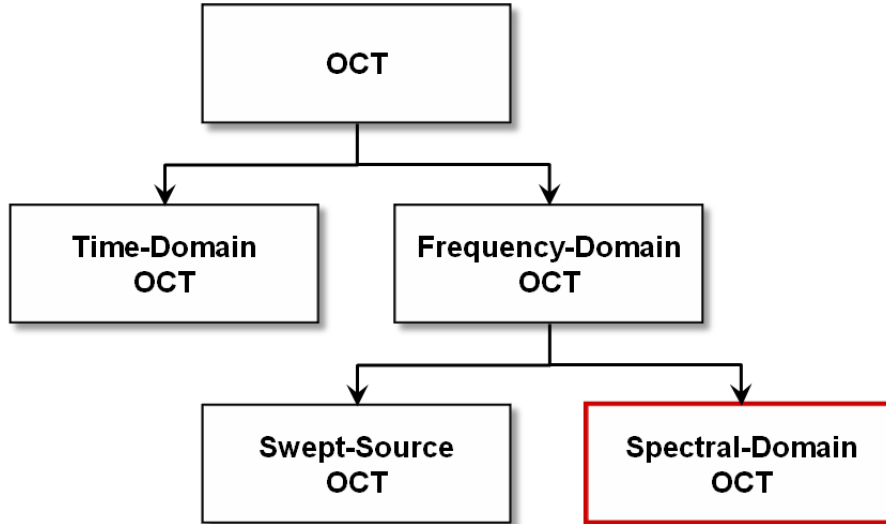


Figure 2.2: Different variants of OCT systems.

2.2 Spectral-Domain OCT

The depth-resolved OCT signal (as expressed in Eq. (2.5)) can be acquired either in time-domain or in Fourier-domain (see Figure 2.2). The latter approach offers advantages in terms of imaging speed and sensitivity (Choma et al., 2003) and allows video-rate imaging (An et al., 2011), whereas the acquisition in time-domain permits dynamic focusing and shows constant sensitivity over the whole depth range (Leitgeb et al., 2003; Nemeth et al., 2013).

In time-domain the magnitude and echo time delay of light can be measured by scanning the reference arm (varying z_r in **Figure 2.1**) and demodulating the interference signal measured with a single-channel photoreceiver. In fact, the mechanical movement of the reference mirror is rather time consuming and may lead to mechanical instabilities and noise.

There are two types of Fourier-domain detection. One approach, known as swept-source OCT uses an interferometer with a narrow bandwidth, frequency swept light source and a detector measuring the interference output as a function of time. The second approach employs an interferometer with a low-coherence light source and measures the interference spectrum using a spectrometer and a high-speed line-scan camera. In this work all measurements were performed with the second approach, namely spectral-domain (SD-)OCT systems. In SD-OCT, information of reflective

points along the sample beam is coded in the frequency of the oscillatory signal, which is a modulation of the original spectrum $S_0(k)$ of the light source. Eq. (2.2) can thus be rewritten in the Fourier domain (as a function of wavenumber) to the following form:

$$\begin{aligned}
 S(k) = & \frac{\rho}{4} S_0(k) \left(R_R + \sum_n R_{S_n} \right) && \text{"DC terms"} \\
 & + \frac{\rho}{4} S_0(k) \sum_{m \neq n} \sqrt{R_{S_n} R_{S_m}} \cos[2k(z_{S_n} - z_{S_m})] && \text{"Auto-correlation terms"} \\
 & + \frac{\rho}{2} S_0(k) \sum_n \sqrt{R_R R_{S_n}} \cos[2k(z_R - z_{S_n})] && \text{"Cross-correlation terms"}
 \end{aligned}
 \tag{2.6}$$

This result is composited by three distinct components (Izatt and Choma, 2008):

- “DC-Terms”: This component is often referred to as constant, because it is usually dominated by the reference reflectivity. It is a path length-independent offset to the detector current. This term is usually removed by subtracting a reference spectrum from the interference spectrum.
- “Auto-correlation terms”: Interference occurring between the different sample reflectors are represented by this component. In typical OCT systems this auto-correlation component appears as an artifact in the measurements.
- “Cross-correlation terms”: This is the desired component for OCT imaging, as it is proportional to the square root of the sample reflectivities.

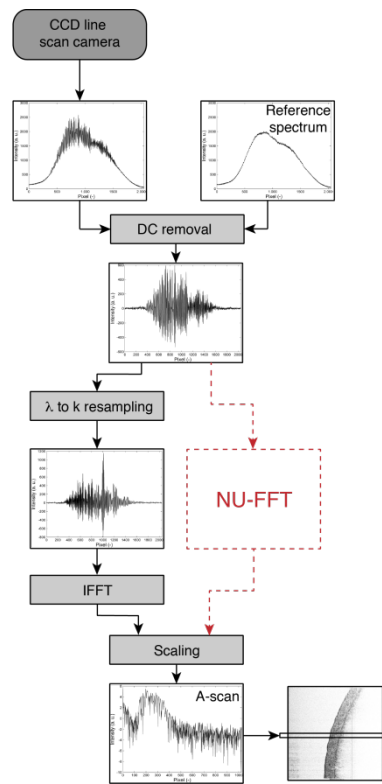


Figure 2.3: The transformation of the OCT data from frequency-domain to time-domain.

The axial structure of the sample under investigation is reconstructed by applying an inverse Fourier transformation yielding $\tilde{I}(z) = \mathcal{F}^{-1}\{S(k)\}$ an approximation of Eq. (2.2). The transformation of the OCT data from frequency-domain to time-domain is usually performed by applying an inverse fast Fourier transform (IFFT),

as illustrated in **Figure 2.3**. The implementation of this transformation is explained in more detail in section 2.6. For practical reasons the interference spectrum is typically measured as a function of optical wavelengths instead of optical frequencies. This causes a non-linear distribution ($k \sim 1/\lambda$) of optical frequencies of the detected signal and further limits the useful imaging range by a depth dependent sensitivity fall-off. The Fourier transformation requires a constant distance between adjacent wavenumbers and thus, the measured spectrum needs to be interpolated on a uniform grid (as a function of wavenumbers). However, this still causes a sensitivity fall-off, which can be further improved by signal post-processing, such as by applying a non-uniform fast Fourier transformation (NU-FFT). A NU-FFT was also applied in this study and is presented in detail in Appendix A.

The reconstructed signal $\tilde{I}(z)$ represents one single depth profile. Such one-dimensional (1-D) axial measurements are labeled as A-scans. However, in OCT a sequence of A-scans is acquired at successive transversal positions allowing the generation of two-dimensional (2-D) images (labeled as B-scans), as illustrated in **Figure 2.4**. A transverse displacement between successive A-scans can either be carried out with the aid of some scanning means (causes a deflection of the optical beam), such as a galvanometer mirror, or by a relative transverse movement of the sample to the sensor head. Moreover, 3-D volumetric data can be created by acquiring sequential B-scan images via a raster pattern scan of the incident optical beam.

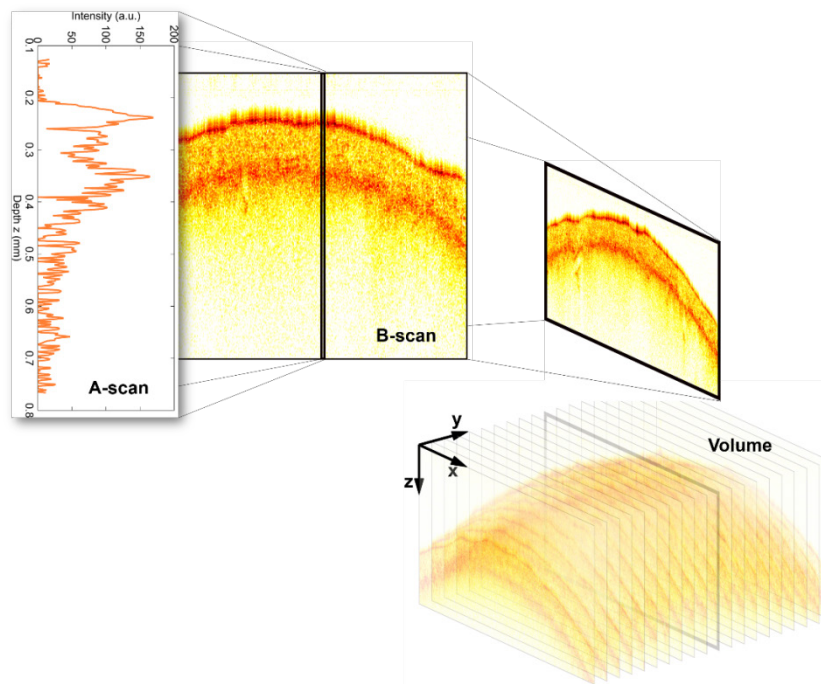


Figure 2.4: OCT data of film-coated tablets. Each B-scan is synthesized by several hundred A-scans. The volume is composed by several hundred B-scans; only every 25th B-scan is displayed.

2.3 Integration of OCT Sensor in Coating Process

The positioning of the OCT sensor in the coating process is of paramount importance regarding the quality of the measurements. The measurement position affects the design of the OCT system and specifically the design of the sensor head. There are several aspects, which must be considered:

- The distance between sensor head and sample must be within a specified range. The distance is defined by the focal length and the construction of the sensor head. The range, in which the distance between sample and sensor head may vary is specified by the imaging depth. This is typically in the range of 1 to 3 mm.
- Resistant against dust. Spraying and attrition of the solid dosage forms generate dust.
- Insensitive to vibrations. The solid dosage forms are moving during the coating, which might cause machine vibrations.

Especially the first aspect limits the number of possible positions in a coater. The design of the OCT system focuses on the coating of tablets, which is typically performed in a pan coater. Therefore, the specifications on the OCT system were defined for the monitoring of tablets in a pan coater.

A suitable mounting position of the OCT sensor head is outside of the perforated pan (see **Figure 2.5**). This is discussed in more detail in chapter 8. Assuming that the beam is aligned with the center of the holes of the perforated pan, a certain number of A-scans are acquired within one hole (henceforth referred to as A-scans/hole). This number depends on the hole diameter and on the acquisition rate of the OCT system. Since the hole diameter is fixed, only the acquisition rate can be adjusted to guarantee a certain number of A-scans/hole, denoted as N_{\min} .

In the following, the required minimum acquisition rate f_{\min} is discussed on the basis of the specifications of pan coaters from L.B. Bohle (Ennigerloh, Germany). These coaters typically have pans with round perforations and correspond to the standard format Rv 3-5 (i.e., hole diameter D_{hole} of 3 mm and hole spacing H of 5 mm).

f_{\min} is directly influenced by the circumferential speed of the perforated pan, which is given by

$$v = \frac{\pi n D_{\text{drum}}}{60}. \quad (2.7)$$

n is the number of revolutions of the pan and D_{drum} is the diameter of the pan. Using Eq. (2.7) the minimum required acquisition rate can be calculated by

$$f_{\min} = \frac{N_{\min} v}{D_{\text{hole}}}. \quad (2.8)$$

Table 2.1 lists the parameters discussed for various pan coaters of L.B. Bohle and the associated extreme values. At least 50 A-scans/solid dosage form are required to accurately analyze a solid dosage form. It is assumed that only 1/3 of the A-scans/hole provide information about a solid dosage form. Therefore, N_{\min} is

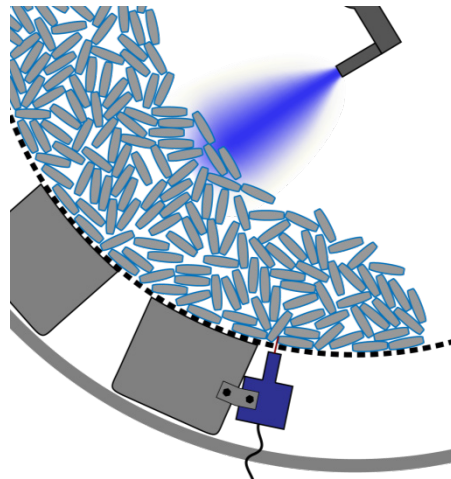


Figure 2.5: Mounting position of the OCT sensor head (highlighted in dark blue) in a pan coater. The entire cross-section model of a pan coater is depicted in **Figure 1.3**.

specified as $3 \cdot 50 = 150$. This results in a minimum acquisition rate of 45 kHz (for BFC 400 in **Table 2.1**), which needs to be considered for the design of the OCT system as discussed in section 2.4.

Table 2.1: Minimum required acquisition rate calculated from given pan coater specifications. The data of the L.B. Bohle tablet coaters were taken from (Müller, 2006). The minimum (referred to as min) and the maximum (referred to as max) values are the extreme values of the apparatuses. The minimum required acquisition rate is determined for a minimum number of A-scans/hole of 150.

				Laboratory			Pilot			Production		
				BFC 5	BFC 10	Tripan 10	Tripan 25	Tripan 50	BFC 40	BFC 200	BFC 400	BFC 600
Pan diameter	D_{drum}		(m)	0.316	0.396	0.406	0.546	0.696	0.660	1.100	1.430	1.640
Number of revolutions	n	min	(1/min)	5	5	2	2	2	2	1	0.5	0.5
		max	(1/min)	40	40	18	18	18	17	15	12	10
Circumferential speed	v	min	(m/s)	0.083	0.104	0.043	0.057	0.073	0.069	0.058	0.037	0.043
		max	(m/s)	0.662	0.829	0.383	0.515	0.656	0.587	0.864	0.898	0.859
Minimum required acquisition rate	f_m	min	(kHz)	4.136	5.184	2.126	2.859	3.644	3.456	2.880	1.872	2.147
		max	(kHz)	33.091	41.469	19.132	25.730	32.798	29.374	43.197	44.925	42.935

2.4 OCT System Design

One of the goals of this work was to develop an OCT system enabling the acquisition of 1-D, 2-D and 3-D data for in-line and off-line analysis of film-coated particles. First, some design parameters relevant for this work are discussed in section 2.4.1. The requirements specifying the design parameters are elaborated in section 2.4.2. On the basis of these requirements, an OCT system has been developed, which is presented in section 2.4.3.

2.4.1 Design Parameters

In the following several design parameters of the OCT system are discussed:

- The transverse resolution is in general specified as the ability of an optical system to distinguish two points separately in a plane perpendicular to the probing light beam. The transverse resolution is thus defined as the FWHM diameter considering a Gaussian beam profile and no movement of the beam. The FWHM diameter can be calculated by

$$\delta x = 2w_0 = \frac{4\lambda_c f}{\pi d}, \quad (2.9)$$

where w_0 is the beam waist radius, f is the focal length and d is the beam diameter of the lens, as illustrated in **Figure 2.6**. In contrast to the axial resolution, the transverse resolution depends on the imaging aperture. This decoupling of the transverse from the axial resolution in terms of the imaging aperture is one of the main advantages of OCT over other optical depth discrimination methods (e.g., confocal microscopy). More details about a Gaussian beam are provided in Appendix B.

- Increasing the numerical aperture ($NA = f/d$) of the objective increases the transverse resolution by reducing the focal spot size, but it decreases the depth of focus, quantified by the confocal parameter b (see **Figure 2.6**). The confocal parameter is defined twice the Rayleigh length given as

$$b = \frac{\pi \delta x^2}{2\lambda_c}. \quad (2.10)$$

The transverse resolution can be improved by increasing NA of the objective, but at the same time this decreases the depth of focus. Therefore,

the design of the objective is a trade-off between axial resolution and depth of focus.

- The finite resolution of the spectrometer gives a sensitivity drop as a function of the depth of the image. The spectral resolution is a measure of the ability of a spectrometer to distinguish between two closely spaced peaks in the spectrum. Typically the effect of finite spectral resolution is modeled by convolving the ideal spectral interferogram from Eq. (2.6) with a Gaussian function having half-maximum width $\delta_r \lambda$, which is interpreted as the FWHM spectral resolution. There occurs an exponential drop of the sensitivity as a function of depth, which can be understood as reduced visibility of the high-frequency interference fringes associated with large object depths. This dependency can be characterized by defining a depth at which the sensitivity has decreased by a factor of $\frac{1}{2}$ or 6 dB in optical SNR (signal to noise ratio) units (Izatt and Choma, 2008):

$$z_{6\text{dB}} = \frac{2 \ln(2)}{\pi} \frac{\lambda_c^2}{\delta_r \lambda}. \quad (2.11)$$

Rearranging Eq. (2.11) gives the spectral resolution as a function of $z_{6\text{dB}}$ and λ_c . The double of the focal depth b is used for $z_{6\text{dB}}$ to obtain a design parameter for the spectrometer:

$$\delta_r \lambda = \frac{2 \ln(2)}{\pi} \frac{\lambda_c^2}{2b}. \quad (2.12)$$

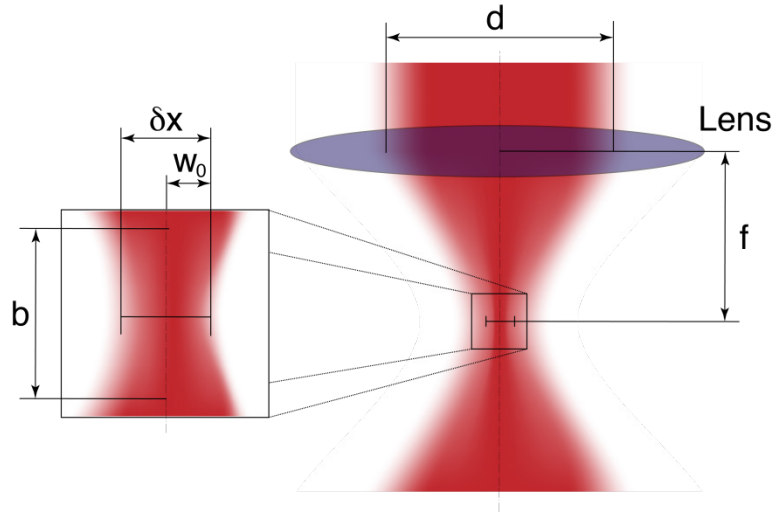


Figure 2.6: Illustration of transverse resolution, beam waist radius and the confocal parameter.

- The imaging depth z_{\max} is limited by the number of CCD pixels M , the center wavelength and the bandwidth of the light source. Based on the Nyquist theorem, the imaging depth is defined as (Izatt and Choma, 2008)

$$z_{\max} = M \frac{\lambda_c^2}{4\Delta\lambda}. \quad (2.13)$$

The minimum number of CCD pixels can thus be calculated by transforming Eq. (2.13) to

$$M = \frac{4\Delta\lambda}{\lambda_c^2} z_{\max}. \quad (2.14)$$

2.4.2 OCT System Requirements

Such an OCT system needs to fulfill specific requirements, which were derived from relevant quality attributes of film-coated tablets. The selection of the quality attributes considered for this analysis was based on the concept of Quality by Design (QbD). In a pharmaceutical QbD approach, characteristics are identified that are critical to the quality from the patient's perspective. Such characteristics are translated into drug product critical quality attributes (CQAs) (Yu et al., 2014). Only CQAs affecting the requirements of the OCT systems and which are relevant for modified-release or active coatings were considered in this elaboration. The selected quality attributes and its effect on the OCT system requirements are listed in **Table 2.2**.

A discussion of the quality attributes and their impact on the requirements for the OCT measurement system required a translation of existing regulations. The pharmacopoeia defines standards for quality, storage, testing and labeling. The US Pharmacopeia was used as basis for this elaboration.

A detailed specification of the layer thickness of tablet coatings is not covered in the US Pharmacopeia. The functionality of the coating must be verified by a standardized dissolution test as described in The United States Pharmacopeial Convention, 2011a. The test can be regarded as successful if a large proportion of the active ingredient was released after a certain time (e.g., 75% after 30 minutes). Since this definition is very imprecise, it cannot be converted directly to a specification of the coating layer thickness. The standard for content uniformity of dosage units (The United States Pharmacopeial Convention, 2011b) conveys information, which can be translated into the specification of the coating thickness.

Although this guideline needs to be considered only for active coatings, it provides a good basis for the definition of the requirements for the OCT measurement system. The definition is grounded on the deviation of the mass of a tablet or of the coating from the specified mass (label claim). A standard deviation of the coating composition to the specified mass of 6.5% must be maintained as stated in the guideline. This standard deviation can be converted into a standard deviation for the coating thickness. This was carried out for different dimensions of spherical, round and bi-convex tablets as presented in Appendix C. In this case, an average standard deviation of 6% was calculated. This means that a coating thickness of 100 μm must stay within 94 and 106 μm in order to comply with the guidelines. Therefore, the OCT measurement system should have a very high axial resolution ($< 5 \mu\text{m}$) enabling the measurement of coatings with such accuracy.

This approach has also been used in order to define of the requirements relative to the detection of defects in the coating. It was assumed that a defect in the coating is equivalent to a thinner coating layer, and therefore causes a degradation of the drug effect.

It is known from literature that the coating on the tablet band tends to be thinner than on the tablet faces (Freireich et al., 2011; Ho et al., 2008; Pérez-Ramos et al., 2005). It is thus advantageous to determine the coating thickness of tablet face and band separately. In addition, the curvature of bi-convex tablets need to be determined enabling the correction of distortions, which would induce an error in the thickness measurements. In order to determine the location and the curvature of the tablet, at least 50 A-scans per solid dosage form are required.

Chapter 2: Optical Coherence Tomography

Table 2.2: Requirements on the OCT system derived from the quality attributes of a film-coated tablet

Quality attribute	Potential effect of failure	Potential cause of failure	Control detection	Requirement on OCT System			Note	
Dissolution	Reduced drug product efficacy	Deviation of actual coating thickness to desired thickness	Coating thickness	Axial resolution	δz (μm)	<5	6% of typical coating thickness	
				Depth of focus (confocal parameter)	b (μm)	<300	Maximum of coating thickness is < 300 μm	
Uniformity	Inter-tablet coating uniformity	Reduced drug product efficacy	Variation of coating thickness between tablets	Coating thickness	Axial resolution	δz (μm)	<5	6% of typical coating thickness
					Depth of focus (confocal parameter)	b (μm)	<300	Maximum of coating thickness is < 300 μm
	Intra-tablet coating uniformity	Reduced drug product efficacy	Impurities, inclusion of air, density variation	Defects	Axial resolution	δz (μm)	<5	6% of typical coating thickness
					Lateral resolution	δx (μm)	<10	
		Variations between tablet faces and tablet band	Orientation of tablet	A-Scans per solid dosage form	(-)	50	Preliminary results show that at least 50 A-Scans per solid dosage form are required.	
		Coating variation on tablet face (bi-convex tablet shape)	Surface curvature	A-Scans per solid dosage form	(-)	50	Preliminary results show that at least 50 A-Scans per solid dosage form are required.	

2.4.3 Developed OCT System

A new OCT system was developed in close collaboration with the Research Center for Non-Destructive Testing (RECENDT) GmbH (Linz, Austria) on the basis of the presented design parameters. The basic setup of such a SD-OCT system is schematically illustrated in **Figure 2.7** and a picture of the setup is provided in **Figure 2.8**. This system is modularly designed allowing the separation and exchange of the sensor head. A superluminescent diode (SLD) Broadlighter (Superlum Diodes Ltd., Carrigtwohill, Co. Cork, Ireland) is employed as a light source, which operates at a central wavelength of 832 nm and has a FWHM spectral bandwidth of 75 nm. The light exiting the light source passes a directional coupler DC (Thorlabs). Either the optical fiber of the 1-D, 2-D or 3-D sensor head can be mounted on the DC. In-line monitoring was usually carried out by the 1-D sensor head, whereas the 3-D sensor head was applied for off-line investigations. OCT images using the 1-D sensor head can only be generated by introducing an external movement of either the sensor head or the sample.

On the contrary, the 3-D sensor head allows the reconstruction of depth-resolved cross-sections or volumes by scanning the probing beam laterally across the sample with the aid of galvanometer mirrors GM1 and GM2 (Cambridge Technologies) and sub-sequent acquisition of depth scans at successive lateral positions. Only a 1-D and 3-D sensor head is available in our current setup. However, disabling one galvanometer mirror (e.g., GM1) in the 3-D sensor head allows the acquisition of 2-D OCT images. The light emerging the fiber in the sensor heads is split at a non-polarizing bulk beam splitter BS (splitting ratio 50/50, Thorlabs) into a reference and a probe beam. The probe beam is focused by a fiber focuser FF (OZ Optics Ltd., Ottawa, Ontario, Canada, $f = 40$ mm) in the 1-D sensor head, and by an achromatic lens L1 (Thorlabs, $f = 36$ mm) in the 3-D sensor head. The light back reflected from both reference and sample is directed towards the spectrometer via the coupler DC. The spectrometer consists of a fiber collimator FC (OZ Optics, diameter = 20 mm), a transmissive diffraction grating DG (Wasatch Photonics Inc., Logan, Utah, USA, 1200 lines/mm), an achromatic lens L3 (Thorlabs, $f = 100$ mm) and a line scan camera with a 2048 pixel CCD array (Atmel Aviiva, $14 \times 28 \mu\text{m}^2$ pixel size, 12 bit resolution). The output voltage of each CCD pixel is proportional to the number of photons hitting an individual pixel accumulated during the CCD exposure time. The exposure time can be varied for each

experiment.

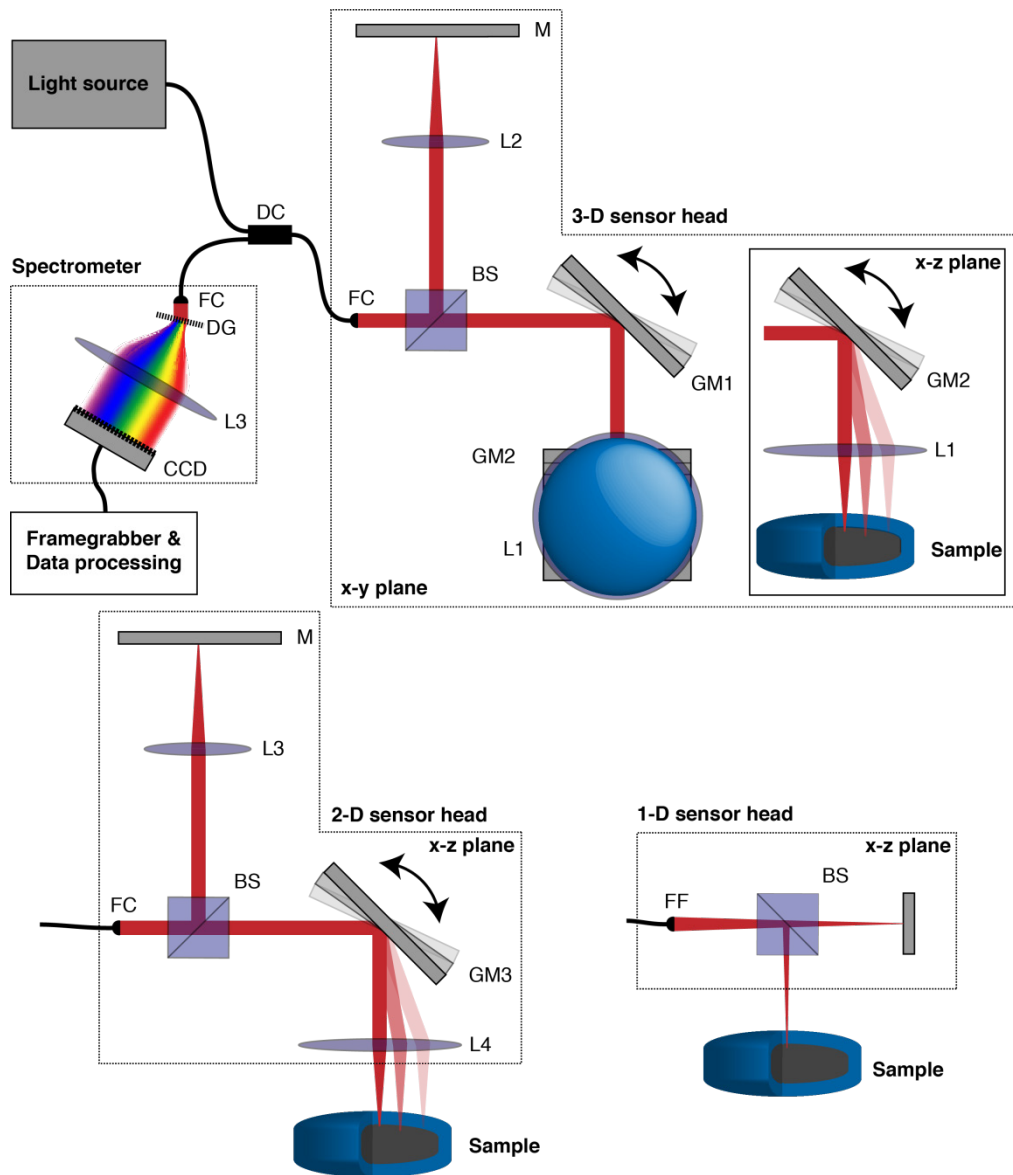


Figure 2.7: Schematic of an SD-OCT system. Schematic of the experimental design. The 1-D, 2-D and 3-D sensor head can be easily exchanged. The 3-D sensor head could be used as 2-D sensor head by disabling one galvanometer mirror. DC—directional coupler, FC—fiber collimator, BS—beamsplitter, GM_x—galvanometer mirror, FF—fiber focuser, L_x—lens, M—mirror, DG—diffraction grating, and CCD—charged coupled device.



Figure 2.8: Picture of the developed OCT system.

Specifications of the newly developed OCT system are summarized in **Table 2.3**. These figures slightly deviate from the requirements due to limitations in terms of costs and available components. The minimum required acquisition rate is given as 45 kHz as discussed in section 2.3. Since some parameters of the OCT system depend on the optical components of the sensor head, these parameters are listed separately in **Table 2.4**. One has to mention that the requirements as listed in **Table 2.2** were specifically considered for the design of the 1-D sensor head as this sensor head is applied for in-line quality control.

Table 2.3: Specifications of the OCT system.

Center wavelength	λ_c	(nm)	832
Spectral bandwidth (FWHM)	$\Delta\lambda$	(nm)	75
Acquisition rate (minimum)	f_{\min}	(kHz)	45
CCD pixels	M	(-)	2048
Imaging depth	z_{\max}	(mm)	4.73
Axial resolution	δz	(μm)	4.07

Table 2.4: Specifications of the 1-D and 3-D sensor head.

			1-D sensor head	3-D sensor head
Beam diameter at lens	d	(mm)	3	4
Focus length	f	(mm)	40	36
Depth of focus	b	(μm)	376.7	171.6
Transverse resolution	δx	(μm)	14.1	9.6
Spectral resolution	$\delta \lambda$	(nm)	0.41	0.89

2.5 Analysis of Coating Thickness

Measuring the delay time between the reflections of the coating surface and the coating/material core interface allows us to determine the coating thickness directly under consideration of the refractive index of the coating material. A number of studies have already demonstrated the application of OCT for measuring the coating thickness (D M Koller et al., 2011; Mauritz et al., 2010).

The acquisition of 3-D OCT data of film-coated tablets using the 3-D sensor head as presented in section 2.4.3 makes it possible to reconstruct the tablet core and the coating layer (see **Figure 2.9**). The detection of the tablet core and the

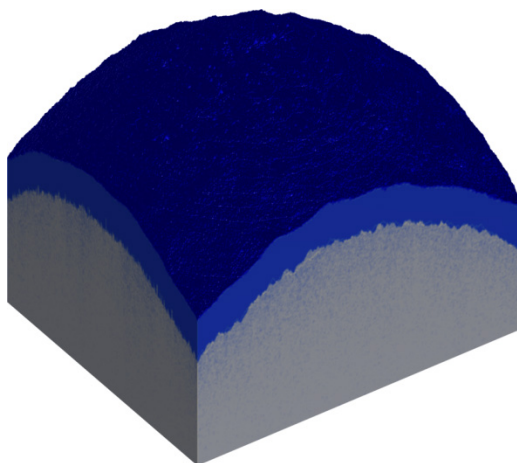


Figure 2.9: Reconstruction of a film-coated tablet from 3-D OCT data. The blue volume corresponds to the coating, the gray one to the tablet core.

coating layer was carried out by applying the algorithm as presented in chapter 0 on each acquired B-scan. Such data allows the analysis of local coating thickness variations, of the coating roughness as well as the roughness of the tablet core. A better analysis of said data can be performed on the basis of thickness maps and histograms as presented in **Figure 2.10**. The thickness maps of tablets allow the analysis of the distribution of the polymer film on the tablet face. High thickness variations most likely correspond to recesses in the tablet core, which are filled by coating. This hypothesis needs to be investigated in more detail and is subject of

further research. A more specific investigation of the coating distribution on the tablet face can be performed by examining the histograms. The longer tail at process start is in general caused by the resolution limit of the OCT sensor. With increasing process time the data follows a normal distribution and finally covers a thickness range from 43.3 μm to 93.4 μm for this example.

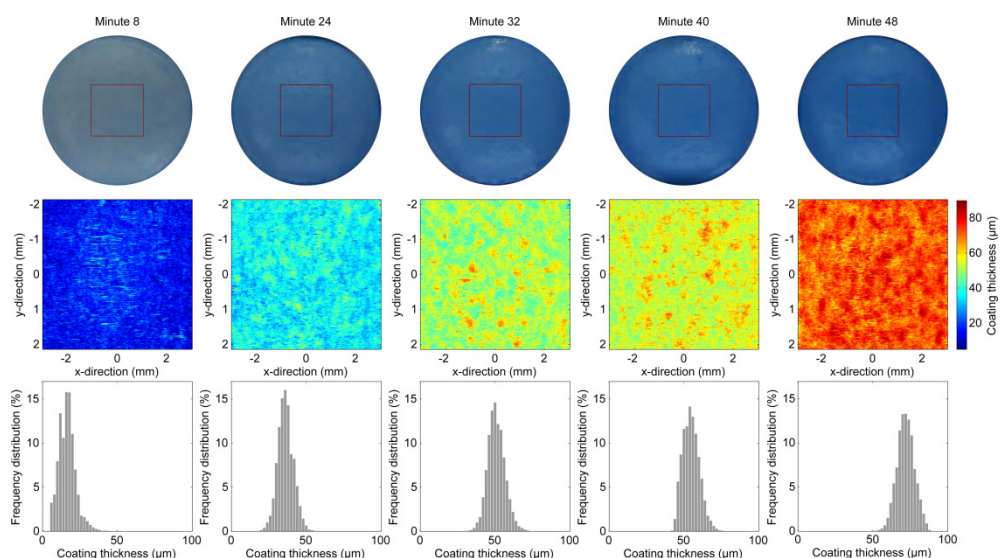


Figure 2.10: Off-line investigation of film-coated tablets (periodically sampled from a pan coating process) using a colored modified-release coating solution. The top row shows pictures of tablets sampled at different process times (after 8, 24, 32, 40 and 48 minutes of process duration). Coating thickness maps (second row) were calculated from off-line OCT measurements covering an area of $6.04 \times 4.27 \text{ mm}^2$ (497×600 pixel) as highlighted with a red rectangle in the tablet pictures. The thickness distribution per sample is depicted in the third row.

2.6 Real-time OCT Imaging

The application of OCT as an in-line sensor requires the calculation of the B-scan from the measured spectrum and further the coating thickness from the OCT image in real-time. The new developed setup enables the generation of 60.000 A-scans per second. A very fast digital signal processing is required to exploit the full potential of such a high acquisition rate. Current central processing units (CPUs) are not capable of processing the OCT signals with such a throughput, and thus limit the sample rate dramatically. Data processing speeds were improved by parallel processing using multi-core CPU (G. Liu et al., 2009; Probst et al., 2010) and field-programmable gate array (FPGA) (Desjardins et al., 2009; Ustun et al., 2008) implementations. The rapid development of general purpose computing on graphics processing units (GPGPU) introduced a revolution in numerical calculations and has made it possible to implement heavy-duty OCT data and image processing.

The full transformation process from the frequency-domain to time-domain data (see **Figure 2.3**) is implemented on a commercial graphics processing unit (GPU), distributing the necessary calculations to many stream processors operating in parallel. Similar implementation are already available in the literature for both streams (see **Figure 2.3**): using interpolation and IFFT (Van der Jeught et al., 2015; Watanabe and Itagaki, 2015), and using NU-FFT (Chan and Tang, 2010; Zhang and Kang, 2010).

Figure 2.11 shows the flowchart of real-time OCT imaging. The GPU is programmed through NVIDIA's compute unified device architecture (CUDA) technology (NVIDIA, 2014a). Initially, a spectral interference image with a size of 2048 x 1000 pixels (2048 pixels from the CCD line scan camera; 1000 A-scans are captured in one chunk) and a resolution of 16 bit is captured and transferred to the GPU memory. In the first step on the GPU, the type of data is converted from a 16 bit integer to a 32 bit floating point. This is carried out together with the DC removal, where a stored reference spectrum is subtracted from the measured interference spectrum. This is followed by either the λ to k remapping (which is implemented by a linear interpolation) and the IFFT or the NU-FFT. In both implementations, the FFT processing is performed using NVIDIA's CUDA FFT library CUFFT (NVIDIA, 2014b). Finally, after scaling the OCT data for a better visualization, the image (1024 x 1000 pixels) is transferred back to the CPU memory, displayed and stored.

The estimated computing time between data transfer to the GPU memory and the data transfer back from the GPU of the λ to k remapping and the IFFT was 9.3 ms. Using the NU-FFT, the estimated computation time increases to 23.0 ms. This was performed on a 64 bit operating system using an Intel(R) Core(TM) i7-3770K CPU at 3.5 GHz, 16 GB RAM and a NVIDIA GeForce GTX 660 Ti. Consequently, the real-time imaging can only be achieved using the linear interpolation and the IFFT for a frame interval of 16 ms (using the CCD line scan camera at 60 kHz as given in **Table 7.1**). However, the image quality is strongly enhanced by the NU-FFT and thus improves the performance of the data evaluation algorithm, which determines the coating thickness from the OCT images. This algorithm as it is described in chapter 0, 0 and 0 is also partly implemented on the GPU, but is out of the scope of this thesis and will be presented in a further study.

In addition, the current CUDA implementation is coupled with a software, which allows the configuration of the algorithms and OCT system and visualization and storage of the data. This software is implemented in C# and uses the .NET 4.5 platform. **Figure 2.12** shows several screenshots of the graphical user interface (GUI). This GUI enables the user to start and stop the acquisition. Furthermore, it allows the configuration of the OCT system and the adjustment of settings of the algorithm (e.g., selecting a color map for visualization, switching between linear interpolation/IFFT and NU-FFT).

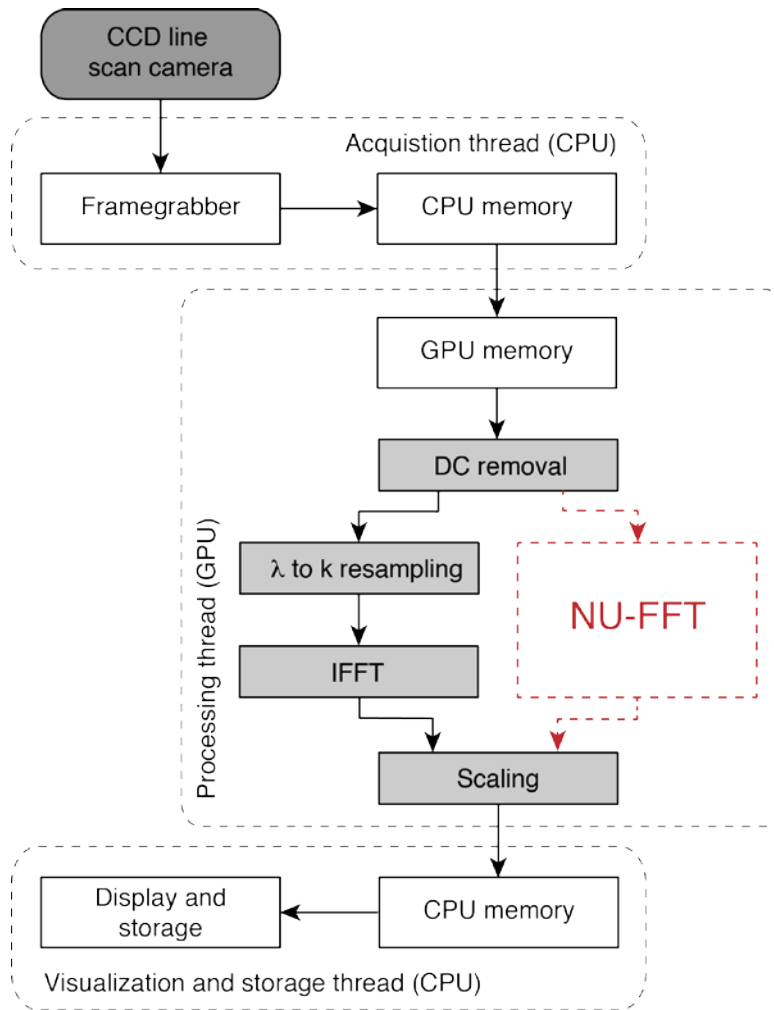


Figure 2.11: CPU-GPU architecture. A linear interpolation for the wavelength (λ) to wavenumber (k) resampling is currently implemented. The user can switch between the classic resampling and the NU-FFT in run-time.

- Chan, K.K.H., Tang, S., 2010. High-speed spectral domain optical coherence tomography using non-uniform fast Fourier transform. *Biomed. Opt. Express* 1, 1309–1319.
- Choma, M., Sarunic, M., Yang, C., Izatt, J., 2003. Sensitivity advantage of swept source and Fourier domain optical coherence tomography. *Opt. Express* 11, 2183.
- Desjardins, A.E., Vakoc, B.J., Suter, M.J., Yun, S.-H., Tearney, G.J., Bouma, B.E., 2009. Real-time FPGA processing for high-speed optical frequency domain imaging. *IEEE Trans. Med. Imaging* 28, 1468–72.
- Freireich, B., Ketterhagen, W.R., Wassgren, C., 2011. Intra-tablet coating variability for several pharmaceutical tablet shapes. *Chem. Eng. Sci.* 66, 2535–2544.
- Hanneschläger, G., Nemeth, A., Hofer, C., Goetzloff, C., Reussner, J., Wiesauer, K., Leitner, M., 2011. Optical coherence tomography as a tool for non destructive quality control of multi-layered foils. In: 6th NDT in Progress 2011. International Workshop of NDT Experts, Prague, p. Paper 7.
- Ho, L., Müller, R., Gordon, K.C., Kleinebudde, P., Pepper, M., Rades, T., Shen, Y., Taday, P.F., Zeitler, J.A., 2008. Applications of terahertz pulsed imaging to sustained-release tablet film coating quality assessment and dissolution performance. *J. Control. Release* 127, 79–87.
- Huang, D., Swanson, E.A., Lin, C.P., Schuman, J.S., Stinson, W.G., Chang, W., Hee, M.R., Flotte, T., Gregory, K., Puliafito, C.A., et al., 1991. Optical coherence tomography. *Science* (80-.). 254, 1178–1181.
- Izatt, J.A., Choma, M.A., 2008. Theory of Optical Coherence Tomography. In: Drexler, W., Fujimoto, J.G. (Eds.), *Optical Coherence Tomography: Technology and Applications*. Springer Verlag Berlin Heidelberg, pp. 47–72.
- Koller, D.M., Hanneschläger, G., Leitner, M., Khinast, J.G., 2011. Non-destructive analysis of tablet coatings with optical coherence tomography. *Eur. J. Pharm. Sci.* 44, 142–148.
- Leitgeb, R., Hitzenberger, C., Fercher, A., 2003. Performance of fourier domain vs time domain optical coherence tomography. *Opt. Express* 11, 889.

- Liu, G., Zhang, J., Yu, L., Xie, T., Chen, Z., 2009. Real-time polarization-sensitive optical coherence tomography data processing with parallel computing. *Appl. Opt.* 48, 6365–6370.
- Markl, D., Zettl, M., Hanneschläger, G., Sacher, S., Leitner, M., Buchsbaum, A., Khinast, J.G., 2014. Calibration-free in-line monitoring of pellet coating processes via optical coherence tomography. *Chem. Eng. Sci.*
- Mauritz, J.M.A., Morrisby, R.S., Hutton, R.S., Legge, C.H., Kaminski, C.F., 2010. Imaging Pharmaceutical Tablets with Optical Coherence Tomography. *J. Pharm. Sci.* 99, 385–391.
- Michelson, A.A., Morley, E.W., 1887. Relative motion of Earth and luminiferous ether. *Am. J. Sci.* 333, 833–845.
- Müller, R., 2006. Systematische Untersuchung zur Einstellung der Prozessparameter im Scale-Up Prozess für die Bohle Film Coater. Heinrich-Heine-Universität Düsseldorf.
- Nemeth, A., Gahleitner, R., Hanneschläger, G., Pfandler, G., Leitner, M., 2012. Ambiguity-free spectral-domain optical coherence tomography for determining the layer thicknesses in fluttering foils in real time. *Opt. Lasers Eng.* 50, 1372–1376.
- Nemeth, A., Hanneschläger, G., Leiss-Holzinger, E., Wiesauer, K., Leitner, M., 2013. Optical Coherence Tomography – Applications in Non-Destructive Testing and Evaluation. In: Kawasaki, M. (Ed.), *Optical Coherence Tomography*.
- NVIDIA, 2014a. *CUDA C Programming Guide Version 6.5*.
- NVIDIA, 2014b. *CUFFT Library User’s Guide Version 6.5*.
- Probst, J., Hillmann, D., Lankenau, E., Winter, C., Oelckers, S., Koch, P., Hüttmann, G., 2010. Optical coherence tomography with online visualization of more than seven rendered volumes per second. *J. Biomed. Opt.* 15, 26014.
- Prykäri, T., Czajkowski, J., Alarousu, E., Myllylä, R., 2010. Optical coherence tomography as an accurate inspection and quality evaluation technique in paper industry. *Opt. Rev.* 17, 218–222.
- Sakata, L.M., Deleon-Ortega, J., Sakata, V., Girkin, C.A., 2009. Optical coherence tomography of the retina and optic nerve - a review. *Clin. Exp. Ophthalmol.* 37, 90–99.

Chapter 2: Optical Coherence Tomography

- Serrels, K.A., Renner, M.K., Reid, D.T., 2010. Optical coherence tomography for non-destructive investigation of silicon integrated-circuits. *Microelectron. Eng.* 87, 1785–1791.
- Stifter, D., 2007. Beyond biomedicine: a review of alternative applications and developments for optical coherence tomography. *Appl. Phys. B* 88, 337–357.
- Stifter, D., Wiesauer, K., Wurm, M., Schlotthauer, E., Kastner, J., Pircher, M., Göttinger, E., Hitzenberger, C.K., 2008. Investigation of polymer and polymer/fibre composite materials with optical coherence tomography. *Meas. Sci. Technol.* 19, 074011.
- The United States Pharmacopeial Convention, 2011a. (711) Dissolution. Stage 6 Harmonization.
- The United States Pharmacopeial Convention, 2011b. (905) Uniformity of Dosage Units. Stage 6 Harmonization.
- Ustun, T.E., Iftimia, N. V, Ferguson, R.D., Hammer, D.X., 2008. Real-time processing for Fourier domain optical coherence tomography using a field programmable gate array. *Rev. Sci. Instrum.* 79, -.
- Van der Jeught, S., Bradu, A., Podoleanu, A.G., 2015. Real-time resampling in Fourier domain optical coherence tomography using a graphics processing unit. *J. Biomed. Opt.* 15, 030511.
- Verboven, P., Nemeth, A., Abera, M.K., Bongaers, E., Daelemans, D., Estrade, P., Herremans, E., Hertog, M., Saeys, W., Vanstreels, E., Verlinden, B., Leitner, M., Nicolai, B., 2013. Optical coherence tomography visualizes microstructure of apple peel. *Postharvest Biol. Technol.* 78, 123–132.
- Watanabe, Y., Itagaki, T., 2015. Real-time display on Fourier domain optical coherence tomography system using a graphics processing unit. *J. Biomed. Opt.* 14, 060506.
- Welzel, J., 2001. Optical coherence tomography in dermatology: a review. *Ski. Res. Technol.* 7, 1–9.
- Yu, L.X., Amidon, G., Khan, M. a, Hoag, S.W., Polli, J., Raju, G.K., Woodcock, J., 2014. Understanding pharmaceutical quality by design. *AAPS J.* 16, 771–83.

Zhang, K., Kang, J.U., 2010. Graphics processing unit accelerated non-uniform fast Fourier transform for ultrahigh-speed, real-time Fourier-domain OCT. *Opt. Express* 18, 23472–23487.

3

In-line Quality Control of Moving Objects by Means of Spectral-Domain OCT²

In-line quality control of intermediate and final products is essential in various industries. This may imply determining the thickness of a foil or evaluating the homogeneity of coating applied to a pharmaceutical tablet. Such a qualitative and quantitative monitoring in a depth-resolved manner can be accomplished using optical coherence tomography (OCT). In-line quality control based on OCT requires additional consideration of motion effects for the system design as well as for data interpretation. This study focuses on transverse motion effects that can arise in spectral-domain (SD-) OCT systems. The impact of a transverse movement is analyzed for a constant relative speed difference up to 0.7 m/s between sample and sensor head. In particular, transverse motion is affecting

² This chapter is based on Markl, D., Hanneschläger, G., Buchsbaum, A., Sacher, S., Khinast, J.G., Leitner, M., 2014. In-line Quality Control of Moving Objects by Means of Spectral-Domain OCT. *Opt. Lasers Eng.* 59, 1–10 with permission from Elsevier.

OCT system properties such as the beam displacement (distance between adjacent A-scans) and transverse resolution. These properties were evaluated theoretically and experimentally for OCT images of a resolution target and pharmaceutical film-coated tablets. Both theoretical and experimental analyses highlight the shift of the transverse resolution limiting factor from the optics to the beam displacement above a relative speed difference between sensor head and sample of 0.42 m/s (for the presented SD-OCT setup). Speeds above 0.4 m/s are often demanded when monitoring industrial processes, such as a coating process when producing film-coated tablets. This emphasizes the importance of a fast data acquisition when using OCT as in-line quality control tool.

3.1 Introduction

New monitoring and process control methods are increasingly advocated by regulatory facilities to enable real-time quality control of final and intermediate products. Beside this regulatory guidelines, in-line quality control and process monitoring has several advantages for the manufacturer, such as reducing production cycle times, preventing product rejections, reducing human errors and facilitating continuous processing to improve efficiency. In particular, manufacturing often requires a chemical and physical product characterization without interrupting the process for physically removing a sample, as it is often necessary for traditional methods.

In-line quality control may include, among other key attributes, the evaluation of physical product properties such as homogeneity and uniformity of the products in real-time. Especially the evaluation of these key attributes in moving samples with varying geometrical (layer thickness, object size, curved surfaces, etc.) and mechanical (density, hardness, etc.) properties requires a very fast, non-destructive acquisition of the desired information. The ability to provide high-resolution depth-resolved information in a contact-free way with a high acquisition rate stresses the potential of optical coherence tomography (OCT) as an in-line quality control tool.

Until now, the driving force of OCT has been the field of biomedical research and diagnostics. The characteristics of OCT, however, make it an attractive method for a broad spectrum of research topics and applications beyond biomedicine (Stifter, 2007). These applications include off-line characterization of paper (Fabritius et al., 2006; Prykäri et al., 2010), silicon integrated-circuits (Serrels et al., 2010), food

(Verboven et al., 2013), fiber composites (Stifter et al., 2008) and pharmaceutical tablets (Zeitler and Gladden, 2009; Zhong et al., 2011). Moreover, OCT was recently demonstrated as an in-line quality control tool for monitoring printed electronics (Alarousu et al., 2013) and in-line characterization of multi-layered foils (Hanneschläger et al., 2011).

There exist several different variants of OCT including time-domain and Fourier-domain (swept-source and spectral-domain) approaches to reveal internal microstructures of (semi-)transparent and turbid materials (Fujimoto, 2003; Wojtkowski, 2010). In this study a spectral-domain (SD)-OCT system was employed, which offers advantages in terms of imaging speed and sensitivity compared to time-domain OCT (Nemeth et al., 2013). In SD-OCT a one-dimensional (1-D) depth profile is acquired with the use of a spectrometer. Therefore, the interference signal from the back-scattered light from the reference mirror and the sample is detected in a spectrally resolved way. A line camera is used as detection device, where the interference spectrum is acquired during a specified exposure time. The depth information can thus be extracted by applying an inverse Fourier transform on the acquired interference signal.

A sequence of such 1-D axial measurements (A-scans) performed at different transversal positions allows the generation of two- (2-D) and three-dimensional (3-D) images. A transverse displacement between successive A-scans can either be carried out with the aid of some scanning means (causes a deflection of the optical beam), such as a galvanometer mirror, or by a relative transverse movement of the sample to the sensor head.

The OCT image reconstruction process typically does not consider a relative transverse, axial or oblique movement between sensor head and sample. Since motion effects might cause a misinterpretation of images, the impact of movements on the image quality has been studied in nearly all imaging modalities, particularly in biomedical applications (Sacchet et al., 2010; Walther and Koch, 2009; Yun et al., 2004). However, in biomedical applications the motion of the object under investigation is mostly inadvertently and unspecified. In the context of in-line quality control the motion of the monitored sample typically occurs in a well-defined manner, such as a constant flow of several samples (e.g., pharmaceutical film-coated tablets), or a continuous object (e.g., foil production). Therefore, a basic understanding of the relationship between the relative speed between sensor head and sample has to be developed.

This study focuses on the evaluation of transverse motion effects caused by a known and constant speed difference between sensor head and sample. Axial movement of the sample is neglected and noise caused by sample motion during the measurement is not analyzed. Transverse motion effects are investigated theoretically and experimentally. Experiments were carried out using pharmaceutical film-coated tablets, since quality control is an important issue in the pharmaceutical industry and process monitoring is also stimulated by the pharmaceutical regulatory facilities (e.g., U.S. Food and Drug Administration (FDA, 2004)). In particular, the determination of the coating thickness and the evaluation of coating homogeneity in film-coated tablets are essential in the manufacture of those.

3.2 Materials and Methods

3.2.1 Theory: Resolution in OCT

The transverse resolution is in general specified as the ability of an optical system to distinguish two points as separate in a plane perpendicular to the probing light beam. Thus, the transverse resolution is defined as the full width at half maximum (FWHM) diameter considering a Gaussian beam profile and no movement of the beam. The FWHM diameter can be calculated by

$$\delta x = 2w_0 = 4 \frac{\lambda_c f}{\pi d}, \quad (3.1)$$

where λ_c is the central wavelength of the optical source, f the focal length and d the beam diameter at the lens.

The axial (depth) resolution is specified as the resolving power of the imaging system in the direction parallel to the probing light beam. The axial resolution δz is defined as half of the coherence length l_c , which is limited by the central wavelength λ_c and the FWHM bandwidth $\Delta\lambda$ of the light source. For a source with Gaussian spectral distribution the axial resolution is thus denoted as (Fercher, 2010)

$$\delta z = \frac{l_c}{2} = \frac{2 \ln(2)}{\pi} \frac{\lambda_c^2}{\Delta\lambda}. \quad (3.2)$$

Therefore, the axial resolution is in contrary to the transverse resolution independent of imaging aperture. This decoupling of the transverse from the axial resolution is one of the main advantages of OCT over other optical depth

discrimination methods (e.g., confocal microscopy).

3.2.2 Theory: Transverse Motion Effects

The transverse motion effects are discussed on the basis of a SD-OCT system equipped with a 1-D and a 2-D sensor head. In OCT a cross-section images is synthesized by a defined number of adjacent (successive) A-scans. The 1-D sensor head provides single A-scans and requires a relative movement between sensor head and sample in order to displace the beam for producing 2-D OCT images. On the contrary, the 2-D sensor head contains a galvanometer mirror as scanning means to transversely move the beam along the sample. The distance which the light beam travels between two successive A-scan measurements is henceforth referred to as the beam displacement.

The theoretical analysis is based on **Figure 3.1**, which shows the trajectories of the 1-D and 2-D sensor head under consideration of a relative speed difference v_y between sensor head and sample. This relative transverse movement pronounces the motion effects in OCT images. The case without such a relative movement is henceforth referred to as the stationary case. This might, however, include a movement of the galvanometer mirror to produce cross-sectional images (in the case of a 2-D sensor head). The following transverse motion effects are discussed: (1) broadening of the beam displacement, (2) degradation of the transverse resolution and (3) blurring of the sample area of a B-scan.

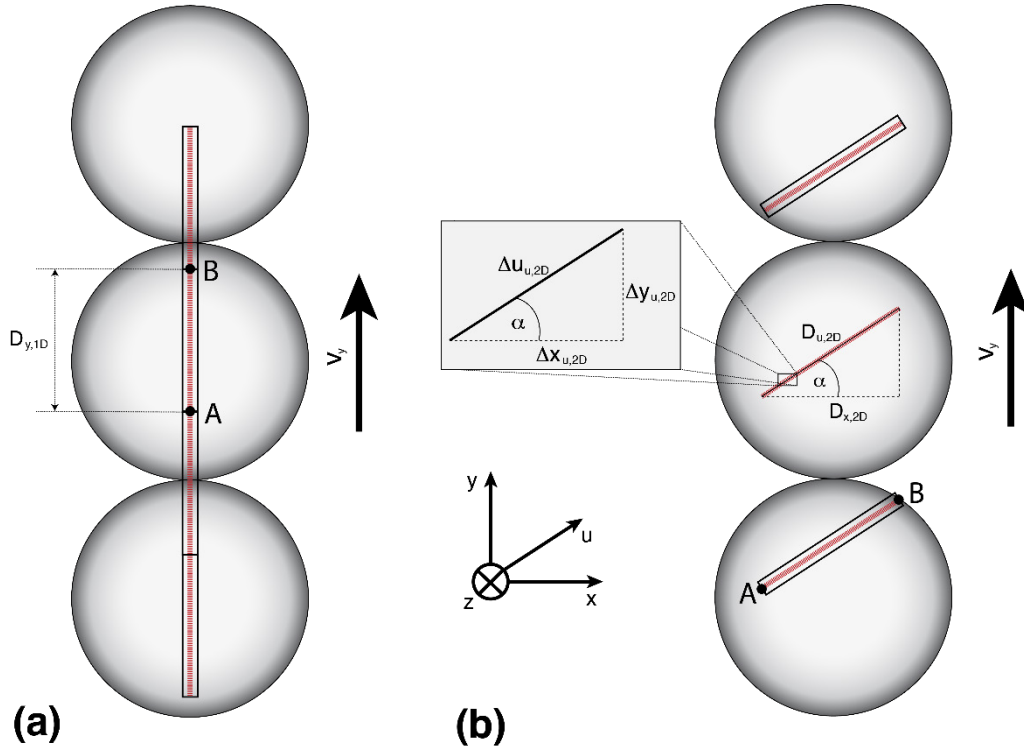


Figure 3.1: Trajectory of B-scans considering the sensor head moves at a speed across a stationary sample. (a) 1-D sensor head: The transversal image size $D_{y,1D}$ of one OCT B-Scan and thus the beam displacement Δy_{1D} directly depends on the speed of the sensor head. (b) 2-D sensor head: The movement of the sensor head causes a broadening of the beam displacement Δu_{2D} and induces a rotation by an angle α of the scanning direction. The markers A and B describe the first and the last A-scan of the B-scan, respectively.

3.2.3 Broadening of Beam Displacement

The beam displacement depends on the exposure time T_{exp} of the line camera, the idle time T_{idle} between two successive A-scan measurements and the transverse speed difference between the beam and the sample. Since the exposure and idle times are fixed throughout all simulations and experiments, this analysis focuses on the impact of the transverse speed difference on the generated OCT image.

In the case of the 1-D sensor head this speed difference is equal to the relative movement v_y between sensor head and sample. The beam displacement can thus be calculated by

$$\Delta y_{1D}(v_y) = v_y T, \quad (3.3)$$

with $T = T_{\text{exp}} + T_{\text{idle}}$ as the acquisition time of one A-scan. Consequently, the beam displacement depends linearly on the relative movement v_y .

In the 2-D sensor head the beam is additionally moved orthogonal to the direction of movement of the sensor head by a galvanometer mirror with a velocity of v_x ($= \Delta x_{2D}/T$), where Δx_{2D} is the beam displacement due to the scanning procedure. The overall beam displacement is a combination of the components acting in both directions: the displacement in x -direction induced by the galvanometer mirror, and the displacement in y -direction stemming from the relative movement between sensor head and sample. Therefore, the displacement is caused by the speed of the galvanometer mirror v_x and the transversal speed difference v_y . In this study v_x is kept constant and the following analysis focuses on the impact of v_y , which is hence used as the only variable in the following equations. This gives a total velocity of $v_u(v_y) = \sqrt{v_x^2 + v_y^2}$ and a beam displacement of

$$\Delta u_{2D}(v_y) = v_u(v_y) T. \quad (3.4)$$

Furthermore, the velocities v_x and v_y act in orthogonal directions and cause a rotation of the scanning direction compared to the stationary case. This rotation can be described by the displacement angle

$$\alpha(v_y) = \tan^{-1} \frac{v_y}{v_x}. \quad (3.5)$$

In order to highlight the strong dependency of the beam displacement Δu_{2D} on the transverse speed difference v_y , it is preferable to define a broadening factor $\mu_{i,2D}$, which is the ratio of the actual beam displacement Δu_{2D} , depending on the sensor head speed v_y , and the one of the stationary case (Δx). Since the number N of A-scans per B-scan is kept constant, this broadening factor additionally represents the ratio between the transverse image size $D_{u,2D}$ at a certain sensor head speed and the stationary case. The broadening factor indicates a scaling of the beam displacement and is denoted as

$$\mu_{i,2D}(v_y) = \frac{\Delta u_{2D}(v_y)}{\Delta x_{2D}}. \quad (3.6)$$

3.2.4 Broadening of Transverse Resolution

In a static imaging system case the transverse resolution is only restricted by the optics of the measurement system and the operating wavelength of the source. However, a relative transverse movement between the sensor head and the sample and the finite exposure time of an A-scan broadens the transverse resolution. In order to analyze the transverse resolution in dependence on the relative speed difference, the irradiance distribution of the Gaussian beam is calculated first:

$$I(r) = I_0 \exp \left\{ \frac{-\ln(2) r^2}{w_0^2} \right\}. \quad (3.7)$$

with $I_0 = I(0) = \frac{P \ln(2)}{\pi w_0^2}$. w_0 is the beam waist radius and P is the total power transmitted by the beam. Eq. (3.7) represents the intensity of the beam at the location (r). A derivation of Eq. (3.7) is given in Appendix B.

As mentioned above, the relative transverse movement between the beam and the sample broadens the irradiance distribution. Therefore, the effective beam profile caused by the speed v_u can be represented by

$$I_{\text{eff}}(u) = \frac{1}{T_{\text{exp}}} \int_{-T_{\text{exp}}/2}^{T_{\text{exp}}/2} I(u + v_u t) dt. \quad (3.8)$$

I_{eff} represents an enlarged area illuminated by the probe beam during the integration time. The effective beam profile depends on the coordinate u which is related to the x -coordinate through $u = \sqrt{x^2 + y^2}$. Basically, this coordinate transformation states the mapping from the Cartesian coordinate to a new coordinate under the consideration of the velocities of the galvanometer mirror v_x and the speed difference v_y . The transverse resolution δu_{2D} is finally obtained by measuring the FWHM diameter from the simulated effective field profiles at a certain speed difference v_y .

Since the impact of the sensor head velocity on OCT imaging is studied in this work, it is interesting to quantify the impact of transverse motion on the transverse resolution. Therefore, the broadening factor $\mu_{r,2D}$ is defined as

$$\mu_{r,2D}(v_y) = \frac{\delta u_{2D}(v_y)}{\delta x_{2D}}. \quad (3.9)$$

3.2.5 Blurring of the Sample Area of a B-scan

Especially important for the analysis of the OCT image is the area investigated during acquisition of one B-scan. Based on Eq. (3.7) and the beam displacement, one can simulate the sample area of adjacent A-scans. A parameter proportional to the information content of adjacent A-scans is preferably used for investigation of the sample area of a B-scan. The smaller the spatial displacement between A-scans i and $i + 1$, the more the sample areas overlap, and the less new information is provided by A-scan $i + 1$. Therefore, the analysis of overlapping areas considering an effective intensity profile would give a good expression of the new information content provided by A-scan $i + 1$. This can be expressed on the basis of the autocorrelation coefficient

$$R_{II}(v_y) = \frac{\iint_{-\infty}^{\infty} I_{\text{eff},i}(r(x,y)) I_{\text{eff},i+1}(r(x,y)) dx dy}{\iint_{-\infty}^{\infty} I(r(x,y))^2 dx dy} \quad (3.10)$$

with $r = \sqrt{x_r^2 + y_r^2}$, $x_r = x + v_x t$ and $y_r = y + v_y t$. The correlation between adjacent A-scans is normalized by the square of the intensity profile of the stationary case. Therefore, R_{II} is in the range of 0 and 1, which respectively correspond to no overlap and a complete overlap of successive A-scans.

When the idle time T_{idle} and the beam displacement between two A-scan measurements are too large, the area between successive A-scans is partially not investigated. In this study this event is defined as the point when the FWHM diameters from successive A-scans are just no longer overlapping. Consequently, an event of maximal efficiency of one B-scan might be defined as a trade-off between an optimum overlap and a gap between the sample areas of successive A-scans.

As discussed in section 0, the FWHM diameter depends on the speed difference between sensor head and sample. Further analysis will be based on a factor $\mu_o(v_y)$, which includes a gain of information due to a loss of overlap when the velocity v_y increases, and a loss of information due to the gap when the velocity exceeds a certain limit (i.e. the beam displacement is larger than the FWHM diameter). This factor will be defined as the efficiency of an A-scan

$$\mu_o(v_y) = 1 - \left| \frac{R_{II}(v_y) - R_{II}(v_{y,\text{opt}})}{1 - R_{II}(v_{y,\text{opt}})} \right|. \quad (3.11)$$

This efficiency parameter ranges from 0 (complete overlap, minimum information)

to 1 (optimum overlap, maximum information) and can be used to evaluate and to optimize the measurement procedure. Maximum information is accomplished for a certain speed difference between sensor head and sample, denoted as $v_{y,\text{opt}}$.

One has to mention that in applications where the sample is stationary, oversampling (i.e., successive A-scans are overlapping) is preferred in order to increase the quality of the image by averaging successive overlapping A-scan measurements. However, measurement systems for in-line quality control applications have to deal with the relative speed between the beam and the sample and therefore, this efficiency parameter can be used to evaluate and optimize the measurement procedure.

3.3 Experiments

3.3.1 OCT system

The measurement principle is based on the correlation of back-scattered light from inside the object and light that has travelled a known reference path. Using this interferometric approach together with high spatial and low temporal coherence light sources enables the investigation of material layers at the level of a few micrometers. The OCT system used for this study illuminates the sample with a SLD Broadlighter (Superlum Diodes Ltd., Ireland, SLD 351 HP2) with a center wavelength of 830 nm and a FWHM bandwidth of 62 nm. This results in an axial resolution of 4.9 μm . The light incident on the sample measures < 0.5 mW.

A schematic of the SD-OCT system including two different sensor heads (a 1-D and a 2-D sensor head) is shown in **Figure 3.2**. The light coming from the source passes a directional coupler DC (50/50 coupling ratio, Thorlabs Inc, Newton, New Jersey, USA) and is directed towards the respective probe head. In both sensor heads the light emerging the fiber is split at a non-polarizing bulk beam splitter BS (splitting ratio 50/50, Thorlabs) into a reference and a probe beam. In both configurations the reference arm is terminated by a gold coated mirror (Thorlabs). The probe beam of the 1-D sensor head is focused by a fiber focuser FF (OZ Optics, focal length $f = 40$ mm). The 1-D sensor head provides a transverse resolution δx_{1D} of 12 μm . In the sample arm of the 2-D sensor head the beam is collimated to a diameter of 4 mm by a fiber collimator FC (OZ Optics, diameter = 12 mm). A

galvanometer mirror GM (VM500+, General Scanning) is used to scan the beam transversely across the sample through a broadband scan lens L1 (LSM03-BB, Thorlabs, focal length, $f = 36$ mm). With this 2-D sensor head a transverse resolution δx_{2D} of $9.51 \mu\text{m}$ can be achieved. In both configurations the light back reflected from both reference and sample is directed towards the spectrometer via the coupler DC. The spectrometer consists of a fiber collimator FC (OZ Optics, diameter = 20 mm), a transmissive diffraction grating DG (Wasatch Photonics, 1200 lines/mm), an achromatic lens L3 (Thorlabs, $f = 100$ mm) and a line scan camera with a 2048 pixel CCD array (Atmel Aviiva, $14 \mu\text{m}^2$ pixel size, 12 bit resolution). The exposure time $T_{\text{exp}} = 34 \mu\text{s}$ and the idle time $T_{\text{idle}} = 1.9 \mu\text{s}$ were fixed throughout all experiments. This gives a duty cycle of 95% ($T_{\text{exp}}/(T_{\text{exp}} + T_{\text{idle}})$) and a readout rate of the camera of 27.8 kHz.

1000 A-scans are acquired during a single B-scan period (35.9 ms). In the case of the 2-D sensor head, the galvanometer mirror is triggered by a saw-tooth wavefront in synchrony with the camera read out. The voltage range of the galvanometer is constant and causes a beam displacement Δx_{2D} between adjacent A-scans of $2.94 \mu\text{m}$ (stationary case). One can thus calculate the horizontal image size by multiplying the beam displacement (i.e., Δy_{1D} or Δu_{2D}) by the number of A-scans (i.e., 1000).

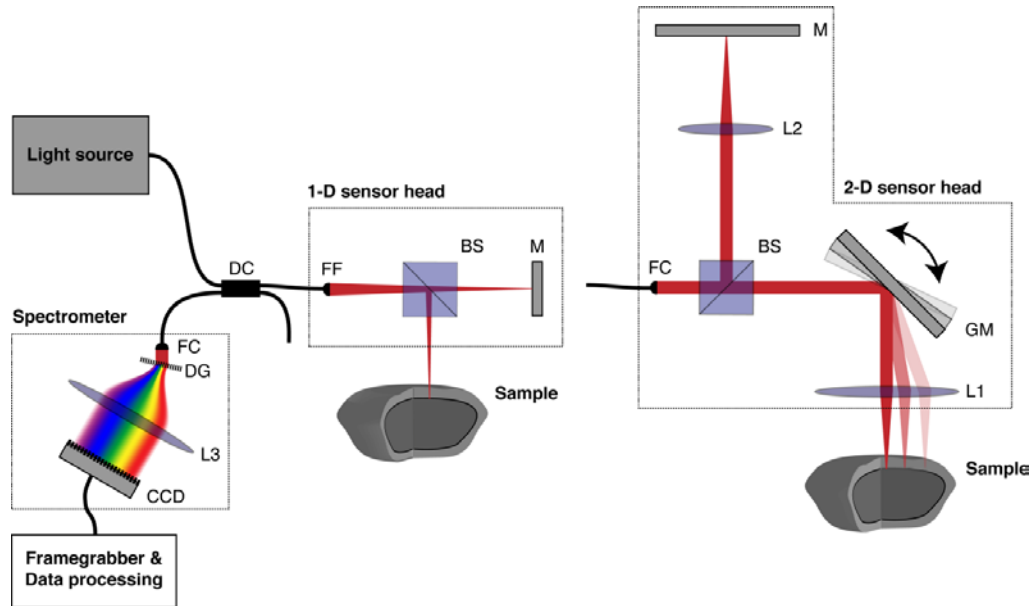


Figure 3.2: Schematic of the experimental design. The 1-D and 2-D sensor head can be easily exchanged. DC – directional coupler, FC – fiber collimator, BS – beamsplitter, GM – galvanometer mirror, FF – fiber focuser, Lx – lens, M – mirror, DG – diffraction grating, CCD – charged coupled device.

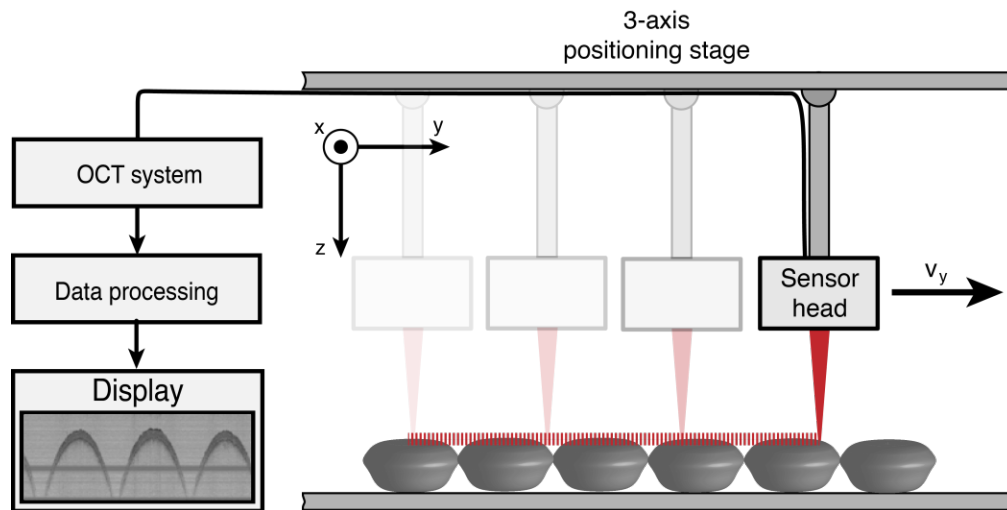


Figure 3.3: Schematic of the 3-axis positioning system. The sensor head (1-D or 2-D) was mounted on the positioning system and moved across the samples with different speeds, ranging from 0.025 m/s to 0.7 m/s.

3.3.2 3-Axis positioning stage

This report only considers the case of a sensor head moving across a static sample.

Without loss of generality, however, this can be seen as identical to the case of a static sensor and a moving sample. Therefore, in this study, motion effects have been investigated experimentally solely by moving the sensor head transversely along stationary samples. The sensor heads (1-D and 2-D) were mounted on an in-house built 3-axis positioning stage, as illustrated schematically in **Figure 3.3**. Such a positioning stage enables the movement of the sensor heads in the x -, y - and z -direction within a $0.7 \times 1.1 \times 0.5 \text{ m}^3$ box. For this report, however, the sensor heads were only moved in the y -direction over a distance of 0.7 m, with speeds ranging from 0.025 m/s to 0.7 m/s.

3.3.3 Samples

Two different samples were used to determine the displacement angle α and to evaluate the motion effects of each sensor head for different velocities. The experiments were carried out for ten different velocities v_y , ranging from 0 m/s to 0.7 m/s, for each sample.

The displacement angle α was determined with the aid of a resolution target (Edmund Industrial Optics, Variable Frequency Target). This resolution target has 25 line pair packages ranging from 5 to 120 line pairs per mm. The step size and the increment of line pairs between each line pair package is 1 mm and 5 line pairs per mm, respectively. For the analysis of the displacement angle the lines of the resolution target were oriented parallel to the x -axis. Consequently the lines of the target can only be captured when the sensor head is moved along the y -axis.

The experimental evaluation of effects of transverse probe motion was based on OCT images of pharmaceutical film-coated tablets acquired with both sensor heads. The tablets were produced with the aid of a rotary press. The tablet core consisted of acetylsalicylic acid (ASA) as API and common excipients and had a standard bi-convex shape of 8 mm diameter. The coating with a mean thickness of 80 μm was applied to the cores using a lab-scale coating pan. The coating suspension was a standard preparation of Eudragit L30D (Evonik Industries AG, Essen, Germany).

3.4 Results and Discussion

3.4.1 Theoretical Results of Transverse Motion Effects

Figure 3.4 shows the calculated transverse resolution for the 2-D sensor head using Eq. (3.7). The effective field profile was normalized by the intensity I_0 at the center of the beam at its waist. As expected, the profile is flattening out with increasing speed. The maximum intensity for the stationary sensor head ($v_y = 0$ m/s) is slightly less than I_0 . This is due to the speed of the galvanometer mirror, which additionally contributes to a degradation of the transverse resolution. The transverse resolution for the stationary case is $9.8 \mu\text{m}$. The results for the 1-D sensor head are similar to those presented in **Figure 3.4**.

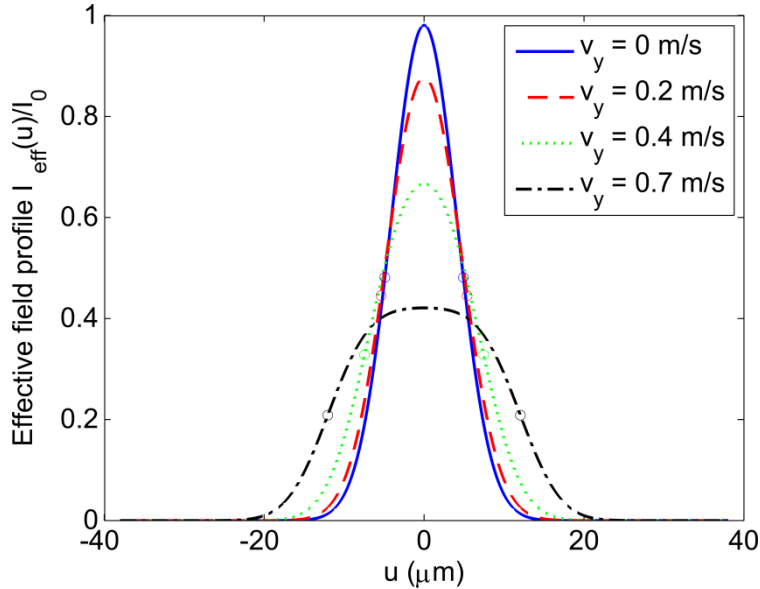


Figure 3.4: Effective field profile depending on the speed difference. The effective field profile at the focal point is normalized by the intensity at the center of the beam at its waist. The graphs show the profiles for different velocities of the sensor head. The markers indicate the transverse resolution (FWHM diameter). The velocity of the galvanometer mirror is considered as constant.

In **Figure 3.5(a)** the transverse resolution and beam displacement of the 1-D and 2-D sensor heads are compared. The slight difference in the transverse resolution between the 1-D and 2-D sensor head is caused by the velocity of the galvanometer mirror. The beam displacement of the 1-D sensor head is 0 for the stationary case, as this measurement system has no internal scanning procedure. The beam displacement linearly increases with the speed of the sensor head. For the 2-D sensor head the beam displacement is non-zero at zero speed and approaches the beam displacement of the 1-D sensor head with increasing speed. For larger sensor head speeds the contribution of the speed of the galvanometer mirror to the total speed v_u is very small. Therefore, the total speed can be assumed to be approximately the speed of the sensor head, and thus the transverse resolution and beam displacement of the 1-D and 2-D sensor heads are almost equal at larger sensor head speeds. It can be seen that there is an intersection between the transverse resolution and the beam displacement at 0.417 m/s and 0.420 m/s for the 1-D and 2-D sensor heads, respectively. This intersection point indicates the transition from optics to the beam displacement as limiting factor for the transverse resolution. **Figure 3.5(b)** shows the broadening factors of the transverse resolution ($\mu_{r,2D}$) and of the beam displacement ($\mu_{i,2D}$) depending on the speed of the 2-D sensor head. Apparently the broadening of the beam displacement is much more affected by movement than the broadening of transverse resolution.

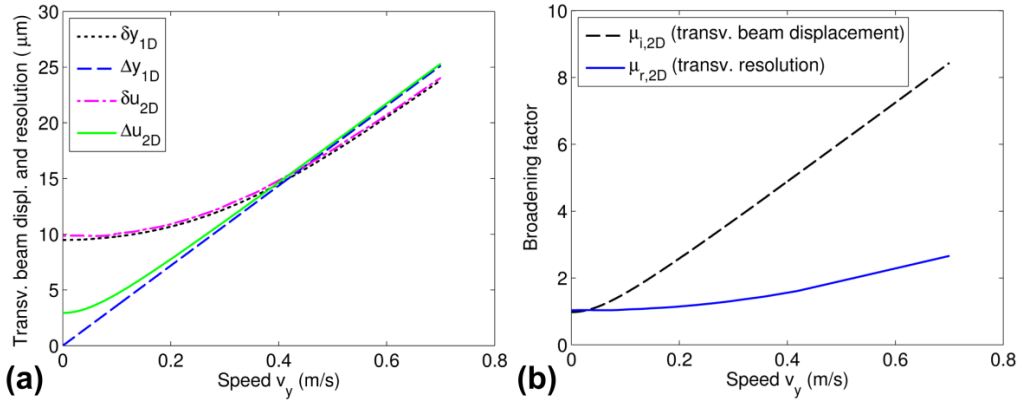


Figure 3.5: Theoretical analysis of broadening effects. (a) Comparison of transverse resolution and beam displacement of the 1-D and 2-D sensor head. (b) Broadening of transverse resolution and beam displacement for the 2-D sensor head.

The area of the effective field profile I_{eff} can also be simulated for both sensor heads, as shown in **Figure 3.6** for different velocities. The impact of the movement of the sensor head is apparent. The angles of rotation for the 2-D sensor head are 51.2° for 0.1 m/s, 78.23° for 0.4 m/s and 83.21° for 0.7 m/s. The flattening of the profile causes a reduction of photons hitting an area $dA (= dx \cdot dy)$ in comparison to the stationary case. The signal from a particular scatterer is collected during a fraction of the time of each A-scan acquisition. Therefore, the transverse motion has the additional effect of decreasing the magnitude of the effective intensity and thus of reducing the signal-to-noise ratio (SNR). The degradation of SNR was already studied and verified through experiments by several research groups (Sacchet et al., 2010; Walther and Koch, 2009; Yun et al., 2004).

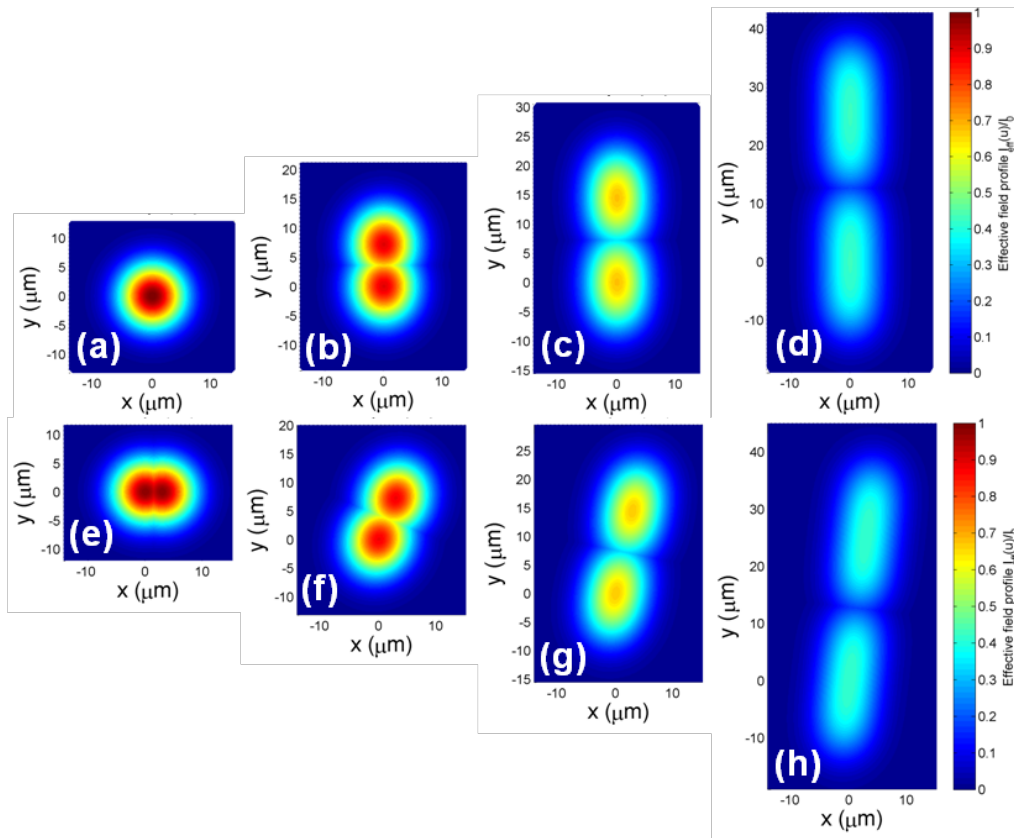


Figure 3.6: Simulations of the 2-D normalized effective beam profile for different speeds of the 1-D and 2-D sensor heads. The velocities of the sensor heads were modified to: (a,e) 0 m/s, (b,f) 0.2 m/s, (c,g) 0.4 m/s and (d,h) 0.7 m/s. Profiles (a)-(d) describe the 1-D sensor head, and profiles (e)-(h) the 2-D sensor head.

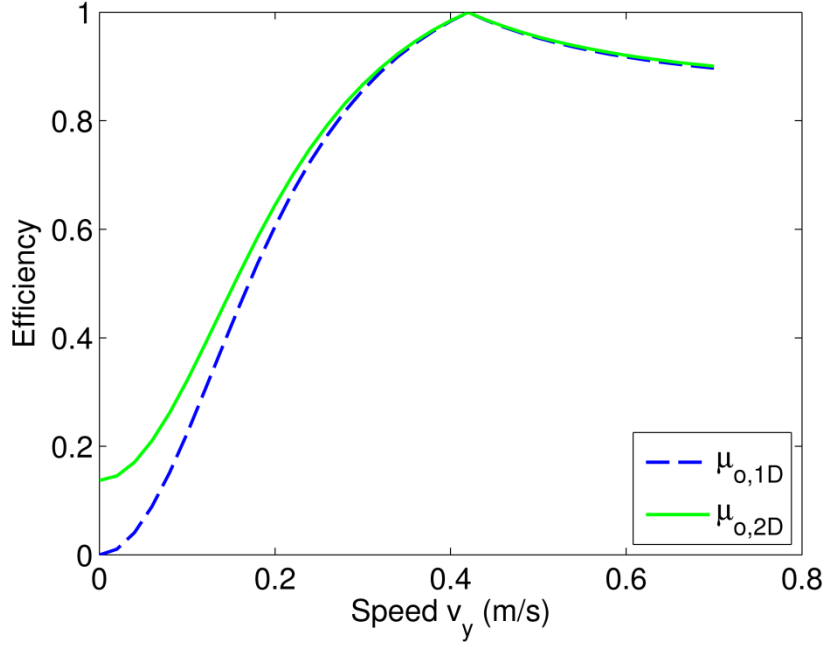


Figure 3.7: The efficiencies for the 1-D sensor head and for the 2-D sensor head in dependence on the sensor heads velocity.

Moreover, **Figure 3.6** emphasizes the broadening effect of the beam displacement. The distance between adjacent A-scans increases with increasing sensor head velocity. The sensor head motion influences the beam displacement more strongly than the transverse resolution. Above the speed of the intersection point (cf. **Figure 3.5(a)**) this effect causes a loss of information about regions located in between the areas of adjacent A-scans. This can be seen in **Figure 3.6(d)** and **(h)**, where the magnitude of the intensity profile between adjacent A-scans is zero, and therefore, no information will be available in the OCT image about this region of the sample.

A more detailed analysis can be carried out on basis of **Figure 3.7**. It shows the efficiency μ_o evaluated by Eq. (3.11) for the 1-D and 2-D sensor head. The efficiency $\mu_{o,1D}$ for the 1-D sensor head for the stationary case is zero as there is no movement and all A-scans do completely overlap. Moreover, the efficiency $\mu_{o,2D}$ of the 2-D sensor head is very small for low velocities and increases with increasing speed. At the intersection point ($v_{y,opt}$ is 0.42 m/s) the maximum efficiency is reached. At sensor head speeds above $v_{y,opt}$ the spacing between individual A-scans is larger than the optical resolution and, hence, the efficiency decreases. Above the intersection point information is lost, defects of the sample that are smaller than

the spacing of the A-scans, might be missed.

3.4.2 Experimental Results of Transverse Motion Effects

Experimental results for the displacement angle α and the corresponding transverse beam displacement for the 2-D sensor head were obtained using the variable frequency resolution target. Those results and the beam displacements for the 1-D sensor head are summarized in **Table 3.1**.

The variable frequency resolution target was additionally used to investigate the transverse resolution and beam displacement, as well as their intersection point depending on the 2-D sensor head speed. **Figure 3.8** depicts B-scans of the resolution target for **(a,b)** the stationary case, and sensor head velocities of **(c)** 0.2 m/s and **(d)** 0.7 m/s. Each image shows a different area of the resolution target, corresponding to different widths of the line pairs. The line widths of the resolution target at the imaged areas are **(a)** 16.6 μm , **(b)** 9.1 μm , **(c)** 11.1 μm , and **(d)** 25.0 μm . Due to the velocity of the 2-D sensor head, the apparent width of the lines in the OCT image needs to be corrected by the displacement angle α . Therefore, the aforementioned line widths of **Figure 3.8(c)** and **(d)** are divided by $\sin \alpha$ resulting in a corrected line width of 12.0 μm and 25.2 μm , respectively.

Table 3.1: Experimental results for the displacement angle α and the transverse beam displacements as a function of the sensor head velocity.

Sensor head velocity	Displacement angle	Transverse beam displacement	Transverse beam displacement
v_y (m/s)	α ($^\circ$)	Δy_{1D} (μm)	Δu_{2D} (μm)
0.025	17.33	0.90	3.00
0.05	31.73	1.80	3.34
0.075	42.97	2.69	3.93
0.1	50.86	3.58	4.62
0.2	67.65	7.16	7.74
0.3	74.79	10.74	11.13
0.4	78.12	14.32	14.63
0.5	80.53	17.90	18.15
0.6	82.26	21.48	21.67
0.7	83.31	25.06	25.23

Each line in **Figure 3.8** is composited by a certain number of pixels in transverse direction, which is determined by the ratio between the line width appearing in the image and the beam displacement. **Figure 3.8(a)** illustrates an OCT image where the width of the lines is significantly higher than the resolution limit and each line is represented in transverse direction by approximately 6 pixels. In order to emphasize the dependence of the transverse resolution limit on the sensor head speed, the line widths in **Figure 3.8(b-d)** have been chosen to barely match the resolution limits for the three different sensor head velocities (cf. **Figure 3.5(a)**). In this case, the number of transverse pixels per line approximately corresponds to the ratio between the transverse resolution and the beam displacement. This ratio becomes smaller with increasing sensor head speed, which can be observed when inspecting the number of transverse pixels per line of **Figure 3.8(b-d)**. These numbers of pixels per line coincide very well with the theoretical ratio between transverse resolution and beam displacement of 3.4, 1.4 and 1.0, respectively. The vertical lines in the image in **Figure 3.8(d)** are thus composited by only one pixel. This indicates that the OCT system is operated at the intersection point of transverse resolution and beam displacement, i.e., maximum efficiency, and therefore, the resolution limiting factor is the distance between successive A-scans, i.e., the beam displacement and not the optics.

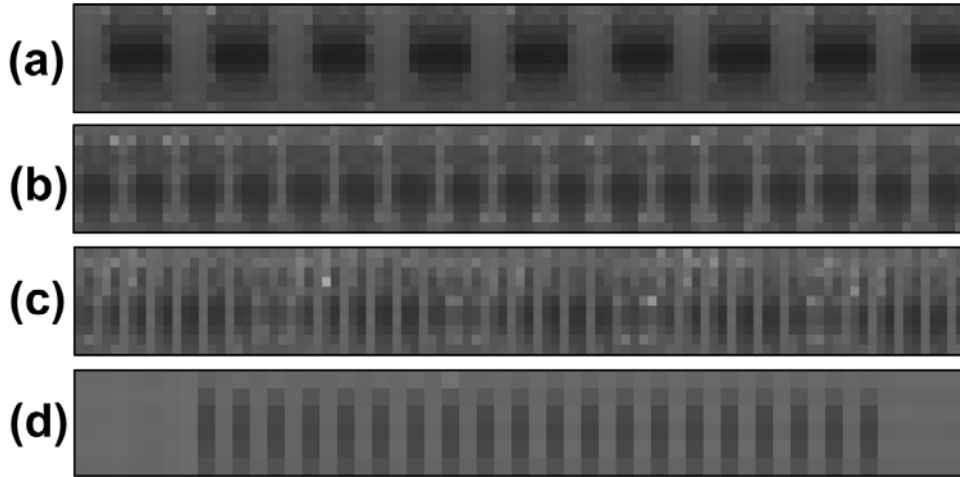


Figure 3.8: Cross-section OCT images of the variable frequency resolution target for (a,b) the stationary case (100 x 10 pixel, 294 x 25 μm^2), (c) 0.2 m/s (100 x 10 pixel, 774 x 25 μm^2) and (d) 0.7 m/s (50 x 5 pixel, 1262 x 12.5 μm^2). Transverse resolutions: (a,b) 9.8 μm , (b) 10.9 μm and (d) 24.0 μm . Beam displacements: (a,b) 2.9 μm , (c) 8.5 μm and (d) 24.8 μm . Corrected line width (considering the displacement angle α) of the variable frequency resolution target: (a) 16.6 μm , (b) 9.1 μm , (c) 12.0 μm and (d) 25.2 μm .

OCT images of pharmaceutical film-coated tablets acquired with both sensor heads at five different sensor head speeds are shown in **Figure 3.9**. The most noticeable effect is the broadening of the beam displacement, which causes the increase in the transverse image size with increasing sensor head speed. From the theoretical analysis of the beam displacement for both sensor heads, the transverse image size of the 1-D sensor head approaches the one of the 2-D sensor at approximately 0.2 m/s. This coincides very well with the experimental results (cf. the beam displacement of the 1-D and 2-D sensor head in **Figure 3.5(a)**). In addition, from **Figure 3.5(b)** one can retrieve the theoretical scaling of the transverse image size. Above a total speed difference v_u of 0.1 m/s the dominating velocity is v_y ($v_u \approx v_y$), and thus, the broadening of the transverse image size behaves approximately linear. Therefore, the theoretical scaling for the 2-D sensor head speeds of 0.2 m/s and 0.7 m/s is equal to the ratio between those velocities (0.7/0.2) and results in 3.5. This scaling of the image size agrees well with that of the tablets for the same velocities.

In industrial production processes usually the speed of the samples is fixed and cannot be modified. Therefore, the simplest way to optimize the data acquisition with respect to minimize loss of information and maximize the signal to noise ratio (SNR) is to adjust the exposure time. The aforementioned efficiency parameter was introduced for this optimization step, where the optimum is given by the maximum efficiency of 1. The maximum efficiency corresponds to the intersection point between transverse resolution and the beam displacement ($v_y = 0.42$ m/s).

When the OCT setup is operated at an efficiency below 1, the images can be post-processed to reduce the amount of data and to improve the SNR ratio. The post-processing includes the averaging of successive overlapping A-scans, which has a similar effect as increasing the exposure time. However, in this OCT setup successive A-scans are only overlapping when $v_y < 0.42$ m/s. The number of averaged A-scans thus depends on the ratio between the transverse resolution and beam displacement, i.e., $\delta y_{1D}/\Delta y_{1D}$ and $\delta u_{2D}/\Delta u_{2D}$ for the 1-D and 2-D sensor head, respectively. **Figure 3.10** presents post-processed images (averaging several successive A-scans) for five different speeds of the 1-D sensor head. In the top row of **Figure 3.10** (left to right) 10, 5, 3 and 2 successive A-scans were averaged and consequently the pixel dimension of the images decreases by the same factor. Since the ratio between the transverse resolution and beam displacement is usually a fractional number, the floor operator was applied on the ratio. Therefore, a ratio

$\delta y_{1D}/\Delta y_{1D} < 2$ implicates that the image dimensions remained the original ones (**Figure 3.10**, $v_y = 0.2$ m/s). As a consequence of the averaging, a gain of SNR and image quality without loss of information can be observed.

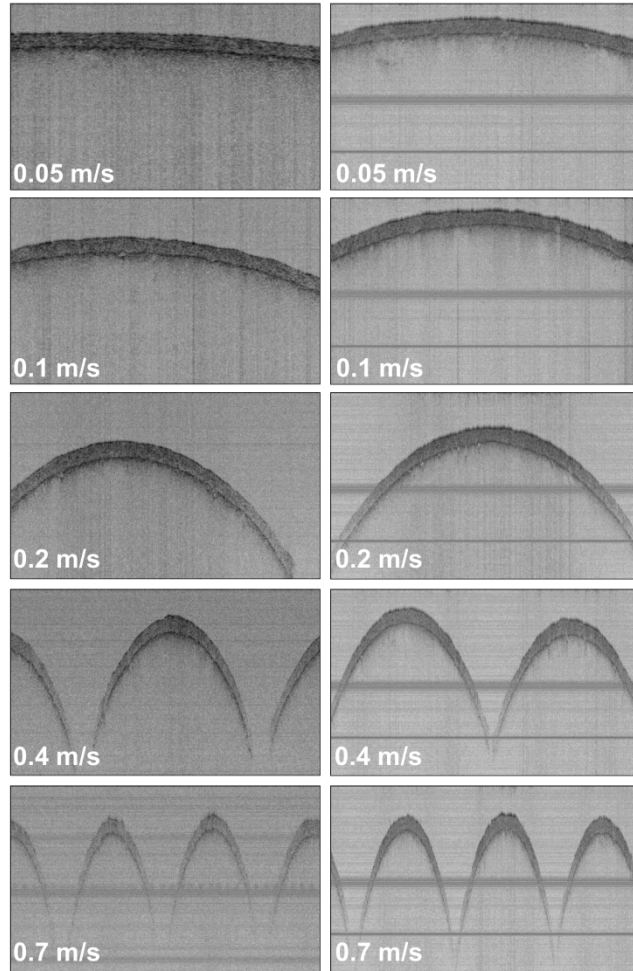


Figure 3.9: B-scans of the tablets for five different velocities of the 1-D (left images) and the 2-D (right images) sensor head. Each image is synthesized by 1000 A-scans which are displaced by $\Delta y_{1D}(v_y)$ (left images) or $\Delta u_{2D}(v_y)$ (right images) as listed in **Table 3.1**. The vertical image size corresponds to a depth of 2.5 mm^2 (in air). The horizontal lines appearing in most of the images in the right column are due to uncompensated fixed pattern noise.

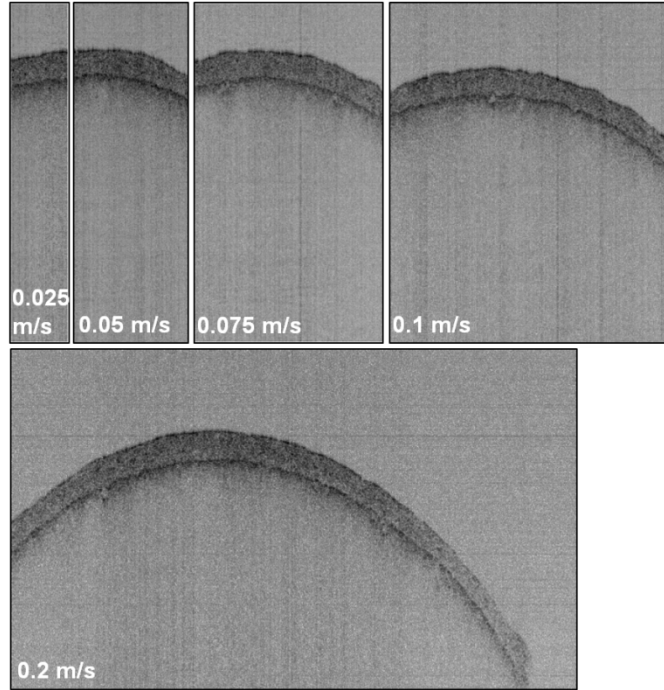


Figure 3.10: Experimental analysis of efficiency of an A-scan for the 1-D sensor head. The image dimensions depend on the ratio $\delta y_{1D}/\Delta y_{1D}$ (transverse resolution/beam displacement). The number of transverse pixels varies: $v_y = 0.025$ m/s: 100 pixels; $v_y = 0.05$ m/s: 200 pixels; $v_y = 0.075$ m/s: 333 pixels; $v_y = 0.1$ m/s: 500 pixels; $v_y = 0.2$ m/s: 1000 pixels.

3.5 Conclusion

In conventional OCT, sample motion effects may be negligible since a relative speed difference between sensor head and sample is usually avoided. In the case of OCT as in-line monitoring tool, the sample is in motion intentionally, and thus the effect of motion has to be considered for the design of an OCT system, as well as for the interpretation of the data. A faster acquisition of A-scans would apparently reduce motion effects, but would not eliminate them. In particular, using half of the exposure time ($= 17 \mu\text{s}$) as used in this study would shift the intersection point between the transverse resolution and the beam displacement in dependence on the relative speed (cf. **Figure 3.5**) from 0.42 m/s to approximately 0.7 m/s. A faster acquisition of an A-scan reduces the beam displacement and therefore may allow a larger number of A-scans to be acquired per sample. To this end it could be useful to use light sources with a higher output power (Zang et al., 2011, 2010). The

higher intensity at the entrance of the OCT device enables shorter integration times while maintaining a high SNR. Small relative speed differences between sensor head and sample, however, may allow merging of successive A-scans to enhance the SNR and improve the image quality. The use of light sources with a higher bandwidth would allow detecting even thinner coatings.

The analysis in this study may be useful for the design of an in-line monitoring system as presented for the characterization of pharmaceutical film-coated tablets. The application of OCT for off-line characterization of film-coated tablets has been studied and compared to other measurement systems in literature (D M Koller et al., 2011; Mauritz et al., 2010; Zhong et al., 2011). However, using OCT as in-line quality control tool in the pharmaceutical industry (e.g., in-line monitoring of a pan coating process) requires an automatic determination of the coating thickness. Such measurements should be carried out perpendicular to the surface in order to avoid measurement errors due to the curvature of the tablets. Therefore, broadening of the beam displacement strongly influences the coating thickness measurements. The consideration of motion effects has to be considered in the further development of automatic evaluation algorithms to ensure high quality products.

3.6 References

- Alarousu, E., Alsaggaf, A., Jabbour, G.E., 2013. Online monitoring of printed electronics by Spectral-Domain Optical Coherence Tomography. *Sci. Rep.* 3, 1562.
- Fabritius, T., Alarousu, E., Prykäri, T., Hast, J., Myllylä, R., 2006. Characterisation of optically cleared paper by optical coherence tomography. *Quantum Electron.* 36, 181–187.
- FDA, 2004. Guidance for Industry. PAT - a framework for innovative pharmaceutical development, manufacturing, and quality assurance, Quality Assurance. US Department of Health, Rockville, MD.
- Fercher, A.F., 2010. Optical coherence tomography - development, principles, applications. *Z. Med. Phys.* 20, 251–276.
- Fujimoto, J.G., 2003. Optical coherence tomography for ultrahigh resolution in vivo imaging. *Nat. Biotechnol.* 21, 1361–7.

- Hanneschläger, G., Nemeth, A., Hofer, C., Goetzloff, C., Reussner, J., Wiesauer, K., Leitner, M., 2011. Optical coherence tomography as a tool for non destructive quality control of multi-layered foils. In: 6th NDT in Progress 2011. International Workshop of NDT Experts, Prague, p. Paper 7.
- Koller, D.M., Hanneschläger, G., Leitner, M., Khinast, J.G., 2011. Non-destructive analysis of tablet coatings with optical coherence tomography. *Eur. J. Pharm. Sci.* 44, 142–148.
- Mauritz, J.M.A., Morrisby, R.S., Hutton, R.S., Legge, C.H., Kaminski, C.F., 2010. Imaging Pharmaceutical Tablets with Optical Coherence Tomography. *J. Pharm. Sci.* 99, 385–391.
- Nemeth, A., Hanneschläger, G., Leiss-Holzinger, E., Wiesauer, K., Leitner, M., 2013. Optical Coherence Tomography – Applications in Non- Destructive Testing and Evaluation. In: Kawasaki, M. (Ed.), *Optical Coherence Tomography*.
- Prykäri, T., Czajkowski, J., Alarousu, E., Myllylä, R., 2010. Optical coherence tomography as an accurate inspection and quality evaluation technique in paper industry. *Opt. Rev.* 17, 218–222.
- Sacchet, D., Brzezinski, M., Moreau, J., Georges, P., Dubois, A., 2010. Motion artifact suppression in full-field optical coherence tomography. *Appl. Opt.* 49, 1480–1488.
- Serreels, K.A., Renner, M.K., Reid, D.T., 2010. Optical coherence tomography for non-destructive investigation of silicon integrated-circuits. *Microelectron. Eng.* 87, 1785–1791.
- Stifter, D., 2007. Beyond biomedicine: a review of alternative applications and developments for optical coherence tomography. *Appl. Phys. B* 88, 337–357.
- Stifter, D., Wiesauer, K., Wurm, M., Schlotthauer, E., Kastner, J., Pircher, M., Götzinger, E., Hitzenberger, C.K., 2008. Investigation of polymer and polymer/fibre composite materials with optical coherence tomography. *Meas. Sci. Technol.* 19, 074011.
- Verboven, P., Nemeth, A., Abera, M.K., Bongaers, E., Daelemans, D., Estrade, P., Herremans, E., Hertog, M., Saeys, W., Vanstreels, E., Verlinden, B., Leitner, M., Nicolai, B., 2013. Optical coherence tomography visualizes microstructure of apple peel. *Postharvest Biol. Technol.* 78, 123–132.

- Walther, J., Koch, E., 2009. Transverse motion as a source of noise and reduced correlation of the Doppler phase shift in spectral domain OCT. *Opt. Express* 17, 19698–19713.
- Wojtkowski, M., 2010. High-speed optical coherence tomography: basics and applications. *Appl. Opt.* 49, 30–61.
- Yun, S.H., Tearney, G., de Boer, J., Bouma, B., 2004. Motion artifacts in optical coherence tomography with frequency-domain ranging. *Opt. Express* 12, 2977–2998.
- Zang, Z., Minato, T., Navaretti, P., Hinokuma, Y., Duelk, M., Velez, C., 2010. High-Power (> 110 mW) Superluminescent Diodes by Using Active Multimode Interferometer. *IEEE Photonics Technol. Lett.* 22, 721–723.
- Zang, Z., Mukai, K., Navaretti, P., Duelk, M., Velez, C., Hamamoto, K., 2011. High Power and Stable High Coupling Efficiency (66%) Superluminescent Light Emitting Diodes by Using Active Multi-Mode Interferometer. *IEICE Trans. Electron.* E-94-C, 862–864.
- Zeitler, J.A., Gladden, L.F., 2009. In-vitro tomography and non-destructive imaging at depth of pharmaceutical solid dosage forms. *Eur. J. Pharm. Biopharm.* 71, 2–22.
- Zhong, S., Shen, Y.-C., Ho, L., May, R.K., Zeitler, J.A., Evans, M., Taday, P.F., Pepper, M., Rades, T., Gordon, K.C., Müller, R., Kleinebudde, P., 2011. Non-destructive quantification of pharmaceutical tablet coatings using terahertz pulsed imaging and optical coherence tomography. *Opt. Lasers Eng.* 49, 361–365.

4

Optical Coherence Tomography as a Novel Tool for In-Line Monitoring of a Pharmaceutical Film-Coating Process³

Optical coherence tomography (OCT) is a contact-free non-destructive high-resolution imaging technique based on low-coherence interferometry. This study investigates the application of spectral-domain OCT as an in-line quality control tool for monitoring pharmaceutical film-coated tablets. OCT images of several commercially-available film-coated tablets of different shapes, formulations and coating thicknesses were captured off-line using two OCT

³ This chapter is based on Markl, D., Hanneschläger, G., Sacher, S., Leitner, M., Khinast, J.G., 2014. Optical coherence tomography as a novel tool for in-line monitoring of a pharmaceutical film-coating process. *Eur. J. Pharm. Sci.* 55, 58–67 with permission from Elsevier, and on Markl, D., Hanneschläger, G., Sacher, S., Khinast, J.G., Leitner, M., 2013. Optical coherence tomography for non-destructive analysis of coatings in pharmaceutical tablets. In: *Proc. SPIE*. pp. 879202–879209.

systems with center wavelengths of 830 nm and 1325 nm. Based on the off-line image evaluation, another OCT system operating at a shorter wavelength was selected to study the feasibility of OCT as an in-line monitoring method. Since in spectral-domain OCT motion artifacts can occur as a result of the tablet or sensor head movement, a basic understanding of the relationship between the tablet speed and the motion effects is essential for correct quantifying and qualifying of the tablet coating. Experimental data was acquired by moving the sensor head of the OCT system across a static tablet bed. Although examining the homogeneity of the coating turned more difficult with increasing transverse speed of the tablets, the determination of the coating thickness was still highly accurate at a speed up to 0.7 m/s. The presented OCT setup enables the investigation of the *intra*- and *inter*-tablet coating uniformity in-line during the coating process.

4.1 Introduction

In pharmaceutical manufacturing, good manufacturing practices (GMP) and numerous quality tests were introduced to guarantee the quality and safety of pharmaceutical products. More recently, a number of regulatory approaches, including Quality by Design (QbD) and Process Analytical Technology (PAT), have raised the interest in an in-depth understanding of a process, product characteristics and in-line monitoring of product quality (FDA, 2004; ICH, 2009). A detailed understanding of the effect that the key process and material parameters have on the product quality can only be achieved by measuring quality attributes of the intermediate or final product and relating them to the key process parameters (D.M. Koller et al., 2011; Scheibelhofer et al., 2013). Implementing an appropriate control strategy, including real-time measurements, is essential for process improvement, optimization and quality assurance.

Manufacturing of pharmaceutical solid dosage forms often involves film coating as a final process. Typically, a thin continuous solid layer that controls the rate of drug release as a function of the environment is applied. The main functionality of such modified-release coatings (i.e., enteric coatings) is to align the initial drug release kinetics with the pH of the environment. In some cases the coating also contains an active pharmaceutical ingredient (API). However, tablets may also be coated for visual attractiveness, taste masking or brand recognition (Suzzi et al., 2010).

The main challenges of film coating are to apply spray droplets uniformly on the surface of a tablet and among the whole batch, and to dry the (typically aqueous) coating materials at a proper evaporation rate. There is still a lack of understanding of how in detail the material and operating parameters affect the product quality. Thus, defects do occur. The most common tablet coating defects are: (1) overwetting/picking (i.e., a part of the film coating is pulled off one tablet and deposited on another), (2) twinning (i.e., two or more of the tablet cores are stuck together), (3) orange peel (i.e., roughened film due to spray drying), (4) bridging (i.e., the film coating protrudes from the tablet logo), (5) cracking (i.e., internal stress in the film), (6) coating thickness variations (i.e., within a batch due to poor process and equipment design) and coating inhomogeneities (i.e., either a visible color variation from tablet to tablet or an unacceptable release profile of the tablets), (7) tablet attrition/erosion (i.e., some portion of the product substrate has a high level of friability), (8) core erosion (i.e., attrition due to overwetting of the tablet), (9) peeling (i.e., large pieces or flakes of the film coating fall off the tablet core), (10) loss of logo definition (i.e., the tablet logo is no longer clearly legible), (11) core stability issues (i.e., discoloration or degradation of the core) and (12) tablet marking (i.e., black marking on the tablet face) (D M Koller et al., 2011; Porter et al., 2009).

An imperfect coating may result in ineffective gastric-juice resistance and render the drug useless. In contrast, too much coating material may interfere with drug absorption in the small intestine (Porter et al., 2009). Thus, traditional biopharmaceutical parameters (i.e., disintegration time, dissolution profile) may be impacted by the coating process and it is important to understand the processing steps and their effect on the final product (Zeitler and Gladden, 2009). Since thickness and homogeneity of the coating are known to be critical for the drug release rate, their direct or indirect monitoring is essential.

Generally, the methods for film analysis can be categorized as destructive and non-destructive. Scanning electron microscopy (SEM) and confocal laser scanning microscopy (CLSM), for example, are destructive since they require a cut through the tablet and cannot be used for in-line monitoring. For a quick feedback, a measurement method should resolve the structure of the dosage form fast and non-destructively. Spectroscopic techniques, such as near-infrared (NIR) and Raman spectroscopy, offer an opportunity of solid dosage form characterization and coating processes monitoring. The quantitative determination of the coating thickness via

Chapter 4: Optical Coherence Tomography as a Novel Tool for In-Line Monitoring of a Pharmaceutical Film-Coating Process

NIR and Raman has already been performed for off-line and in-line product characterization (Cahyadi et al., 2010; Kirsch and Drennen, 1995; Romero-Torres et al., 2006). In combination with multivariate data analysis (MVDA), these methods allow real-time non-invasive and quantitative process monitoring (Müller et al., 2012; Römer et al., 2008). The major drawbacks of spectroscopic techniques are that they do not provide an absolute value of the coating thickness directly and have a limited capability for *inter*- and *intra*-tablet coating uniformity analysis. Since a calibration based on primary measurements (e.g., SEM) providing an absolute value is required, the prediction of the coating thickness is only as accurate as the reference measurements.

The above mentioned disadvantages can be overcome by using tomographic methods, which provide spatially (transversally and axially) resolved information regarding the coating. Several tomographic techniques are available, such as X-ray computed microtomography (X μ CT), magnetic resonance imaging (MRI), terahertz pulse imaging (TPI) and optical coherence tomography (OCT) (Zeitler and Gladden, 2009). Most of them have already been successfully applied for the tablet coating analysis. However, only TPI and OCT fulfill the requirements for an in-line measurement system, such as high spatial (transverse and axial) resolution, high sensitivity regarding the detection of coating layers and impurities, large penetration depth, and separation of sensor head and processing module.

TPI is highly suitable for pharmaceuticals characterization, since terahertz radiation easily penetrates the excipients used in pharmaceutical tablets and reveals a contrast between them (Shen and Taday, 2008). TPI's high potential as an in-line coating process measurement was demonstrated by May et al., 2010 who successfully applied an in-line sensor for terahertz measurements of the film coating ranging from 40 μ m to 1 mm. However, the transversal and axial spatial resolutions in TPI are limited to 50 μ m and 40 μ m, respectively. Since the coating thickness of most commercially-available pharmaceutical tablets ranges from 5 μ m to 200 μ m, a better axial resolution would be preferable. Moreover, TPI is expensive and requires relatively long measurement times.

These problems may be overcome using OCT, which is easily deployable and has a high data acquisition rate, a good transversal resolution and an extremely high axial resolution. OCT is a contact-free non-destructive high resolution imaging technique that originates from the field of biomedicine with the main applications in ophthalmology (Sakata et al., 2009), cardiology (Bezerra et al., 2009),

dermatology (Welzel, 2001) gastroenterology and endoscopy (Adler et al., 2009) However, over the last years, the number of OCT applications in non-destructive testing and evaluation (NDT, NDE) of non-biological materials has substantially increased (Stifter, 2007).

OCT off-line applications for determining the coating thickness and detecting film defects have been studied in the literature and have been compared to other measurement techniques (D M Koller et al., 2011; Mauritz et al., 2010; Zhong et al., 2011). In the current study, the feasibility of OCT as an in-line method for monitoring of pharmaceutical tablet film coating is reported. First, the feasibility of OCT for the analysis of the tablet coatings was examined. Off-line investigations of several different commercially-available tablets with film coating were conducted using two spectral-domain (SD)-OCT systems. Secondly, the influence of a moving tablet bed on OCT images was analyzed in a static tablet bed by moving the sensor head along the tablet bed. The effect of the movement on the OCT image was examined and verified via experimental data.

4.2 Materials and Methods

4.2.1 Optical Coherence Tomography

OCT is used to generate cross-sectional depth-resolved two- and three-dimensional images of translucent materials. Physically, OCT is based on low-coherence interferometry (LCI) and uses light sources with high spatial and low temporal coherence (i.e., a large bandwidth spectrum corresponding to coherence lengths of several microns). Since OCT is an interferometric approach, such a short coherence length acts as a temporal filter for photons that are back-reflected and back-scattered from different sample structures, such as interfaces, impurities, pores and cells. A depth scan is performed by comparing the arrival times of single scattered photons with a reference light beam. Low-coherence light sources generally have a coherence length in the region of 1 - 15 μm , and enable therefore an excellent axial-(depth) resolution (Fercher et al., 2003). The axial resolution δ_c is defined as half of the coherence length l_c , which is limited by the center wavelength λ_c and the full width at half maximum (FWHM) bandwidth $\Delta\lambda$ of the light source:

$$\delta z = \frac{l_c}{2} = K \frac{\lambda_c^2}{\Delta\lambda}. \quad (4.1)$$

K is a constant factor given as 0.44 for a source with Gaussian spectral distribution. The depth-resolved OCT signal can be acquired either in time-domain or in Fourier-domain. In time-domain, the reference arm in the interferometer is varied and a signal is detected only when the photons reflected from both interferometer arms have travelled the same optical distance to the photodetector. The mechanical movement of a reference mirror can cause mechanical instabilities and noise. Acquiring the signal via OCT in Fourier-domain has advantages in terms of imaging speed and sensitivity and can be used for in-line process monitoring. In this approach the reference arm is fixed and the interference signal of the light that back-reflects and back-scatters from the reference mirror and the sample is detected in a spectrally resolved way. This can be performed either in parallel (spectral-domain) by using a dispersive element and a CCD or CMOS line scan camera, or sequentially, by scanning a narrow laser line over a broad spectral region (swept-source OCT) (Fercher, 2010; Leitgeb et al., 2004). In both approaches, the depth is accessed by applying an inverse Fourier transform to the acquired interference spectrum.

The OCT nomenclature is analogous to the one used in ultrasound tomography. In **Figure 4.1**, single- depth scans and cross-sections are labeled as A- and B-scans, respectively. Cross-sectional images are synthesized from adjacent A-scans, which are generated by scanning the incident optical beam transversely. Moreover, three-dimensional volumetric data can be created by acquiring sequential B-scan images via a raster pattern scan of the incident optical beam.

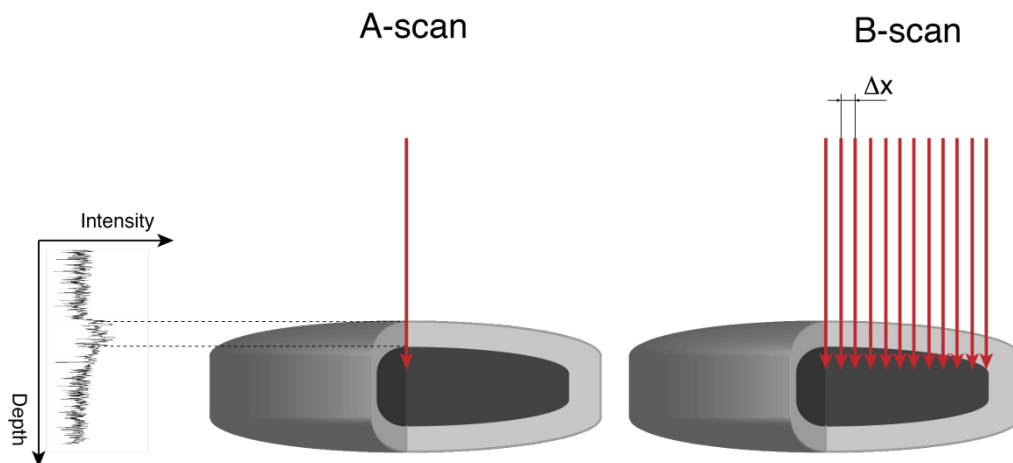


Figure 4.1: An A-scan is a single-depth scan. The signal of one A-scan is expressed by the magnitude of the reflected light as a function of the axial distance. Cross-sectional images are generated by transversally scanning the light beam. The displacement of the light beam is denoted as Δx .

4.2.2 OCT Systems

In this study three different SD-OCT systems (two applied off-line and one in-line) in spectral-domain configuration were employed. The results from the off-line investigation of several tablets (presented in section 4.2.3.1) were the basis for the selection of an OCT system operating at a central wavelength of 830 nm. The system presented for in-line analysis was designed especially for such in-line measurements.

4.2.2.1 OCT Systems for Off-line Analysis

Off-line investigation of film-coated tablets was carried out with two SD-OCT systems: (1) a TELESTO™ OCT Imaging System (Thorlabs Inc, Newton, New Jersey, USA) and (2) an OCT system developed in-house (presented in D M Koller et al., 2011 and hereinafter referred to as 830nmOCT). The illumination wavelengths of the two systems differ from each other. The TELESTO™ OCT Imaging System operates at a central wavelength of 1325 nm and provides a bandwidth of 150 nm. 830nmOCT was designed for a SLD Broadlighter (Superlum Diodes Ltd., Carrigtwohill, Co. Cork, Ireland) with a central wavelength of 830 nm and a bandwidth of 62 nm. The axial resolutions measured in air were 7.5 μm and 4.9 μm for the TELESTO™ and the 830nmOCT system, respectively.

4.2.2.2 OCT System for In-line Analysis

The in-line feasibility study was performed with a third SD-OCT system, which was specifically developed for in-line applications. This system allows the use of two simply interchangeable sensor heads, as shown in **Figure 4.2**. A SLD Broadlichter (Superlum Diodes Ltd.) with a central wavelength of 830 nm and a FWHM spectral bandwidth of 62 nm was used as a light source, resulting in an axial resolution of 4.9 μm . The light exiting the light source passed a directional coupler DC (Thorlabs). Either the optical fiber of the 1-D or the 2-D sensor head can be mounted on the DC. The 1-D sensor head employed a fiber focuser FF (OZ Optics, focal length $f = 40$ mm) and only allows for the generation of single A-scans. To produce a 2-D OCT image with this sensor head, it is necessary to introduce an external movement of either the sensor head or the sample. In the 2-D sensor head, the light was collimated by a fiber collimator FC (OZ Optics, Ottawa, Canada) and the sample beam was scanned across the object by using a galvanometer mirror GM (Cambridge Technologies) and an achromatic lens L1 (Thorlabs, focal length, $f = 36$ mm). In both sensor heads, the light beam was split into reference and sample beams by a non-polarizing beamsplitter BS (Thorlabs). The light that was reflected back from the reference mirror and the sample (the coated tablet) was recombined in the beamsplitter BS, injected into the same optical fiber and transmitted to the spectrometer. In the spectrometer, the light beam was collimated with an fiber collimator FC (OZ Optics), dispersed on a transmissive diffraction grating DG (Wasatch Photonics, 1200 lines/mm) and focused onto a linear CCD camera (Atmel Aviiva, 2048 pixel, 14 μm^2 pixel size, 12 bit resolution) through an achromatic lens L3 (Thorlabs, $f = 100$ mm). The output voltage of each CCD pixel was proportional to the number of photons hitting an individual pixel accumulated during the CCD exposure time.

Data processing of the measured spectra was performed on hardware basis by a field-programmable gate array (FPGA). This included the re-mapping of the interference spectra from a uniform wavelength space to a uniform wavenumber space by interpolation prior to the inverse discrete Fourier transform (IDFT). The analysis of the images was carried out via a dedicated MATLAB (Mathworks Inc, Natick, Massachusetts, USA) tool.

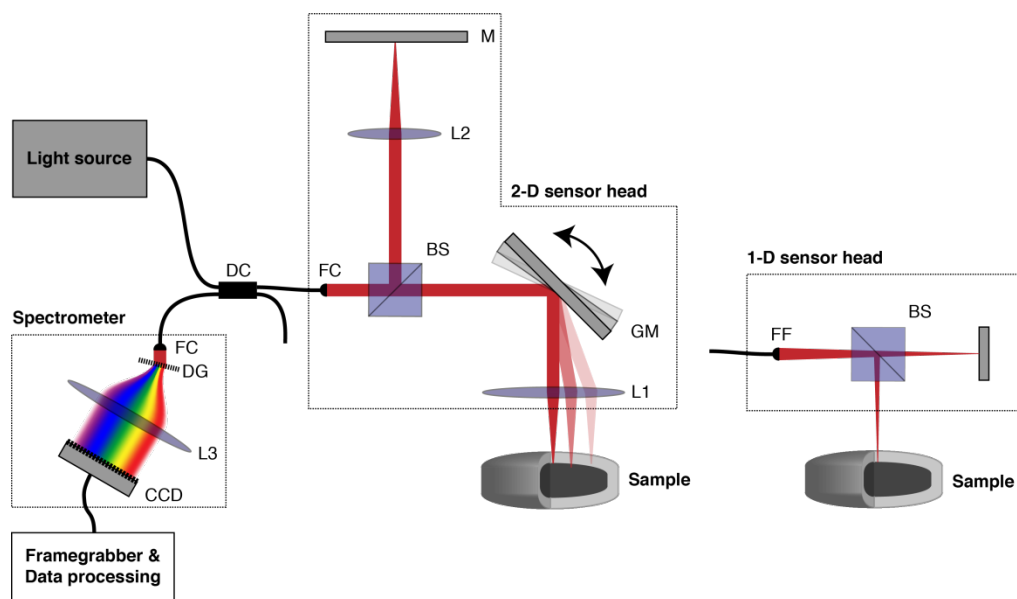


Figure 4.2: Schematic of the experimental design. The 1-D and 2-D sensor heads can easily be exchanged. DC – directional coupler, FC – fiber coupler, BS – beamsplitter, GM – galvanometer mirror, FF – fiber focuser, L – lenses, M – mirror, DG – diffraction grating, CCD – charged coupled device.

4.2.3 Used Tablets

4.2.3.1 Tablets for Off-line Analysis

Off-line measurements of several commercially-available tablets were carried out on seven different types of coated tablets. Generally, each tablet core consists of an API (e.g., acetylsalicylic acid) and several pharmaceutical excipients (e.g., magnesium stearate, lactose or MCC). The formulation of a film coating varies widely depending on the purpose. Moreover, the tablets vary in shape and size. The main focus of this work was to investigate tablets with modified-release (enteric) coating. All investigated tablets are shown in **Table 4.1**.

Table 4.1: Tablets investigated during the off-line studies.

Brand name
Diclofenac G.L. [®] retard 100 mg
Glucophage [®] 500 mg
Pantoloc [®] 40 mg
Thrombo ASS [®] 50 mg
Tromcardin [®]
Voltaren [®] 50 mg
Zurcal [®] 40 mg

Table 4.2: Composition of the enteric film coating suspension.

Parameter	(mg)/tablet	%
Talcum	3.795	25.3
Glyceryl triacetate	1.020	6.8
Eudragit L30D-55	10.185	67.9
Aqua purificata	38.0	-

4.2.3.2 Tablets for In-line Feasibility Study

For the in-line experiments, a number of tablets with modified-release (enteric) coating were produced. The tablet cores with a standard bi-convex shape having a diameter of 8 mm were manufactured in a rotary press. The core consisted of acetylsalicylic acid (ASA) as an API and other common excipients. The coating was applied to the cores using a lab-scale coating pan. The composition of the enteric film coating suspension is presented in **Table 4.2**. A standard preparation of Eudragit L30D (Evonik Industries AG, Essen, Germany) was used.

4.2.4 In-line Analysis

4.2.4.1 Background

When applying OCT for in-line monitoring one has to deal with a relative movement between the sample and the sensor head, which is typically not assumed during the image reconstruction process, and can result in image artifacts (e.g., if the sample is in motion during the data acquisition). Motion artifacts have been an important research topic in nearly all imaging methods since they may cause inaccurate image interpretation (Walther and Koch, 2009; Yun et al., 2004).

Generally, motion artifacts are caused by transverse (orthogonal to the light beam), axial (parallel to the light beam) or oblique (combination of transverse and axial) sample movements. This study assumes that the sample was exclusively moved in one transverse direction and the axial distance between sample and sensor head was constant. Such a movement does not affect the axial resolution of SD-OCT systems (Yun et al., 2004), even though it strongly influences the transverse resolution. The transverse resolution determines the lower limit of barely detectable imperfections in the coating and additionally constrains the number of coating thickness measurements per tablet. Ideally, uniformly distributed measurements of the coating thickness of one tablet are required to evaluate *intra*-tablet coating uniformity.

The limitation in the transverse resolution is primarily due to the optics of the OCT system. In addition, the transverse speed of the sample or the sensor head contributes to a degradation of the transverse resolution. The higher the speed, the more crucial is the limitation of the transverse resolution. Hence, a basic understanding of the relationship between image properties and sample speed is required. This is fundamentally important for the application of OCT as an in-line process monitoring method, since OCT images are recorded continuously.

4.2.4.2 Relative Movement between Sensor Head and Tablets

Analyzing a sample in motion requires a good understanding of how a B-scan is generated. The special case, in which neither the sensor head nor the tablet bed is moved, is hereinafter referred to as the stationary case. It may, however, include moving the galvanometer mirror in order to produce B-scan images.

As mentioned above, one B-scan image is produced with a defined number of A-scans. The A-scans are displaced according to the exposure time T_{exp} of the CCD and the idle time T_{idle} between the two adjacent A-scan measurements. An exposure time of 34 μs and an idle time of 1.91 μs were used for all experiments (1-D and 2-D sensor head). The acquisition time of one A-scan can thus be written as:

$$T = T_{\text{exp}} + T_{\text{idle}}. \quad (4.2)$$

The exposure and idle time of the camera resulted in a duty cycle of 95% ($= \frac{T_{\text{exp}}}{T_{\text{exp}} + T_{\text{idle}}}$) and a readout rate of 27.8 kHz.

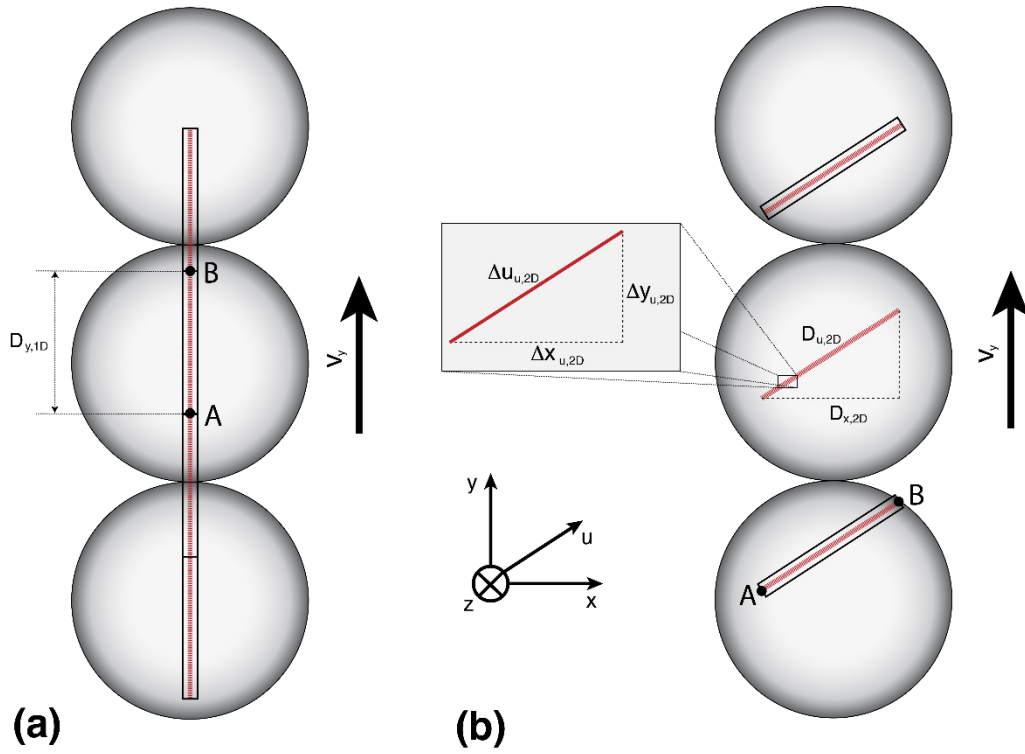


Figure 4.3: Trajectory of B-scans considering the sensor head moves at a certain speed. (a) 1-D sensor head: the transversal measurement range of one OCT image and the transversal pixel size directly depend on the speed of the sensor head. (b) 2-D sensor head: the movement of the sensor head causes broadening of the transversal beam displacement. The markers A and B are the first and last A-scans of the B-scan, respectively.

Moreover, the beam displacement represents the distance that the light beam travels between two adjacent A-scans. The beam displacement depends on the speed difference between sample and beam, and thus, varies for different velocities and both sensor heads.

Figure 4.3(a) shows the trajectory of the 1-D sensor head for the transversal velocity v_y . The information coded in the OCT images with the 1-D sensor head greatly depends on the speed of the tablets or sensor head. Since this sensor head does not have an internal scanning procedure, OCT measurements are acquired in parallel to the movement of the sensor head (y -direction).

The beam displacement Δy for the 1-D sensor head can be calculated as the acquisition time T of one A-scan times the velocity v_y of the sensor head. As such, the transversal image size $D_{y,1D}$ can be expressed by:

$$D_{y,1D}(v_y) = N \Delta y(v_y) = N T v_y, \quad (4.3)$$

where N is the number of A-scans per OCT image. The number of A-scans corresponds to the number of transversal pixels of the OCT image. The transversal image size depends linearly on the speed of the sensor head under the consideration of a constant acquisition time of an A-scan.

In the case of the 2-D sensor head, the galvanometer mirror deflects the light beam onto the sample with respect to a defined beam displacement Δx_{2D} (see **Figure 4.1**). The transversal image size $D_{x,2D}$ for the stationary case is obtained via the procedure established for the 1-D sensor head.

The B-scans are influenced by transverse broadening of the OCT image, as illustrated in **Figure 4.3(b)**. This effect is caused by the speed difference between sensor head and sample in the y -direction, which results in a displacement of the starting position A and the end position B of one B-scan. The velocity of the sensor head implies broadening of the beam displacement. The width of this extended beam displacement can be calculated as:

$$\Delta u_{2D}(v_y) = \sqrt{\Delta x_{2D}^2 + \Delta y_{2D}(v_y)^2}. \quad (4.4)$$

The beam displacement is proportional to the transverse image size and is expressed as:

$$D_{u,2D}(v_y) = N \Delta u_{2D}(v_y). \quad (4.5)$$

Since the number of A-scans (1000) was kept constant during this analysis, the quantization step size of the OCT image (i.e., the beam displacement) increased drastically at higher velocities of the sensor head. The broadening of the beam displacement is equivalent to that of the transverse image size of a certain sensor head speed.

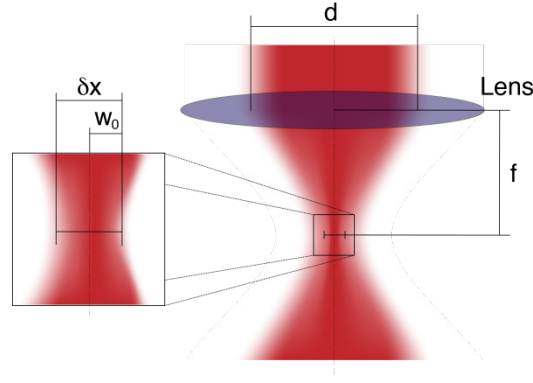


Figure 4.4: The transverse resolution δx is proportional to the ratio of the focal length f and the beam diameter d at lens L1 (**Figure 4.2**).

In addition to the beam displacement, the exposure time affects the transversal resolution, which depends on the optics of the system and the operating wavelength of the source. Therefore, the transverse resolution is limited by the beam waist at the focus (**Figure 4.4**), and provided a sufficiently high sampling rate of the A-scans for the 2-D sensor head. For a Gaussian sample beam, the transverse resolution is defined as the full width at half maximum (FWHM) diameter:

$$\delta x = 2w_0 = 4 \frac{\lambda_c f}{\pi d}, \quad (4.6)$$

where w_0 is the beam waist radius, λ_c the central wavelength of the optical source, f the focal length and d the beam diameter at the lens (see **Figure 4.4**). The transverse resolution for the setup used during the in-line measurements is $9.51 \mu\text{m}$.

Transverse motion and a certain exposure time of the CCD cause broadening of the transverse resolution. This study does not address this effect, but it must be taken into account when designing an OCT image for in-line monitoring.

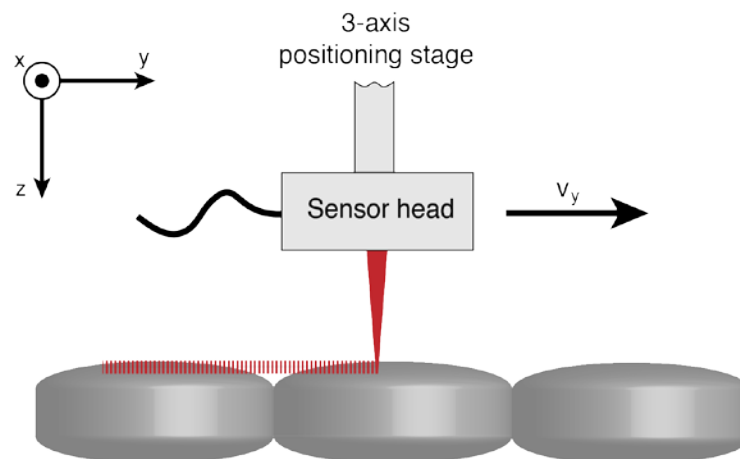


Figure 4.5: Schematic of the 3-axis positioning system. The sensor heads (1-D and 2-D) were mounted on the positioning system and moved across a tablet bed with different speeds, ranging from 0.025 m/s to 0.7 m/s.

4.2.4.3 3-Axis Positioning System

The in-line capability of the OCT system for tablet coating monitoring was tested via a 3-axis positioning system. In general, motion effects caused by moving tablets with the sensor head in the same position are the same as those caused by moving the sensor head across a static tablet bed. As such, the sensor heads (1-D and 2-D) were mounted to the 3-axis positioning stage and moved between defined positions. A schematic of the experimental setup is depicted in **Figure 4.5**. The sensor head was moved only in y -direction across the tablet bed. Experiments were carried out for 10 velocities ranging from 0.025 m/s to 0.7 m/s. In order to gather more information for lower velocities, 0.025 m/s increments were used for speeds below 0.1 m/s. The remaining increments were set to 0.1 m/s. A typical circumferential speed of an industrial pan coater is between 0.4 m/s and 0.6 m/s.

4.3 Results

4.3.1 Off-Line Measurements

Figure 4.6 shows off-line OCT images (stationary sensor head) of several commercially-available tablets. The images were obtained using the 830nmOCT and the TELESTO™ from Thorlabs. All OCT images of the tablets with modified-release coating (Tromcardin®, Zurcal®, Pantoloc®, Voltaren® and Thrombo

Chapter 4: Optical Coherence Tomography as a Novel Tool for In-Line Monitoring of a Pharmaceutical Film-Coating Process

ASS®) except for Glucophage® and Diclofenac® provided enough contrast to determine the coating thickness.

Penetration depth and image contrast strongly depend on the optical properties of the tablets, i.e., refractive index, scattering and absorption properties. Optical properties of the tablets vary depending on the operating wavelengths of the light source.

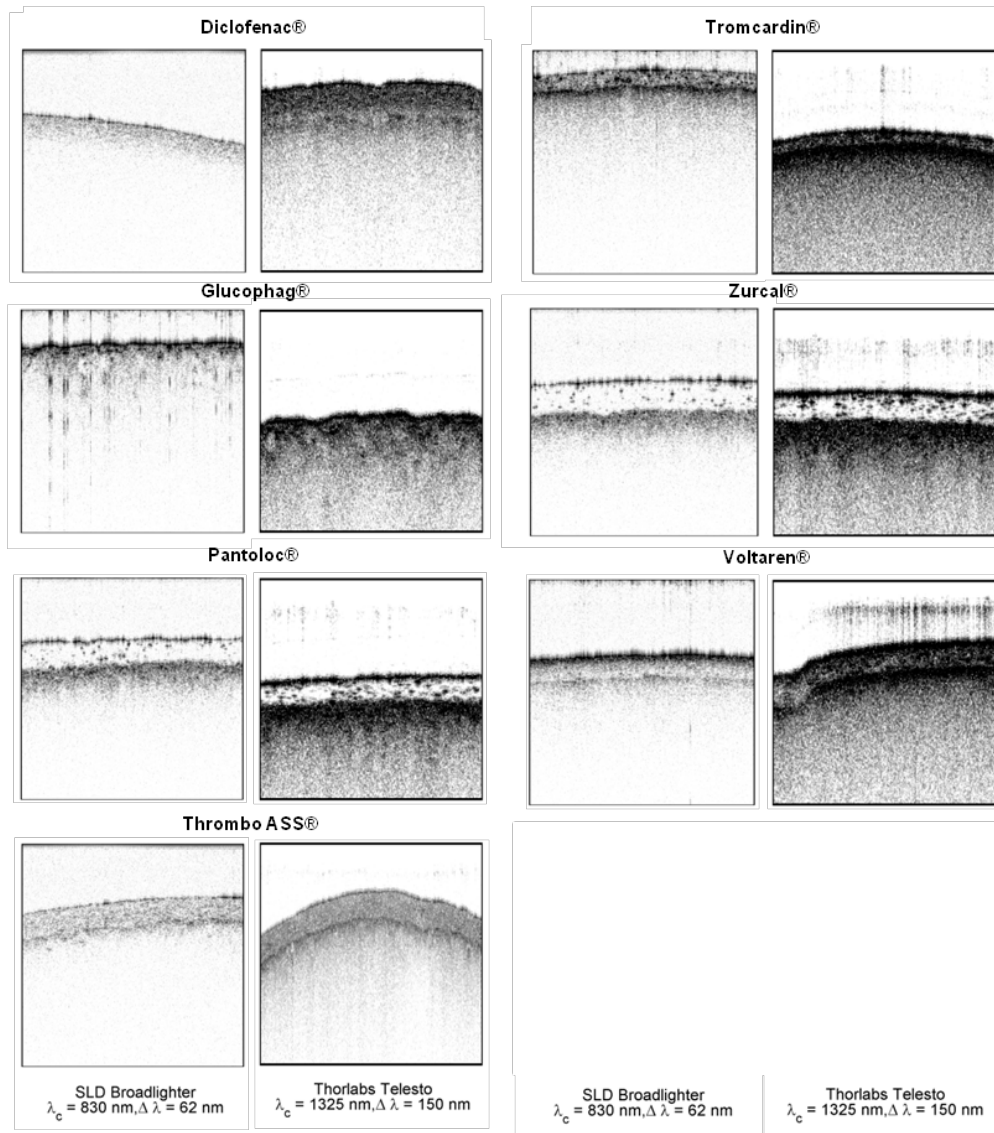


Figure 4.6: OCT images of Diclofenac®, Tromcardin®, Glucophage®, Zurcal®, Pantoloc®, Voltaren® and Thrombo ASS®. Optical image dimensions (in air): (1) SLD Broadlighter: $3.208 \times 1.332 \text{ mm}^2$ and (2) TELESTO™: $4 \times 1.335 \text{ mm}^2$.

It is evident that the coating layer of Diclofenac is only visible in the OCT image acquired by the TELESTO™ system. In addition to aesthetic reasons (as is the case for Diclofenac®), colorants may serve as protection for photo-labile APIs (Porter et al., 2009). Since colorants act as a scatterer and an absorber of certain light wavelengths, they set limitations to performing the analysis of the coating thickness using OCT at shorter wavelengths (e.g., 830 nm). Due to strong scattering and absorption in these spectral regions, only low penetration in solid dosage forms can be achieved. This could be overcome by selecting a light source with a longer central wavelength, which however, implies degradation of the axial resolution and makes the selection of an appropriate light source a trade-off between penetration depth and axial resolution. The higher axial resolution of the 830nmOCT allows the detection of smaller coating thicknesses compared to the TELESTO™ system. This can be observed at the OCT images of Glucophage®, where the images acquired with the system operating at a shorter central wavelength (first column) partly enable the identification of a coating film. However, both images do not show a high contrast of the coating layer due to the thin coating layer and the coarse tablet surface.

Since the system operating at a lower wavelength provided satisfying results, we chose a system with a central wavelength of 830 nm for our in-line application of OCT. This provides excellent axial resolution and allows an analysis of the coating homogeneity. However, the limited penetration depth has to be taken into account for every new case.

4.3.2 Experimental Results of the In-Line Feasibility Study

Figure 4.7 depicts B-scans at 10 velocities acquired with the 1-D and 2-D sensor heads. For both sensor heads, broadening of the image section was the most noticeable effect. **Table 4.3** lists the transverse image sizes for each sensor head speed.

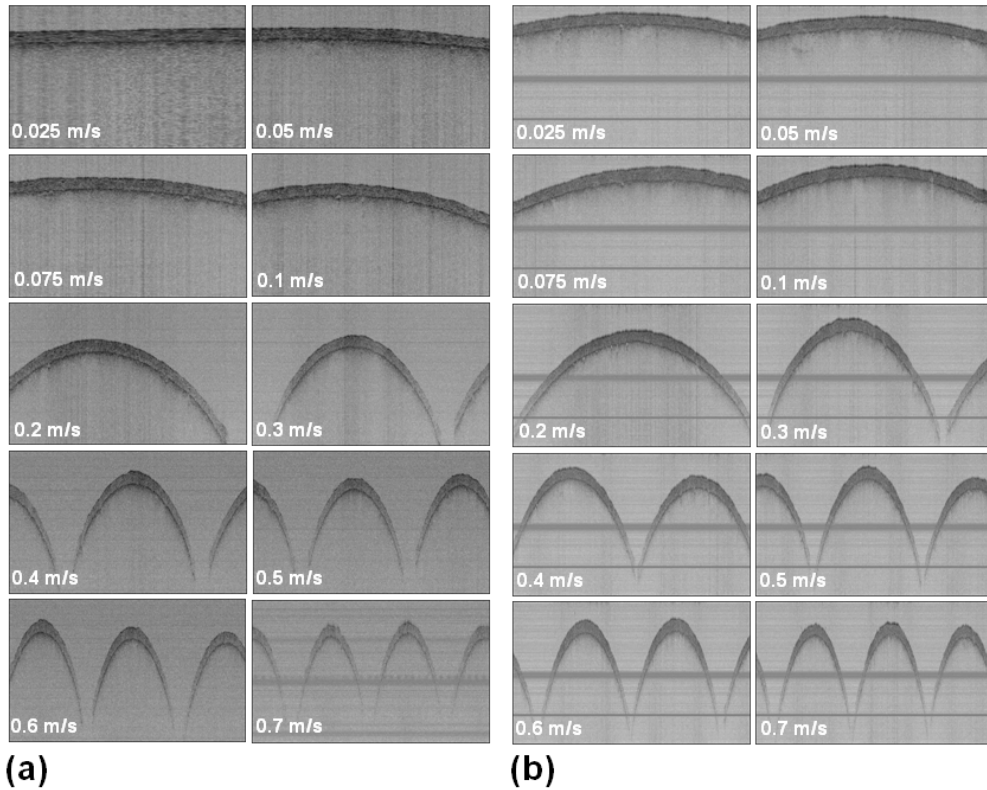


Figure 4.7: B-scans of the tablets at 10 velocities of (a) the 1-D and (b) the 2-D sensor head. Optical image dimensions (in air): (a) $D_{y,1D}(v_y) \times 2.5 \text{ mm}^2$ and (b) $D_{u,2D}(v_y) \times 2.5 \text{ mm}^2$, where $D_{y,1D}$ and $D_{u,2D}$ are listed in **Table 4.3**.

Beyond a speed of 0.3 m/s each B-scan shows a cross-section image of more than one tablet. This implies that less A-scans per tablet were acquired, which degrades the illustrative presentation of a tablet and limits the potential number of thickness measurements per tablet. Clearly, fewer measurements lead to a less accurate analysis of the *intra*-tablet coating uniformity. However, OCT images acquired with a sensor head speed of 0.7 m/s provide almost 200 A-scans per tablet, albeit the curvature of the coating layer has to be adjusted in order to determine the coating thickness for all measurements correctly.

At a sensor head speed above 0.2 m/s, the transverse image sizes of the OCT images of both sensor heads are approximately the same. Moreover, comparing the transverse image size at speeds of 0.2 m/s and 0.7 m/s showed that the image should theoretically be scaled by a factor of 3.5. This agrees well with the experimental results.

Table 4.3: Transverse image size for the 1-D and 2-D sensor heads as a function of the sensor head speed. It was calculated on the basis of Eqs. (4.3) and (4.5) for the 1-D and 2-D sensor heads, respectively.

Sensor head velocity v_y (m/s)	Transverse image size $D_{y,1D}$ (mm)	Transverse image size $D_{u,2D}$ (mm)
0.025	0.90	3.07
0.05	1.80	3.44
0.075	2.69	3.98
0.1	3.59	4.64
0.2	7.18	7.76
0.3	10.77	11.17
0.4	14.36	14.66
0.5	17.96	18.19
0.6	21.55	21.74
0.7	25.14	25.31

These experiments emphasize the difference between the sensor heads. The beam displacement of the 1-D sensor head was zero in the stationary case due to the absence of an internal scanning procedure. Therefore, the system was basically an LCI or white light interferometer. The image size linearly increases with the speed of the sensor head. For the 2-D sensor head, the beam displacement was non-zero at zero speed and, with increasing speed, approached the beam displacement of the 1-D sensor head. Since the contribution of the galvanometer mirror speed to the total speed v_u is very small at higher sensor head speeds, the total speed can be assumed to be approximately the speed of the sensor head. As such, the beam displacements of the 1-D and 2-D sensor heads are almost equal and thus, the accuracy of the coating thickness measurements is expected to be similar.

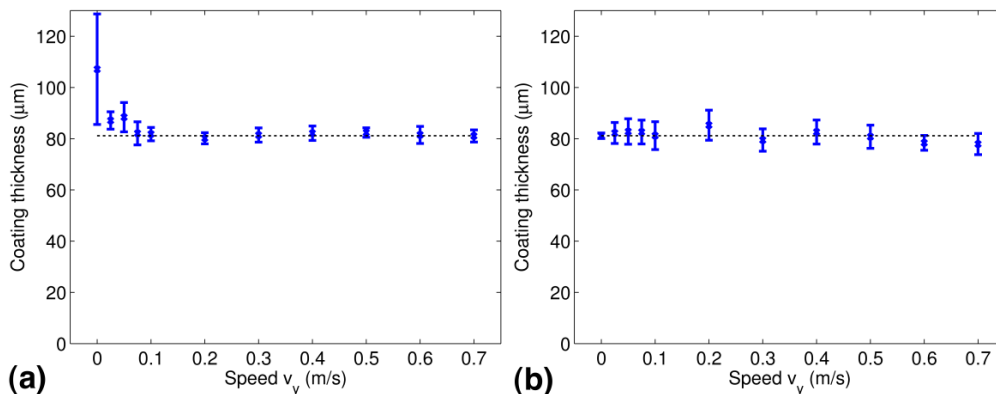


Figure 4.8: Coating thickness for the (a) 1-D and (b) 2-D sensor heads. The mean and standard deviations for each sensor head speed were calculated based on 32 measurements of eight tablets. This standard deviation is calculated for the mean coating thickness of each tablet and thus, it indicates the inter-tablet coating uniformity.

Determining the coating thickness and evaluating the *inter*- and *intra*-tablet coating uniformity was carried out by analyzing eight images for each sensor head speed. Four thickness measurements were performed for each tablet. The means of the 32 measurements for each sensor head speed are illustrated in **Figure 4.8**. The standard deviation was calculated for the mean coating thicknesses of the eight tablets, and therefore it is directly related to the *inter*-tablet coating uniformity. To determine the coating thickness accurately based on the measurements acquired with the 1-D sensor head, a sensor head speed above 0.075 m/s was required. For the remaining measurements, the standard deviation was between 1.8 µm and 4.5 µm and thus provided an accurate determination of the coating thickness. The 2-D sensor head, however, allowed the analysis of the coating thickness along the entire speed range.

Since OCT allows the analysis of each tablet separately, also the *intra*-tablet coating uniformity can be investigated. **Figure 4.9** illustrates the coating thickness standard deviations of each measured tablet depending on the sensor head speed. The broad distribution of the standard deviations of the 1-D sensor head for speeds below 0.075 m/s are due to the inaccurate coating thickness measurements as mentioned above. For higher speeds, the distributions and the mean of the standard deviations are similar for both sensor heads.

Comparing the *inter*- and *intra*-tablet coating uniformities on the basis of the standard deviations from **Figure 4.8** and **Figure 4.9** shows that the *inter*-tablet

coating uniformity is better. Due to the averaging of several measurements of one tablet, non-uniformities on one tablet are not contributing to the standard deviation for the *inter*-tablet coating uniformity as much as it is for the *intra*-tablet coating uniformity.

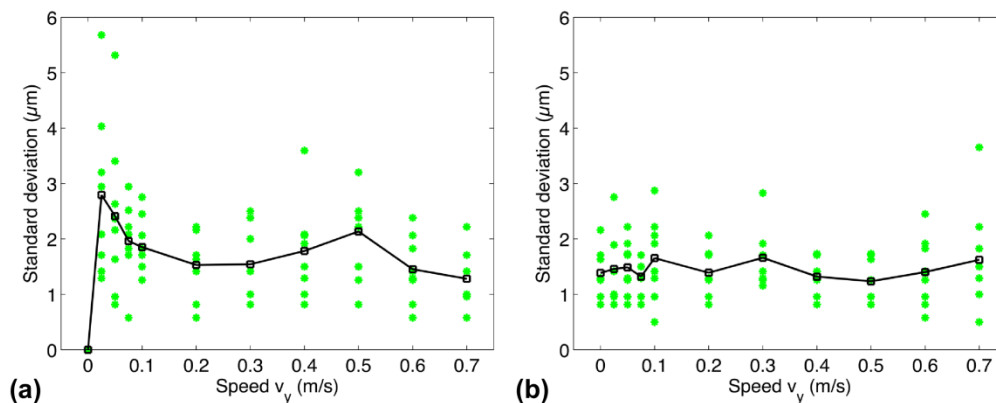


Figure 4.9: Standard deviation for the (a) 1-D and (b) 2-D sensor heads showing the intra-tablet coating uniformity. Each cross marker corresponds to the coating thickness standard deviation of one tablet consisting of 4 measurements. The line depicts the mean of the coating thickness standard deviations for each sensor head speed.

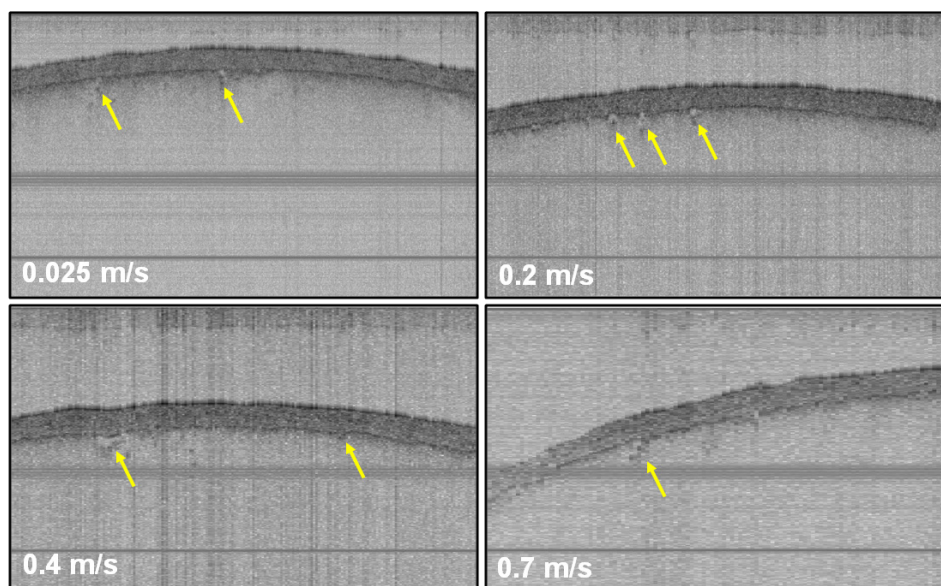


Figure 4.10: OCT images of tablets at four velocities of the 2-D sensor head. The images are cut and scaled transversely to obtain the same optical image dimensions along different velocities. The arrows are used to point to the imperfections in the coating. Optical image dimensions in air: $2.94 \times 1.46 \text{ mm}^2$.

Beside the identification of coating thickness variations on a single tablet, one would also be interested in detecting defects in the coating layer. Such imperfections may be caused by (1) the coating solution that fills core pores on the surface, i.e., diffuses into the core to a certain extent, (2) inclusions of air during the coating process, and (3) density variations, cracks or pores in the coating layer itself. Defects in the coating or the underlying bulk material can be seen in **Figure 4.10**, which are indicated by arrows. The number of A-scans per B-scan was adapted to keep the image size $D_{x,2D}$ of the stationary case constant for all velocities. Since the optical image dimension was constant, the number of A-scans decreased with increasing speed, resulting in pixelated images. The widths of the indicated defects in the OCT image at 0.025 m/s are approximately 30 μm . Due to the beam displacement scaling, these imperfections cannot be identified using the images at 0.4 m/s and 0.7 m/s. The width of one pixel of the OCT images for a speed of 0.7 m/s is 25 μm and the indicated inhomogeneity has a width of approximately 200 μm . At least a few pixels are necessary to differentiate inhomogeneities from noise. Thus, the higher the speed of the sensor head is, the less accurate inhomogeneity detection becomes. This could be overcome by decreasing the exposure time of the CCD of the OCT system and thus increasing the acquisition rate of OCT images.

4.4 Conclusion

OCT images of several commercially-available tablets with cosmetic and enteric coating acquired with two different OCT systems working at different central wavelengths were presented. Based on excellent off-line results, an optical light source operating at a central wavelength of 830 nm was chosen for an in-line feasibility study. Since using OCT as in-line monitoring method requires accounting for speed-related effects, the influence of the relative transverse movement between the sensor head and samples was investigated.

In general, the application of a 1-D or 2-D sensor heads depends on the speed of the samples or sensor head. The acquisition of B-scans could be performed continuously with the 1-D sensor head. Due to the mechanical movement of the galvanometer mirror of the 2-D sensor head, a loss of information between two adjacent B-scans occurred. The configuration of the acquisition parameters must be chosen carefully in order to enhance efficiency and reduce loss of information.

The OCT images acquired at various velocities provided enough information to detect and quantitatively determine the coating thickness of the tablets, and to evaluate the *intra*- and *inter*-tablet coating uniformity. However, broadening of the beam displacement may result in a loss of information about inhomogeneities during an in-line analysis of tablet coating. Since the presence of imperfections in the coating may cause reduced gastric resistance, the configuration parameters of the OCT system must be chosen carefully. Broadening of both resolution and image size must be taken into account when applying OCT as an in-line method.

It should be emphasized that OCT has limitations with regard to chemical analysis of solid dosage forms, which can be performed via TPI, Raman or NIR spectroscopy. However, OCT's non-destructive nature, high axial (1 - 10 μm) and transversal (1 - 10 μm) resolutions and high acquisition rate (MHz acquisition rates have already been shown) make it a promising technology for tablet diagnostics. OCT's ease of use and low costs compared to other methods provide an attractive alternative for in-line process monitoring.

However, applying OCT as in-line quality control tool implies the consideration of sensor head specifications. In particular, the distance from the sensor head to the sample has to lie in a specified range. The depth range of OCT lies between 1 and 3 mm and therefore, the tablets must pass the inspection window within this distance. A suitable mounting position of the OCT sensor head in the coating process is thus more challenging than it is for NIR or Raman probes. A suggested mounting position would be from the outside of the rotated pan through the perforations. Most of the common coaters have such perforated pans and provide enough space for the sensor head. Moreover, investigating the coating quality during manufacturing requires further development of automatic evaluation algorithm to ensure 100% quality control.

4.5 References

- Adler, D.C., Zhou, C., Tsai, T.-H., Schmitt, J., Huang, Q., Mashimo, H., Fujimoto, J.G., 2009. Three-dimensional endomicroscopy of the human colon using optical coherence tomography. *Opt. Express* 17, 784–796.

Chapter 4: Optical Coherence Tomography as a Novel Tool for In-Line Monitoring of a Pharmaceutical Film-Coating Process

- Bezerra, H.G., Costa, M. a, Guagliumi, G., Rollins, A.M., Simon, D.I., 2009. Intracoronary optical coherence tomography: a comprehensive review clinical and research applications. *JACC Cardiovasc. Interv.* 2, 1035–1046.
- Cahyadi, C., Karande, a D., Chan, L.W., Heng, P.W.S., 2010. Comparative study of non-destructive methods to quantify thickness of tablet coatings. *Int. J. Pharm.* 398, 39–49.
- FDA, 2004. Guidance for Industry. PAT - a framework for innovative pharmaceutical development, manufacturing, and quality assurance, Quality Assurance. US Department of Health, Rockville, MD.
- Fercher, A.F., 2010. Optical coherence tomography - development, principles, applications. *Z. Med. Phys.* 20, 251–276.
- Fercher, A.F., Drexler, W., Hitzenberger, C.K., Lasser, T., 2003. Optical coherence tomography - principles and applications. *Reports Prog. Phys.* 66, 239–303.
- ICH, 2009. ICH Q8(R2), Pharmaceutical Development, Part I: Pharmaceutical development, and Part II: Annex to pharmaceutical development, Current.
- Kirsch, J.D., Drennen, J.K., 1995. Determination of film-coated tablet parameters by near-infrared spectroscopy. *J. Pharm. Biomed. Anal.* 13, 1273–1281.
- Koller, D.M., Hanneschläger, G., Leitner, M., Khinast, J.G., 2011. Non-destructive analysis of tablet coatings with optical coherence tomography. *Eur. J. Pharm. Sci.* 44, 142–148.
- Koller, D.M., Posch, A., Hörl, G., Voura, C., Radl, S., Urbanetz, N., Fraser, S.D., Tritthart, W., Reiter, F., Schlingmann, M., 2011. Continuous quantitative monitoring of powder mixing dynamics by near-infrared spectroscopys. *Powder Technol.* 205, 87–96.
- Leitgeb, R., Drexler, W., Unterhuber, A., Hermann, B., Bajraszewski, T., Le, T., Stingl, A., Fercher, A., 2004. Ultrahigh resolution Fourier domain optical coherence tomography. *Opt. Express* 12, 2156–2165.
- Mauritz, J.M.A., Morrisby, R.S., Hutton, R.S., Legge, C.H., Kaminski, C.F., 2010. Imaging Pharmaceutical Tablets with Optical Coherence Tomography. *J. Pharm. Sci.* 99, 385–391.
- May, R.K., Evans, M.J., Zhong, S., Warr, I., Gladden, L.F., Shen, Y., Zeitler, J.A., 2010. Terahertz in-line sensor for direct coating thickness measurement of

- individual tablets during film coating in real-time. *J. Pharm. Sci.* 100, 1535–1544.
- Müller, J., Brock, D., Knop, K., Axel Zeitler, J., Kleinebudde, P., 2012. Prediction of dissolution time and coating thickness of sustained release formulations using Raman spectroscopy and terahertz pulsed imaging. *Eur. J. Pharm. Biopharm.* 80, 690–697.
- Porter, S., Sackett, G., Liu, L., 2009. Chapter 33 - Development, Optimization, and Scale-up of Process Parameters: Pan Coating. In: Qiu, Y., Chen, Y., Zhang, G.G.Z., Liu, L., Porter, W.R. (Eds.), *Developing Solid Oral Dosage Forms*. Academic Press, San Diego, pp. 761–805.
- Römer, M., Heinämäki, J., Strachan, C., Sandler, N., Yliruusi, J., 2008. Prediction of tablet film-coating thickness using a rotating plate coating system and NIR spectroscopy. *AAPS PharmSciTech* 9, 1047–1053.
- Romero-Torres, S., Pérez-Ramos, J.D., Morris, K.R., Grant, E.R., 2006. Raman spectroscopy for tablet coating thickness quantification and coating characterization in the presence of strong fluorescent interference. *J. Pharm. Biomed. Anal.* 41, 811–819.
- Sakata, L.M., Deleon-Ortega, J., Sakata, V., Girkin, C.A., 2009. Optical coherence tomography of the retina and optic nerve - a review. *Clin. Exp. Ophthalmol.* 37, 90–99.
- Scheibelhofer, O., Balak, N., Koller, D.M., Khinast, J.G., 2013. Spatially Resolved Monitoring of Powder Mixing Processes via Multiple NIR-Probes. *Powder Technol.* 243, 161–170.
- Shen, Y.-C., Taday, P.F., 2008. Development and Application of Terahertz Pulsed Imaging for Nondestructive Inspection of Pharmaceutical Tablet. *IEEE J. Sel. Top. Quantum Electron.* 14, 407–415.
- Stifter, D., 2007. Beyond biomedicine: a review of alternative applications and developments for optical coherence tomography. *Appl. Phys. B* 88, 337–357.
- Suzzi, D., Radl, S., Khinast, J.G., 2010. Local analysis of the tablet coating process: Impact of operation conditions on film quality. *Chem. Eng. Sci.* 65, 5699–5715.
- Walther, J., Koch, E., 2009. Transverse motion as a source of noise and reduced correlation of the Doppler phase shift in spectral domain OCT. *Opt. Express* 17, 19698–19713.

Chapter 4: Optical Coherence Tomography as a Novel Tool for In-Line Monitoring of a Pharmaceutical Film-Coating Process

- Welzel, J., 2001. Optical coherence tomography in dermatology: a review. *Ski. Res. Technol.* 7, 1–9.
- Yun, S.H., Tearney, G., de Boer, J., Bouma, B., 2004. Motion artifacts in optical coherence tomography with frequency-domain ranging. *Opt. Express* 12, 2977–2998.
- Zeitler, J.A., Gladden, L.F., 2009. In-vitro tomography and non-destructive imaging at depth of pharmaceutical solid dosage forms. *Eur. J. Pharm. Biopharm.* 71, 2–22.
- Zhong, S., Shen, Y.-C., Ho, L., May, R.K., Zeitler, J.A., Evans, M., Taday, P.F., Pepper, M., Rades, T., Gordon, K.C., Müller, R., Kleinebudde, P., 2011. Non-destructive quantification of pharmaceutical tablet coatings using terahertz pulsed imaging and optical coherence tomography. *Opt. Lasers Eng.* 49, 361–365.

5

Calibration-free In-Line Monitoring of Pellet Coating Processes via Optical Coherence Tomography⁴

This study presents a new in-line measurement technique for determining the coating thickness and uniformity of pharmaceutical pellets during film coating in a fluid-bed apparatus. Non-destructive and contact-free process monitoring was performed via an optical coherence tomography (OCT) sensor providing cross-section images. Through the OCT measurements, the coating thickness could be determined directly, without a chemometric calibration model required for the quantification. The direct integration of the OCT sensor head into the fluid-bed systems allowed continuous monitoring of the coating growth. Moreover, the in-line investigation of the *intra*- and *inter*-pellet coating uniformity was possible due to OCT's high acquisition rate. Results of the in-line

⁴ This chapter is based on Markl, D., Zettl, M., Hanneschläger, G., Sacher, S., Leitner, M., Buchsbaum, A., Khinast, J.G., 2014. Calibration-free in-line monitoring of pellet coating processes via optical coherence tomography. Chem. Eng. Sci., in press with permission from Elsevier.

OCT measurements were validated using both off-line OCT images and particle size analysis by performing an image analysis of samples that were periodically removed from the process during the production. Three batches were produced under the same process conditions demonstrating the reproducibility of the results. Rather than providing the temporal and spatial average of a large number of pellets, the OCT sensor characterized local pellet properties of up to 130 individual pellets per minute. Therefore, the OCT technology allows the operator to directly monitor the coating thickness and uniformity in sub-micron resolution, which makes it a promising in-line PAT method.

5.1 Introduction

Film coating is used for various purposes, such as taste masking, increase of the visual attractiveness, brand recognition and protection of the active pharmaceutical ingredient (API) from the acidic environment of the stomach and/or the gastric mucosa from an aggressive API (Porter et al., 2009). Pharmaceutical coating is typically carried out in a pan coater or a fluid-bed apparatus, depending on the size of the product substrate and the batch. Since fluid-bed coating is typically used for smaller products (5 - 6 mm or less in diameter) (Porter et al., 2009), pellet coating is performed in a fluid-bed apparatus and most tablet coating is done in modern pan coaters.

Because the quality of the coated end-products is greatly affected by the film thickness, uniformity and morphology, these key parameters must be precisely controlled. Quality control of intermediate and final products during the production process, i.e., in real-time, receives more attention on the part of the pharmaceutical industry as it may pave the way for real-time release. In-line monitoring is important not only for guaranteeing the high product quality but also for improving the process understanding. Developing a better understanding of pharmaceutical processes is one of the key goals of the process analytical technology (PAT) initiative of the U.S. Food and Drug Administration (FDA) (FDA, 2004) and the Quality-by-Design framework.

Knop and Kleinebudde, 2013 recently reviewed various analytical tools for examining the coating characteristics. Monitoring of tablet coating processes has been investigated considerably more extensively than coating of pellets or granules. Most in-line measurements in a fluid-bed coater were performed via Raman

(Bogomolov et al., 2010) or near-infrared (NIR) spectroscopy (Andersson et al., 2000a; Bogomolov et al., 2010; Lee et al., 2011) to predict weight gain, mean coating thickness or release rate. These quality parameters can only be indirectly determined via such spectroscopic methods, i.e., by correlating reference measurements from samples with the attenuation of the spectral features of one of the mutually exclusive constituents found either in the product substrate or in the coating formulation. However, the development of such multivariate calibration models that relate the spectral information to a key parameter is tedious and even slight variations in the process conditions or raw material properties may render the model invalid.

An increase in the thickness of pellets can also be estimated via particle size determination (e.g., laser diffraction measurements or image analysis (Heinicke and Schwartz, 2005; Larsen et al., 2003; Mozina et al., 2010)), which however requires a narrow size distribution and a large number of pellets to determine the coating thickness accurately. Since these coating characterization methods represent the temporal and spatial average over a large number of pellets, the above techniques cannot provide any information about single pellets and local coating properties, which is necessary to better predict and understand the coating functionality. Only a few papers in the literature have described a non-destructive analysis of local coating properties, mostly based on off-line image analysis (e.g., terahertz pulsed imaging (TPI) (Ho et al., 2009a, 2009b, 2007; Zeitler et al., 2007) or confocal scanning laser microscopy (CSLM) (Laksmana et al., 2009; Lee et al., 2011).

As such, a calibration-free, non-destructive, direct and in-line measurement of the coating thickness and its distribution in the product substrate is highly desirable. Optical coherence tomography (OCT) offers an approach to quantify both overall and local coating properties (i.e., *inter*- and *intra*-pellet coating uniformity). It is a high-resolution imaging technique, which provides depth profiles of semi-transparent and turbid materials in a contactless and non-destructive manner (Fercher, 2010; Wojtkowski, 2010). This method utilizes the coherence properties of light to produce cross-section images. Generation of these images is based on the measure of the magnitude and the time delay of light reflected back from a particular investigated sample via an interferometric approach. Within the sample the light is back reflected at scattering particles and interfaces between materials with different refractive indices. Through the interferometric detection, OCT allows for a measurement of optical path lengths, which are related to the geometric

structure of the sample. OCT offers non-invasive optical imaging of multi-layered structures located in a sample at depths of up to 1 mm with excellent spatial resolution ($< 10 \mu\text{m}$). This outstanding optical sectioning performance was one of the key factors for the successful deployment of OCT in the biomedical field, which is currently the driving force behind the OCT research and the main field of application.

However, OCT is receiving more and more attention in other domains (Stifter, 2007). It was utilized as an off-line quality control tool for paper (Fabritius et al., 2006; Prykäri et al., 2010), silicon integrated-circuits (Serrels et al., 2010), fiber composites (Stifter et al., 2008), pharmaceutical tablets (D M Koller et al., 2011; Mauritz et al., 2010; Zeitler and Gladden, 2009; Zhong et al., 2011) and pharmaceutical pellets (Li et al., 2014). Moreover, it was shown that OCT has the potential for in-line monitoring of printed electronics (Alarousu et al., 2013) and multi-layered foils (Hanneschläger et al., 2011). Nevertheless, to the best of the authors' knowledge, no OCT sensor has to date been applied as an in-line quality control tool in a pharmaceutical process. However, the feasibility of OCT for monitoring moving samples was already shown (Markl et al., 2014b).

In this study, a fluid-bed apparatus was used to coat pharmaceutical pellets. The coating process was continuously monitored via OCT. The gathered data were post-processed to provide not only the mean coating thickness but also information about the *inter*- and *intra*-pellet coating uniformity. Three replication experiments were carried out to confirm the reproducibility of the results. The coating thickness determined in-line via OCT was validated using samples removed from the process at six successive intervals and a theoretical growth model based on the process parameters and raw material specifications.

5.2 Materials and Methods

5.2.1 Pellet Preparation

The pellets were manufactured in-house via hot melt extrusion using a co-rotating twin screw extruder (Coperion, Germany) and our newly developed hot die-face cutter (Automatik Plastics Machinery GmbH, Germany). They are composed of 75% (w/w) calcium stearate (CaSt, stearic acid 44% and palmitic acid 54%, EP,

Werba-Chem GmbH, Austria, density = 1.08 g/cm³) as a matrix carrier, 20% (w/w) Paracetamol (density = 1.26 g/cm³) as an API and 5% (w/w) glycerol monostearate (GMS, Apoka, Austria, density = 0.97 g/cm³) as a plasticizer (Roblegg et al., 2011).

5.2.2 Pellet Coating

Pellet coating was performed with a lab-scale air flow technology coater (Innojet VENTILUS® V-2.5). The product was transported on a cushion of air flowing in an orbital spiral and circular fashion to the cylindrical container wall. Coating occurred in the center of the product container, where the spray nozzle was located. The sprayed coating material was molten Dynasan 118 (glyceryl tristearate, Cremer Oleo, Germany). The temperature of the coating material at the spraying nozzle is approximately 90 °C.

Each batch had 450 g of pellets and 218 g of coating mass. The process conditions, i.e., the spray rate, atomizing pressure, air flow rate and inlet air temperature, were kept constant at 7 g/min, 1.5 bar, 60 m³/h and 35°, respectively. Due to the combination of the used coating material and the spraying equipment, the spray rate slightly varied with process time. The actual spray rate was determined by monitoring the weight loss of the coating material in the heated vessel using a weighing scale. The mean spray rate was thus for all three batches 6.8 g/min. Each coating process was run for 32 minutes in total, with sampling of 10 g every 6 minutes. To assess reproducibility, every coating experiment was repeated three times (referred to as B01, B02 and B03) under exactly the same process conditions.

5.2.3 Methods

5.2.3.1 Optical Coherence Tomography

The OCT system in Markl et al., 2014a equipped with the two-dimensional (2-D) sensor head is the same system as used in this study. The experiments were performed with a spectral-domain (SD-) OCT system. Generally, OCT is based on low-coherence interferometry (LCI), which uses light sources with high spatial and low temporal coherence. Therefore, OCT is an interferometric approach where the short coherence length acts as a temporal filter for photons back-reflected and back-scattered from different sample structures where a change in the refractive index occurs. In this study such changes in refractive indices appear at the

Chapter 5: Calibration-free In-Line Monitoring of Pellet Coating Processes via Optical Coherence Tomography

air/coating and coating/pellet core interfaces. A depth profile is carried out by comparing the arrival times of single scattered photons with a reference light beam. The generation of cross-section images requires a relative movement between the optical beam and the sample. This OCT system uses a galvanometer mirror in the sensor head to transversely move the optical beam along the sample. The galvanometer mirror is triggered by a saw-tooth wavefront in synchrony with the camera read out. The constant voltage range (0.4 V) of the mirror thus causes a displacement between successive depth profiles of 2.94 μm . Each cross-section image in this study was synthesized by 1000 depth profiles (corresponding to the number of transverse pixels of the OCT images). The exposure time of 34 μs and the idle time of 1.9 μs of the camera were fixed throughout all experiments. This gives a duty cycle of 95% and a readout rate of the camera of 27.8 kHz.

The OCT system is equipped with a SLD Broadlighter (Superlum Diodes Ltd.) as a light source, operating at a central wavelength λ_c of 830 nm and a full-width half maximum (FWHM) spectral bandwidth $\Delta\lambda$ of 62 nm. The power of the incident light measures < 1 mW and hence, heat transfer to the tablet is negligible. The axial resolution of the OCT system is 4.9 μm , which is defined as half of the coherence length l_c of the light source:

$$\delta z = \frac{l_c}{2} = 0.44 \frac{\lambda_c^2}{\Delta\lambda}. \quad (5.1)$$

The lateral resolution depends on the optics and the central wavelength of the OCT system and is thus decoupled from the axial resolution. It is limited by the beam waist radius w_0 at the focus, which is defined as

$$\delta x = 2w_0 = 4 \frac{\lambda_c f}{\pi d}, \quad (5.2)$$

with f being the focal length and d as the beam diameter at the lens of the system. The lateral resolution is thus theoretically given as 9.51 μm ($f = 36$ mm, $d = 4$ mm). This theoretical value agrees well with the actual lateral resolution as discussed in Markl et al., 2014a.

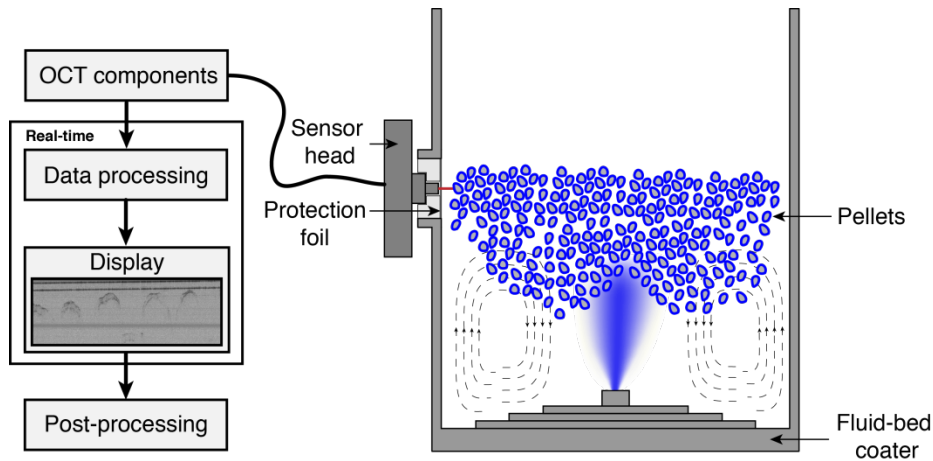


Figure 5.1: Schematic of the fluid-bed coater, the OCT system and data processing. The block of the OCT components basically represents the light source and the spectrometer.

5.2.3.2 Experimental Setup

Figure 5.1 schematically illustrates the experimental setup, including the fluid-bed coater, the OCT system and the data processing unit. Since the OCT system was modularly designed, it was possible to separate the core system (light source, spectrometer) from the sensor head. The OCT sensor head was mounted on a customizable stage and was connected to the core system with an optical fiber. The stage was adjusted to align the sensor head with the inspection window and to position the focus of the light from the OCT system inside the product container. The sensor head was protected from the pellets and coating by a thin plastic foil (i.e., protection foil in **Figure 5.1**).

In-line measurements were carried out every 2nd minute for 60 seconds due to software limitations with regard to the acquisition time (maximum 60 seconds). The acquired measurements were processed to generate depth-resolved images and were displayed in real-time. A break of one minute between the measurements was required to store the generated data accordingly. These stored images were further post-processed (see below for details). Validation of the in-line measurements was performed by analyzing the samples off-line using the same OCT system and a dynamic image analysis system.

5.2.3.3 Pellet Size Measurements and Theoretical Growth Model

In addition to the off-line OCT analysis of the samples, the pellet size was measured

Chapter 5: Calibration-free In-Line Monitoring of Pellet Coating Processes via Optical Coherence Tomography

using a Qicpic particle analyzer (Sympatec GmbH, Germany) based on dynamic image analysis. The image analysis was additionally used to determine the shape of the pellets. The shape of the uncoated pellets was expressed by the mean aspect ratio (ratio of the minimal and maximal Feret diameter) of 0.84 and the mean sphericity (ratio of the perimeter of the equivalent circle to the real perimeter) of 0.92. Both parameters show that the pellets can be well approximated by spheres. Therefore, in the theoretical growth model the pellets are represented as spheres with one parameter, i.e., the mean volume diameter. The coating thickness was thus half of the difference between the mean diameters of the coated pellets and product substrate.

Furthermore, the coating thickness was predicted based on the properties of the raw materials and the process parameters. Assuming the spherical shape of the pellets, the mass of the pellet core (without coating) is

$$m_{\text{core}} = \frac{4\pi r^3}{3} \rho_{\text{core}}, \quad (5.3)$$

where ρ_{core} is the density and r is the radius of the pellet core. The density of the product substrate is 1.1105 g/cm³, assuming an ideal mixture (no pores were formed during the pellet production). Depending on the process time, the coating mass can be denoted as

$$m_{\text{coating}}(t) = 4\pi d_c(t)(r^2 + d_c(t)r + \frac{1}{3}d_c(t)^2)\rho_{\text{coating}}, \quad (5.4)$$

where ρ_{coating} is the density of the coating and d_c is the coating thickness. The density dependence on the temperature, specifically the different densities in liquid and solid state, was neglected since the evaluation of the coating is assumed to occur after solidification at 30 °C. The density of the coating in the solid state is 1.056 ± 0.001 g/cm³ at 30 ± 5 °C (product temperature range at the measurement spot) (Board, 2002). Moreover, the OCT measurements were acquired at a measurement spot where it is assured that the coating is in solid form and the temperature dependence of the density has no impact on the coating thickness measured by OCT.

Since the coating mass per pellet is unknown, the coating thickness could be calculated using the weight gain by relating the coating and pellet core masses. This ratio can be expressed by

$$\frac{m_{\text{coating}}(t)}{m_{\text{core}}} = \frac{3d_c(t)}{r^3} \left(r^2 + d_c(t)r + \frac{1}{3}d_c(t)^2 \right) \frac{\rho_{\text{coating}}}{\rho_{\text{core}}}. \quad (5.5)$$

This ratio equals the total coating mass applied to the pellets over the total mass of the product substrate m_{pellets} . Since a minor loss of coating material may occur during processing, e.g., due to spray drying, the total coating mass $m_{\text{feed, coating}}$ fed from the spray gun is greater than the coating mass applied to the pellets (Andersson et al., 2000a). This loss is accounted for by fraction q that is assumed to be constant within a batch. It was also assumed that the total coating material was equally distributed on the pellets. Therefore, the ratio from Eq. (5.5) is equal to:

$$q \frac{m_{\text{feed, coating}}(t)}{m_{\text{pellets}}} = q \frac{c_r t}{m_{\text{pellets}}}, \quad (5.6)$$

where c_r is the constant spray rate. In turn, Eqs. (5.5) and (5.6) give the coating thickness

$$d_c(t) = r \left(\left(q \frac{c_r t}{m_{\text{pellets}}} \frac{\rho_{\text{core}}}{\rho_{\text{coating}}} + 1 \right)^{\frac{1}{3}} - 1 \right). \quad (5.7)$$

The pellet radius r was determined from the volume mean diameter measured with the above-mentioned Qicpic particle analyzer. Non-linear curve fitting via least-squares method was used to determine the fraction q . This was carried out on the basis of the volume mean diameters of the samples. Thus, Eq. (5.7) allows the prediction of the coating thickness as a function of process time.

5.2.4 Post-Processing and Data Analysis

OCT provides cross-section images of pellets as schematically illustrated in **Figure 5.2(a)**, which can be used to determine the thickness of the coating layer. The coating thickness was measured off-line and manually from the OCT images at three sites on each pellet (see **Figure 5.2(b)**) using a special MATLAB tool. The first measurement position was at the center of the pellet. The other two thickness measurements were displaced from the center. Both displaced measurements are affected by the pellets velocity and by its curvature.

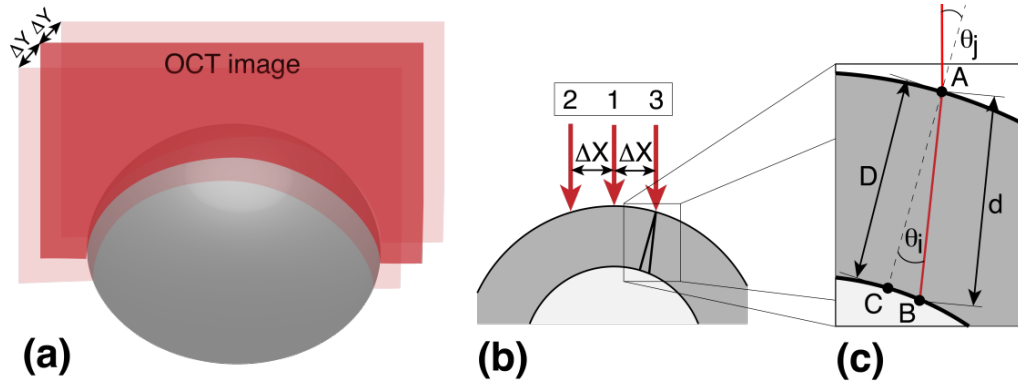


Figure 5.2: (a) Surface model of a pellet. The imaging plane might be displaced from the center of the pellet, which introduces a thickness measurement error. (b) Cross-section model of one pellet. Three coating thickness measurements were performed (indicated by the red arrows); one at the center and two equally displaced from the center considering the constraint: $20 \text{ pixels} < \Delta X < 30 \text{ pixels}$. (c) Detailed view of the cross-section model. The path of the optical beam is highlighted in red and represents one OCT depth profile. d is the OCT measured coating thickness and D is the true coating thickness when measuring perpendicular to the surface.

The velocity of the pellet affects the displacement between successive depth measurements, which causes a horizontal stretching of the pellets in the OCT image. Since the pellets' velocity is unknown, the thickness measurements were performed independent of the displacement between successive depth measurements. Therefore, the coating thickness was determined in axial (vertical) direction in the OCT image instead of perpendicular to the surface. Such a thickness measurement introduces a measurement error that depends on the pellet curvature. However, measuring the thickness perpendicular to the surface might result in a much larger measurement error compared to the measurement error in axial direction.

In order to analyze the measurement error, one has to consider the actual path of the optical beam in the coating material, as illustrated in **Figure 5.2(c)**. The optical beam is refracted by the air/coating interface depending on the incident angle θ_j and the refractive indices of air n_a and coating n_c . The relation between the incident angle and the angle of refraction θ_i can be described by Snell's law $n_a \sin \theta_j = n_c \sin \theta_i$. With increasing incident angle of the OCT beam less light is back-reflected from the interfaces, specifically from the coating/pellet core interface. A maximum incident angle of 30° , where both interfaces could be clearly identified, was experimentally determined.

On the one hand this maximum incident angle bounds the displacement of the thickness measurements from the center in the imaging plane (ΔX in **Figure 5.2(b)**). For all measurements, ΔX was between 20 and 30 pixels (the actual displacement in μm depends on the pellet speed). On the other hand the maximum incident angle gives a limit on the displacement of the imaging plane (ΔY in **Figure 5.2(a)**). It is not guaranteed that the imaging plane lies in the center of the pellet. If the imaging plane is displaced from the center, the incident angle of the OCT beam is larger compared to the corresponding center position. For a maximum incident angle of 30° , the displacement ΔY is $70 \mu\text{m}$.

The maximum thickness measurement error considering the above discussed maximal displacements (ΔX and ΔY) is theoretically $3.8 \mu\text{m}$ for a $100 \mu\text{m}$ thick coating layer. This error is the difference between the real thickness and the thickness measurements which are carried out in vertical direction. However, in case of the off-line investigations (i.e., no relative speed difference between OCT sensor head and pellet) the thickness measurements were performed perpendicular to the surface.

The mean coating thickness μ_i and standard deviation σ_i were determined for pellet i on the basis of the above discussed thickness measurements, as schematically illustrated in **Figure 5.3**. Since the number of measured pellets per second highly varied, several measurements were aggregated for further analysis. The size N of such an aggregation block, i.e., the number of combined measurements, was calculated on the basis of a specified constant time interval. This time interval was determined as a trade-off between capturing high-frequency variations of the coating thickness and the statistical power of such a block. At least ten pellets per block were measured and used for the calculation of the empirical mean and standard deviations. This lower limit was chosen on the basis of the content uniformity specifications of the U.S. pharmacopeia, which requires the assessment of at least ten samples. The different number of measured pellets within the time interval results in a varying block size. Each block was represented by three parameters:

- (1) the mean coating thickness μ_B ,

$$\mu_B = \frac{1}{N} \sum_{i=1}^N \mu_i, \quad (5.8)$$

- (2) the mean of the standard deviation σ_i of the coating thickness of each pellet

$$\mu_{B,\sigma} = \frac{1}{N} \sum_{i=1}^N \sigma_i, \quad (5.9)$$

and (3) the standard deviation of the mean coating thickness of each pellet

$$\sigma_B = \sqrt{\frac{1}{N-1} \sum_{i=1}^N (\mu_i - \mu_B)^2}. \quad (5.10)$$

The parameters $\mu_{B,\sigma}$ and σ_B were further used for the analysis of the *intra-* and *inter-*pellet coating uniformity, respectively. Specifically, process analysis was carried out by investigating those parameters in relation to the process time.

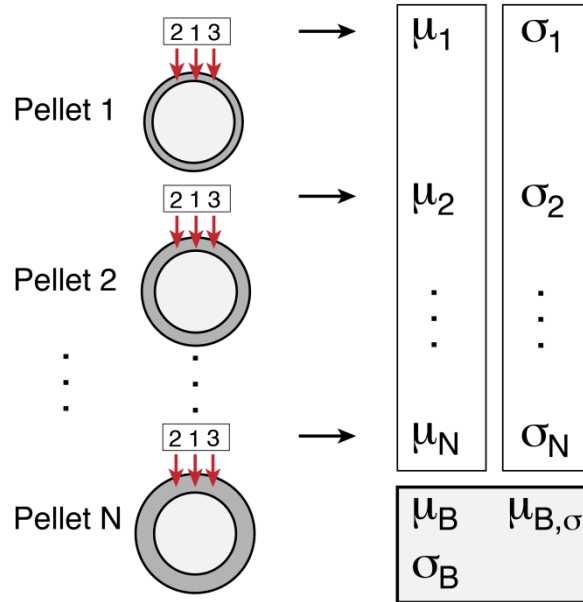


Figure 5.3: Schematic of the post-processing of coating thickness measurements. The following parameters were determined: μ_i - mean coating thickness of pellet i , σ_i - standard deviation of pellet i , μ_B - mean coating thickness of N pellets (defined as a block), σ_B - standard deviation of a block (inter-pellet coating uniformity), $\mu_{B,\sigma}$ - mean of standard deviation of each pellet in a block (intra-pellet coating uniformity).

5.3 Results and Discussion

5.3.1 Coating Thickness

Figure 5.4 shows a selection of images from in-line OCT measurements. The top two horizontal lines denote the protection foil, which shelters the pellets from damaging the OCT sensor head and prevents them from leaving the coating apparatus. Vibrations originated by the coating process are partly responsible for the bad image quality. The imaging depth is limited by the attenuation properties of the optical beam in the coating and the pellet core and therefore, most of the images show only half of the pellet.

The pellet width on the image depends on the pellet's real size and speed, especially the speed parallel to the protection foil (transverse speed) that causes a distortion of the pellet (see Markl et al., 2014b for details). Since the pellet speed varies and is unknown, the distortion of the pellet cannot be corrected. In order to estimate a speed range of the pellets when passing the OCT measurement spot, an additional replication experiment (same process conditions and same raw materials as used for the in-line OCT measurements) was carried out. In this experiment the OCT sensor was replaced by a high-speed camera and the pellet speed was extracted by a frame-by-frame analysis. These measurements provide a pellet speed in the range of 0 to 0.2 m/s.

At a pellet speed of 0.2 m/s, a thickness error of 34.7 μm for a 100 μm thick coating layer would be introduced when measuring the thickness perpendicular to the surface at the outer two measurement positions. This emphasizes the choice of measuring the coating thickness in axial direction and accepting a maximum thickness error of 3.8 μm (for a 100 μm thick coating layer) which is independent of the pellet speed.

While a transverse speed does not affect the depth measurement, i.e., the determination of the coating thickness, an axial speed (orthogonal to the protection foil) results in a degradation of the signal-to-noise ratio (SNR) (Yun et al., 2004). Hence, images suffering from axial pellet movements were neglected during the post-processing phase. Furthermore, only pellets where the thickness could be determined at the measurement positions (one at the center and two equally displaced by 20 - 30 pixels from the center) were accepted for the further analysis. However, the pellet speed does not influence the measurements in axial direction

Chapter 5: Calibration-free In-Line Monitoring of Pellet Coating Processes via Optical Coherence Tomography

as it was discussed in Markl et al., 2014b for tablets.

The validation was performed by analyzing samples taken at 4, 10, 16, 22, 28 and 32 minutes. **Figure 5.5** shows selected OCT images of the samples. OCT images of ten different pellets were acquired and used for the further analysis. In the absence of motion effects and vibrations, the contrast and image quality was higher compared to the in-line measurements.

The coating thickness was measured manually based on the images. However, to obtain the absolute geometric value, the refractive index of the coating material was required since only optical path lengths between interfaces (air/coating and coating/pellet core) could be measured based on the images. The refractive index of the coating material, i.e., Dynasan 118, is 1.4385 (O'Neil, 2001).

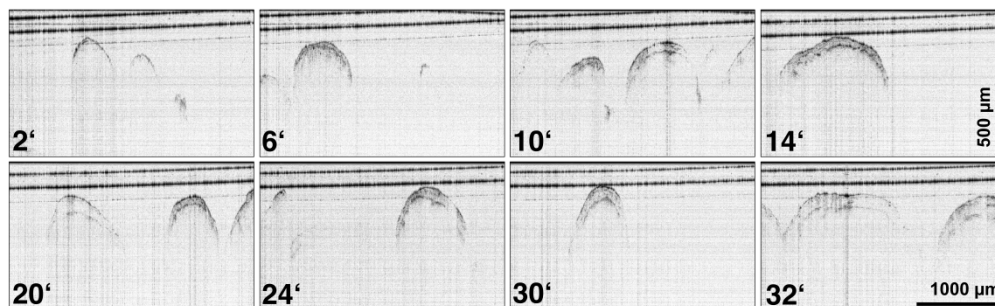


Figure 5.4: OCT images of film-coated pellets at different process times (in minutes). Image dimension (in air): $2.94 \times 1.46 \text{ mm}^2$ (1000 x 600 pixels). The top two horizontal lines indicate the protection foil. The pellet width (parallel to the protection foil) depends not only on the pellet size but also on its speed.

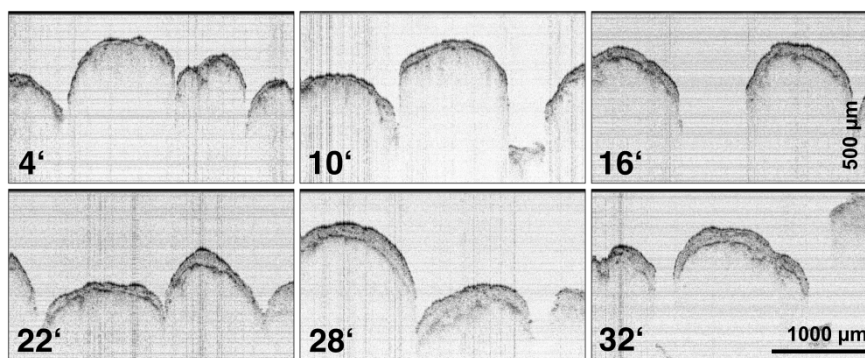


Figure 5.5: Off-line OCT images of film-coated pellets sampled at different process times (in minutes). Image dimension (in air) are $2.94 \times 1.46 \text{ mm}^2$ (1000 x 600 pixels).

Figure 5.6 shows the mean coating thickness of batch B02 as a function of process time. The time interval was chosen so that at least ten pellets (block size N in **Figure 5.3**) could be used for the evaluation of each data point. Since the pellet hits per image varied greatly, the block sizes ranged from 10 to 55. In addition, **Figure 5.6** shows the results for the sampled pellets that were investigated off-line via OCT and the particle size analyzer. We used the theoretical growth model with a volume mean diameter of $1422\ \mu\text{m}$ of the substrate product. Since removing the samples (10 g each) reduced the total amount of pellets in the product container, the same coating amount was applied onto fewer pellets. This was also considered in the non-linear least-squares fitting algorithm, which gave a parameter q of 0.90. Consequently, 10% (21.8 g) of the total coating mass $m_{\text{feed,coating}}$ (218 g) fed through the spray gun was considered a loss of material due to fouling of the product container, filter bags and injection tube. As such, 90 % (196 g) of $m_{\text{feed,coating}}$ were applied onto the pellets. Since the spraying stopped at minute 32, the coating thickness predicted by the theoretical growth model was constant for the remaining time.

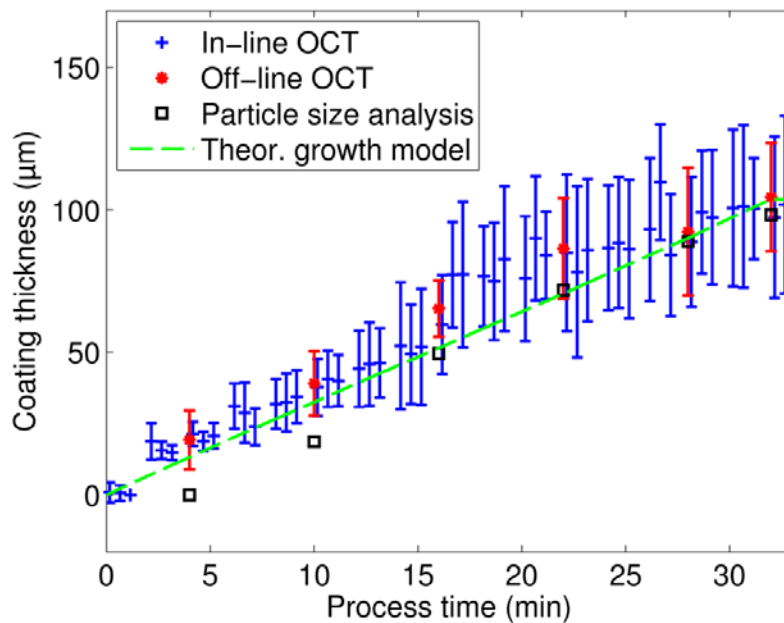


Figure 5.6: The mean coating thickness of B02 depending on the process time for a time interval T of 20 seconds. The error bars indicate the inter-tablet coating uniformity (Eq. (5.10)), which were calculated from a variable number of measured pellets. The theoretical growth model is depicted in Eq. (5.7).

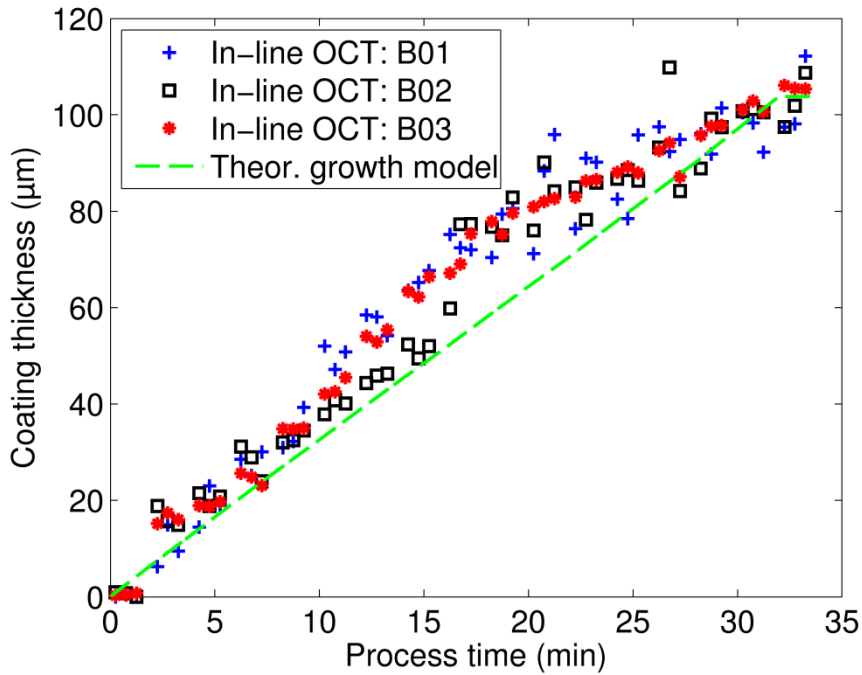


Figure 5.7: Coating thickness of all three replication experiments as a function of process time and for a time interval T of 20 seconds.

The mean coating thickness (of all three batches as illustrated in **Figure 5.7**) at end of the process was $104.0 \mu\text{m}$, which differed only slightly from the theoretical coating thickness ($103.8 \mu\text{m}$). However, all three batches showed a similar trend that deviated slightly from the result of the theoretical growth model. The reason for the local convex curvature at half the process time will be subject to further investigations.

5.3.2 Coating Uniformity

The *inter*- and *intra*-pellet coating uniformity was determined along the entire process time on the basis of the in-line OCT data, as shown in **Figure 5.8**. The decrease in both uniformity parameters was apparent. Furthermore, the in- and off-line results agree very well, indicating that measuring the thickness measurements using the in-line data is as accurate as off-line analysis. The reason for the high RSD at the start of the process may be that at this point of time only a few pellets were coated and most of the measured pellets did not pass the spraying window. In addition, during the first 4 minutes the coating thickness ($< 10 \mu\text{m}$) was below the minimum axial resolution of the OCT system, possibly making the

coating analysis inaccurate.

In all three replication experiments the *intra*-pellet coating uniformity was lower than that between the pellets during the entire process time. At the end of the process the average coating thickness variation (of all three batches) between the pellets was 127 % larger than the average variations of each pellet. Consequently, a small variation in the average coating thickness between pellets (i.e., large *inter*-pellet coating variability) cannot be inferred from a narrow coating thickness distribution of each pellet (i.e., small *intra*-pellet coating variability). However, the *intra*-pellet coating uniformity is more critical since it is responsible for the coating functionality. One has to mention that the *intra*-pellet coating uniformity is calculated from three measurements which are very close to each other and thus, the *intra*-coating variability of the entire surface might vary from the estimated one.

The mean coating thickness and the uniformities at the end of the process are shown in **Table 5.1** for all three batches. Slight deviations between the batches can be observed for all three parameters, with larger coating thickness variations between pellets compared to the *intra*-pellet coating uniformity in all three batches.

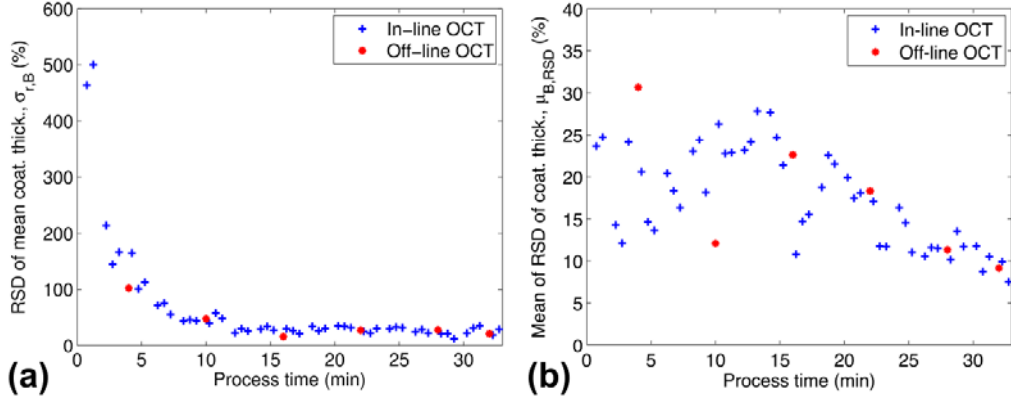


Figure 5.8: Coating uniformity as a function of process time for B01. (a) Inter-pellet coating uniformity represented by the RSD of the mean coating thickness (using Eq. (5.10) divided by the mean coating thickness μ_B). (b) Intra-pellet coating uniformity as the mean of the RSD of the coating thicknesses per block (using Eq. (5.9), where standard deviation σ_i is divided by the mean coating thickness of pellet i).

Table 5.1: Summary of the results for all three batches.

	Total number measured pellets (-)	Process end		
		Mean coating thickness	Inter-pellet coating uniformity	Intra-pellet coating uniformity
		(μm)	(μm)	(μm)
B01	1642	100.50	23.55	9.89
B02	1310	103.67	28.39	9.37
B03	1395	105.76	14.64	10.04

As can be seen from **Table 5.1** significantly more pellets can be sampled using the in-line technique compared to an off-line analysis. Thus, the full distribution of the coating thickness could be sampled. On the basis of the frame rate of this OCT system (3.3 fps) and process conditions, 0.43 pellets were detected per image on average, i.e., 0.75 pellets per second.

The system configuration can significantly be enhanced in terms of increasing the number of pellets measured per second. Improvements may include increasing the acquisition rate of the OCT system (MHz acquisition rates are described in Wojtkowski, 2010) or adjusting the sensor head position. Moreover, the current acquisition procedure of the OCT data limits the number of successive OCT images. This software-related issue is basically caused by the time-consuming computation of the OCT images and the limited bulk of data storage capacity. By moving the algorithms from a field-programmable gate array (FPGA) chip and/or a central processing unit (CPU) to a graphical processing unit (GPU), a speed increase of more than 100 could be achieved, allowing continuous data acquisition and processing. However, an automatic evaluation of the in-line measurements is essential to increase the thickness measurements per pellet, which is currently only limited by the labor-intensive manual evaluation procedure of the OCT data. Specifically, increasing the measurements per pellet would provide more reliable *inter-* and *intra-*pellet coating uniformities.

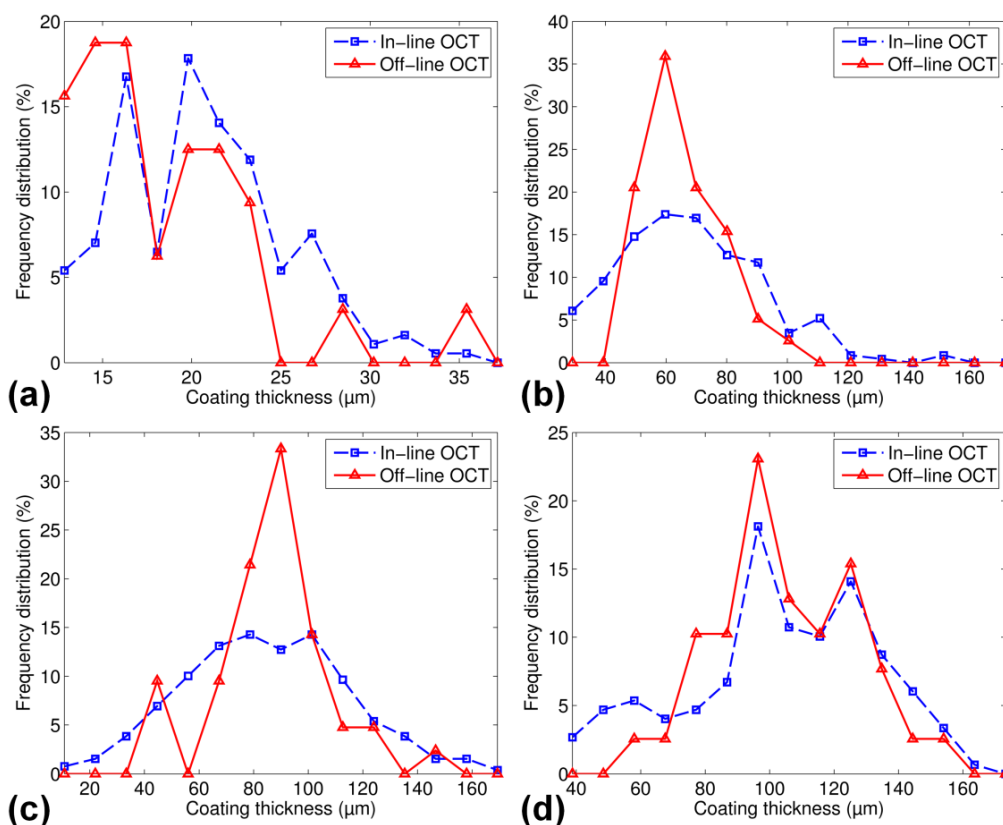


Figure 5.9: Examples of coating thickness distribution (frequency) from B02. (a) Minute 4: 186 (in-line OCT) and 39 (off-line OCT) thickness measurements (b) Minute 16: 231 (in-line OCT) and 39 (off-line OCT) thickness measurements (c) Minute 22: 258 (in-line OCT) and 42 (off-line OCT) thickness measurements (d) Minute 32: 150 (in-line OCT) and 39 (off-line OCT) thickness measurements.

5.3.3 Coating Distribution

Since the coating thickness was measured for many pellets for one minute, a coating thickness distribution can be generated as illustrated in **Figure 5.9**. The distributions of the in- and off-line data show similar characteristics. There are several coinciding peaks indicating a process- or product-related feature. The distances between the peaks in the in-line measurements were 33.9 μm and 28.8 μm in **Figure 5.9(c)** and **(d)**, respectively. Similar peaks are visible in the histograms of the other batches, showing that two different thicknesses were very frequently measured. Such thickness differences are not seen in the frequency distribution of the particle size as illustrated in **Figure 5.10**. However, the particle size distribution of the fully coated pellets is broader than that of the uncoated

pellets, which is also an indicator for a high *inter*-pellet coating uniformity.

5.4 Conclusion

This study shows for the first time how optical coherence tomography can be used to quantitatively measure the coating thickness of randomly moving pellets in a fluid-bed coater using an in-line sensor. Direct thickness measurements of film coatings were taken with high resolution and without prior calibration. The experimental observation of the broad thickness distributions shown in **Figure 5.9** confirms that a better process understanding is required to improve the *inter*- and *intra*-pellet coating uniformity, i.e., to achieve a uniform coating distribution throughout the batch. Such coating thickness variability is expected to have a significant impact on the product's performance and is particularly critical when using modified-release coatings. However, the current manual determination of the coating thickness is not suitable for real-time application of the in-line OCT sensor. The implementation of an automatic evaluation procedure is a significant challenge, but is essential to make the approach suitable for in-process application. Therefore, future research is required to exploit the full potential of the OCT technology.

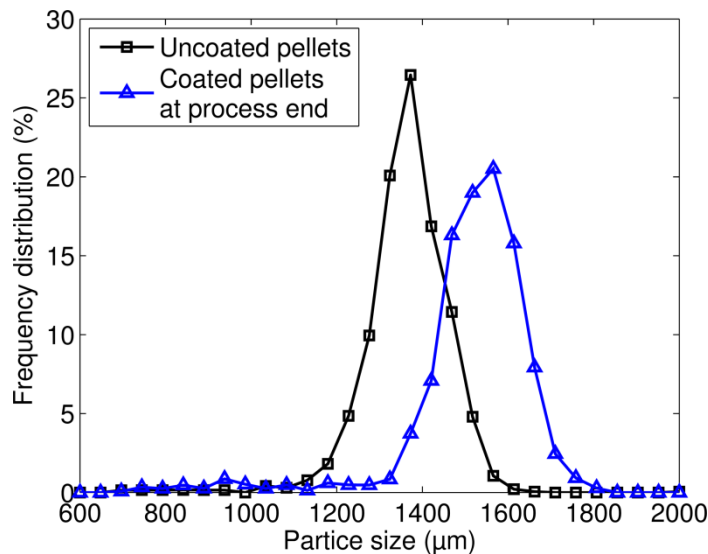


Figure 5.10: Number weighted frequency distribution of the particle size of uncoated and fully coated pellets determined by the Qicpic particle size analyzer.

5.5 References

- Alarousu, E., Alsaggaf, A., Jabbour, G.E., 2013. Online monitoring of printed electronics by Spectral-Domain Optical Coherence Tomography. *Sci. Rep.* 3, 1562.
- Andersson, M., Folestad, S., Gottfries, J., Johansson, M.O., Josefson, M., Wahlund, K.G., 2000. Quantitative analysis of film coating in a fluidized bed process by in-line NIR spectrometry and multivariate batch calibration. *Anal. Chem.* 72, 2099–108.
- Board, N., 2002. *Modern Technology Of Oils, Fats & Its Derivatives*. National Institute Of Industrial Re.
- Bogomolov, A., Engler, M., Melichar, M., Wigmore, A., 2010. In-line analysis of a fluid bed pellet coating process using a combination of near infrared and Raman spectroscopy. *Int. J. Pharm.* 24, 544–557.
- Fabritius, T., Alarousu, E., Prykäri, T., Hast, J., Myllylä, R., 2006. Characterisation of optically cleared paper by optical coherence tomography. *Quantum Electron.* 36, 181–187.
- FDA, 2004. *Guidance for Industry. PAT - a framework for innovative pharmaceutical development, manufacturing, and quality assurance, Quality Assurance*. US Department of Health, Rockville, MD.
- Fercher, A.F., 2010. Optical coherence tomography - development, principles, applications. *Z. Med. Phys.* 20, 251–276.
- Hanneschläger, G., Nemeth, A., Hofer, C., Goetzloff, C., Reussner, J., Wiesauer, K., Leitner, M., 2011. Optical coherence tomography as a tool for non destructive quality control of multi-layered foils. In: *6th NDT in Progress 2011. International Workshop of NDT Experts, Prague*, p. Paper 7.
- Heinicke, G., Schwartz, J.B., 2005. Particle Size Distributions of Inert Spheres and Pelletized Pharmaceutical Products by Image Analysis. *Pharm. Dev. Technol.* 9, 359–367.
- Ho, L., Müller, R., Gordon, K.C., Kleinebudde, P., Pepper, M., Rades, T., Shen, Y., Taday, P.F., Zeitler, J.A., 2009a. Monitoring the Film Coating Unit Operation and Predicting Drug Dissolution Using Terahertz Pulsed Imaging. *J. Pharm. Sci.* 98, 4866–4876.

Chapter 5: Calibration-free In-Line Monitoring of Pellet Coating Processes via Optical Coherence Tomography

- Ho, L., Müller, R., Gordon, K.C., Kleinebudde, P., Pepper, M., Rades, T., Shen, Y., Taday, P.F., Zeitler, J.A., 2009b. Terahertz pulsed imaging as an analytical tool for sustained-release tablet film coating. *Eur. J. Pharm. Biopharm.* 71, 117–23.
- Ho, L., Müller, R., Römer, M., Gordon, K.C., Heinämäki, J., Kleinebudde, P., Pepper, M., Rades, T., Shen, Y.C., Strachan, C.J., Taday, P.F., Zeitler, J. a, 2007. Analysis of sustained-release tablet film coats using terahertz pulsed imaging. *J. Control. Release* 119, 253–61.
- Knop, K., Kleinebudde, P., 2013. PAT-tools for process control in pharmaceutical film coating applications. *Int. J. Pharm.* 457, 527–536.
- Koller, D.M., Hanneschläger, G., Leitner, M., Khinast, J.G., 2011. Non-destructive analysis of tablet coatings with optical coherence tomography. *Eur. J. Pharm. Sci.* 44, 142–148.
- Laksmmana, F.L., Van Vliet, L.J., Hartman Kok, P.J. a, Vromans, H., Frijlink, H.W., Van der Voort Maarschalk, K., 2009. Quantitative image analysis for evaluating the coating thickness and pore distribution in coated small particles. *Pharm. Res.* 26, 965–76.
- Larsen, C.C., Sonnergaard, J.M., Bertelsen, P., Holm, P., 2003. Validation of an image analysis method for estimating coating thickness on pellets. *Eur. J. Pharm. Sci.* 18, 191–6.
- Lee, M.-J., Seo, D.-Y., Lee, H.-E., Wang, I.-C., Kim, W.-S., Jeong, M.-Y., Choi, G.J., 2011. In line NIR quantification of film thickness on pharmaceutical pellets during a fluid bed coating process. *Int. J. Pharm.* 403, 66–72.
- Li, C., Zeitler, J.A., Dong, Y., Shen, Y.-C., 2014. Non-destructive evaluation of polymer coating structures on pharmaceutical pellets using full-field optical coherence tomography. *J. Pharm. Sci.* 103, 161–6.
- Markl, D., Hanneschläger, G., Buchsbaum, A., Sacher, S., Khinast, J.G., Leitner, M., 2014a. In-line Quality Control of Moving Objects by Means of Spectral-Domain OCT. *Opt. Lasers Eng.* 59, 1–10.
- Markl, D., Hanneschläger, G., Sacher, S., Leitner, M., Khinast, J.G., 2014b. Optical coherence tomography as a novel tool for in-line monitoring of a pharmaceutical film-coating process. *Eur. J. Pharm. Sci.* 55, 58–67.

- Mauritz, J.M.A., Morrisby, R.S., Hutton, R.S., Legge, C.H., Kaminski, C.F., 2010. Imaging Pharmaceutical Tablets with Optical Coherence Tomography. *J. Pharm. Sci.* 99, 385–391.
- Mozina, M., Tomazevic, D., Leben, S., Pernus, F., Likar, B., 2010. Digital imaging as a process analytical technology tool for fluid-bed pellet coating process. *Eur. J. Pharm. Sci.* 41, 156–62.
- O’Neil, M.J. (Ed.), 2001. *The Merck Index: An Encyclopedia of Chemicals, Drugs, and Biologicals*, 13th ed. Merck, New Jersey.
- Porter, S., Sackett, G., Liu, L., 2009. Chapter 33 - Development, Optimization, and Scale-up of Process Parameters: Pan Coating. In: Qiu, Y., Chen, Y., Zhang, G.G.Z., Liu, L., Porter, W.R. (Eds.), *Developing Solid Oral Dosage Forms*. Academic Press, San Diego, pp. 761–805.
- Prykäri, T., Czajkowski, J., Alarousu, E., Myllylä, R., 2010. Optical coherence tomography as an accurate inspection and quality evaluation technique in paper industry. *Opt. Rev.* 17, 218–222.
- Roblegg, E., Jäger, E., Hodzic, A., Koscher, G., Mohr, S., Zimmer, A., Khinast, J., 2011. Development of sustained-release lipophilic calcium stearate pellets via hot melt extrusion. *Eur. J. Pharm. Biopharm.* 79, 635–645.
- Serrels, K.A., Renner, M.K., Reid, D.T., 2010. Optical coherence tomography for non-destructive investigation of silicon integrated-circuits. *Microelectron. Eng.* 87, 1785–1791.
- Stifter, D., 2007. Beyond biomedicine: a review of alternative applications and developments for optical coherence tomography. *Appl. Phys. B* 88, 337–357.
- Stifter, D., Wiesauer, K., Wurm, M., Schlotthauer, E., Kastner, J., Pircher, M., Götzinger, E., Hitztenberger, C.K., 2008. Investigation of polymer and polymer/fibre composite materials with optical coherence tomography. *Meas. Sci. Technol.* 19, 074011.
- Wojtkowski, M., 2010. High-speed optical coherence tomography: basics and applications. *Appl. Opt.* 49, 30–61.
- Yun, S.H., Tearney, G., de Boer, J., Bouma, B., 2004. Motion artifacts in optical coherence tomography with frequency-domain ranging. *Opt. Express* 12, 2977–2998.

Chapter 5: Calibration-free In-Line Monitoring of Pellet Coating Processes via Optical Coherence Tomography

- Zeitler, J.A., Gladden, L.F., 2009. In-vitro tomography and non-destructive imaging at depth of pharmaceutical solid dosage forms. *Eur. J. Pharm. Biopharm.* 71, 2–22.
- Zeitler, J.A., Shen, Y., Baker, C., Taday, P.F., Pepper, M., Rades, T., 2007. Analysis of Coating Structures and Interfaces in Solid Oral Dosage Forms by Three Dimensional Terahertz Pulsed Imaging. *J. Pharm. Sci.* 96, 330–340.
- Zhong, S., Shen, Y.-C., Ho, L., May, R.K., Zeitler, J.A., Evans, M., Taday, P.F., Pepper, M., Rades, T., Gordon, K.C., Müller, R., Kleinebudde, P., 2011. Non-destructive quantification of pharmaceutical tablet coatings using terahertz pulsed imaging and optical coherence tomography. *Opt. Lasers Eng.* 49, 361–365.

6

Automated Pharmaceutical Tablet Coating Layer Evaluation of Optical Coherence Tomography Images⁵

Film coating of pharmaceutical tablets is often applied to influence the drug release behavior. The coating characteristics such as its thickness and uniformity are critical quality parameters, which need to be precisely controlled. Optical coherence tomography (OCT) shows not only high potential for off-line quality control of film-coated tablets but also for in-line monitoring of coating processes. However, an in-line quality control tool must be able to determine coating thickness measurements automatically and in real-time. This study proposes an automatic thickness evaluation algorithm for bi-convex tables, which provides about 1000 thickness measurements within 1 second. Beside

⁵ This chapter is based on Markl, D., Hanneschläger, G., Sacher, S., Leitner, M., Khinast, J.G., Buchsbaum, A., 2014. Automated pharmaceutical tablet coating layer evaluation of optical coherence tomography images. *Meas. Sci. Technol.*, in press

the segmentation of the coating layer, optical distortions due to refraction of the beam by the air/coating interface are corrected. Moreover, during in-line monitoring the tablets might be in oblique orientation, which needs to be considered in the algorithm design. Experiments were conducted, where the tablet was rotated to specified angles. Manual and automatic thickness measurements were compared for varying coating thicknesses, angles of rotations, and beam displacements (i.e., lateral displacement between successive depth scans). The automatic thickness determination algorithm provides highly accurate results up to an angle of rotation of 30°. The computation time was reduced to 0.53 seconds for 700 thickness measurements by introducing feasibility constraints in the algorithm.

6.1 Introduction

Optical coherence tomography (OCT) is becoming an increasingly important modality for non-destructive quality control in various industries beyond biomedicine (Stifter, 2007). The dominant NDT (non-destructive testing) applications of OCT are off-line investigations such as characterization of paper (Fabritius et al., 2006; Prykäri et al., 2010), silicon integrated-circuits (Serrels et al., 2010), food (Verboven et al., 2013), fiber composites (Stifter et al., 2008) and pharmaceutical tablets (Zeitler and Gladden, 2009; Zhong et al., 2011) and pellets (Li et al., 2014). However, OCT has also a high potential to serve as an in-line quality control tool, which was recently demonstrated for the in-line monitoring of pharmaceutical pellets (Markl et al., 2014e), the in-line characterization of multi-layered foils (Hanneschläger et al., 2011) and monitoring printed electronics (Alarousu et al., 2013).

For functional tablet coatings the thickness of the coating is a critical parameter in quality control. The main purpose of the coating is to control the rate of drug release as a function of the environment (Porter et al., 2009). The initial drug release kinetics should be aligned with the pH of the environment. Therefore, coating thickness and uniformity are highly influencing the performance of the drug release and an imperfect coating might render the drug useless. In active coated tablets the coating even includes active pharmaceutical ingredients, thus making coating quality an even more critical parameter.

The performance of OCT for the characterization of film-coated tablets was already

demonstrated and compared to other measurement methods (D M Koller et al., 2011; Mauritz et al., 2010; Zhong et al., 2011). However, a real-time in-process control of the coating thickness requires an automatic evaluation of the coating layer. The in-line application of OCT holds several challenges. The main challenges are variations of the coating thickness on single tablets and between different tablets, an oblique orientation of the tablet, and effects caused by the movement of the tablets during data acquisition. Specifically, during in-line monitoring one cannot guarantee that the tablets (i.e., tablet cap) are orientated orthogonal to the probe beam. An oblique orientation of a tablet and its curvature (in case of bi-convex or round tablets) causes optical distortions, which must be corrected prior to the coating thickness determination. Each one of these challenges needs to be addressed carefully and requires the consideration of product (i.e., tablet geometry and refractive index) and process (i.e., tablet speed and mounting position) specific properties.

The accuracy of the results highly depends on the performance of the algorithm used to detect the surface of the tablet and the interface between the coating layer and the tablet core. Plenty of different OCT specific segmentation algorithms are described in literature. Most of them are applied for the segmentation of the retinal cell layers (Garvin et al., 2009; Kafieh et al., 2013; Mishra et al., 2009). The requirements on these algorithms differ to those needed in this study. Specifically the detection of up to ten *intra*-retinal layers makes the algorithms very complex and time-consuming (i.e. from several seconds up to hours) (Kafieh et al., 2013). Such long processing times do not match the requirements of a real-time monitoring tool, where the computation time should be below one second. Nevertheless, some of the concepts are suitable for the detection of the coating layer, and were therefore investigated more deeply, but optimized in terms of processing speed.

One promising segmentation method is the graph-based approach, where two-dimensional (2-D) graphs are constructed from the OCT dataset. This approach was already demonstrated to achieve high accuracy for the segmentation of *intra*-retinal layers (Garvin et al., 2009; LaRocca et al., 2011; Yang et al., 2010). The interfaces are primarily detected by applying a shortest path search and using the concept of dynamic programming. Moreover, one can additionally integrate in the graph-based approach hard constraints defined by surface set feasibilities (Dufour et al., 2013; Garvin et al., 2009). Such a graph-based approach with feasibility constraints is used in this study.

The proposed algorithm is basically composed of three steps: (a) the detection of the coating interfaces, (b) correction of optical distortions and (c) the determination of coating properties. Two different data sets were used to evaluate the performance of the algorithm. The first one is the same as used in Koller et al., 2011 to examine the accuracy of automatically measured coating layers with different thickness. The second data set was acquired by a specific experimental setup, which simulates the oblique tablet orientation that might occur during in-line monitoring.

6.2 Materials and Methods

6.2.1 Materials

Tablets of equal composition from two different batches have been used for the evaluation of the performance of the automatic thickness determination algorithm. The first batch was already used in Koller et al., 2011. Tablets from both batches were drawn during the coating process at different process stages, i.e., exhibiting differently thick coating layers. In case of the first batch, the samples from different process stages are labeled as Lot 1 to 15 (Lot 1 – uncoated tablet, Lot 15 – fully coated tablet). From the second batch only samples from two different stages of the process were taken and analyzed. These samples are henceforth distinguished by giving the process time T (37 or 96 minutes) corresponding to the elapsed process time when the samples were drawn.

The geometry of the investigated round, bi-convex tablet cores is illustrated in **Figure 6.1**. Each tablet contains 50 mg acetylsalicylic acid (ASA) as an API and lactose monohydrate (LM), microcrystalline cellulose (MCC), highly dispersed silicone dioxide (SiO₂), starch, talc, and triacetin. The coating process of both batches was carried out with a pan coater using a modified-release coating suspension (Eudragit L30D-55).

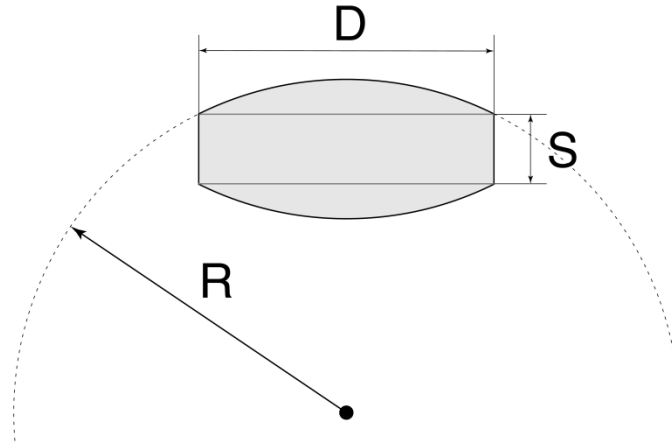


Figure 6.1: Front view of an uncoated round and bi-convex tablet model. This front view of the tablet shows the tablet diameter ($D = 7$ mm), the tablet band ($S = 1.8$ mm) and the curvature radius ($R = 7$ mm).

6.2.2 Optical Coherence Tomography

The spectral-domain (SD-) OCT system presented in D M Koller et al., 2011 was used in this study. This setup is equipped with a Koheras SuperK Versa (NKT Photonics, Denmark) as light source operating at a central wavelength of 820 nm and a full-width half maximum (FWHM) spectral bandwidth of 150 nm. Such a light source provides an axial resolution of 1.98 μm assuming a Gaussian spectral distribution. The lateral resolution depends on the optics (i.e., the numerical aperture) and is given as 13.05 μm (focal length of the lens is 50 mm and the beam diameter at the lens is 4 mm). The depth of focus of the imaging optics is calculated to be around 330 μm .

This OCT system uses a galvanometer mirror to displace the optical beam allowing the generation of cross-section images. Each cross-section image (i.e., B-scan) is synthesized by 1000 depth profiles, where a single depth scan is labeled as an A-scan. The A-scans are acquired at a rate of 20 kHz, which results in an achievable frame rate of 20 Hz.

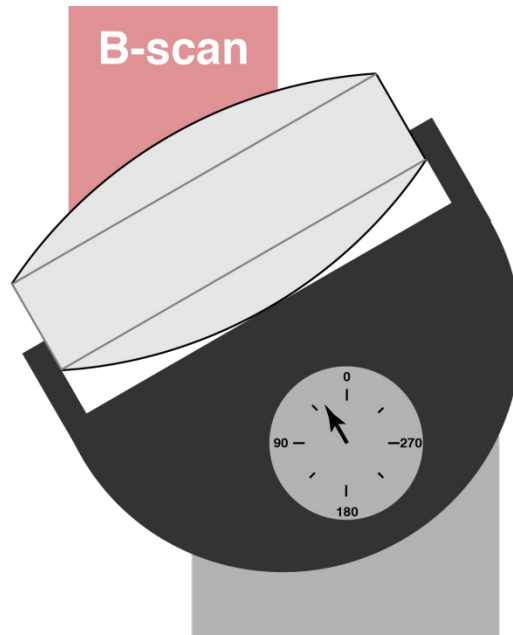


Figure 6.2: Schematic of the rotation stage. The tablet was rotated to several specified angles. At each orientation several B-scans were acquired.

6.2.3 Experimental Setup

During the in-line monitoring of film-coated tablets it is not guaranteed that the tablets are orientated orthogonal to the optical beam of the OCT system. Therefore, experiments were conducted, where the tablets were measured at several specified angles, which were set by means of a rotation stage, as shown in **Figure 6.2**. In these experiments the tablets were rotated from 0° to 30° in steps of 5° .

In case of OCT as an in-line monitoring tool the samples under investigation usually are moving. This allows the generation of cross-section images without an internal scanning procedure (i.e., galvanometer mirror). However, in both cases scanning by galvanometer mirror and scanning by moving the tablet across a stationary measurement head, the displacement Δx between successive depth profiles is directly related to the relative speed difference between sensor head and sample. The effects due to different speeds are discussed in Markl et al., 2014a and Markl et al., 2014b. In order to simulate the effects of motion the tablets were measured using different deflection amplitudes of the galvanometer mirror, which directly relates to the beam displacement Δx between successive A-scans. The beam displacements used were $2.48 \mu\text{m}$, $4.02 \mu\text{m}$ and $16.50 \mu\text{m}$.

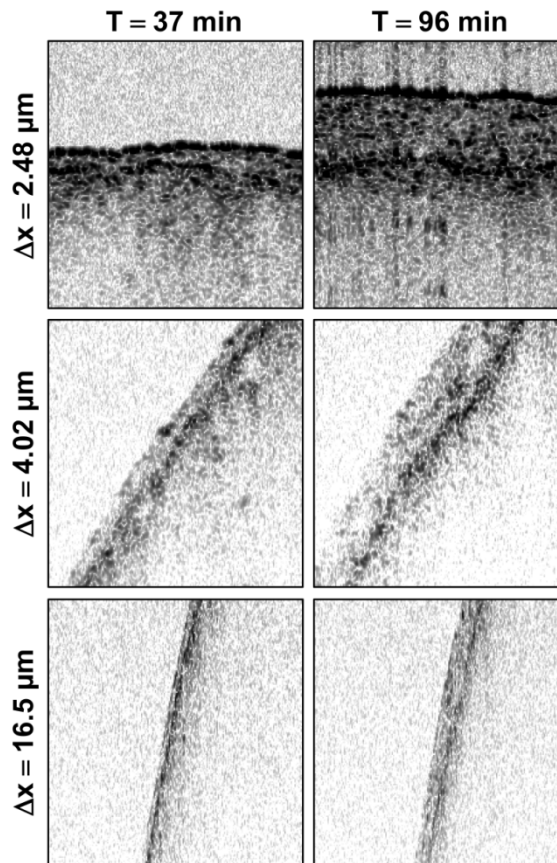


Figure 6.3: OCT images (each 200 x 200 pixels) of film-coated tablets sampled at two different process times T (resulting in different coating thicknesses) and three different displacements Δx between successive A-scans. The second and third row show OCT images of rotated tablets (30°).

6.2.4 Methods

The major challenges for an automatic in-line monitoring procedure are that (i) coating thicknesses up to 500 μm need to be detected, (ii) the speed of the tablet under investigation can vary (up to 0.6 m/s), and (iii) during data acquisition the tablet might appear in an oblique orientation.

Effects of these challenges are demonstrated in **Figure 6.3**. An increase of the transverse displacement and/or the angle of rotation of the tablet causes a decrease of the pixel intensities at both interfaces. A larger rotation angle of the tablet causes an increased incident angle of the beam on the tablet, and thus, less back-scattered and back-reflected photons are captured by the CCD camera of the OCT system.

Chapter 6: Automated Pharmaceutical Tablet Coating Layer Evaluation of Optical Coherence Tomography Images

Moreover, the sharpness and contrast of the coating/tablet core interface is less distinctive compared to the surface. This is primarily due to a smaller refractive index difference between coating and tablet core (henceforth referred to as CT interface) compared to that between air and coating (henceforth referred to as AC interface). This might further be increased by a penetration of the coating solution into the core (Ruotsalainen et al., 2003) leading to diffuse scattering of the beam and thus to a less sharp contour.

Beside the consideration of these challenges in the algorithm design, the implementation also needs to be reliable, robust, and fast. In case of the in-line OCT application, the computation time is specifically important as the coating thickness evaluation needs to be performed in real-time. Therefore, the implementation has to be efficient and should be parallelized to a high degree.

6.2.4.1 Overview of Thickness Evaluation Algorithm

The algorithm was designed to tackle all challenges presented above. Therefore, it provides accurate values of coating thickness even if the tablet is rotated and moved during the OCT measurements. An overview of the algorithm design is illustrated in **Figure 6.4**. As a first step, the region of interest (ROI) of the AC interface is extracted in order to allow a fast execution of the algorithm. Then this interface is detected accurately based on the image data by the algorithm described in section 6.2.4.2. The ROI for the CT interface is determined solely based on the location of the detected AC interface and subsequently the CT interface is detected.

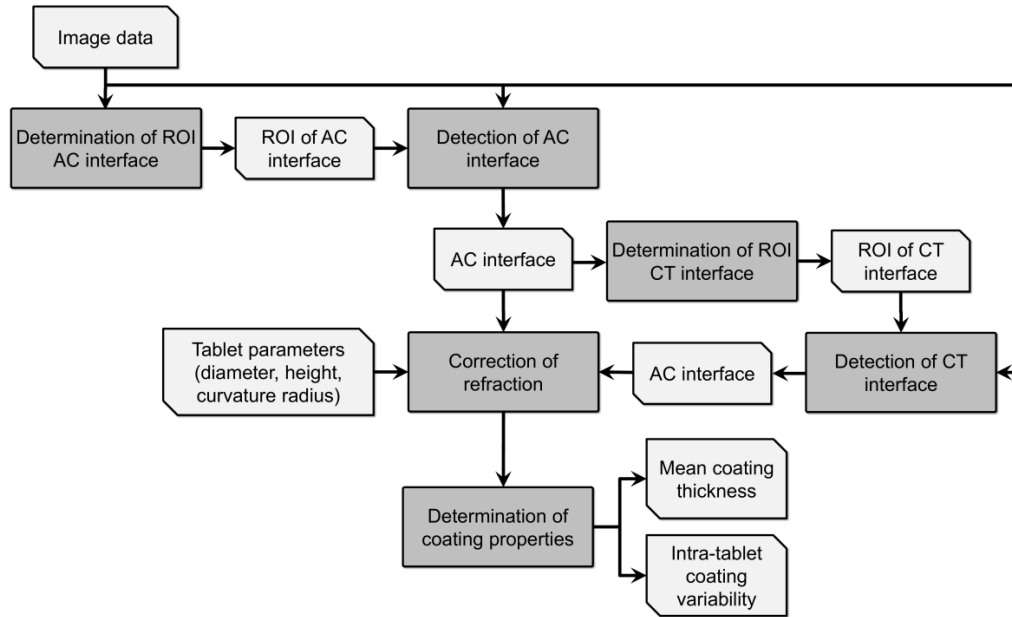


Figure 6.4: Overview of coating thickness evaluation algorithm. The brighter blocks indicate data and the darker one processing steps.

Prior to the calculation of the coating thickness from the detected interfaces, the CT contour is corrected from distortions arising from optical refraction by the preceding surface. This correction procedure requires geometrical details of the tablet core (see **Figure 6.1**) which are usually given *a priori*. Finally, the coating properties, mean coating thickness and its standard deviation (corresponds to the *intra*-tablet coating variability) are determined.

6.2.4.2 Coating Layer Detection

Initially, the region of interest \mathcal{R}^{AC} of the AC interface is determined based on single A-scans. For that purpose the sum over a moving window of 25 pixels is computed. The index of the minimum moving sum window of each A-scan is used as a rough estimate of the location of the coating layer. After smoothing and neglecting of outliers, these indices are finally used as the upper bound of the \mathcal{R}^{AC} , denoted as $R_{\max}^{AC}[j]$ for A-scan j . The lower bound $R_{\min}^{AC}[j]$ is then specified by subtracting a predefined value ($\Delta_{\max}/2$) from $R_{\max}^{AC}[j]$. The lower and upper bound R_{\min}^{CT} and R_{\max}^{CT} of the \mathcal{R}^{CT} are calculated by adding Δ_{\min} and Δ_{\max} , respectively, to the AC contour (see **Figure 6.5**). Δ_{\min} and Δ_{\max} are the minimum and the maximum expected thickness of the coating and are manually defined. Therefore, these two parameters are used as hard constraints in the interface detection algorithm. For in-line application these hard constraints might be adapted

Chapter 6: Automated Pharmaceutical Tablet Coating Layer Evaluation of Optical Coherence Tomography Images

depending on the last estimated coating thicknesses and standard deviations.

To each candidate point in \mathcal{R}_{AC} and \mathcal{R}_{CT} an edge cost needs to be assigned. This edge cost is denoted as

$$E[i, j] = w_1 E_{\text{Intensity}}[i, j] + w_2 E_{\text{Filter}, \sigma_1}[i, j] + w_3 E_{\text{Filter}, \sigma_2}[i, j]. \quad (6.1)$$

$E[i, j]$ is thus a linear combination of normalized intensities of the image and costs computed from a filtered image.

Methods that work in transmission, such as X-rayed tomography, usually image different materials by corresponding shades of gray. In contrast, OCT that works in reflection visualizes primarily the interfaces between different materials. Materials with comparable dispersion characteristics show exactly the same shade of gray on OCT images. In such cases, nothing but the interfaces are visible (Drexler and Fujimoto, 2008). The tablets, as shown in **Figure 6.3**, show both, the interfaces as black lines, and in addition different shades of gray, due to the different dispersion behavior of air, coating and tablet core. This requires an approach to determine the exact position of such interfaces that is different from the approach for e.g. X-rayed tomography. $\mathbf{E}_{\text{Intensity}}$ (henceforth referred to as intensity image) is therefore considered in the edge cost as it provides specific information about the edges. It is calculated by a linear normalization of the OCT data presented as floating point values in the range [0,1] (for visualization: 0 - black, 1 - white). The other two terms represent the costs associated to the filtered images \mathbf{I}_{z, σ_1} and \mathbf{I}_{z, σ_2} , which are convolved in vertical direction (z direction) using second-order derivative 1-D Gaussian kernels with two different standard deviations (σ_1 and σ_2). Such a kernel pronounces the edges in these OCT images more than using a first order derivative and it allows discrimination between local minima and maxima. The filtered image especially facilitates the detection of both interfaces at larger angles of incident of the beam to the tablet. Moreover, using information of two different kernel sizes preserves local details while interpolating information in low contrast regions.

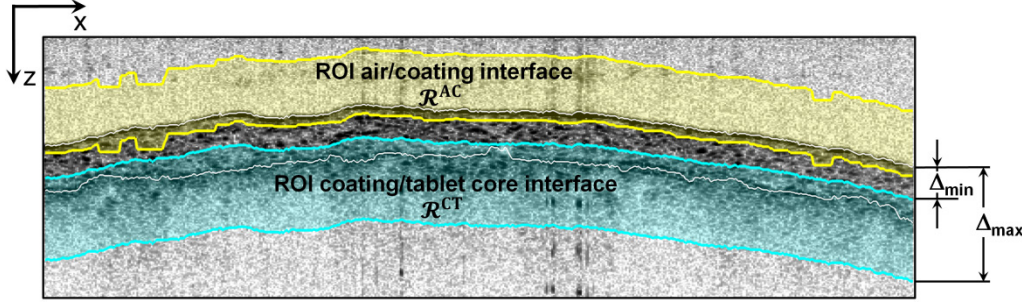


Figure 6.5: Definition of the region of interests (ROI) of the air/coating (AC) and coating/tablet core (CT) interfaces.

Specifically, local minima (corresponding to edges) and maxima in the intensity image are possessed in the filtered image (using a second derivative kernel) by local maxima ($\mathbf{I}_z > 0$) and minima ($\mathbf{I}_z < 0$), respectively. Therefore, the maxima (i.e., positive values) in the filtered image indicate the edges and not zero crossings as used in normal edge detection procedures. All negative values in the filtered image are thus set to 0 and the resulting scores $\mathbf{I}_{z,>0}$ are then normalized in the range $[0,1]$. However, the cost function concept requires the opposite of the normalized magnitude resulting in $\mathbf{E}_{\text{Filter}} = \mathbf{J} - (|\mathbf{I}_{z,>0}| - |\mathbf{I}_{z,>0}|_{\min}) / (|\mathbf{I}_{z,>0}|_{\max} - |\mathbf{I}_{z,>0}|_{\min})$ (where \mathbf{J} is a matrix of ones). The standard deviations ($\sigma_1 = 3$ and $\sigma_2 = 5$) and the size of the 1-D Gaussian kernels are the same for both interfaces. However, the weights w_1 and w_2 differ between the two interfaces. Due to the sharper edge of the AC contour the filtered image using the lower standard deviation is more pronounced ($w_2 = 0.5$ and $w_3 = 0.2$). On the contrary, the transition from coating to tablet core is blurred or more gradual and thus the filtered image with a higher standard deviation of the Gaussian kernel is emphasized by choosing the weights as $w_2 = 0.2$ and $w_3 = 0.5$. The weight w_1 for both interfaces is set to 0.3.

Based on the edge cost \mathbf{E} , a polyline of n points $\mathbf{C} = \{p_1, p_2, \dots, p_N\}$ is estimated, where point p_i corresponds to the vertical pixel position in column j on the interface (AC or CT). By expressing the edge cost by local functions $E[i, p_i]$ an object function for a possible contour \mathbf{C} of N points can be written as

$$s(\mathbf{C}, N) = s(p_1, p_2, \dots, p_N) = \sum_{j=1}^N E[p_j, j]. \quad (6.2)$$

The desired contour \mathbf{C}^* minimizes $s(\mathbf{C}, N)$ and is called the minimum cost path (see **Figure 6.6**). The minimum cost path search is executed by applying a dynamic programming (DP) algorithm. The key of the DP is to write Eq. (6.2) in

Chapter 6: Automated Pharmaceutical Tablet Coating Layer Evaluation of Optical Coherence Tomography Images

a recursion form to construct a cost map by forward recursion, which contains the minimal intermediate costs. The optimal path is then found through back tracing. Therefore, the cumulative cost for each point in the region of interest (\mathcal{R}^{AC} or \mathcal{R}^{CT}) is computed and the pointer to the local pivot is stored. This object function is defined as

$$S[i, j] = \begin{cases} \infty, & i < R_{\min}[j], i > R_{\max}[j] \\ E[i, j], & j = 0 \\ \min_{i-\delta_{\max} \leq k \leq i+\delta_{\max}} (S[k, j-1]) + E[i, j], & \text{otherwise} \end{cases}, \quad (6.3)$$

where $S[i, j]$ is the minimum cumulative cost to reach point $[i, j]$. The optimal path \mathbf{C}^* is finally determined by backtracking the cumulative cost \mathbf{S} . Due to the fact that the surface is a continuous function, the axial position of neighboring pixels deviates only slightly. This was considered by introducing a hard constraint δ_{\max} bounding the maximum axial deviation of neighboring pixels assigned as a contour (see **Figure 6.6**).

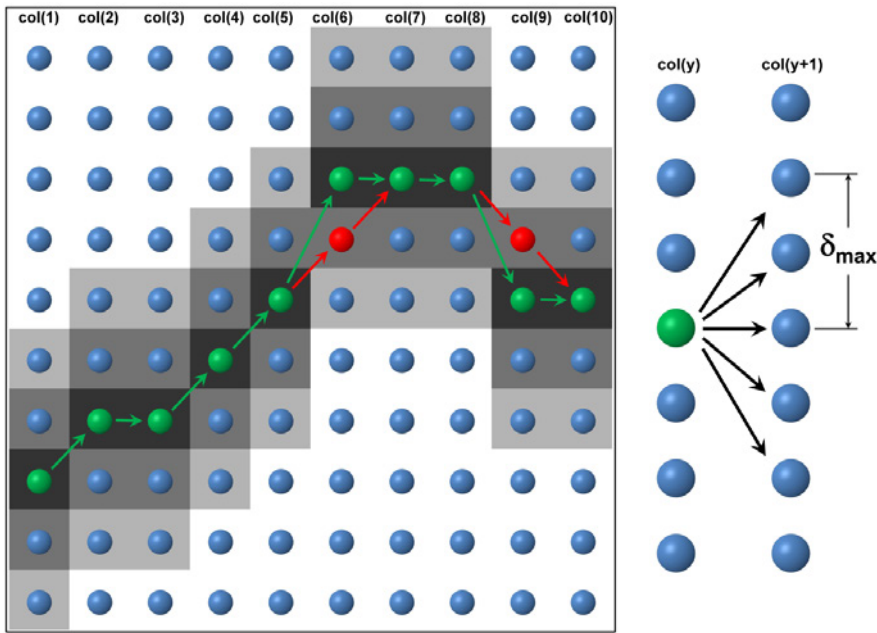


Figure 6.6: Example image and graph representation. The gray value represents the cost (black – 0 and white - 1) assigned to a pixel. The green nodes are the optimal path using a δ_{\max} of 2 pixels. If δ_{\max} is changed to 1 pixel, the contour would differ as highlighted by the red nodes in col(6) and col(9). The right image emphasizes the possible paths for a δ_{\max} of 2 pixels, where the optimal one is calculated from the minimum cost of the five feasible nodes. The number of feasible nodes is always $2\delta_{\max} + 1$.

However, this constraint needs to be large enough to allow the capturing of coating thickness variations and the tracking of the actual surface even though the tablet is rotated. To overcome the latter challenge the constraint is calculated under consideration of a maximum traceable slope of $\alpha = 30^\circ$. Thus, the maximum axial displacement of the neighbouring pixel on the surface can be calculated by $\Delta x \tan \alpha$. The displacement in pixels is then the $\Delta x \tan \alpha$ divided by the axial pixel size. Since this might result in a rational number, the ceil operator is applied to calculate

$$\delta_{\max} = \lceil \Delta x \tan \phi \rceil. \quad (6.4)$$

6.2.4.3 Correction of Refraction

The curved surface AC of the coated tablet separates two media, air and the coating layer, which exhibit different indices of refraction. The optical beam (A-scan j) intersects the surface at point A_j of coordinates (x_j^A, z_j^A) , as illustrated in **Figure 6.7**. The optical beam is refracted depending on the incident angle θ_j and the refractive indices of air n_a and coating n_c . The relation between the incident angle and the angle of refraction θ is described by Snell's law

$$n_a \sin \theta_j = n_c \sin \theta. \quad (6.5)$$

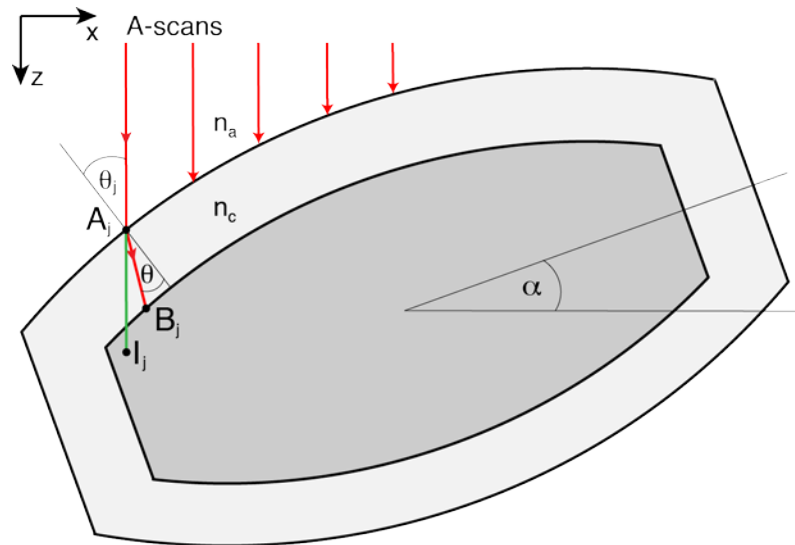


Figure 6.7: Cross-section model of a bi-convex tablet. Due to the curvature of the tablet and its rotation by an angle of α , the optical beam is refracted at the surface.

Subsequently, the refracted beam intersects the CT surface at the point B_j with the coordinates (x_j^B, z_j^B) . For an object point B_j an image point I_j with the coordinates (v_j^I, h_j^I) is generated. For one single A-scan, one would expect to collect points along the line \overline{AI} , but the OCT system acquires the data along the line \overline{AB} and places them along the line \overline{AI} (Podoleanu et al., 2004). This introduces an error when measuring the coating thickness and therefore, it should be corrected before determining the coating thickness.

First, the incident angle θ_j has to be determined for the correction of the distortions. For the determination of the incident angle, the AC surface is assumed spherical. This leads to the task of fitting a circle with the center coordinates (x_M, z_M) in the previously determined AC contour. This is performed by the gradient projection algorithm which is an extension of the steepest descent algorithm to bound constrained problems (Kelley, 1999). A boundary is only set for the radius of the circle in order to make the estimation of the center coordinates more robust. The constraints of the radius is set to r_{\min} and $R + \Delta_{\max}$ with R as the curvature radius of the tablet (see **Figure 6.1**). It is not guaranteed that the imaging plane lies in the center of the spherical cap. If the imaging plane is displaced, then the radius of the circle is smaller than the curvature radius of the tablet. The lower bound r_{\min} is determined by $\sqrt{R^2 - D/2}$ with D as the tablet diameter and assuming the imaging plane at the outer edge of the tablet. For the given tablet parameters r_{\min} is calculated as 6.06 mm.

The circle coordinates can then be used to calculate the incident angle

$$\theta_j = \frac{x_j^A - x_M}{z_M - z_j^A}. \quad (6.6)$$

The coordinates in the object space can be calculated by

$$x_j^B = h_j^I + \frac{v_j^I - z_j^A}{n_c} |\sin(\theta_j - \theta)|, \quad (6.7)$$

$$z_j^B = z_j^A + \frac{v_j^I - z_j^A}{n_c} \cos(\theta_j - \theta), \quad (6.8)$$

using Eqs. (6.5) and (6.6) for the angle of refraction and the incident angle (Podoleanu et al., 2004). In OCT images henceforth referred to as corrected OCT image, each pixel corresponding to the surface or the core is corrected according to the Eqs. (6.7) and (6.8) under consideration of the refractive index of coating or tablet core.

Moreover, the radius of the circle for the CT contour can be calculated by $\hat{r}^{CT} = \frac{1}{N} \sum_{j=1}^N \sqrt{(x_j^B - x_M)^2 + (z_j^B - z_M)^2}$ using the same center points (x_M, z_M) as for the circle fitted in the AC contour. From \hat{r}^{CT} one can roughly estimate the displacement of the imaging plane by $\sqrt{R^2 - \hat{r}^{CT}}$. However, this displacement does not influence the thickness measurements considerably as the center points of the fitted circle are used for the coating thickness analysis.

6.2.4.4 Coating Properties

In this study the investigated coating properties are the mean coating thickness and the standard deviation of the coating thicknesses of one single tablet. The latter one is directly related to the *intra*-tablet coating variability, which is a significant parameter for the performance of the film-coated tablet. The more thickness measurements per tablet are carried out, the more accurately the coating properties are measured. Therefore, each A-scan which contains information about the coating layer is used for the coating thickness calculation.

Since the measurements have to be carried out perpendicular to the surface, the measurements are simplified after transforming each point on the surface from a Cartesian to a polar coordinate system. Each point (x_j, z_j) is then represented by a distance r_j (i.e., radial coordinate) from the previously fitted circle center (x_M, z_M) and an angle ϕ_j (i.e., polar angle) from a fixed direction. The circles of the AC and CT interfaces are concentric, and thus the center point is the same for both interfaces. The coating thickness is hence calculated by subtracting the distance of the point at the CT interface from the point on the AC interface with the same polar angle. However, due to the discrete points and thus different polar angles between the outer and inner surfaces an interpolation has to be performed. The nearest neighbor interpolation is used:

$$k_j = \arg \min_{0 < i \leq N} |\phi_j - \phi_i|, \quad (6.9)$$

$$d_j = r_j^{AC} - r_{k_j}^{CT}. \quad (6.10)$$

The mean coating thickness μ and the standard deviation σ are calculated from the thickness measurements d_j with $0 < j < N$ for N successive A-scans.

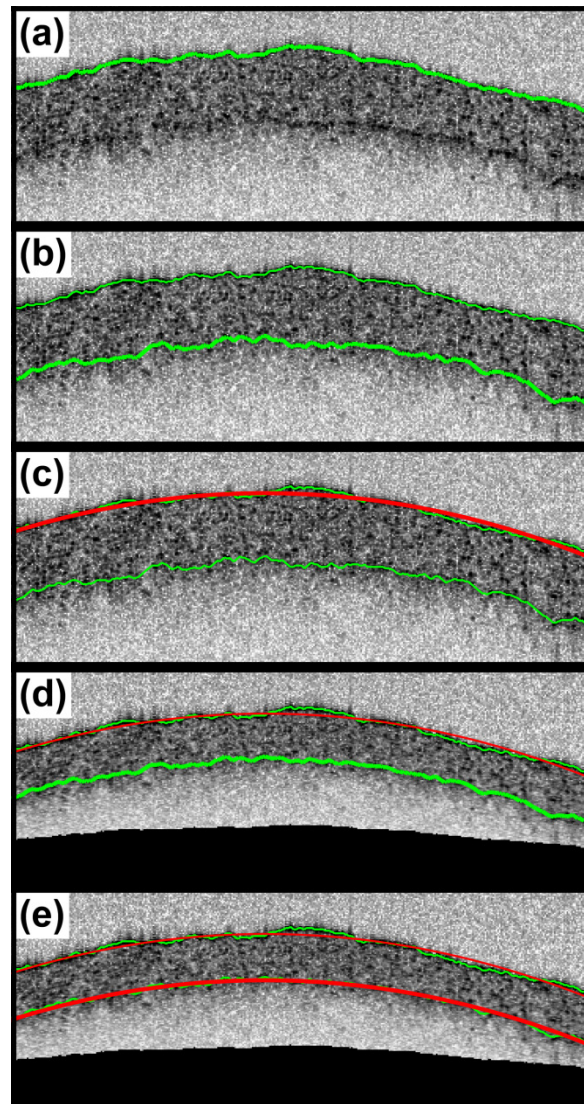


Figure 6.8: OCT images at different steps of the thickness evaluation algorithm. The coating thickness evaluation algorithm includes the following steps: detection of the (a) AC and (b) CT interfaces (green), (c) fitting the circle of the AC interface, (d) correction of optical refraction and (e) fitting the circle of the CT interface (red). (d) and (e) show the corrected OCT image. The constraint δ_{\max} was calculated by Eq. (6.4) and set to 2 pixels for this tablet.

6.3 Results

Figure 6.8 shows all intermediate results of the coating thickness evaluation algorithm. According to the algorithm described in section 6.2, the region of interest

\mathcal{R}^{AC} is extracted as a first step. Then the AC interface is determined (**Figure 6.8(a)**), which also provides the region of interest \mathcal{R}^{CT} of the second interface, and subsequently the CT interface is detected (**Figure 6.8(b)**). **Figure 6.8(c)** shows the circle fitted to the AC contour, which is further used for the correction of distortions of the CT contour. The corrected image and corrected CT contour is depicted in **Figure 6.8(d)**. The final contour CT approximately follows a circle (spherical shape of the tablet cap, **Figure 6.8(e)**).

6.3.1 Evaluation of Variable Coating Thicknesses

The accuracy of the automatic thickness determination was evaluated using the data from Koller et al., 2011, where the coating thickness was quantified manually from OCT images from different stages of a coating process (uncoated tablets, Lot 1, to fully coated tablets, Lot 15). In Koller et al., 2011 different reference methods (i.e., tablet weight gain, tablet diameter measurements and investigations with scanning electron microscopy (SEM)) were applied to compare the performance of OCT measurements with the actual thickness. In this study we use the same OCT images to automatically determine the coating thickness. **Figure 6.9** shows corrected OCT images, where the automatically detected interfaces are highlighted in green.

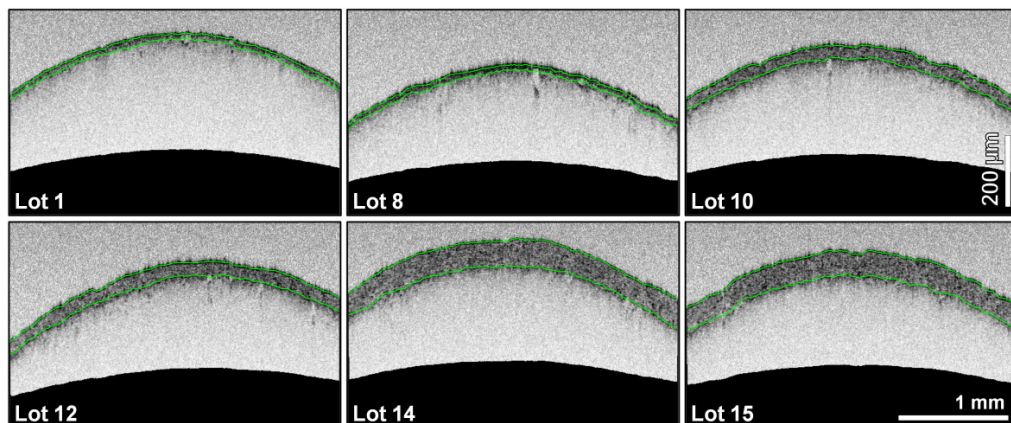


Figure 6.9: Corrected OCT images from different stages of a coating process. Lot 1 corresponds to uncoated tablets and Lot 15 to fully-coated tablets (process end). The detected interfaces (AC and CT) are highlighted in green. Optical image dimensions (in air): $3.00 \times 0.57 \text{ mm}^2$ ($570 \times 330 \text{ px}$).

Chapter 6: Automated Pharmaceutical Tablet Coating Layer Evaluation of Optical Coherence Tomography Images

The image processing was carried out on samples with different coating thickness (Lot 1 to 15). To enhance the detection robustness, the constraints Δ_{\min} and Δ_{\max} were iteratively adapted based on the previously determined coating thicknesses. Specifically Δ_{\min} needs to be adapted carefully in order to allow for the detection of smaller coating thicknesses compared to the preceding one, as occurring for the results of Lot 14 and 15. This can be compared to the drying of the coated tablets. The film contracts as the film coat dries, and thus, the overall thickness of the film may decrease (Pérez-Ramos et al., 2005). Therefore, the new Δ_{\min} was calculated from the mean coating thickness minus two times the standard deviation of the currently analyzed tablet.

A comparison of the manually and automatically determined coating thickness measurements from OCT images is illustrated in **Figure 6.10**. The automatic coating layer segmentation is limited to a minimum thickness of 10 μm , thus the measurements of Lot 1, 7 and 8 differ from the actual thickness. However, automated measurements of the coating thickness above 10 μm coincide very well with the manually measured thicknesses except for the thickness measurement of Lot 10. This slight mismatch may be caused by an overestimation of the mean due to the small sample size (10 measurements per tablet) of the manual thickness measurements compared to 570 automatic thickness measurements. The mean signed and unsigned errors between manual and automatic measurements are $-1.11 \pm 1.66 \mu\text{m}$ and $1.34 \pm 1.45 \mu\text{m}$ excluding Lot 1, 7 and 8.

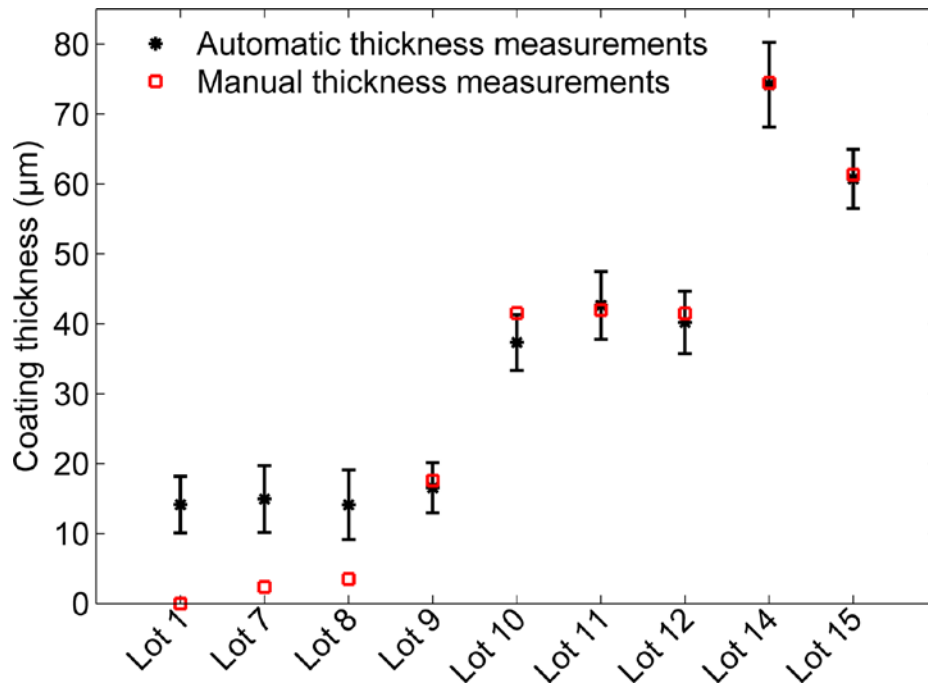


Figure 6.10: Comparison of manual (red squares) and automatic (black asterisks) determined coating thickness measurements. The error bar of the automatic measured thickness is the standard deviation of the coating thickness of one single tablet and corresponds to the intra-tablet coating variability.

6.3.2 Evaluation of Different Tablet Orientations and Varying Beam Displacements

Figure 6.11 depicts corrected OCT images of tablets oriented at three different angles, which were acquired at three different beam displacements. The interface detection algorithm performs highly accurate up to an angle of rotation of 30° and a beam displacement of $16.5 \mu\text{m}$. Particularly, the bottom right image shows very low contrast in the lower region of the coating layer, where the coating interfaces are barely detectable by the human eye. Therefore, the algorithm provides accurate results as long as one can visually identify the interfaces.

The center of the OCT image corresponds to the tablet apex. Thus, the angle of rotation of the tablet matches the incident angle at the tablet apex. Using the slope of the fitted circle at the image center, one can calculate the angle of rotation of the tablet. The insets in **Figure 6.11** shows tablets, which are rotated by an angle calculated from the slope of the fitted circle.

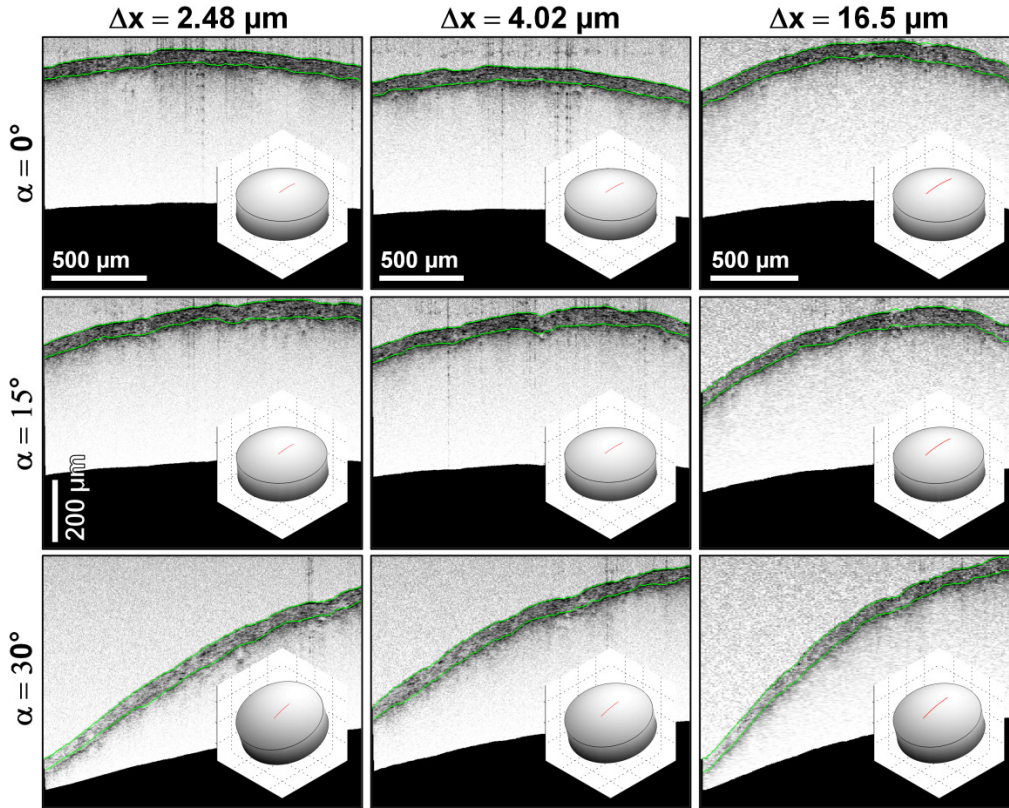


Figure 6.11: Corrected OCT images for different angles of rotation α (rows) and beam displacements Δx (columns). The refractive index of the tablet core was assumed as 1.56 (corresponds to the refractive index of ASS). The insets show the tablet with an estimated angle of rotation (from the circle fit) and an estimated position of the B-scan on the tablet surface (i.e., estimation of the displacement of the scan from the center). The constraint δ_{\max} was calculated by Eq. (6.4) and yielded 1, 2 and 9 pixels for a Δx of 2.48, 4.02 and 16.5 μm , respectively. Optical image dimensions (in air): 1.66 mm (670 px), 1.89 mm (470 px) and 1.80 mm (110 px) in horizontal direction from the left to the right column and 0.80 mm (670 px) in vertical direction for all images.

Results of the algorithm for a displacement $\Delta x = 4.02 \mu\text{m}$ and different angles of rotation are depicted in **Figure 6.12**. The measurements were carried out on the same tablet for each process time. Since the measurement position could not be guaranteed to be exactly the same for each angle, the deviations might be due to a slightly displaced imaging plane resulting in different contours of the coating layer. More details on the thickness measurements can be found in **Table 6.1**. There are only slight deviations between the different angles of rotations (indicated by the small standard deviations of the thickness measurements) and between the varied beam displacements.

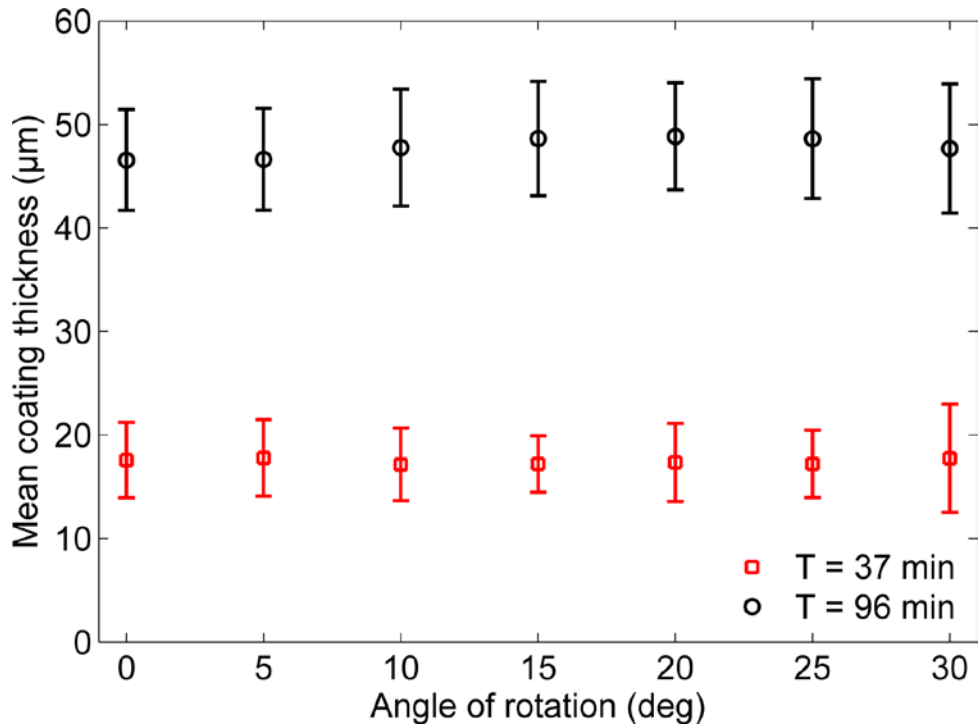


Figure 6.12: Thickness measurements as a function of rotation angle for a beam displacement of $4.02 \mu\text{m}$. The mean thickness and its standard deviation per angle were calculated from 200 and 400 measurements for samples taken from a coating process after an elapsed time T of 37 minutes and 96 minutes, respectively. The standard deviation corresponds to the intra-tablet coating variability.

The results (cf. **Figure 6.12** and **Table 6.1**) show that the coating thickness can be measured accurately up to a rotation angle of 30° . For larger angles, however, the algorithm fails to detect the surfaces at lower imaging regions corresponding to larger depths. The mean squared error of the fitted circle and the underlying contour was used as a parameter to detect such images. The tablet was not used for further analysis if the error exceeds a specified threshold.

At large rotation angles and large imaging depths, i.e., lower regions in the OCT images, the algorithm fails to detect the interfaces due to a loss of signal and contrast. The loss of signal is mainly caused by steeper slopes of the tablet surface, the sensitivity fall-off with depth in SD-OCT (Drexler and Fujimoto, 2008) and the point of focus being in the upper part of the images (the depth of field is quantified by the confocal parameter of the focused beam and is for the used system about $330 \mu\text{m}$).

Chapter 6: Automated Pharmaceutical Tablet Coating Layer Evaluation of Optical Coherence Tomography Images

Table 6.1: Coating thickness results determined automatically through application of the algorithm presented in this study. The thickness values are the mean of all thickness measurements for seven different angles of rotation (0° to 30° with 5° increments) and a variable number of measurements per angle, as given in the table. Its standard deviations were calculated from the mean values per angle. The thickness variations per tablet were quantified by averaging the standard deviation of the coating thicknesses per angle. Signed and unsigned errors are calculated using the manual measurements.

Process time T	Displacement Δx	Thickness (mean \pm SD)	Signed error (mean \pm SD)	Unsigned error (mean \pm SD)	Thickness variations per angle	Number measurements per angle	Computation time (mean \pm SD)
(min)	(μm)	(μm)	(μm)	(μm)	(μm)	(-)	(ms)
37	2.48	17.42 ± 2.12	0.18 ± 2.12	1.75 ± 0.97	4.03	200	138.5 ± 26.5
	4.02	17.43 ± 0.27	0.19 ± 0.27	0.24 ± 0.22	3.69	200	127.7 ± 1.9
	16.50	17.53 ± 1.12	0.29 ± 1.12	0.97 ± 0.51	4.34	100	82.1 ± 2.4
96	2.48	46.75 ± 1.83	0.78 ± 1.83	1.75 ± 0.70	5.13	700	530.8 ± 30.8
	4.02	47.83 ± 0.95	1.85 ± 0.95	1.85 ± 0.95	5.45	500	338.1 ± 10.9
	16.50	46.46 ± 1.11	0.49 ± 1.11	0.97 ± 0.66	5.62	200	138.9 ± 5.9
Mean \pm SD			0.63 ± 1.23	1.25 ± 0.67	4.71		

The thicknesses determined automatically by the proposed algorithm are compared to manual thickness measurements. Therefore, three thicknesses (one from each beam displacement) per process time were measured manually from non-rotated tablets. The coating thicknesses were determined on ten different positions uniformly distributed on each tablet. During the manual measurements the mean coating thicknesses were $17.24 \pm 3.14 \mu\text{m}$ and $45.97 \pm 4.31 \mu\text{m}$ for process times of 37 and 96 minutes, respectively. The automated thickness measurements coincide very well with the manual ones (see **Table 6.1**).

In order to compare the impact of the correction of optical distortions, the same data set as used for the results presented in **Table 6.1** were analyzed without correcting optical distortions. Moreover, the thickness is measured from single A-scans and, hence, the thickness was not measured perpendicular to the surface, which certainly introduces a measurement error. Results of the uncorrected thickness analysis are denoted in **Table 6.2**.

The uncorrected thickness measurements only slightly deviate from the corrected ones in **Table 6.2**. The differences between those results are increasing with increasing coating thickness and angle of rotation. The theoretical error would be $1.06 \mu\text{m}$ and $2.93 \mu\text{m}$ for a $17 \mu\text{m}$ and a $47 \mu\text{m}$ thick coating layer, respectively, and an incident beam angle of 30° . This error increases to $9.35 \mu\text{m}$ for a $150 \mu\text{m}$

thick coating layer. The theoretical analysis was performed by assuming a perfectly coated tablet and a spherical surface of the tablet core. The underlying equations for the correction of the optical distortions have the same assumptions. However, tablets are never perfectly coated as there is always a variation of the coating thickness on each tablet (i.e., *intra*-tablet coating variability) and the tablet cores typically have a rough surface. In addition to these two causes, the difference between the theoretical and the numerical results occurs due to the limited resolution of the OCT system as well as the accuracy of the interface detection algorithm.

Table 6.1 and **Table 6.2** additionally show the computation time for the different configurations. As one would expect, the computation time increases with increasing number of analyzed A-scans (i.e., number of measurements per angle). However, for 700 A-scans the computation time is still below 0.6 seconds. The difference in the computation time (comparing **Table 6.1** and **Table 6.2**) is primarily caused by the iterative circle fitting algorithm, which is required for the distortion correction algorithm.

Table 6.2: Coating thickness results determined automatically through application of the algorithm presented in this study. The thickness values are the mean of all thickness measurements for seven different angles of rotation (0° to 30° with 5° increments) and a variable number of measurements per angle, as given in the table. Its standard deviations were calculated from the mean values per angle. The thickness variations per tablet were quantified by averaging the standard deviation of the coating thicknesses per angle. Signed and unsigned errors are calculated using the manual measurements.

Process time T	Displacement Δx	Thickness (mean \pm SD)	Signed error (mean \pm SD)	Unsigned error (mean \pm SD)	Thickness variations per angle	Number measurements per angle	Computation time (mean \pm SD)
(min)	(μm)	(μm)	(μm)	(μm)	(μm)	(-)	(ms)
37	2.48	17.62 ± 2.23	0.37 ± 2.23	1.74 ± 1.27	4.03	200	98.3 ± 11.2
	4.02	17.60 ± 0.35	0.36 ± 0.35	0.37 ± 0.32	3.70	200	94.0 ± 1.9
	16.50	17.67 ± 0.99	0.42 ± 0.99	0.92 ± 0.44	4.39	100	46.8 ± 1.4
96	2.48	47.06 ± 2.01	1.09 ± 2.01	2.02 ± 0.82	5.11	700	505.0 ± 31.9
	4.02	48.02 ± 1.05	2.05 ± 1.05	2.05 ± 1.05	5.43	500	304.8 ± 7.2
	16.50	46.69 ± 1.14	0.72 ± 1.14	1.14 ± 0.63	5.62	200	107.4 ± 2.4
Mean \pm SD			0.83 ± 1.30	1.37 ± 0.76	4.71		

6.4 Conclusion

The successful implementation of a real-time and in-line evaluation of film-coated tablets requires an automatic thickness evaluation algorithm as presented in this study. This algorithm includes the detection of the coating interfaces, correction of optical distortions and the determination of coating properties (i.e., mean coating thickness and its standard deviation).

The automatic detection algorithm provides highly accurate results independent of tablet orientation and beam displacement. The integration of feasibility constraints makes the algorithm more robust and faster. However, it was also shown that the optical distortions do not affect the thickness measurements considerably. For measurements of such small thicknesses, the estimation of the surface slope might introduce a larger error than it might occur without the correction of the optical distortions. Motion effects also need to be considered more carefully when applying the algorithm on in-line data (Markl et al., 2014a). This is specifically important for the beam displacement, which might be unknown or vary during a production run. The speed of the sample under investigation, which is directly proportional to the beam displacement, thus needs to be estimated. Errors in this estimation might highly influence the thickness measurements. On the contrary, if the beam displacement and the slope of the surface are known precisely, the algorithm corrects for the systematic error.

In a next step, the algorithm will be ported to another programming language allowing real-time processing. Since the algorithm was designed to be parallelized, the execution of parts of the algorithm on the graphical processing unit (GPU) will speed up the entire processing significantly. This will enable the analysis of several tablets per second and provides data to evaluate the *intra*- and *inter*-tablet coating variability within seconds.

6.5 References

- Alarousu, E., Alsaggaf, A., Jabbour, G.E., 2013. Online monitoring of printed electronics by Spectral-Domain Optical Coherence Tomography. Sci. Rep. 3, 1562.

- Drexler, W., Fujimoto, J.G., 2008. *Optical Coherence Tomography: Technology and Applications*. Springer.
- Dufour, P. a, Ceklic, L., Abdillahi, H., Schröder, S., De Dzanet, S., Wolf-Schnurrbusch, U., Kowal, J., 2013. Graph-based multi-surface segmentation of OCT data using trained hard and soft constraints. *IEEE Trans. Med. Imaging* 32, 531–43.
- Fabritius, T., Alarousu, E., Prykäri, T., Hast, J., Myllylä, R., 2006. Characterisation of optically cleared paper by optical coherence tomography. *Quantum Electron.* 36, 181–187.
- Garvin, M.K., Abramoff, M.D., Wu, X., Russell, S.R., Burns, T.L., Sonka, M., 2009. Automated 3-D intraretinal layer segmentation of macular spectral-domain optical coherence tomography images. *IEEE Trans. Med. Imaging* 28, 1436–47.
- Hanneschläger, G., Nemeth, A., Hofer, C., Goetzloff, C., Reussner, J., Wiesauer, K., Leitner, M., 2011. Optical coherence tomography as a tool for non destructive quality control of multi-layered foils. In: *6th NDT in Progress 2011. International Workshop of NDT Experts, Prague*, p. Paper 7.
- Kafieh, R., Rabbani, H., Abramoff, M.D., Sonka, M., 2013. Intra-retinal layer segmentation of 3D optical coherence tomography using coarse grained diffusion map. *Med. Image Anal.* 17, 907–28.
- Kelley, C.T., 1999. *Iterative Methods for Optimization*, *Frontiers in Applied Mathematics*. Society for Industrial and Applied Mathematics, Philadelphia.
- Koller, D.M., Hanneschläger, G., Leitner, M., Khinast, J.G., 2011. Non-destructive analysis of tablet coatings with optical coherence tomography. *Eur. J. Pharm. Sci.* 44, 142–148.
- LaRocca, F., Chiu, S.J., McNabb, R.P., Kuo, A.N., Izatt, J. a, Farsiu, S., 2011. Robust automatic segmentation of corneal layer boundaries in SDOCT images using graph theory and dynamic programming. *Biomed. Opt. Express* 2, 1524–38.
- Li, C., Zeitler, J.A., Dong, Y., Shen, Y.-C., 2014. Non-destructive evaluation of polymer coating structures on pharmaceutical pellets using full-field optical coherence tomography. *J. Pharm. Sci.* 103, 161–6.

Chapter 6: Automated Pharmaceutical Tablet Coating Layer Evaluation of Optical Coherence Tomography Images

- Markl, D., Hanneschläger, G., Buchsbaum, A., Sacher, S., Khinast, J.G., Leitner, M., 2014a. In-line Quality Control of Moving Objects by Means of Spectral-Domain OCT. *Opt. Lasers Eng.* 59, 1–10.
- Markl, D., Hanneschläger, G., Sacher, S., Leitner, M., Khinast, J.G., 2014b. Optical coherence tomography as a novel tool for in-line monitoring of a pharmaceutical film-coating process. *Eur. J. Pharm. Sci.* 55, 58–67.
- Markl, D., Zettl, M., Hanneschläger, G., Sacher, S., Leitner, M., Buchsbaum, A., Khinast, J.G., 2014c. Calibration-free in-line monitoring of pellet coating processes via optical coherence tomography. *Chem. Eng. Sci.*
- Mauritz, J.M.A., Morrisby, R.S., Hutton, R.S., Legge, C.H., Kaminski, C.F., 2010. Imaging Pharmaceutical Tablets with Optical Coherence Tomography. *J. Pharm. Sci.* 99, 385–391.
- Mishra, A., Wong, A., Bizheva, K., Clausi, D. a, 2009. Intra-retinal layer segmentation in optical coherence tomography images. *Opt. Express* 17, 23719–28.
- Pérez-Ramos, J.D., Findlay, W.P., Peck, G., Morris, K.R., 2005. Quantitative analysis of film coating in a pan coater based on in-line sensor measurements. *AAPS PharmSciTech* 6, 127–136.
- Podoleanu, A., Charalambous, I., Plesea, L., Dogariu, A., Rosen, R., 2004. Correction of distortions in optical coherence tomography imaging of the eye. *Phys. Med. Biol.* 49, 1277–1294.
- Porter, S., Sackett, G., Liu, L., 2009. Chapter 33 - Development, Optimization, and Scale-up of Process Parameters: Pan Coating. In: Qiu, Y., Chen, Y., Zhang, G.G.Z., Liu, L., Porter, W.R. (Eds.), *Developing Solid Oral Dosage Forms*. Academic Press, San Diego, pp. 761–805.
- Prykäri, T., Czajkowski, J., Alarousu, E., Myllylä, R., 2010. Optical coherence tomography as an accurate inspection and quality evaluation technique in paper industry. *Opt. Rev.* 17, 218–222.
- Ruotsalainen, M., Heinämäki, J., Guo, H., Laitinen, N., Yliruusi, J., 2003. A novel technique for imaging film coating defects in the film-core interface and surface of coated tablets. *Eur. J. Pharm. Biopharm.* 56, 381–388.

- Serrels, K.A., Renner, M.K., Reid, D.T., 2010. Optical coherence tomography for non-destructive investigation of silicon integrated-circuits. *Microelectron. Eng.* 87, 1785–1791.
- Stifter, D., 2007. Beyond biomedicine: a review of alternative applications and developments for optical coherence tomography. *Appl. Phys. B* 88, 337–357.
- Stifter, D., Wiesauer, K., Wurm, M., Schlotthauer, E., Kastner, J., Pircher, M., Göttinger, E., Hitzenberger, C.K., 2008. Investigation of polymer and polymer/fibre composite materials with optical coherence tomography. *Meas. Sci. Technol.* 19, 074011.
- Verboven, P., Nemeth, A., Abera, M.K., Bongaers, E., Daelemans, D., Estrade, P., Herremans, E., Hertog, M., Saeys, W., Vanstreels, E., Verlinden, B., Leitner, M., Nicolai, B., 2013. Optical coherence tomography visualizes microstructure of apple peel. *Postharvest Biol. Technol.* 78, 123–132.
- Yang, Q., Reisman, C. a, Wang, Z., Fukuma, Y., Hangai, M., Yoshimura, N., Tomidokoro, A., Araie, M., Raza, A.S., Hood, D.C., Chan, K., 2010. Automated layer segmentation of macular OCT images using dual-scale gradient information. *Opt. Express* 18, 21293–307.
- Zeitler, J.A., Gladden, L.F., 2009. In-vitro tomography and non-destructive imaging at depth of pharmaceutical solid dosage forms. *Eur. J. Pharm. Biopharm.* 71, 2–22.
- Zhong, S., Shen, Y.-C., Ho, L., May, R.K., Zeitler, J.A., Evans, M., Taday, P.F., Pepper, M., Rades, T., Gordon, K.C., Müller, R., Kleinebudde, P., 2011. Non-destructive quantification of pharmaceutical tablet coatings using terahertz pulsed imaging and optical coherence tomography. *Opt. Lasers Eng.* 49, 361–365.

7

Real-time Data Processing for In-line Monitoring of a Pharmaceutical Coating Process by Optical Coherence Tomography⁶

Coating of tablets is a widely applied unit operation in the pharmaceutical industry. Thickness and uniformity of the coating layer are crucial for efficacy as well as for compliance. Not only due to different initiatives it is thus essential to monitor and control the coating process in-line. Optical coherence tomography (OCT) was already shown in previous works to be a suitable candidate for in-line monitoring of coating processes. However, to utilize the full potential of the OCT technology an automatic evaluation of the OCT measurements is essential. The automatic evaluation is currently implemented in

⁶ This chapter is based on Markl, D., Ziegler, J., Hanneschläger, G., Sacher, S., Buchsbaum, A., Leitner, M., Khinast, J.G., 2014. Real-time data processing for in-line monitoring of a pharmaceutical coating process by optical coherence tomography. Proc. SPIE.

MATLAB and includes several steps: (1) extraction of features of each A-scan, (2) classification of A-scan measurements based on their features, (3) detection of interfaces (air/coating and coating/tablet core), (4) correction of distortions due to the curvature of the bi-convex tablets and the oblique orientation of the tablets, and (5) determining the coating thickness. The algorithm is tested on OCT data acquired by moving the sensor head of the OCT system across a static tablet bed. The coating thickness variations of single tablets (i.e., *intra*-tablet coating variability) can additionally be analyzed as OCT allows the measurement of the coating thickness on multiple displaced positions on one single tablet. Specifically, the information about those parameters emphasizes the high capability of the OCT technology to improve process understanding and to assure a high product quality.

7.1 Introduction

Film coating is often involved as a final process in the manufacturing of pharmaceutical solid dosage forms. In general, during a coating process a thin continuous solid layer is applied on tablets or granules containing one or more active pharmaceutical ingredients (APIs). The primary uses of such a coating are visual attractiveness, taste masking, brand recognition or functional coating. In case of functional coating, the thin layer controls the rate of drug release as a function of the environment. Therefore, the main functionality is to align the initial drug release kinetics with the pH of the environment (Porter et al., 2009). Coating thickness and uniformity are thus highly influencing the performance of the drug release and might render the drug useless if the coating is imperfect. Controlling the coating properties is essential to guarantee high quality products.

Most of the quality control approaches are carried out off-line to characterize the final products. These traditional approaches (e.g., dissolution test, scanning electron microscopy) have some disadvantages, such as the limited number of samples which can be investigated due to the labor-intensive characterization, and their destructive nature. Both drawbacks do not allow the application of these methods as an in-line quality control tool, which can be overcome by spectroscopic (near-infrared (NIR) (Cahyadi et al., 2010; Gendre et al., 2011a; Kirsch and Drennen, 1995) and Raman (Müller et al., 2012; Romero-Torres et al., 2006)) or tomographic (optical coherence tomography (OCT) and terahertz pulse imaging (TPI) (May et al., 2010)) methods (Knop and Kleinebudde, 2013).

This study focuses on the application of OCT for in-line process monitoring of pharmaceutical film-coated tablets. This approach allows the direct determination of several coating thickness measurements per tablet. The measurements are performed from cross-section images of the tablets, which are acquired non-destructively. However, the use of OCT requires the consideration of product (i.e., tablet geometry and refractive index) and process (i.e., tablet speed and sensor mounting position) specific properties. Specifically, motion effects arising from the movement of the tablets during data acquisition need to be addressed carefully during data analysis (Markl et al., 2014a, 2014b).

For the in-line application of OCT in real-time processes an automatic evaluation algorithm is required. This algorithm requires several steps prior to the determination of the coating thickness. This prior data processing includes detection of tablets, identification of interfaces (air/coating and coating/tablet core contours) and the correction of distortions due to the curvature of the tablet surface. The data used for the design and evaluation of the proposed algorithm is acquired by an experimental setup that simulates real conditions in a pan coating process.

7.2 Materials and Methods

7.2.1 Optical Coherence Tomography

OCT provides cross-sectional depth-resolved two-dimensional (2-D) images of translucent or turbid materials. OCT is an interferometric approach and uses light sources with high spatial and low temporal coherence (i.e., spectrum with a large bandwidth results in coherence lengths of 1 - 15 μm). Such a short coherence length acts as a temporal filter for photons back-reflected and back-scattered from different sample structures, such as interfaces or impurities (Fercher et al., 2003). By comparing the arrival times of these photons with a reference light beam, a single depth measurement can be performed.

In this study a spectral-domain (SD-) OCT system equipped with a SLD (Superlum Diodes Ltd., Ireland, SLD 351 HP2) as light source was used. This light source with a center wavelength of 830 nm and a full-width at half maximum (FWHM) bandwidth of 62 nm provides a theoretical axial resolution of 4.9 μm . The light coming from the source passes a directional coupler DC (50/50 coupling ratio,

Thorlabs Inc, New Jersey, USA) as schematically illustrated in **Figure 7.1**. The light focused by a fiber focuser FF (OZ Optics, focal length = 40 mm) is split into a reference and a probe beam at a non-polarizing bulk beam splitter BS (splitting ratio 50/50, Thorlabs). This configuration allows a lateral resolution of 12 μm . The light back-reflected from both the reference and the sample is directed towards the spectrometer. The spectrometer consists of a fiber collimator FC (OZ Optics, diameter = 20 mm), a transmissive diffraction grating DG (Wasatch Photonics, 1200 lines/mm), an achromatic lens L (Thorlabs, focal length = 100 mm) and a line scan camera with a 2048 pixel CCD array (Atmel Aviiva, 14 μm^2 pixel size, 12 bit resolution). The exposure time of 67.56 μs for one single depth scan was fixed throughout all experiments giving a readout rate of the camera of 14.8 kHz.

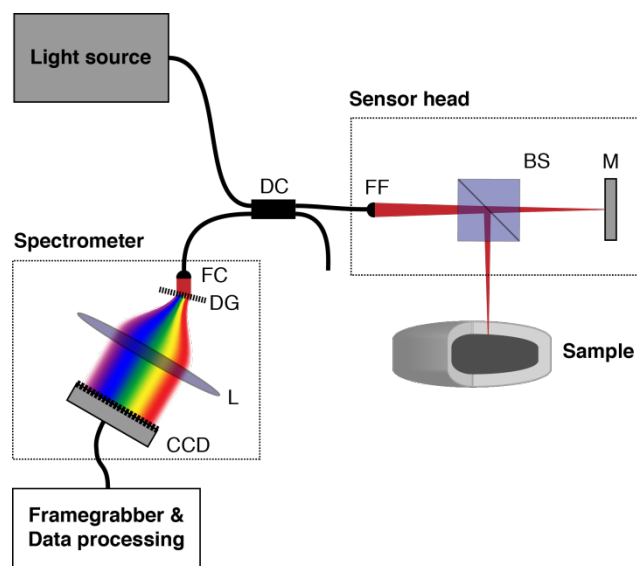


Figure 7.1: Schematic of the OCT system. The system is modularly designed allowing the separation of the sensor head from the rest of the system. DC – directional coupler, FC – fiber coupler, BS – beamsplitter, FF – fiber focuser, L – lens, M – mirror, DG – diffraction grating, CCD – charged coupled device.

A single depth scan is labeled as an A-scan. In the context of OCT, a cross-section image is synthesized by a certain number of successive uniformly displaced A-scans. Such a displacement can either be carried out by displacing the optical beam on the sample (typically performed by a galvanometer mirror integrated in the sensor head) or by moving the sample during the acquisition of successive A-scans. In the case of OCT used as an in-line monitoring tool, the samples under investigation are moving. Therefore cross-section images of the tablets can be generated without an internal scanning procedure.

7.2.2 Experimental Setup

For the application of OCT as an in-line quality control tool, the distance between sensor head and tablets is crucial. As the axial field of view of the OCT probe ranges from 1 to 3 mm, the tablets must pass the OCT probe in an appropriate distance. Therefore suitable mounting is more challenging than it is for NIR or Raman. A suggested mounting position of the OCT sensor head in a pan coater is outside of the perforated pan (Markl et al., 2013a). In particular, using this mounting position means that the tablets are monitored through the holes of the perforated plate. This affects the measurements and needs to be addressed in the automatic evaluation procedure.

The experimental setup used to investigate and analyze the requirements arising from this particular sensor head position on the automatic coating evaluation algorithm is shown in **Figure 7.2**. The in-line application of OCT was tested via a 3-axis positioning stage, which was used to move the OCT sensor head across a tablet bed covered by a perforated plate. Motion effects arising from moving the sensor head across a static tablet bed are in general the same as those caused by moving tablets with the sensor head in the same position. The sensor head was moved only in y-direction across a perforated plate with a speed of 0.2 m/s. The tablets below this plate are measured through the holes of the perforated plate. Therefore, this experimental setup allows the simulation of process conditions considering the above suggested mounting position.

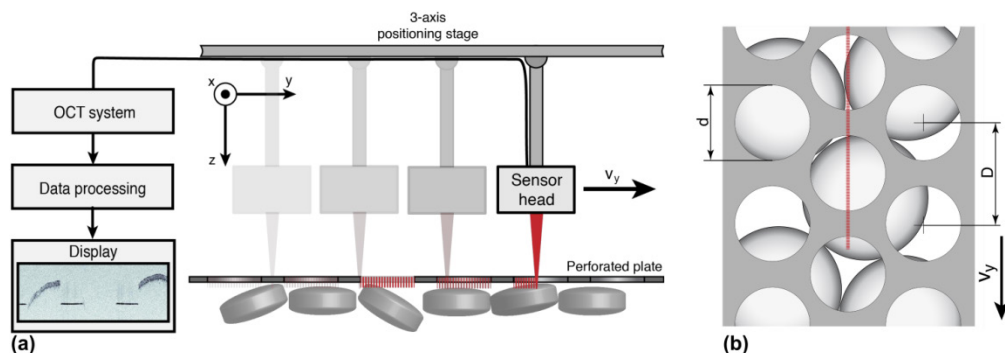


Figure 7.2: (a) Schematic of the experimental setup. The sensor head is moved with a velocity $v_y = 0.2$ m/s across a static tablet bed covered by a perforated plate. (b) Top view of the perforated plate and the underlying tablets. The red dotted line represents the beam from the OCT sensor head. The distance between hole centers is $D = 5$ mm and the diameter of the holes is $d = 3$ mm. The thickness of the perforated plate is 2 mm.

7.2.3 Tablets and Coating

Tablets used in the experiments contain 50 mg acetylsalicylic acid (ASA) as an API, lactose monohydrate (LM), microcrystalline cellulose (MCC), highly dispersed silicone dioxide (SiO₂), starch, talc, and triacetin. The coating was carried out with a pan coater using a modified-release coating suspension, i.e., Eudragit L30D-55. Film-coated tablets from four different stages of the coating process were sampled. The process ran for 127 minutes, where the samples were taken after an elapsed process time of 10, 37, 96 and 127 minutes (process end). The coating thickness of the tablets increased with increasing process time and approached a final thickness of 70 μ m.

7.2.4 Automatic Coating Thickness Evaluation Algorithm

Prior to the evaluation of the coating thickness the measured spectra acquired by SD-OCT have to be processed to provide a depth profile of the sample. This data processing includes the re-mapping of the interference spectra from a uniform wavelength space to a linear-in-wavenumber space by interpolation. This is followed by the inverse Fourier transform (IDFT) to calculate a depth profile.

The algorithm for the evaluation of the coating thickness processes 1000 successive A-scans (represented by one cross-sectional image, see **Figure 7.4**) per iteration and is implemented in MATLAB (Mathworks Inc, Massachussets, USA). The

algorithm includes five steps (see **Figure 7.3**): (1) extraction of features from each A-scan allowing the discrimination between air, the perforated metal plate and a tablet (correspond to three distinct states), (2) classification of each A-scan based on the extracted features to one of the three states, (3) detection of the interfaces air/coating and coating/tablet core for each classified tablet, (4) correction of distortions arising from the curvature and oblique orientation of the tablet, and (5) determination of the coating thicknesses of each tablet. The last step includes the calculation of the mean coating thickness and the standard deviation. This standard deviation quantifies the coating thickness variability of the tablet under investigation (i.e., *intra*-tablet coating variability). Furthermore, the investigation of the mean coating thicknesses of several different tablets within a time frame enables the analysis of the variability of the coating thickness between tablets, i.e., the *inter*-tablet coating variability.

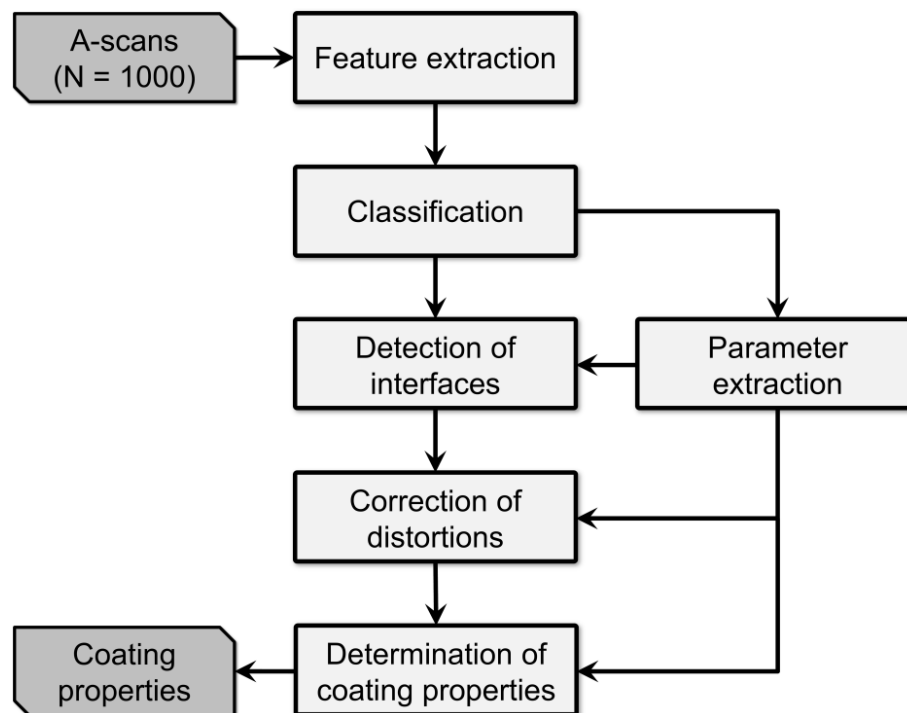


Figure 7.3: Overview of the coating thickness evaluation algorithm. The darker blocks correspond to the input and output data of the algorithm. The input data include 1000 successive A-scans and the output data contain the mean coating thickness and the corresponding standard deviation of each analyzed tablet. The parameter extraction block represents the determination of the beam displacement from the A-scan measurements classified as perforated plate.

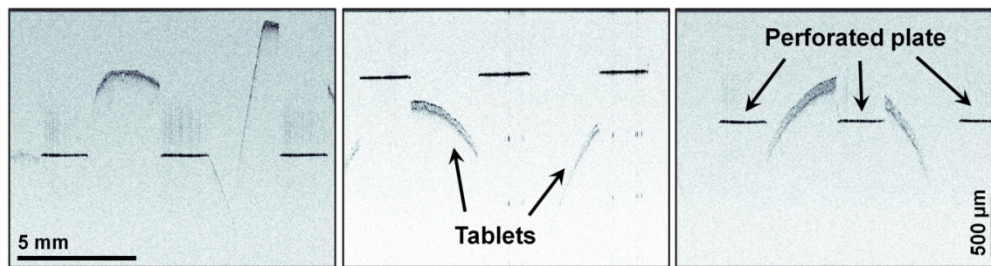


Figure 7.4: OCT images of different tablets acquired at a sensor head speed of 0.2 m/s. These images highlight the challenges for the automatic evaluation algorithm regarding different coating thicknesses, oblique orientations and positions of the tablets and varying distances of the perforated plate to the OCT sensor head. Optical dimensions of each image (1000 x 776 px): 13.62 x 2.13 mm².

7.2.4.1 Feature Extraction

The classification of A-scans has to be independent of several properties of the OCT images. Such properties include varying coating thicknesses, tablet orientation and its position (specifically the vertical position in the OCT image), and the varying vertical distance between sensor head and perforated plate. **Figure 7.4** shows examples of these properties. The varying vertical distance between sensor head and perforated plate can also cause artifacts, as e.g. tablets might appear positioned above the perforated plate (the three horizontal lines). Considering the arrangement of the sensor head, the perforated plate and the tablets, this does not seem to be feasible. This artifact is caused by the Fourier transform of a real valued function (the acquired spectrum in SD-OCT) producing a signal which is Hermitian symmetric. The perforated plate as appearing in the OCT image is a mirror image of the desired true image about the zero-phase delay line (top border of the image). The mirror image cannot be suppressed using the presented SD-OCT system.

Table 7.1: Listing of the used features. Each feature was calculated per A-scan.

Feature number	Description
1	Maximum sliding window sum (window size of 10 pixels)
2	Maximum sliding window sum (window size of 30 pixels)
3	Median within the window of feature #1
4	Maximum value within the window of feature #1
5	Gray value distribution within the window of feature #2

The successful detection of the tablet and the perforated plate requires the extraction of features which are invariant to the vertical position of the object (tablet or perforated plate), the orientation of the tablet, and the coating thickness. In addition to these feature requirements, an accurate and fast classification requires the definition of distinctive features on an A-scan basis. The feature extraction is based on the calculation of different properties of moving windows with two different sizes (10 and 30 pixels), as summarized in **Table 7.1**. As the windows slide along an A-scan (axial direction), the data within each window is summed up. The first two features (#1 and #2 for window sizes of 10 and 30 pixels, respectively) are the maximum sums for both window sizes. The window (size of 10 pixels) at the axial position of feature #1 is further used to extract feature #3 and #4 by calculating the median and the maximum value within this window. The last feature (#5) is the gray value distribution within the window of feature #2. Therefore, five features were extracted for each A-scan and further used for the classification.

7.2.4.2 Classification

The classification is performed in two stages. First, the conditional probability of each state (air, plate or tablet) is calculated for the given features on an A-scan basis. Therefore, the conditional probability of one state indicates how likely the analyzed A-scan contains information about this state. This classification was performed by a support vector machine (SVM) with a Gaussian radial basis function as kernel ($\sigma = 0.003$). The SVM package `libsvm` (Chang and Lin, 2013) was used for training and prediction. This package uses the “one-against-one” approach for multi-class classification and it also provides probability estimates (Wu et al., 2004), which are required for the next step. Since the development of a SVM corresponds to a supervised learning problem, a target class had to be assigned to each A-scan. Therefore, 120.000 A-scans were labeled manually, where

one half was used for training the SVM and the other one for validation. The training and validation data set is composed of equal numbers of tablet, plate and air A-scans.

The fact that successive A-scans are very likely corresponding to the same state has been integrated in the classification procedure by using a hidden Markov model (HMM) (Rabiner, 1989). The HMM consists of three states - the initial and emission probabilities of each state, and the transition probabilities between the states. The initial and transition probabilities are calculated for the same training set as used for the development of the SVM, and the emission probabilities are the estimated conditional probabilities from the SVM. The most likely sequence of labels is decoded by the Viterbi algorithm (Bishop, 2006). The Viterbi algorithm is applied sequentially on ten successive A-scans. This gives a hybrid SVM-HMM classifier (Altun et al., 2003; Valstar and Pantic, 2007).

Besides the detection of tablets, this classification additionally allows the identification of the perforated plate. Hence, the transversal beam displacement can be calculated from the known and measured distances of the holes (cf. **Figure 7.2(b)**) of the perforated plate. The beam displacement is a critical parameter regarding the determination of the coating thickness, as it highly depends on the relative speed difference between the tablet and the OCT sensor head. This speed difference is usually not known with the required accuracy, and therefore the determination of this parameter directly from the OCT measurements is highly beneficial.

7.2.4.3 Interface Detection

The detection of the interface is carried out by a shortest path search to find the most likely contour (Chiu et al., 2010; LaRocca et al., 2011; Yang et al., 2010). Prior to the determination of the shortest path, each pixel needs to be assigned to a specific cost value. This cost value is calculated by an equally weighted linear combination of normalized intensities of the image (in the range [0,1]) and costs based on a filtered image. The latter one is calculated from the second derivative of the image intensity function in both directions (horizontal and vertical) using a Gaussian kernel ($\sigma = 4$ for air/coating and $\sigma = 5$ for coating/tablet core interface). The magnitude of the second derivative function in both directions is normalized to the range [0,1] and used as the second cost term.

Furthermore, the shortest path algorithm is performed in two steps. First, the

air/coating interface is detected in a specified region of interest (ROI). The lower bound of this region is the vertical position of the second feature (maximum sum of moving window with a window size of 30 pixels). The upper bound is a constant of 50 pixels. After the detection of the air/coating contour, the second interface (i.e., coating/tablet core) is determined under consideration of another ROI. The upper bound of this ROI is calculated from the previously determined air/coating interface. The region of the air/coating interface is therefore neglected in the search procedure of the second interface making the algorithm much more robust. The lower bound is again a constant and set to 50 pixel. This constant corresponds to a maximum detectable coating thickness of 93 μm .

7.2.4.4 Correction of Distortions

The curved surface of the film layer separates two media (i.e. air and coating) with different indices of refraction. When an optical beam intersects this surface it is refracted, causing a change in the direction of the beam. Therefore, distortions of the coating/tablet core interface arise from the refraction of the beam by the surface above, i.e. air/coating interface. In order to determine the coating thickness at several displaced points of the tablet accurately, these optical distortions must be corrected. This correction procedure basically requires the knowledge of the refractive indices of air and the coating, and the shape of the surface. Both refractive indices are known and the shape of the surface can be approximated by a sphere. A bi-convex tablet has beside the two spherical caps also a cylindrical band. Due to a rotation of the tablet it might occur that the cylindrical band appears in the OCT image. The detection and analysis of the tablet band is currently not implemented and will be integrated in a future version of this algorithm.

The used correction procedure is based on the study of Podoleanu et al., 2004, who corrected distortions that occur when imaging the cornea. Since OCT provides cross-section images, the shape of the surface can only be approximated by a circle. Hence, a circle was fitted to the previously determined air/coating interface, and the center and radius of the circle were calculated. This was performed by the gradient projection algorithm, which is an extension of the steepest descent algorithm to bound constrained problems (Kelley, 1999). The advantage of this algorithm is that it allows for boundaries of the fitted parameters (i.e., center point and radius) to make the algorithm more robust. Specifically, the radius was

constrained to the range of 300 μm below and above the curvature radius of the uncoated tablet; the center point was not bounded.

Finally, the coating thickness at each detected point on the air/coating interface was calculated perpendicular to the surface. For each tablet a mean coating thickness and a standard deviation was calculated. The standard deviation calculated from several coating thickness measurements of a single tablet enables the investigation of the *intra*-tablet coating variability.

7.3 Results and Discussion

Figure 7.5 shows the results of the different steps, as performed by the automatic coating thickness evaluation algorithm. Prior to the segmentation of the coating interfaces, the tablets, and the perforated plate have to be detected. **Figure 7.5(a)** shows one tablet and three parts of the plate. Both objects are classified correctly and highlighted by different colors. The transitions from one class to another can be extracted from the classification result. The transition from a tablet or air to a plate part was used for the determination of the beam displacement. The distance between the successive plate transitions is 371 pixels, corresponding to a beam displacement of 13.5 μm (hole center distance D of 5 mm divided by 371). From the beam displacement and the exposure time of the CCD line scan camera (67.56 μs) the sensor head speed can be calculated. The calculated speed is 0.20 m/s, which perfectly coincides with the preset speed of the 3-axis positioning stage.

The accuracy of classification of the hybrid SVM-HMM classifier is 95.61% and 95.83% for the training and validation data, respectively. The misclassified A-scans are mostly corresponding to a region of the transition from one state to another. These A-scans cannot be assigned unambiguously. Consequently, the combination of SVM and HMM allowed an excellent classification of successive A-scans.

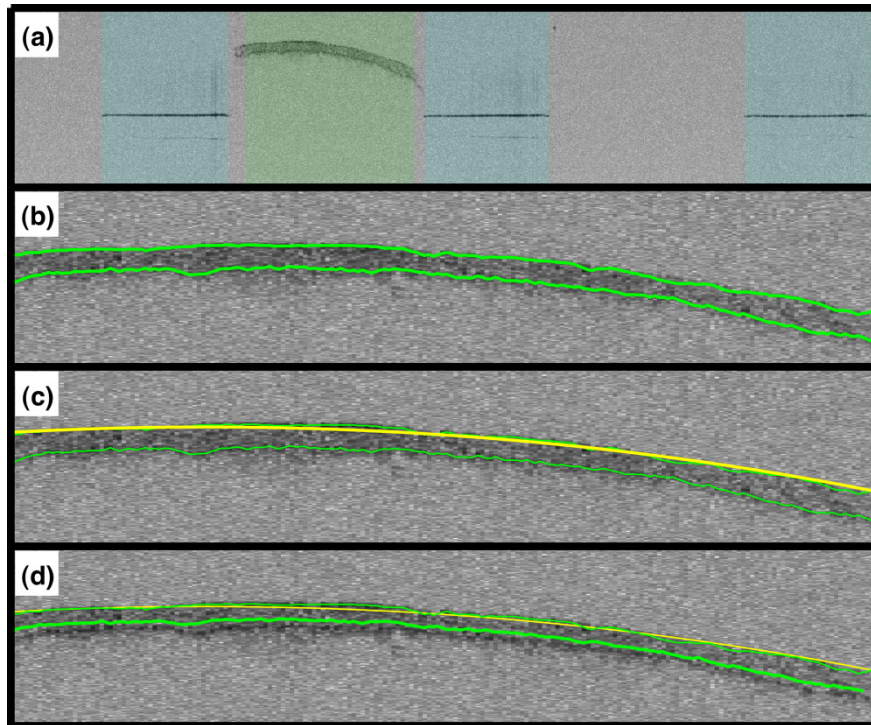


Figure 7.5: Results of the different steps of the automatic coating thickness algorithm. (a) Detection of tablets (green) and the perforated plate (blue). The remaining uncolored area is classified as air. (b) Identification of the air/coating and coating/tablet core interfaces from the detected tablet. (c) Fitting a circle and determine its center point and radius. (d) Correction of distortions caused by the surface curvature.

For the further steps only the A-scans which were classified as tablets were used. The air/coating and coating/tablet core interfaces were then extracted by the shortest path search algorithm. The contours are depicted in **Figure 7.5(b)**. The upper interface was further fitted by a circle (see **Figure 7.5(c)**) allowing for the correction of optical distortion due to refraction. The corrected coating/tablet core interface is plotted in the original uncorrected image as illustrated in **Figure 7.5(d)**.

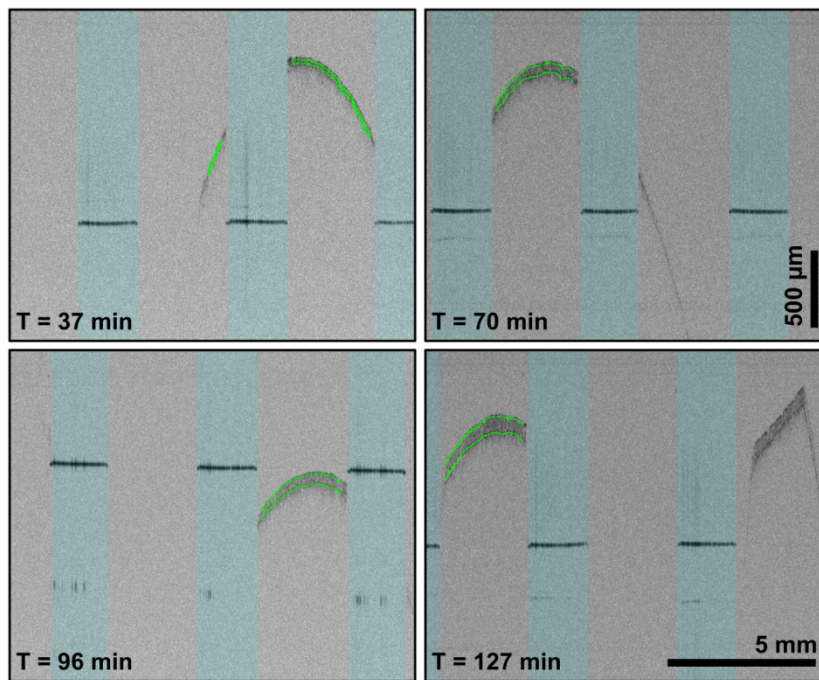


Figure 7.6: Selected OCT images of tablets sampled at four different process times. The detected coating interfaces are highlighted in green. The bottom right image shows two tablets, where only one was analysed. The other one (right tablet) represents the tablet band, which is neglected in the current implementation. Optical dimensions of each image (1000 x 776 px): 13.62 x 2.13 mm².

This algorithm was applied on 30 images composited by six images per process time (10, 37, 70, 96, and 127 minutes). **Figure 7.6** shows four selected OCT images acquired from tablets sampled at different process times. All tablets and parts of the plate are classified correctly. However, the image of the tablet according to a process time of 127 minutes shows a tablet band with a curvature that cannot be fitted by a circle (right hand side of the image). The parameter used for the withdrawal of such tablets is the mean squared error of the fitted circle and the underlying contour. If the error exceeds a specified threshold, this tablet is not used for further analysis. This also applies to tablets where either the classification or the interface detection failed.

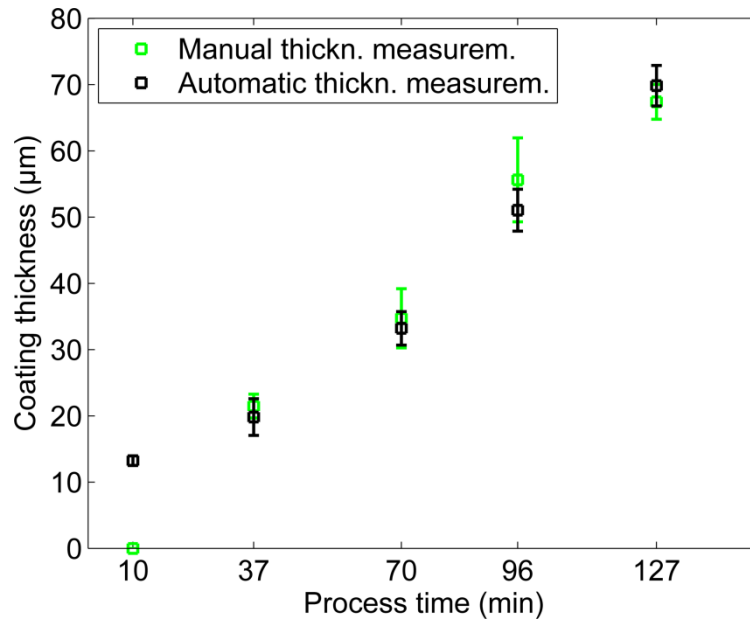


Figure 7.7: Comparison of manual and automatic coating thickness measurements. The mean and the standard deviation (error bars) of the manual and automatic coating thickness measurements were calculated from six different tablets for each process time. Each tablet was manually measured six times. The automatic coating measurements are based on six images per process time. The number of measured tablets depended on the number of detected tablets per image. A total of 30 tablets were investigated by the automatic thickness measurement algorithm.

Figure 7.7 shows a comparison between automatically and manually measured coating thicknesses as a function of the process time. At a process time of 10 minutes the coating thickness is below the resolution limit of the used OCT system, and thus no coating is visible in the OCT images. Due to the algorithm design of the interface detection procedure, the automatically measured coating thickness always exceeds a thickness of 10 μm . The manually measured tablets might not be the same as those analyzed automatically. This may cause the slight deviations between the manual and the automatic thickness measurements. If excluding the first measurements ($T = 10$ minutes), the mean absolute difference of the automatic and manual thickness data is 2.55 μm .

Beside the accuracy of the proposed algorithm, the execution time is a critical factor in real-time applications. The processing time per A-scan depends on the classification result, as only A-scans assigned to a tablet are further processed (except for the calculation of the beam displacement from A-scans labeled as a

plate). The classification per A-scan requires on average 0.61 ms (64 bit operating system, Intel(R) Core(TM) i7-3770K CPU at 3.5 GHz and 16 GB RAM). The remaining steps for A-scans classified as tablets need on average an execution time of 1.33 ms. Therefore, the processing of one image containing one tablet (size of 100 A-scans) requires about 0.74 s. This might allow the characterization of almost 3 tablets (size of 100 A-scans) per second using a sequential implementation in MATLAB.

7.4 Conclusion

The presented algorithm for the automatic thickness evaluation of film-coated tablets is the first step towards a real-time implementation of OCT for coating process monitoring. The algorithm successfully detects and evaluates film-coated tablets in OCT images under consideration of the bi-convex shape of the used tablets.

Several improvements and optimizations of the algorithm need to be implemented. One of those is the detection of the tablet band and the respective coating thickness evaluation. Moreover, the algorithm has to be ported to another programming language which allows real-time processing. This will include the execution of the core algorithms on the graphical processing unit (GPU), which will speed up the entire algorithm.

7.5 References

- Altun, Y., Tsochantaridis, I., Hofmann, T., 2003. Hidden Markov Support Vector Machines. In: ICML. pp. 3–10.
- Bishop, C.M., 2006. Pattern Recognition and Machine Learning. Springer, New York.
- Cahyadi, C., Karande, a D., Chan, L.W., Heng, P.W.S., 2010. Comparative study of non-destructive methods to quantify thickness of tablet coatings. *Int. J. Pharm.* 398, 39–49.
- Chang, C., Lin, C., 2013. LIBSVM: A Library for Support Vector Machines.

- Chiu, S.J., Li, X.T., Nicholas, P., Toth, C. a, Izatt, J. a, Farsiu, S., 2010. Automatic segmentation of seven retinal layers in SDOCT images congruent with expert manual segmentation. *Opt. Express* 18, 19413–28.
- Fercher, A.F., Drexler, W., Hitzenberger, C.K., Lasser, T., 2003. Optical coherence tomography - principles and applications. *Reports Prog. Phys.* 66, 239–303.
- Gendre, C., Boiret, M., Genty, M., Chaminade, P., Pean, J.M., 2011. Real-time predictions of drug release and end point detection of a coating operation by in-line near infrared measurements. *Int. J. Pharm.* 421, 237–43.
- Kelley, C.T., 1999. *Iterative Methods for Optimization*, Frontiers in Applied Mathematics. Society for Industrial and Applied Mathematics, Philadelphia.
- Kirsch, J.D., Drennen, J.K., 1995. Determination of film-coated tablet parameters by near-infrared spectroscopy. *J. Pharm. Biomed. Anal.* 13, 1273–1281.
- Knop, K., Kleinebudde, P., 2013. PAT-tools for process control in pharmaceutical film coating applications. *Int. J. Pharm.* 457, 527–536.
- LaRocca, F., Chiu, S.J., McNabb, R.P., Kuo, A.N., Izatt, J. a, Farsiu, S., 2011. Robust automatic segmentation of corneal layer boundaries in SDOCT images using graph theory and dynamic programming. *Biomed. Opt. Express* 2, 1524–38.
- Markl, D., Hanneschläger, G., Buchsbaum, A., Sacher, S., Khinast, J.G., Leitner, M., 2014a. In-line Quality Control of Moving Objects by Means of Spectral-Domain OCT. *Opt. Lasers Eng.* 59, 1–10.
- Markl, D., Hanneschläger, G., Sacher, S., Khinast, J.G., Leitner, M., 2013. Optical coherence tomography for non-destructive analysis of coatings in pharmaceutical tablets. *Proc. SPIE*.
- Markl, D., Hanneschläger, G., Sacher, S., Leitner, M., Khinast, J.G., 2014b. Optical coherence tomography as a novel tool for in-line monitoring of a pharmaceutical film-coating process. *Eur. J. Pharm. Sci.* 55, 58–67.
- May, R.K., Evans, M.J., Zhong, S., Warr, I., Gladden, L.F., Shen, Y., Zeitler, J.A., 2010. Terahertz in-line sensor for direct coating thickness measurement of individual tablets during film coating in real-time. *J. Pharm. Sci.* 100, 1535–1544.
- Müller, J., Brock, D., Knop, K., Axel Zeitler, J., Kleinebudde, P., 2012. Prediction of dissolution time and coating thickness of sustained release formulations

Chapter 7: Real-time Data Processing for In-line Monitoring of a Pharmaceutical Coating Process by Optical Coherence Tomography

- using Raman spectroscopy and terahertz pulsed imaging. *Eur. J. Pharm. Biopharm.* 80, 690–697.
- Podoleanu, A., Charalambous, I., Plesea, L., Dogariu, A., Rosen, R., 2004. Correction of distortions in optical coherence tomography imaging of the eye. *Phys. Med. Biol.* 49, 1277–1294.
- Porter, S., Sackett, G., Liu, L., 2009. Chapter 33 - Development, Optimization, and Scale-up of Process Parameters: Pan Coating. In: Qiu, Y., Chen, Y., Zhang, G.G.Z., Liu, L., Porter, W.R. (Eds.), *Developing Solid Oral Dosage Forms*. Academic Press, San Diego, pp. 761–805.
- Rabiner, L., 1989. A tutorial on hidden Markov models and selected applications in speech recognition. *Proc. IEEE* 77, 257–286.
- Romero-Torres, S., Pérez-Ramos, J.D., Morris, K.R., Grant, E.R., 2006. Raman spectroscopy for tablet coating thickness quantification and coating characterization in the presence of strong fluorescent interference. *J. Pharm. Biomed. Anal.* 41, 811–819.
- Valstar, M.F., Pantic, M., 2007. Combined Support Vector Machines and Hidden Markov Models for Modeling Facial Action Temporal Dynamics. In: Lew, M., Sebe, N., Huang, T.S., Bakker, E.M. (Eds.), *Human–Computer Interaction*. Springer Berlin Heidelberg, pp. 118–127.
- Wu, T.-F., Lin, C.-J., Weng, R.C., 2004. Probability Estimates for Multi-class Classification by Pairwise Coupling. *J. Mach. Learn. Res.* 5, 975–1005.
- Yang, Q., Reisman, C. a, Wang, Z., Fukuma, Y., Hangai, M., Yoshimura, N., Tomidokoro, A., Araie, M., Raza, A.S., Hood, D.C., Chan, K., 2010. Automated layer segmentation of macular OCT images using dual-scale gradient information. *Opt. Express* 18, 21293–307.

8

In-line Monitoring of a Pharmaceutical Pan Coating Process by Optical Coherence Tomography⁷

This work demonstrates a new in-line measurement technique for monitoring the coating growth of randomly moving tablets in a pan coating process. In-line quality control is performed by an optical coherence tomography (OCT) sensor allowing non-destructive and contact-free acquisition of cross-section images of film coatings in real-time. The coating thickness can be determined directly from these OCT images and no chemometric calibration models are required for quantification. Coating thickness measurements are extracted from the images by a fully automated algorithm, which

⁷ This chapter is based on Markl, D., Hanneschläger, G., Sacher, S., Leitner, M., Buchsbaum, A., Pescod, R., Baele, T., Khinast, J.G., 2015. In-line Monitoring of a Pharmaceutical Pan Coating Process by Optical Coherence Tomography. *Int. J. Pharm.*

includes the following steps: (1) detection of tablets in an OCT image, (2) segmentation of the coating layer, (3) correction of distortions due to the curvature of the bi-convex tablets and the oblique orientation of the tablets, and (4) determination of the coating thickness. Results of the in-line measurements are validated using off-line OCT images, thickness calculations from tablet dimension measurements (tablet diameter and thickness) and weight gain measurements. Validation measurements are performed on sample tablets periodically removed from the process during production. Reproducibility of the results is demonstrated by three batches produced under the same process conditions. OCT enables a multiple direct measurement of the coating thickness on individual tablets rather than providing the average coating thickness of a large number of tablets. This gives substantially more information about the coating quality, i.e., *intra*- and *inter*-tablet coating variability, than standard quality control methods. The information about those parameters specifically emphasizes the high capability of the OCT technology to improve process understanding and to assure a high product quality.

8.1 Introduction

Although tablet coating is a well-established unit operation in pharmaceutical industry, the achievable quality of coating is still limited by the fact that it is a highly complex process depending on many parameters, such as coater geometry, air pattern, degree of filling, rotation rate, spray suspension properties, spray gun numbers, spray patterns, thermal management and tablet shape (Suzzi et al., 2012, 2010; Toschkoff and Khinast, 2013). This is specifically critical for a functional-tablet coating, which requires a uniform layer with a specified thickness and density to fulfill its purpose. The aim of such coatings is to control the rate of drug release as a function of the environment, i.e., the initial drug release kinetics should be aligned with the pH of the environment. There are significant gaps remaining in the full scientific understanding of the process, which makes it a difficult task to produce tablets with an exact thickness and density and with only small tablet-to-tablet variations between batches or even within one single batch. As mixing of the tablets in the coater, and their appearance in the spray zone, are stochastic processes the coating thickness of the final product will always follow a distribution. The goal is to make this distribution as narrow as possible. On the one hand, the

understanding of the process can be improved through advances in the field of modeling film coating processes (Suzzi et al., 2012; Toschkoff and Khinast, 2013). On the other hand, the use of process analytical technology (PAT) facilitates the understanding of physico-chemical changes of the film during manufacturing. This is also relevant in view of real-time release, which is the ultimate goal of pharmaceutical manufacturing.

In-line monitoring of film coating has been reported previously. Several studies highlighted the application of spectroscopic sensors, such as near-infrared (NIR) and Raman spectroscopy to monitor the coating thickness (Pérez-Ramos et al., 2005; Romero-Torres et al., 2006), dissolution time (Gendre et al., 2011a; Müller et al., 2012) or coating deposit mass (Gendre et al., 2011b). Nevertheless, spectroscopic methods typically measure the characteristic coating property indirectly, by correlating reference measurements from samples with the attenuation of spectral features of one of the mutually exclusive constituents in the product substrate or in the coating formulation. This approach therefore requires reference measurements of samples, which are combined with the spectral information in a multivariate calibration model. Such a model then allows the prediction of the characteristic coating property, i.e., the actual coating thickness. The development and validation of such chemometric models is tedious and even slight variations in the process conditions or raw material properties may render the model invalid.

Consequently, a calibration-free direct measurement of coating properties is highly desirable. The most promising methods allowing a direct in-line measurement of the coating thickness are terahertz pulse imaging (TPI) and optical coherence tomography (OCT). TPI was successfully applied to quantitatively measure the coating thickness of tablets in a pan coater (May et al., 2010). However, TPI has limited resolutions (i.e., a transversal of 50 μm and axial resolution of 40 μm) and requires relatively long measurement times (in the range 50 ms for one single depth measurement). Both drawbacks of TPI can be overcome by OCT, which can achieve resolutions below 10 μm and allows the acquisition of hundreds of frames per second. One has to mention, however, that OCT has limited capabilities in terms of penetration depth compared to TPI and in some cases OCT fails to image through the coating or does not show a clear tablet/coating interface (e.g., when the refractive index of tablet and coating materials are too similar).

This study reports that OCT is a superior technology to non-destructively measure

the thickness (and variability) of tablet coating layers directly inside the coating pan. OCT is a high-resolution imaging technique providing depth profiles of semi-transparent and turbid materials in a contactless and non-destructive manner. In OCT an optical beam generated by a broadband light source is focused onto the surface of the tablet. The main part of the light is directly reflected by the surface of the tablet. A substantial fraction of the light penetrates into the coating structure and is then back-reflected by subsequent interfaces separating two media with different index of refraction, e.g., coating and tablet core. Measuring the delay time between the reflections of the coating surface and the coating/tablet core interface allows the determination of the coating thickness directly. A number of studies have already demonstrated the applicability of OCT for measuring the coating thickness of film-coated tablets off-line (D M Koller et al., 2011; Zhong et al., 2011), as well as for in-line monitoring of the film formation during fluid-bed coating (Markl et al., 2014d). In addition it was shown that OCT allows the in-line analysis of both tablet-to-tablet (*inter-tablet*) coating variations and the coating homogeneity of each measured tablet (*intra-tablet*) (Markl et al., 2014b).

8.2 Materials and Methods

8.2.1 Tablet Core and Coating Material

Round bi-convex tablets without break lines were used in the experiments. The tablet cores contained 50 mg acetylsalicylic acid (ASA) as an API, lactose monohydrate (LM), microcrystalline cellulose (MCC), highly dispersed silicone dioxide (SiO₂), starch, talc, and triacetin. Tablet diameter (7.14 mm), thickness (3.75 mm), curvature radius (7.56 mm) and weight (149.7 mg) were measured and averaged over 20 tablet cores. The composition of the applied enteric coating is listed in **Table 8.1**.

Table 8.1: Composition of the enteric coating suspension.

Function	Ingredient	Quantity	
		(g)	(%)
Polymer	Eudragit® L30 D-55	213.4	42.3
Plasticizer	Triethyl citrate	6.2	1.2
Anti-tacking	Talc	31.2	6.2
Diluent	Water	254.1	50.3
Total		504.9	

8.2.2 Tablet Coating

The coating process was carried out with a lab-scale pan coater (ProCepT, Zelzate, Belgium) equipped with a 1 liter drum with an inner diameter $D_{\text{drum}} = 200$ mm and a Schlick spray nozzle with a 0.8 mm tip. This nozzle generates an elliptical spray pattern. Wing-like baffles were mounted on the perforated pan to achieve good mixture of the tablets and a uniform coating distribution. Each coating experiment started with 350 g of tablets in the pan. The process conditions for coating, i.e., pan speed, spray rate, inlet air flow rate, inlet air temperature, were kept constant at 40 min^{-1} , 1.40 g/min , $0.4 \text{ m}^3/\text{h}$ and $42 \text{ }^\circ\text{C}$, respectively. Exhaust air temperature and tablet temperature were monitored during the coating runs at temperatures of $34.1 \pm 0.3^\circ$ and $34.8 \pm 0.8^\circ$, respectively. The process was stopped at a total mass of 120 g coating material sprayed onto the tablets. This was determined by measuring the weight loss of the coating material in the storage vessel using a weighing scale.

Tablet samples of approximately 1.50 – 2.25 g (10 – 15 tablets) were drawn every 8 minutes. To assess reproducibility, every coating experiment was repeated three times (referred to as B01, B02 and B03) under exactly the same process conditions.

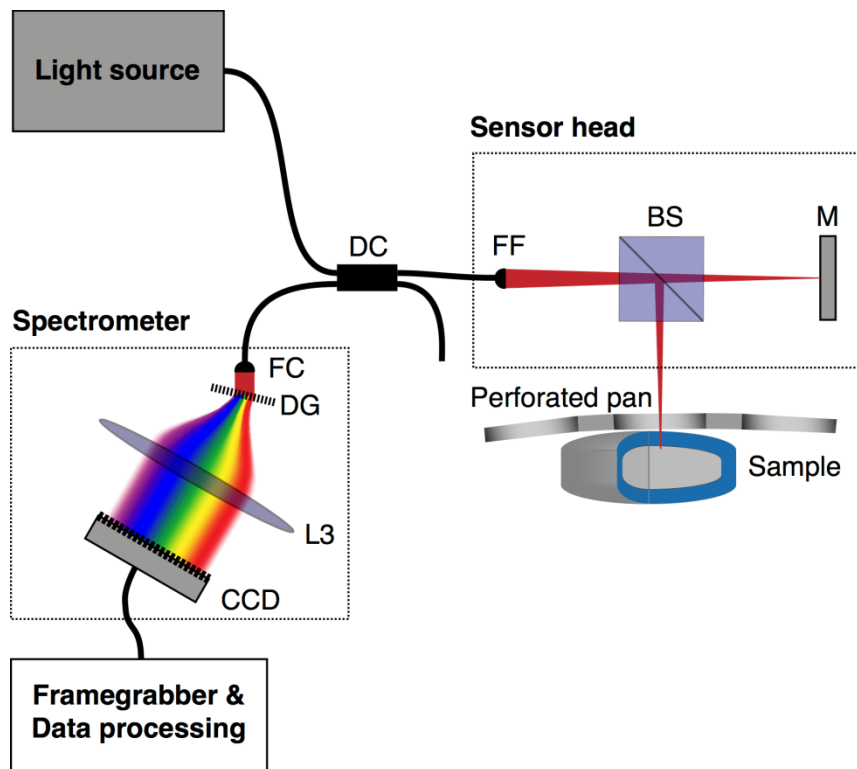


Figure 8.1: Schematic of OCT system. DC – directional coupler, FF – fiber focuser, BS – beamsplitter, M – mirror, FC – fiber coupler, DG – diffraction grating, L – lens, CCD – charged coupled device.

8.2.3 Optical Coherence Tomography

A spectral-domain (SD) OCT system was developed for the in-line application. This system is modularly designed allowing separation of the sensor head from light source, spectrometer and processing unit, as schematically illustrated in **Figure 8.1**. A superluminescent diode (SLD) Broadlighter (Superlum Diodes Ltd., Carrigtwohill, Co. Cork, Ireland) operating at a central wavelength of 832 nm and a full-width half maximum (FWHM) spectral bandwidth of 75 nm was employed as a light source. This light source provides a theoretical axial resolution of 4.1 μm .

The light exiting the source passes a directional coupler DC (50/50 coupling ratio, Thorlabs Inc, Newton, New Jersey, USA) and is directed towards the probe head. In the sensor head the light emerging the fiber is split by a non-polarizing bulk beam splitter BS (splitting ratio 50/50, Thorlabs) into a reference and a probe beam. The reference arm is terminated by a gold coated mirror (Thorlabs). The probe beam is focused by a fiber focuser FF (OZ Optics Ltd., Ottawa, Ontario,

Canada, focal length = 40 mm). This gives a theoretical transversal resolution of 14 μm and a depth of focus of 377 μm (at zero path length difference). The light reflected back from both reference and sample is directed towards the spectrometer via the coupler DC. The spectrometer consists of a fiber collimator FC (OZ Optics, diameter = 20 mm), a transmissive diffraction grating DG (Wasatch Photonics Inc., Logan, Utah, USA, 1200 lines/mm), an achromatic lens L (Thorlabs, focal length = 100 mm) and a line scan camera with a 2048 pixel CCD array (Atmel Aviiva, 14 μm^2 pixel size, 12 bit resolution). The output voltage of each CCD pixel is proportional to the number of photons hitting an individual pixel accumulated during the CCD exposure time. The exposure time $T_{\text{exp}} = 15 \mu\text{s}$ and idle time $T_{\text{idle}} = 1.9 \mu\text{s}$ were fixed throughout all experiments. This gives a duty cycle of 95% ($T_{\text{exp}} / (T_{\text{exp}} + T_{\text{idle}})$) and a readout rate of the camera of 59.2 kHz.

This setup requires an external movement of either the sensor head or the sample to construct two dimensional (2-D) images (labeled as B-scans) from successive 1-D axial measurements (labeled as A-scans). A relative velocity difference between sensor head and sample, and thus a transverse displacement between successive A-scans, occurs when measuring moving tablets in a pan coater. The speed difference theoretically corresponds to the rotational speed of the drum $v_u = \frac{D_{\text{drum}}\pi n}{60} = 0.31 \text{ m/s}$.

However, off-line OCT measurements were performed using the same light source and spectrometer, but a different sensor head allowing the generation of 2-D images without the need of an external movement. In this sensor head the light is collimated by a fiber collimator (OZ Optics, Ottawa, Canada) and the probe beam is scanned across the sample with the aid of a galvanometer mirror (Cambridge Technologies Inc., Bedford, Canada). An achromatic lens with a focal length of 36 mm (Thorlabs) focuses the probe beam onto the sample. This setup provides a theoretical transversal resolution of 10 μm and a depth of focus of 172 μm .

As mentioned above, SD-OCT is based on spectral interferometry, where recombined light from reference and sample arm is spectrally separated, detected and converted into a depth profile. The information on the location of the reflective points along the sample beam is coded in the frequency of an oscillatory signal modulating the original spectrum of the light source. This demodulation of the depth profile often limits the useful imaging range by a depth dependent sensitivity fall-off. This sensitivity fall-off can be improved by non-uniform fast Fourier transformation (NU-FFT) as presented in detail in Appendix A (Chan and Tang,

2010; Greengard and Lee, 2004). Applying the NU-FFT allows the analysis of more tablets appearing in deeper imaging regions compared to other post-processing methods.

8.2.4 Experimental Setup

The OCT sensor head was positioned outside of the perforated pan, as illustrated in **Figure 8.2** and **Figure 8.3**. A precise positioning of the sensor head was performed by two translational stages. Specifically, the sensor head was positioned radially to set the focus of the beam behind the inner surface of the drum enabling the measuring of tablets. The distance from the sensor head housing to the beam focus was approximately 11 mm. The second translational stage was used to align the beam with the center of the holes of the perforated pan. This adjustment maximized the measurement area through the holes on the tablets. The optical fiber was directed towards the OCT system via an opening in the exhaust air tube.

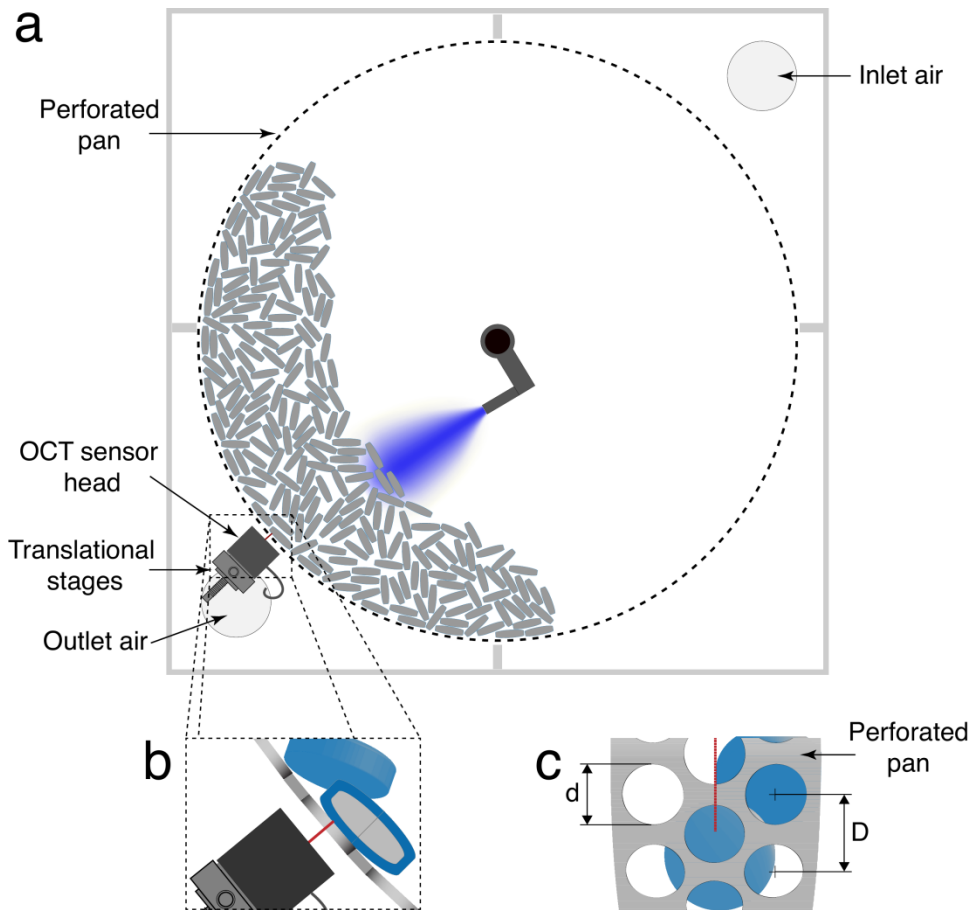


Figure 8.2: Schematic of the experimental setup. (a) Cross-section model of the coater. The OCT sensor head was mounted outside of the perforated pan. (b) Cross-section of the sensor head, the perforated pan and a tablet. The distance of the sensor head to the tablet was adjusted by a translational stage. (c) Front view (from the perspective of the sensor head) of the perforated pan and the tablets. The sensor head was aligned with the center of the holes by a translational stage. The distance between hole centers is $D = 4.5$ mm and the diameter of the holes is $d = 3$ mm. The thickness of the perforated plate is 2 mm.

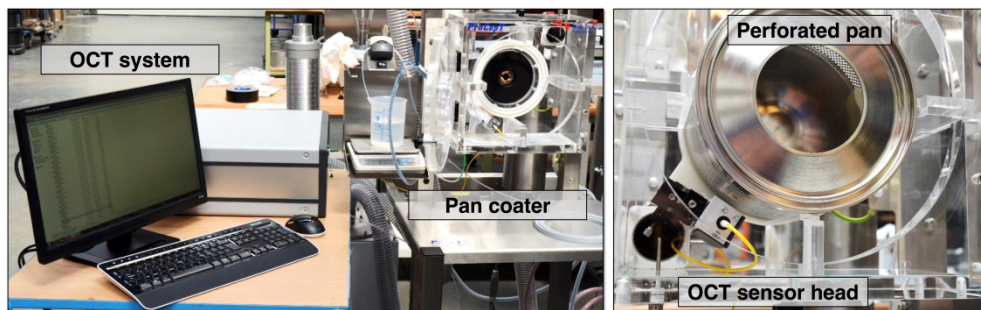


Figure 8.3: Pictures of the experimental setup.

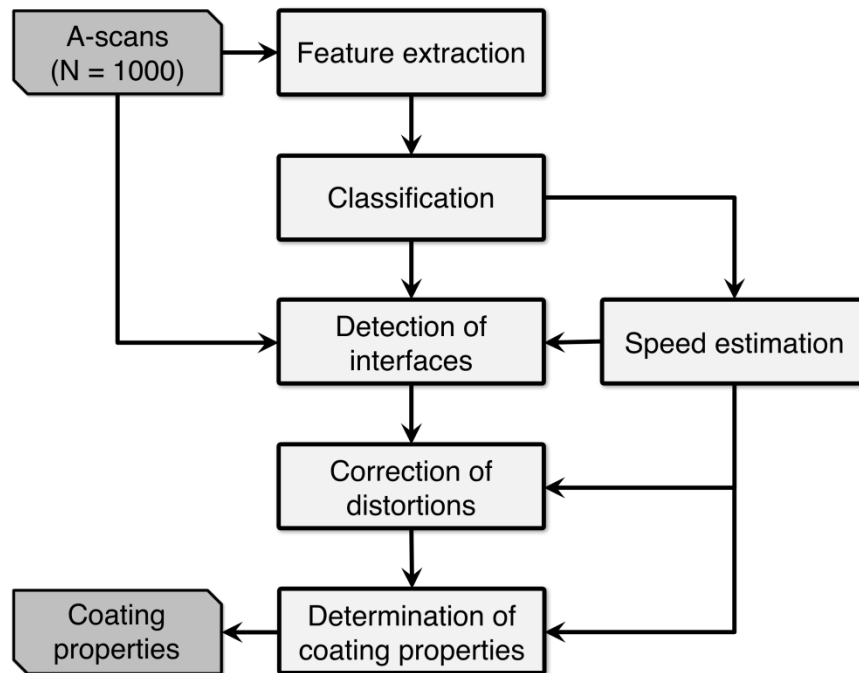


Figure 8.4: Overview of the coating thickness evaluation algorithm. The darker blocks correspond to the input and output data of the algorithm. The input data include 1000 successive A-scans and the output data contain the mean coating thickness and the corresponding standard deviation of each analyzed tablet. The speed estimation block represents the determination of the relative speed difference between sensor head and measured tablets.

8.2.5 Automatic Thickness Evaluation Algorithm

Each acquired OCT image (1000 x 1024 pixel) was processed by a dedicated algorithm to determine the coating properties. Prior to the processing, a linear normalization of the A-scan data presented as floating point values in the range [0,1] (for visualization: 0 - black, 1 - white) was performed. The fully automated evaluation algorithm includes five steps (an overview is illustrated in **Figure 8.4**): (1) extraction of features from each A-scan allowing the discrimination between three distinct states: air, metal of the perforated plate and a tablet, (2) classification of each A-scan based on the extracted features to one of the three states, (3) detection of the interfaces air/coating and coating/tablet core for each image area assigned as tablet, (4) correction of distortions arising from the curvature and oblique orientation of the tablet, and (5) determination of coating properties for each analyzed tablet. The last step involves the calculation of the mean coating thickness and the standard deviation. This standard deviation quantifies the

coating thickness variability of the tablet under investigation (i.e., *intra*-tablet coating variability). Furthermore, the investigation of the mean coating thicknesses of different tablets within a time frame enables the analysis of tablet-to-tablet variations, i.e., the *inter*-tablet coating variability.

8.2.5.1 Feature Extraction

Figure 8.5 shows examples of OCT images taken at different tablet orientations, different vertical distance of the tablet and the perforated pan to the sensor head, and different coating thicknesses. The closer the measured objects are positioned to the OCT sensor head, the further up the objects appear in the cross-section image. Even though the perforated metal plate is closer to the sensor head than the tablets, the metal plate appears at the bottom of the OCT images. This artifact is caused by the Fourier transform of the real valued signal (i.e., the acquired spectrum). This transformation yields a Hermitian symmetric signal, which results in a mirrored image of the desired true image about the zero-phase delay line (top border of the image).

In order to discriminate the three specified classes (namely air, metal, and tablet) appearing in the OCT images distinct features need to be selected which unambiguously characterize the classes on the one hand but do not include irrelevant information on the other hand.

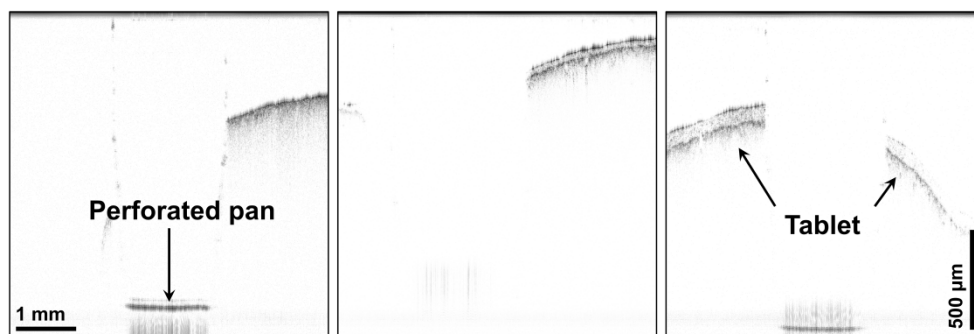


Figure 8.5: OCT images of different tablets acquired during the coating process. These images highlight the challenges for the automatic evaluation algorithm regarding different coating thicknesses, oblique orientations and positions of the tablets and varying distances of the perforated pan to the OCT sensor head. Optical dimensions of each image (1000 x 1024 px): 6.54 x 1.64 mm².

The feature extraction is based on the calculation of different properties of moving windows with two different sizes, as schematically illustrated in **Figure 8.6** and summarized in **Table 8.2**. The values within each window are summed up as the windows slide along an A-scan (axial direction). The first two features (#1 and #2 for window sizes of 10 and 30 pixels, respectively) are the minimum sums for both window sizes. Feature #3 is the element position counted in pixels within an A-scan, where position 0 corresponds to the top of the image. The last feature (#4) is the gray value distribution (using 10 bins) within the window of feature #2. Therefore, four features are extracted for each A-scan, which are denoted for A-scan i as

$$\phi_i = [p_{i1} \quad p_{i2} \quad p_{i3} \quad \mathbf{p}_{i4}^T]^T. \quad (8.1)$$

p_1 , p_2 and p_3 are scalars and represent features #1, #2 and #3, respectively. \mathbf{p}_{i4}^T is a vector with a size of the number of bins chosen for the gray value distribution (i.e., 10 bins). This gives an L -dimensional feature space ϕ_i (i.e., $L = 14$).

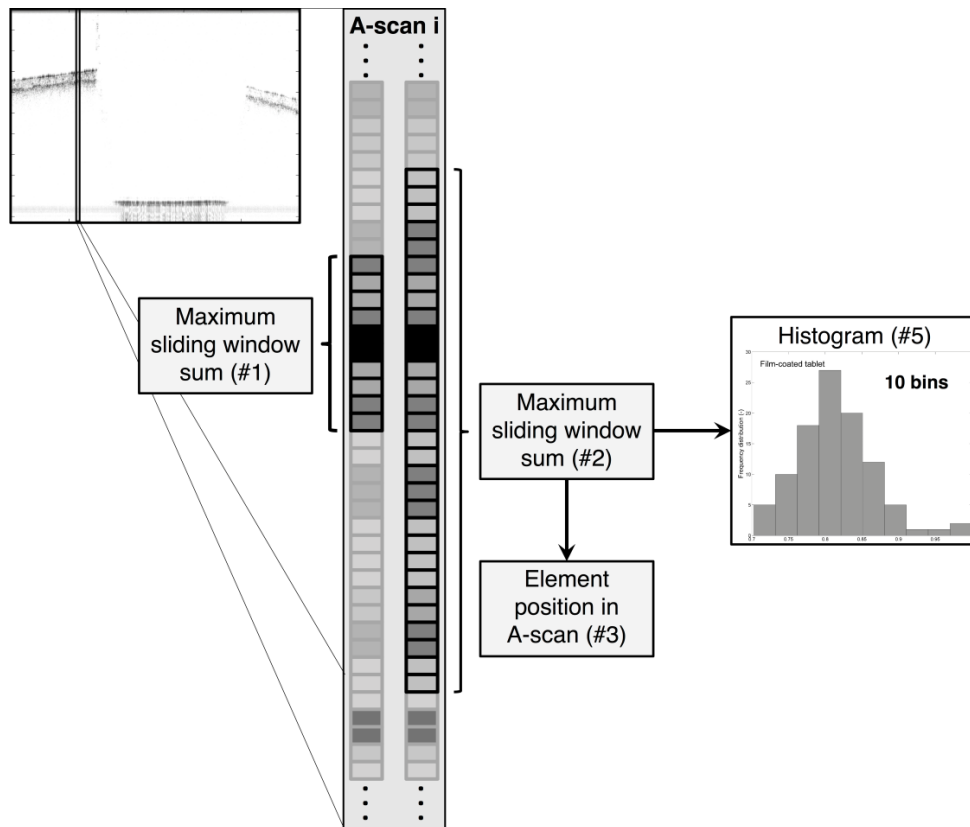


Figure 8.6: Schematic of the extracted features used for the classification. The feature extraction is performed on an A-scan basis. A more detailed description of the features is given in **Table 8.2**

Table 8.2: List of used features. Each feature is calculated per A-scan.

Feature number	Description
1	Maximum sliding window sum (window size of 10 pixels)
2	Maximum sliding window sum (window size of 30 pixels)
3	Element position within an A-scans of feature #2
4	Grey value distribution within the window of feature #2

8.2.5.2 Classification

The classification which assigns the feature vector ϕ_i to one of the three speied classes $\mathcal{C} = \{c_1, c_2, c_3\}$ is performed in two stages. First, the *posterior* probability of each class is calculated for the given features on an A-scan basis. The *posterior* probability of one class indicates how likely the analyzed A-scan contains information about this class. A probabilistic discriminative model, namely logistic regression (LG), is implemented to compute the *posterior* probability of class c_k with $k \in \mathbb{Z} | 1 \leq k \leq 3$. This method is then integrated in a hidden Markov model (HMM) based classification enabling the consideration of a dependence of neighboring A-scans. This approach thus defines two concurrent stochastic processes: a set of state output processes modeling the locally stationary property of the A-scan signal, and the sequence of HMM states (i.e., three classes) modeling the temporal dynamics of successive A-scans.

The *posterior* probabilities are given by a softmax transformation of linear functions of the feature variable, denoted as

$$P_k(q_i|\phi_i) = \frac{e^{\mathbf{w}_k^T \phi_i}}{\sum_j e^{\mathbf{w}_j^T \phi_i}} \quad \{k \in \mathbb{Z} | 1 \leq k \leq 3\} \quad (8.2)$$

for A-scan i . A supervised learning strategy is used to find the probability of a certain class $q_i \in \mathcal{C}$ of the finite sequence $\mathcal{Q} = \{q_1, \dots, q_N\}$ (N is the number of A-scans under investigation). This technique requires labeled training data. 120,000 A-scans were assigned manually to one of the three classes, where 2/3 of these data were used for training and the remaining ones for validation. Maximum *posterior* (MAP) is then applied to determine the parameters $\{\mathbf{w}_k\}$. This technique integrates a regularization term to avoid overfitting. An overfitted model means that it fits the training data well, but describes noise instead of the underlying relationship and consequently performs poor on the validation data. This regularization term was therefore optimized with respect to the performance of the validation data.

A HMM is built from a finite set of possible states (classes) \mathcal{C} (Rabiner, 1989). The system undergoes a change of state (possibly back to the same state) according to a set of probabilities associated with the state, i.e. the transition probabilities. Therefore, the model is characterized by a transition matrix describing the probabilities of particular transitions between states. The transition probabilities, as well as the initial probabilities (how likely the sequence starts in state c_k), were determined from the training data by computing the frequencies of each state transition and the frequency of each state, respectively. The *posterior* probabilities $P_k(q_i|\phi_i)$ with $k \in \mathbb{Z}|1 \leq k \leq 3$ of the LG classifier are used as emission probabilities of the HMM. The most likely sequence of labels is decoded by the Viterbi algorithm (Bishop, 2006). The Viterbi algorithm is applied sequentially on ten successive A-scans ($N = 10$). This gives a local optimal state sequence \mathcal{Q} , which might deviate slightly from the global optimal sequence. However, tests showed that using more successive A-scans (100, 200, 500, 1000) improves the classification only slightly, albeit it increases the computation time dramatically (10, 16, 41 and 82 times the computation time compared to 10 successive A-scans).

8.2.5.3 Layer Segmentation and Distortion Correction

The layer segmentation and distortion correction is carried out by the algorithm presented in Markl et al., 2014c. The settings of the algorithm used in this work are the same as in Markl et al., 2014c except the properties depending on system parameters (i.e., transversal beam displacement and axial displacement). Also the correction of distortion due to the refraction of the beam by the air/coating interface are corrected in the same manner as presented in Markl et al., 2014c. The refractive index was set to 1.48 as validated for the same coating materials in D M Koller et al., 2011. Finally, the coating thickness at each detected point on the air/coating interface was calculated perpendicular to the surface.

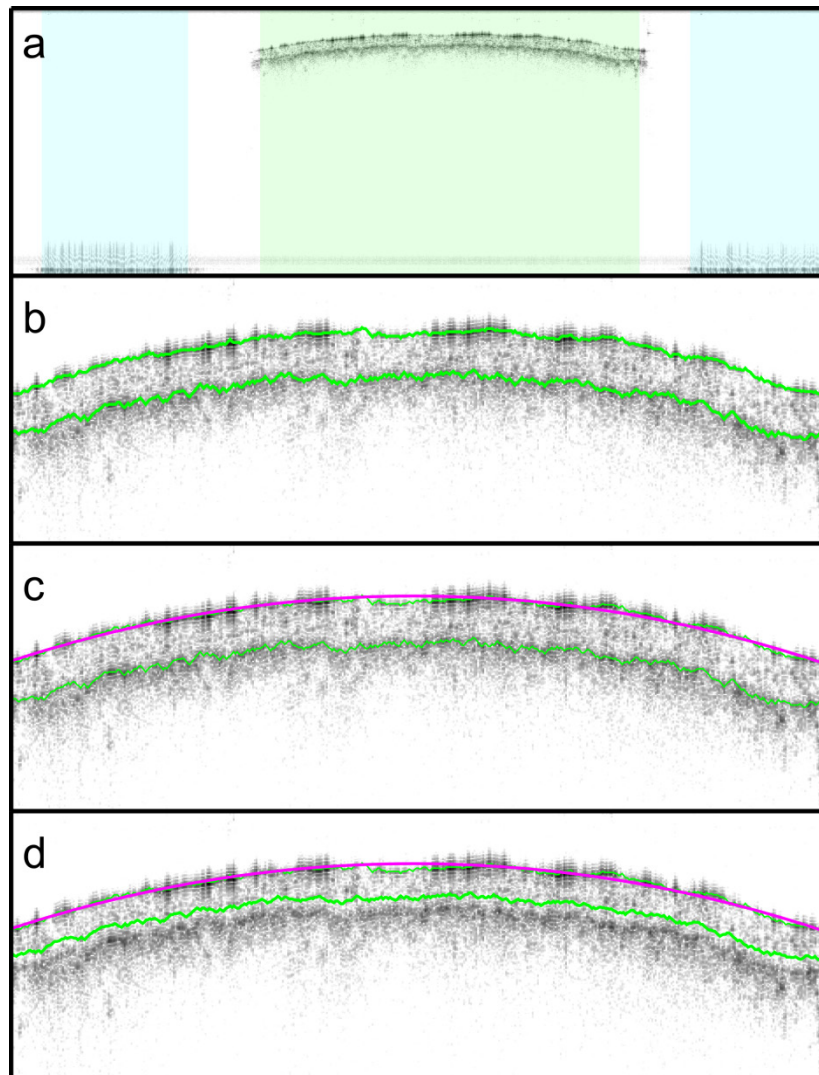


Figure 8.7: Results of the different steps of the automatic coating thickness algorithm. (a) Detection of tablets (green) and the perforated pan (blue). The remaining uncolored area is classified as air. (b) Identification of the air/coating and coating/tablet core interfaces (green) within the image region assigned as tablet (green highlighted image region in (a)). (c) Fitting a circle (magenta) and determination of its center point and radius. (d) Correction of distortions caused by the surface curvature and the refractive index.

8.3 Results

Image acquisition and visualization were performed continuously, whereas only a fraction of all images could be saved for the analysis due to storage and performance

limitations. The automated evaluation algorithm was thus applied on all saved OCT images. **Figure 8.7** shows a typical result of several steps of the fully automated evaluation algorithm. As mentioned before, each A-scan is assigned to one of the three classes emphasized by different colors in **Figure 8.7(a)**. Only regions labeled as tablet and metal consisting of at least 50 successive A-scans are further analyzed. Obviously the coating layer detection and characterization is performed on the parts of the image classified as tablet. The regions labeled as metal are used to determine the velocity of the measured tablets allowing the calculation of the transversal beam displacement. The beam displacement is a critical parameter regarding the determination of the coating thickness, and it highly depends on the relative speed difference between the tablet and the OCT sensor head (Markl et al., 2014a, 2014b). This speed difference is usually not known with the required accuracy, and therefore, the determination of this parameter directly from the OCT measurements is highly beneficial.

The tablet speed is calculated from the known and the apparent (in the OCT images) distance of the hole centers and the known exposure (T_{exp}) and idle (T_{idle}) times of the line-scan camera. The transversal beam displacement was calculated and adapted automatically along the entire process time. The maximum measured speed was 0.38 m/s which translates to a beam displacement of 16.9 μm , well below the limitations of the OCT setup (see Markl et al., 2014a). Such a relative speed difference between sensor head and tablets was still below the critical speed for this system configuration of 0.7 m/s. A speed above this critical speed would cause the transition from optics to the beam displacement as limiting factor for the transverse resolution as extensively discussed in Markl et al., 2014a.

Table 8.3: Classification error for LG and LG-HMM.

	Training data				Validation data			
	Metal (%)	Tablet (%)	Air (%)	Total (%)	Metal (%)	Tablet (%)	Air (%)	Total (%)
LG	4.46	5.96	10.38	10.40	4.29	5.96	10.18	10.22
LG-HMM	3.56	5.83	9.34	9.37	3.40	5.18	8.51	8.54

Table 8.4: Counts of transitions between different classes and between the same class for all A-scans of the validation data.

	Manual			LG			LG-HMM		
	Metal	Tablet	Air	Metal	Tablet	Air	Metal	Tablet	Air
Metal	10584	5	38	10893	4	586	11789	4	42
Tablet	5	17926	44	5	17663	337	6	18256	48
Air	38	43	13316	586	337	11588	41	49	11764

A prerequisite for the speed estimation and certainly for the coating thickness determination is a precise classification of each A-scan. The accuracy of the LG and the LG-HMM classifiers are summarized in **Table 8.3** for training and validation data separately. It shows that the classification is more accurate using LG-HMM, whereas the overall performance improvement is highlighted only poorly by this data. Examining the transition counts between each class, as listed in **Table 8.4**, emphasizes the benefit of integrating the HMM. These data denote that much more false transitions – mostly caused by single misclassified A-scans - are occurring without the HMM (i.e., specifically transitions from air to metal or air to tablet). Since further analysis showed that at least 50 successive A-scans labeled with the same class are needed to guarantee an accurate thickness calculation, the overall performance is increased drastically using the HMM by correcting single misclassified A-scans. However, there is still a large number of misclassified A-scans, which are mostly corresponding to a region of the transition from one class to another. These A-scans cannot be assigned unambiguously due to the high tablet speed and the finite transversal resolution of the OCT system.

Results of the classification and interface detection algorithm can be seen in **Figure 8.8**. The image acquired at minute 40 of the coating process shows two measured tablets, however, only one of them was used for the calculation of the coating thickness. Even though this tablet was detected correctly by the classification procedure, the extraction of coating layer failed. Such a failure is detected by calculating the mean squared error of the fitted circle and the underlying contour. If the error exceeds a specified threshold, this tablet is withdrawn and not used for further analysis.

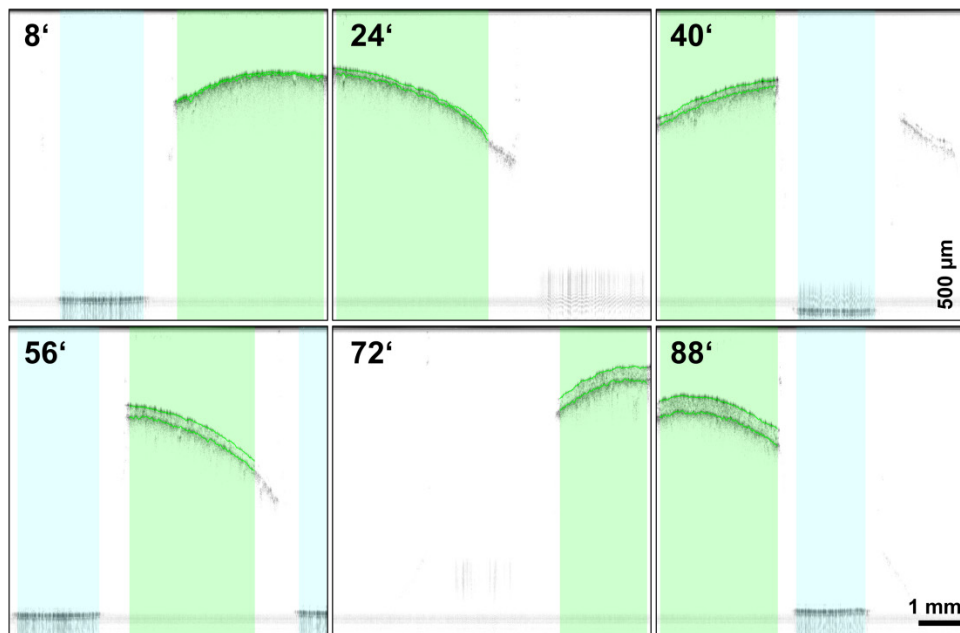


Figure 8.8: OCT images acquired in-line at different process times (in minutes) from B01. The blue and green areas correspond to the perforated pan and tablets (only tablets used for the analysis are marked), respectively. The interfaces of the coating layer are emphasized in green. Optical dimensions of each image (1000 x 1024 px): 6.54 x 1.64 mm².

Apart from the refractive index of the coating layer no prior knowledge is required to quantify the coating thickness. The refractive index might be influenced by process conditions in a pan coater. Future research will be necessary to study the impact of process conditions on the refractive index and thus, on the accuracy of the thickness measurements. However, previous work shows for the application of TPI, that the refractive index of the coating polymer does not change significantly during process time (Ho et al., 2009a, 2007).

The coating thickness from the in-line data increases steadily as expected and agrees well with the measurements of the sprayed coating mass and the off-line thickness measurements. Each data point (in-line OCT) in **Figure 8.9** represents the mean coating thickness for each analyzed tablet. The number of thickness measurements per tablet ranged between 82 and 633 for the in-line measurements of batch B01. The off-line coating thickness measurements were calculated automatically for each tablet on 1000 different positions. The thickness measurements before a process time of 10 minutes are below the sensor detection limit, and thus, these data are not reliable and not used for the interpretation.

As each data point is an average of several tens to hundreds of thickness measurements per tablet the variation of the coating thickness can be determined during the whole process. This *intra*-tablet coating variability is investigated on the basis of the relative standard deviation (RSD) of the coating thickness (**Figure 8.10**). The RSD decreases with increasing process time, which implies an enhancement of the coating uniformity. At the end of the process the standard deviation of the coating thickness approaches a value of 4.8 μm . The OCT measurements therefore reveal that the coating layer is evenly distributed over the surface of the individual tablet faces.

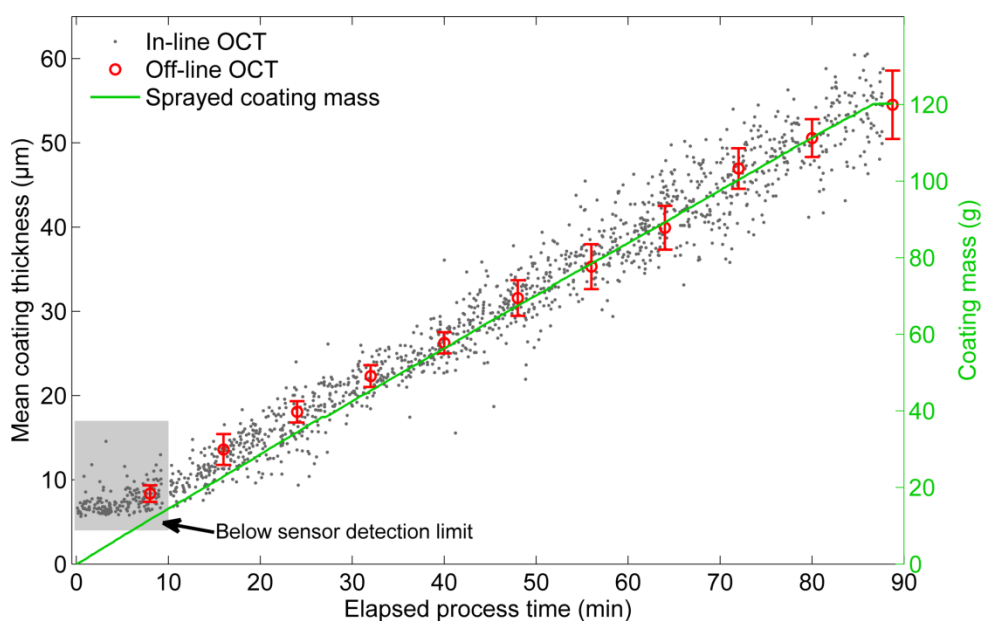


Figure 8.9: Coating thickness and coating mass as a function of process time. Each data point of the in-line process sensor indicates the average of several thickness measurements of one tablet. The sprayed coating mass was measured each second and the process was stopped at a final coating mass of 120 g. The red circles represent the average thickness measurements from off-line OCT images of 10 – 15 tablets (depending on sample size). The error bars indicate the tablet-to-tablet thickness variations (i.e., inter-tablet coating variability).

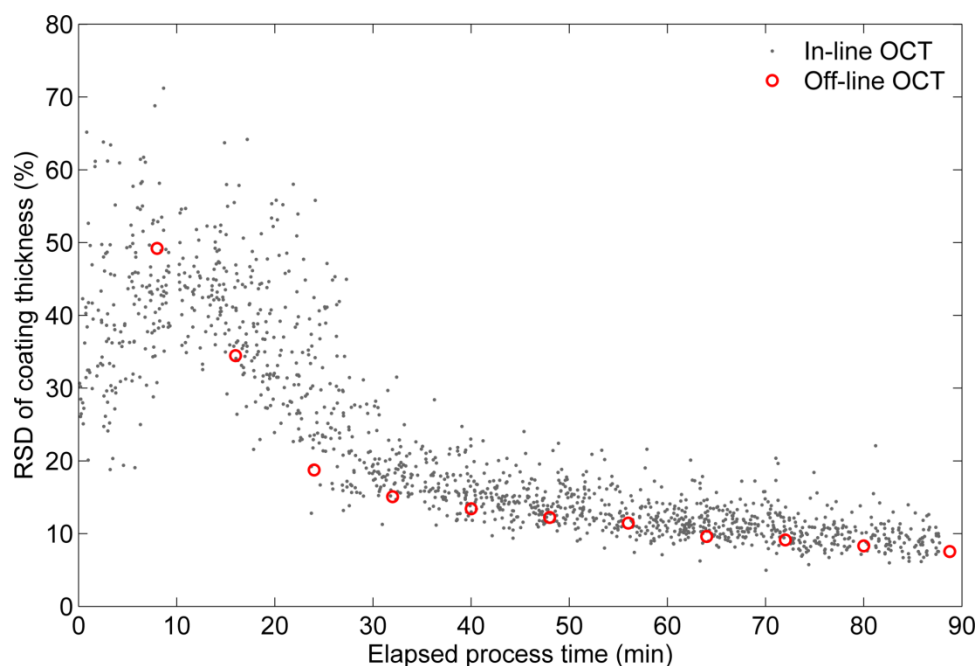


Figure 8.10: RSD of coating thickness measurements per tablet of batch B01. This RSD corresponds to the intra-tablet coating variability. The red circles represent the average RSD from off-line OCT images of 10 – 15 tablets (depending on sample size). The RSD was calculated automatically for each tablet from 1000 different measurement positions.

The mean and standard deviation (SD) of thickness measurements are reported in **Figure 8.11(a)**. Each data point corresponds to 60 s measurement time. The results are compared to off-line measurements of the tablet dimension and the tablet weight gain. The measurements of the tablet dimension were carried out by measuring the tablet thickness of the uncoated tablets and of the coated tablets with a micrometer gauge (with an SD of 5 μm). The actual coating thickness was derived by subtracting a mean value of the tablet thickness from uncoated tablets and dividing this difference by a factor of two. Tablet weight was measured with a high-precision balance (AW-224, Sartorius AG, Göttingen, Germany) with a SD of 0.1 mg. As can be seen, the agreement between off-line and in-line data is very good. Due to the fact that an individual tablet cannot be traced during the process, both thickness calculations from tablet dimensions and the weight gain cannot be used to analyze tablet-to-tablet variations. Moreover, these measurements are highly influenced by the considerable variation of the dimension ($\pm 24 \mu\text{m}$) and weight measurements of the tablet cores ($\pm 2.2 \text{ mg}$).

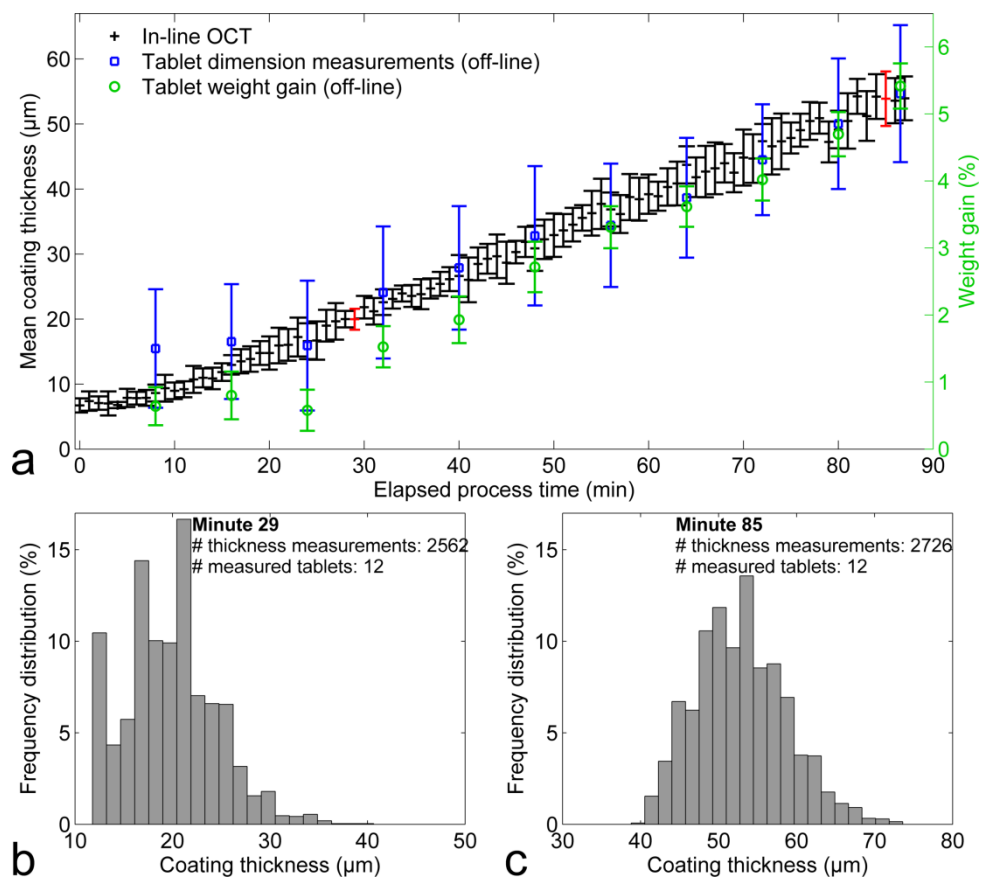


Figure 8.11: Coating thickness analysis of B01. (a) Mean coating thickness from in-line OCT measurements. The measurements are subdivided into bins of 60 second duration and each data point from the in-line OCT measurements corresponds to the average thickness during each 60 second bin. The green circles and blue squares indicate the average weight gain and the average coating thickness from tablet dimension measurements of 10 – 15 tablets (depending on sample size). Histograms were calculated from the in-line OCT measurements highlighted in red in (a). These frequency distributions are depicted for the bins at an elapsed process time of (b) 29 minutes and (c) 85 minutes.

The in-line OCT sensor also provides the distribution of coating thickness in the coating pan at any given time during the process (see **Figure 8.11(b)** and **(c)**). By means of OCT a large number of tablets can be measured (compared to off-line methods) to determine the full distribution of coating thickness even though the measured distribution at early process times can be biased due to unreliable thickness measurements below 10 μm . In general, coating uniformity can be subdivided into *intra*-tablet coating variability, describing the uniformity of the film coating within a single tablet, and *inter*-tablet coating variability, which corresponds to the uniformity of the film coating between multiple tablets of a

Chapter 8: In-line Monitoring of a Pharmaceutical Pan Coating Process by Optical Coherence Tomography

batch. The coating thickness distribution of individual tablets and between tablets cannot be investigated *in situ* with any of the currently available near-infrared or Raman spectroscopy systems. These sensor techniques inherently represent the temporal and spatial average over a large number of tablets and do not allow the analysis of single tablets. Moreover, OCT has the additional advantage that no chemometric calibration models are required to determine the coating thickness.

Reproducibility is shown by evaluating OCT measurements of three batches (B01, B02 and B03) produced with the same materials and the same process conditions (**Figure 8.12** and **Table 8.5**). The results are in excellent agreement in terms of mean coating thickness and RSD as a function of process time. This in-line analysis reflects the measurements of about 50 % of all tablets in the coating pan over a total run duration of 90 minutes. Some tablets might be measured more than once. Nevertheless, the statistics are built on a substantial number of thickness measurements (~300,000) allowing therefore the analysis of process dynamics, which are not accessible experimentally otherwise.

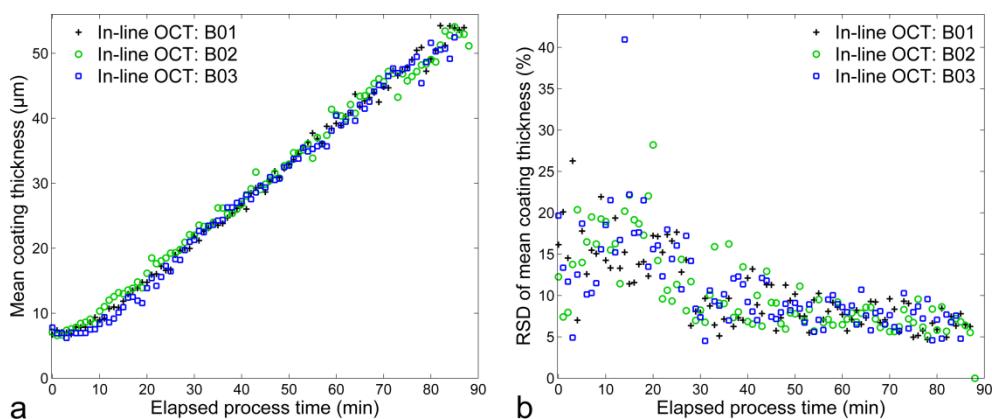


Figure 8.12: Comparison of the results of three replication experiments (B01-B03). The coating thickness measurements were averaged over 60 seconds for each data point. (a) Mean coating thickness and (b) RSD of mean coating thickness corresponding to the inter-tablet coating variability are shown in dependence on the elapsed process time.

Table 8.5: Results of all three batches. The batch size of 2335 tablets was calculated by relating the total mass of the batch (350.2 g) to the mass of an individual tablet (150 mg).

	Process end			Number of analyzed tablets	Percentage of analyzed tablets from batch size	Total thickness measurements
	Mean coating thickness	Inter-tablet coating variability	Intra-tablet coating variability			
	(μm)	(μm)	(μm)			
B01	54.9	3.4	4.9	1,449	62.1	358,993
B02	51.1	2.9	3.9	1,095	46.9	268,953
B03	52.5	2.5	4.7	1,324	56.7	345,619

The number of analyzed tablets could be increased massively by evaluating the OCT data in real-time. Currently there is a significant loss of informative data due to the fact that only every 25th image is saved for post-processing, i.e., tablet detection, interface extraction, distortion correction and coating thickness determination. The number of saved images per second is limited by the time-consuming saving procedure and the limited bulk of data storage capacity. This software-related issue could be overcome by implementing the entire evaluation algorithm on the graphical processing unit (GPU). This will speed up the entire evaluation procedure and will enable the analysis of approximately 10 tablets per second.

8.4 Conclusion

This work demonstrates for the first time an OCT sensor for in-line monitoring of the coating process of randomly moving tablets in a pan coating process. The presented automated thickness evaluation algorithm is the first step towards a real-time implementation of OCT for coating process monitoring. The algorithm successfully detects and evaluates film-coated tablets in OCT images under consideration of their bi-convex shape. Nevertheless, several improvements and optimizations of the algorithm need to be implemented. One of those is the detection of the tablet band and the respective coating thickness evaluation.

This proof-of-concept study emphasizes that OCT could have a considerable impact on the control strategy and development of film coating processes. The additional information as captured by the OCT sensor - *intra*- and *inter*-tablet coating

variability - could be a useful critical quality attribute (CQA) for the development and control of a coating process within the process analytical technology (PAT) and quality-by-design (QbD) framework (FDA, 2004). The combination of theoretical models of the coating process and OCT will allow achieving a narrow thickness distribution of the final coated tablets. An in-line OCT sensor might further facilitate the understanding of currently unknown or less investigated process features. There is also a need for analytical methods, which can be implemented to lab scale, pilot scale, and production scale processes without adapting the coating thickness extraction procedure. However, future research is required to exploit the full potential of OCT and to make it an easily employable tool for monitoring coating processes.

8.5 References

- Bishop, C.M., 2006. *Pattern Recognition and Machine Learning*. Springer, New York.
- Chan, K.K.H., Tang, S., 2010. High-speed spectral domain optical coherence tomography using non-uniform fast Fourier transform. *Biomed. Opt. Express* 1, 1309–1319.
- FDA, 2004. *Guidance for Industry. PAT - a framework for innovative pharmaceutical development, manufacturing, and quality assurance, Quality Assurance*. US Department of Health, Rockville, MD.
- Gendre, C., Boiret, M., Genty, M., Chaminade, P., Pean, J.M., 2011a. Real-time predictions of drug release and end point detection of a coating operation by in-line near infrared measurements. *Int. J. Pharm.* 421, 237–43.
- Gendre, C., Genty, M., Boiret, M., Julien, M., Meunier, L., Lecoq, O., Baron, M., Chaminade, P., Péan, J.M., 2011b. Development of a Process Analytical Technology (PAT) for in-line monitoring of film thickness and mass of coating materials during a pan coating operation. *Eur. J. Pharm. Sci.* 43, 244–250.
- Greengard, L., Lee, J., 2004. Accelerating the Nonuniform Fast Fourier Transform. *SIAM Rev.* 46, 443–454.
- Ho, L., Müller, R., Gordon, K.C., Kleinebudde, P., Pepper, M., Rades, T., Shen, Y., Taday, P.F., Zeitler, J.A., 2009. Monitoring the Film Coating Unit

- Operation and Predicting Drug Dissolution Using Terahertz Pulsed Imaging. *J. Pharm. Sci.* 98, 4866–4876.
- Ho, L., Müller, R., Römer, M., Gordon, K.C., Heinämäki, J., Kleinebudde, P., Pepper, M., Rades, T., Shen, Y.C., Strachan, C.J., Taday, P.F., Zeitler, J. a, 2007. Analysis of sustained-release tablet film coats using terahertz pulsed imaging. *J. Control. Release* 119, 253–61.
- Koller, D.M., Hanneschläger, G., Leitner, M., Khinast, J.G., 2011. Non-destructive analysis of tablet coatings with optical coherence tomography. *Eur. J. Pharm. Sci.* 44, 142–148.
- Markl, D., Hanneschläger, G., Buchsbaum, A., Sacher, S., Khinast, J.G., Leitner, M., 2014a. In-line Quality Control of Moving Objects by Means of Spectral-Domain OCT. *Opt. Lasers Eng.* 59, 1–10.
- Markl, D., Hanneschläger, G., Sacher, S., Leitner, M., Khinast, J.G., 2014b. Optical coherence tomography as a novel tool for in-line monitoring of a pharmaceutical film-coating process. *Eur. J. Pharm. Sci.* 55, 58–67.
- Markl, D., Hanneschläger, G., Sacher, S., Leitner, M., Khinast, J.G., Buchsbaum, A., 2014c. Automated pharmaceutical tablet coating layer evaluation of optical coherence tomography images. *Meas. Sci. Technol.*
- Markl, D., Zettl, M., Hanneschläger, G., Sacher, S., Leitner, M., Buchsbaum, A., Khinast, J.G., 2014d. Calibration-free in-line monitoring of pellet coating processes via optical coherence tomography. *Chem. Eng. Sci.*
- May, R.K., Evans, M.J., Zhong, S., Warr, I., Gladden, L.F., Shen, Y., Zeitler, J.A., 2010. Terahertz in-line sensor for direct coating thickness measurement of individual tablets during film coating in real-time. *J. Pharm. Sci.* 100, 1535–1544.
- Müller, J., Brock, D., Knop, K., Axel Zeitler, J., Kleinebudde, P., 2012. Prediction of dissolution time and coating thickness of sustained release formulations using Raman spectroscopy and terahertz pulsed imaging. *Eur. J. Pharm. Biopharm.* 80, 690–697.
- Pérez-Ramos, J.D., Findlay, W.P., Peck, G., Morris, K.R., 2005. Quantitative analysis of film coating in a pan coater based on in-line sensor measurements. *AAPS PharmSciTech* 6, 127–136.

Chapter 8: In-line Monitoring of a Pharmaceutical Pan Coating Process by Optical Coherence Tomography

- Rabiner, L., 1989. A tutorial on hidden Markov models and selected applications in speech recognition. *Proc. IEEE* 77, 257–286.
- Romero-Torres, S., Pérez-Ramos, J.D., Morris, K.R., Grant, E.R., 2006. Raman spectroscopy for tablet coating thickness quantification and coating characterization in the presence of strong fluorescent interference. *J. Pharm. Biomed. Anal.* 41, 811–819.
- Suzzi, D., Radl, S., Khinast, J.G., 2010. Local analysis of the tablet coating process: Impact of operation conditions on film quality. *Chem. Eng. Sci.* 65, 5699–5715.
- Suzzi, D., Toschkoff, G., Radl, S., Machold, D., Fraser, S.D., Glasser, B.J., Khinast, J.G., 2012. DEM simulation of continuous tablet coating: Effects of tablet shape and fill level on inter-tablet coating variability. *Chem. Eng. Sci.* 69, 107–121.
- Toschkoff, G., Khinast, J.G., 2013. Mathematical modeling of the coating process. *Int. J. Pharm.* 457, 407–22.
- Zhong, S., Shen, Y.-C., Ho, L., May, R.K., Zeitler, J.A., Evans, M., Taday, P.F., Pepper, M., Rades, T., Gordon, K.C., Müller, R., Kleinebudde, P., 2011. Non-destructive quantification of pharmaceutical tablet coatings using terahertz pulsed imaging and optical coherence tomography. *Opt. Lasers Eng.* 49, 361–365.

9

Conclusion and Outlook

Material characterization and quality control is a necessary and crucial step in the pharmaceutical industry. The results of this thesis show that OCT reveals a promising potential for the quality control of solid dosage forms. The direct thickness measurement of film coatings with high resolution and without prior calibration by means of this novel process analytical tool is an alternative for the currently established technologies, such as near-infrared (NIR) and Raman spectroscopy.

9.1 Conclusive Findings

The analysis carried out in chapter 3 and 4 provides the basis for the design of an OCT system, which can be used for in-line monitoring of film-coated tablets. In this case, the sample is put in motion intentionally; and thus the effect of motion has to be considered when creating the design of an OCT system as well as when interpreting the data. Several transverse motion effects are discussed: (1) broadening of the beam displacement, (2) degradation of the transverse resolution and (3) blurring of the sample area of a B-scan. The experimental and theoretical analysis of the transverse resolution is particularly important.

One of the major findings is the shift of the transverse resolution limiting factor from the optics to the beam displacement above a relative speed difference between sensor head and sample of 0.42 m/s (for the presented SD-OCT setup). Speeds above 0.4 m/s are often demanded when monitoring industrial processes, such as a coating process when producing film-coated tablets. This emphasizes the importance of a fast data acquisition when using OCT as in-line quality control tool. It is further shown that in-line OCT measurements acquired with a one-dimensional (1-D) sensor head are less influenced by motion effects than using a two-dimensional (2-D) one. Therefore, in-line OCT measurements should be carried out with a 1-D sensor head.

Chapter 4 further presents OCT images of several commercially-available tablets with cosmetic and enteric coating acquired with two different OCT systems working at different central wavelengths. Based on excellent off-line results, an optical light source operating at a center wavelength of 830 nm is used for the development of a new system and further coating investigations.

The successful implementation of a real-time and in-line evaluation of film-coated tablets requires an automatic thickness evaluation algorithm, as presented in chapter 6. This algorithm includes the detection of the coating interfaces, correction of optical distortions and the determination of coating properties (i.e., mean coating thickness and its standard deviation). The automatic detection algorithm provides highly accurate results independent of tablet orientation and beam displacement.

The algorithm discussed in chapter 6 forms the basis for the determination of coating thickness measurements from in-line OCT data. The final fully automated algorithm includes the following steps: (1) detection of tablets in an OCT image, (2) segmentation of the coating layer, (3) correction of distortions due to the curvature of the bi-convex tablets and the oblique orientation of the tablets, and (4) determination of the coating thickness. The results presented in chapter 8 rest upon this algorithm.

The in-line results of both fluid-bed (see chapter 5) and pan coating (see chapter 8) are in excellent agreement with the off-line OCT measurements. Direct thickness measurements of film coatings are taken with high resolution and without prior calibration. Such a coating analysis is independent of the size and the roughness of the tablet or pellet core. The results additionally show that OCT has the ability to sample a far great number of pellets or tablets to determine the full distribution range of coating thickness. The coating thickness distribution of individual samples

and between samples cannot be investigated *in situ* with any of the currently available near-infrared or Raman spectroscopy systems. These sensor techniques inherently represent the temporal and spatial average over a large number of samples and do not allow the analysis of single particles as it can be performed with OCT. On grounds of these findings, an outlook on future trends, ideas and developments may be outlined.

9.2 Outlook

One can assume that process analysis will play a significant role in the design and control of future intelligent and smart manufacturing of pharmaceuticals. This includes a knowledge-based production at all levels which is proactive instead of reactive. Proactive control requires a complete understanding and an accurate monitoring of the chemical, biochemical and physical processes involved in the production. Spectroscopic (e.g., terahertz, photoacoustic, coherent anti-Stokes Raman spectroscopy) and imaging systems (e.g., hyper spectral imaging, optical coherence tomography) will act as key technologies to control chemical, biochemical and physical parameters in-line or on-line in a contactless and non-destructive manner.

Advancements in existing laboratory methods and technologies will allow the in- and on-line monitoring of quality attributes, which are currently only measurable off-line (Kessler, 2013). OCT is counted among aforesaid methods, providing information during production about the product and the process – which has not been available until present day. Yet, there are several points which should be addressed before OCT can make its way from research to industry: (1) development of a CE and GMP conform OCT system, and (2) the implementation of a real-time OCT data evaluation. Although the current MATLAB implementation is not capable to analyze the data in real-time, as the presented setup enables the generation of 60 frames per second. In order to exploit the full potential of this high acquisition rate, the current algorithm needs to be ported to another programming language that allows real-time processing. Several parts of the algorithm are already ported and can be executed on a graphics processing unit (GPU), as presented in chapter 2. Currently, the classification (see chapter 8) required for the in-line data evaluation remains to be ported. Eventually, the GPU implementation will allow the analysis of approximately 10 tablets per second.

However, the results of the pan coating are more accurate due to the fact that each in-line data point is calculated from much more thickness measurements (at least 50 per tablet) than that of fluid-bed coating (three measurements per pellet). The current manual determination of the coating thickness of the pellets is not suitable for the OCT data stream. The implementation of an automatic evaluation procedure is a significant challenge, but is essential to make the approach suitable for in-line monitoring of a fluid-bed coater.

The final goal of an OCT sensor is, apart from monitoring a coating process, an active control of the process. In order to integrate an OCT sensor in a process control system (e.g., feedback controller), the OCT system requires a standardized interface providing real-time data to a supervisory control and data acquisition (SCADA) system in periodical intervals (Markl et al., 2013; Treffer et al., 2014). This could be implemented by the OPC (OLE for process control) standard allowing the transfer of several measurements per second.

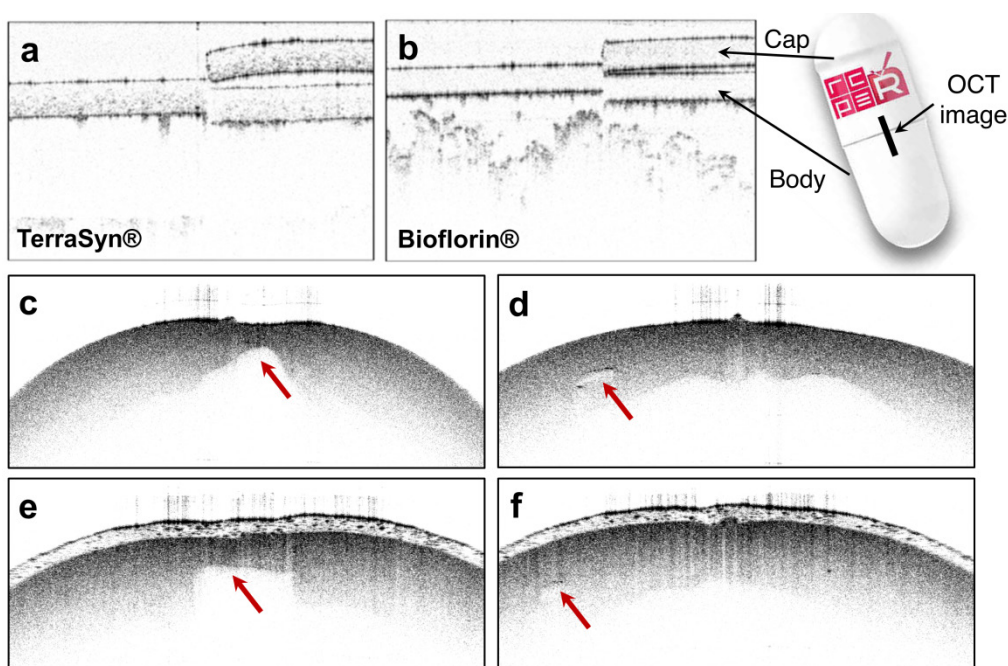


Figure 9.1: OCT images of capsules. (a,b) Hard gelatin capsules at the overlap of the cap and the body. (c,d) Soft gelatin capsules at the point of closure of the two halves (capsule seam). (e,f) Film-coated soft gelatin capsules at the point of closure of the two halves (capsule seam). Red arrows indicate defects of the capsule or inclusions of air in the capsule.

Furthermore, multilayer and active coatings gain more and more attention and therefore, monitoring of such coating structures with OCT should be focused in future research. Since such coatings are often thicker than single modified-release coating layers, a deeper penetration into the tablet may be necessary to resolve the entire coating structure. Therefore, OCT systems operating at longer wavelengths might be more suitable – which have to be tested and validated. Moreover, determining the absolute coating thickness requires the knowledge about the refractive index of each coating layer. Thus, a standard procedure to determine the refractive index has to be established.

OCT has an extremely high potential to act as an in-line and off-line quality control tool of pharmaceutical products beyond the characterization of film-coated tablets and pellets. This might include the control of capsules (see **Figure 9.1**), i.e., the overlap of the body and cap of a hard gelatin capsule or the seam of soft gelatin capsules. This part may require a complete three dimensional reconstruction of the capsule seam in order to detect defects. Another application of OCT in the pharmaceutical industry might be the monitoring of suspensions, i.e., analyzing particles in a solution as shown by two examples in **Figure 9.2**. The design and construction of a bypass of the suspension is necessary to provide a suitable inspection window for the OCT sensor head. Recent research is also performed in the field of compressing pellets to tablets. OCT could act as a tool to investigate the pellet deformation and/or fragmentation in a tablet (see **Figure 9.3**).

There are several extensions of OCT, which might allow the extraction and analysis of information in addition to the subsurface structure. This could include the analysis of flow profiles using Doppler-OCT. This OCT extension would allow the investigation of flow profiles at the die of an extrusion process or even at different positions above the screws of an extruder. This experimental analysis of flow profiles at different screw position would be highly appreciated for the validation of extrusion process simulations. The analysis of the flow profile at the extrusion die is especially interesting for in-line probes used at the same position to predict the active pharmaceutical ingredient (API) concentration, such as NIR or Raman spectroscopy sensor systems (Treffer et al., 2013; Wahl et al., 2013).

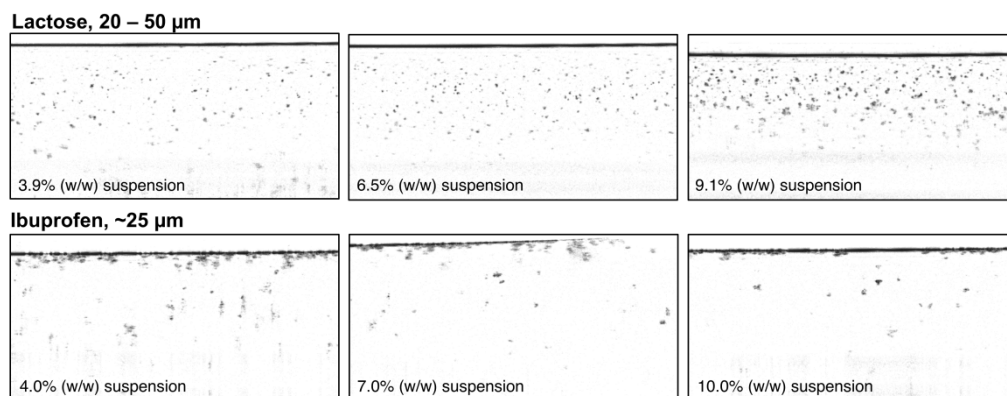


Figure 9.2: Monitoring of suspensions by means of OCT. Particles were dispersed, agitated manually and measured during the settling.

Moreover, the combination of existing techniques, known as the concept of multimodality, will provide additional information about the product and the process state. This could include the simultaneous acquisition of microstructural and compositional information of a solid dosage form enabling the determination of the chemical composition of the tablet core and coating as well as the analysis of the coating thickness. However, the fusion of complex sensor data (e.g., spectra, images or multimodal measurements) and process data; and the use of hard, soft and hard-soft models and self-modeling concepts are required to provide a fingerprint of the process over time and thus the very essentials for smart production.

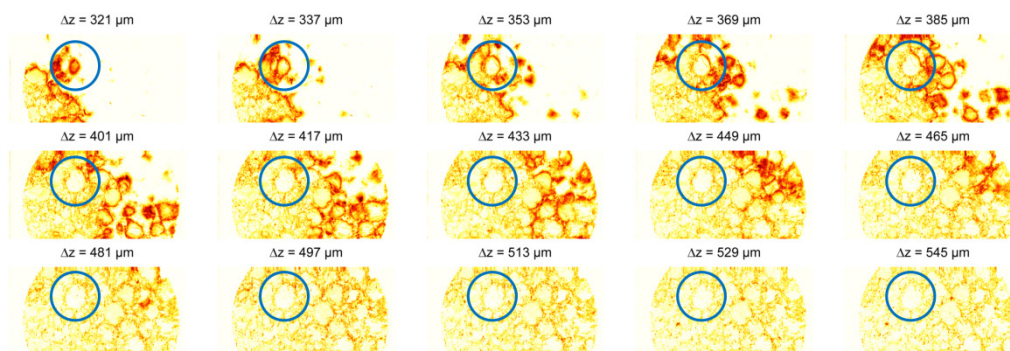


Figure 9.3: En-face OCT images of a tablet produced by compressing pellets. En-face images are images acquired at a constant depth (Δz). The blue circle highlight one specific pellet.

9.3 References

- Kessler, R.W., 2013. Perspectives in process analysis. *J. Chemom.* 27, 369–378.
- Markl, D., Wahl, P.R., Menezes, J.C., Koller, D.M., Kavsek, B., Francois, K., Roblegg, E., Khinast, J.G., 2013. Supervisory Control System for Monitoring a Pharmaceutical Hot Melt Extrusion Process. *AAPS PharmSciTech*.
- Treffer, D., Wahl, P., Markl, D., Koscher, G., Roblegg, E., Khinast, J.G., 2013. Hot Melt Extrusion as a Continuous Pharmaceutical Manufacturing Process. In: Repka, M.A., Langley, N., DiNunzio, J. (Eds.), *Melt Extrusion: Materials, Technology and Drug Product Design*. Springer New York, pp. 363–396.
- Treffer, D., Wahl, P.R., Hörmann, T., Markl, D., Schrank, S., Jones, I., Cruise, P., Mürb, R.-K., Koscher, G., Roblegg, E., Khinast, J.G., 2014. Implementation and Application of a novel in-line particle size analysis method to hot melt extruded pellets produced by die face pelletizing. submitted.
- Wahl, P.R., Treffer, D., Mohr, S., Roblegg, E., Koscher, G., Khinast, J.G., 2013. Inline monitoring and a PAT strategy for pharmaceutical hot melt extrusion. *Int. J. Pharm.* 455, 159–168.

Publications

Peer-Refereed Journals

- Markl, D., Hanneschläger, G., Sacher, S., Buchsbaum, A., Pescod, R., Baele, T., Khinast, J.G., 2015. In-line Characterization of Pharmaceutical Coatings by Means of Optical Coherence Tomography. *Pharm. Technol. To be submitted*
- Markl, D., Hanneschläger, G., Sacher, S., Leitner, M., Buchsbaum, A., Pescod, R., Baele, T., Khinast, J.G., 2015. In-line Monitoring of a Pharmaceutical Pan Coating Process by Optical Coherence Tomography. *Int. J. Pharm. To be submitted*
- Toschkoff, G., Schinwald, C., Markl, D., Koller, D., Leitner, M., Reiter, F., Schlingmann, M., Scharrer, G., Khinast, J.G., 2013. Influence of tablet coating parameters: combining non-destructive measurements and dissolution testing. *Submitted*
- Markl, D., Hanneschläger, G., Sacher, S., Leitner, M., Khinast, J.G., Buchsbaum, A., 2014. Automated pharmaceutical tablet coating layer evaluation of optical coherence tomography images. *Meas. Sci. Technol. In press*
- Markl, D., Zettl, M., Hanneschläger, G., Sacher, S., Leitner, M., Buchsbaum, A., Khinast, J.G., 2014. Calibration-free in-line monitoring of pellet coating processes via optical coherence tomography. *Chem. Eng. Sci. In press*
- Markl, D., Hanneschläger, G., Sacher, S., Leitner, M., Khinast, J.G., 2014. Optical coherence tomography as a novel tool for in-line monitoring of a pharmaceutical film-coating process. *Eur. J. Pharm. Sci.* 55, 58–67.
- Markl, D., Hanneschläger, G., Buchsbaum, A., Sacher, S., Khinast, J.G., Leitner, M., 2014. In-line Quality Control of Moving Objects by Means of Spectral-Domain OCT. *Opt. Lasers Eng.* 59, 1–10.

Conference Proceedings

Markl, D., Hanneschläger, G., Sacher, S., Buchsbaum, A., Khinast, J.G., 2014. Optical coherence tomography data processing for in-line monitoring of a pharmaceutical film-coating process. In: Proceedings of the 10th Minisymposium Verfahrenstechnik. Vienna University of Technology, Vienna, pp. 142–145.

Markl, D., Ziegler, J., Hanneschläger, G., Sacher, S., Buchsbaum, A., Leitner, M., Khinast, J.G., 2014. Real-time data processing for in-line monitoring of a pharmaceutical coating process by optical coherence tomography. In: Proc. SPIE. p. 91290M–91290M–10.

Markl, D., Hanneschläger, G., Sacher, S., Khinast, J.G., Leitner, M., 2013. Optical coherence tomography for non-destructive analysis of coatings in pharmaceutical tablets. In: Proc. SPIE. pp. 879202–879209.

Patent Applications

Markl, D., Hanneschläger, G., Leitner, M., Sacher, S., Koller, D.M., Khinast, J.G., 2014. Device and method for monitoring a property of a coating of a solid dosage form during a coating process forming the coating of the solid dosage form. US 2014/0322429 A1.

Markl, D., Hanneschläger, G., Leitner, M., Sacher, S., Koller, D.M., Khinast, J.G., 2014. A device and a method for monitoring a property of a coating of a solid dosage form during a coating process forming the coating of the solid dosage form. EP 2 799 842 A1.

Magazine Article

Markl, D., Sacher, S., Khinast, J.G., 2015. Optical Coherence Tomography: An alternative methodology to monitor pharmaceutical coating processes. G.I.T. Lab. J. Eur. 7-8 17–19.

Talks

- Markl, D., Hanneschläger, G., Sacher, S., Leitner, M., Pescod, R., Buchsbaum, A., Khinast, J.G., 2015. In-line monitoring of pharmaceutical pan coating process by means of optical coherence tomography. In: IFPAC 2015 Annual Meeting, Arlington.
- Markl, D., Hanneschläger, G., Sacher, S., Buchsbaum, A., Khinast, J.G., 2014. Optical coherence tomography data processing for in-line monitoring of a pharmaceutical film-coating process. In: 10th Minisymposium Verfahrenstechnik. Vienna.
- Markl, D., Ziegler, J., Hanneschläger, G., Sacher, S., Buchsbaum, A., Leitner, M., Khinast, J.G., 2014. Real-time data processing for in-line monitoring of a pharmaceutical coating process by optical coherence tomography. In: Photonics Europe 2014, Brussels.
- Markl, D., Hanneschläger, G., Sacher, S., Khinast, J.G., 2014. Optical coherence tomography for in-line quality control of pharmaceutical film-coated tablets. In: IFPAC 2014 Annual Meeting, Arlington.
- Markl, D., Hanneschläger, G., Sacher, S., Leitner, M., Khinast, J.G., 2014. Optical coherence tomography for non-destructive tablet coating characterization. In: OCT4NDT 2013 Linz.
- Markl, D., Hanneschläger, G., Sacher, S., Leitner, M., Khinast, J.G., 2013. In-line process monitoring of film thickness on pharmaceutical pellets by mean of optical coherence tomography as novel PAT technology. In: EuPAT 6, Porto.
- Markl, D., Hanneschläger, G., Sacher, S., Khinast, J.G., Leitner, M., 2013. Optical coherence tomography for non-destructive analysis of coatings in pharmaceutical tablets. In: Optical Methods for Inspection, Characterization, and Imaging of Biomaterials, Optical Metrology, Munich.

Poster

- Sacher, S., Markl, D., Hanneschläger, G., Leitner, M., Khinast, J.G., 2013. In-line monitoring of a fluid-bed coating process with optical coherence tomography as novel PAT technology. In: AIChE 2013 Annual Meeting, San Francisco.

Appendices

Appendix A

NU-FFT for SD-OCT

A.1 NU-FFT

The image reconstruction is primarily based on the discrete Fourier transform (DFT) of the interference signal by transforming the data from wavenumber k domain to axial depth z domain. If the data are uniformly distributed in the k domain, the DFT can be computed using the fast Fourier transform (FFT) algorithm. Nevertheless, the used SD-OCT system employs a diffraction grating, which separates spectral components almost linearly in wavelength λ . Due to the inverse relationship, $k = 2\pi/\lambda$, the spectral fringe pattern is unevenly sampled in k domain. Therefore, the spectral data need to be resampled to achieve uniform spacing in the k domain. The accuracy of this resampling is a crucial step in the image reconstruction process. Traditional methods, such as linear and cubic spline interpolation, introduce a large amount of interpolation error or require long processing times. Moreover, the performance of most traditional interpolation methods degrades as the signal frequency approaches the Nyquist sampling rate. This causes a decrease of sensitivity for signals originating at greater depths, which correspond to higher oscillation frequencies in the interference signal (Chan and Tang, 2010).

Non-uniform Fourier transform (NU-FFT) is an alternative technique to reduce the interpolation error and to overcome speed limitations of other methods. In this work a fast Gaussian gridding method was used as presented by Greengard and Lee, 2004. First, the interference signal is oversampled by convolution with a Gaussian interpolation kernel on a uniform grid, which can be defined as

$$S_\tau(k) = S(k) * G_\tau(k) = \int_{-\infty}^{\infty} S(y)G_\tau(k - y) dy \quad (\text{A.1})$$

The Gaussian interpolation kernel $G_\tau(k)$ was selected on the basis of the work of

Appendices

Greengard and Lee, 2004 and can be expressed as

$$G_\tau(x) = e^{-\frac{x^2}{4\tau}}. \quad (\text{A.2})$$

The accuracy of the fast gridding algorithm is controlled by two parameters: the oversampling ratio $R = M_r/M$ (ratio between the length of the oversampled signal and the number of sample points, i.e., number of pixels of the CCD camera) and the spreading distance M_{SP} . The spreading distance defines the number grid points on each side of the original data point to which the Gaussian kernel is accounted for in calculation. These parameters are considered in the algorithm by the Gaussian kernel parameter τ , which is set according to

$$\tau = \frac{1}{M^2} \frac{\pi}{R(R-0.5)} M_{sp}. \quad (\text{A.3})$$

For a detailed analysis of the introduces parameters and the selection of this kernel is referred to (Greengard and Lee, 2004) and (Chan and Tang, 2011).

As indicated above, $S(k)$ is resampled in an evenly spaced grid $k_\tau[n] = \frac{n}{M_r} \Delta K$, $\{n \in \mathbb{Z} | 0 \leq n \leq M_r - 1\}$ (ΔK is the wavenumber range). The resampled signal can be defined in discrete form as

$$S_\tau[n] = \sum_{m=0}^{M_r-1} S(k[m]) G_\tau(k_\tau[n] - k[m]) \quad \{n \in \mathbb{Z} | 0 \leq n \leq M_r - 1\}. \quad (\text{A.4})$$

The FFT algorithm can then be applied on Eq. (A.4) to compute the discrete Fourier transform, denoted as

$$s_\tau[u] = \frac{1}{M_r} \sum_{m=0}^{M_r-1} s_\tau[m] e^{-j2\pi um/M_r} \quad \{u \in \mathbb{Z} | 0 \leq u \leq M_r - 1\}. \quad (\text{A.5})$$

Once $s_\tau[u]$ has been calculated, the actual depth profile can be computed by deconvolution of $G_\tau(k)$ in k space or alternatively with a simple division of its Fourier transform

$$g_\tau(w) = \mathcal{F}^{-1}\{G_\tau(x)\}(x) = \sqrt{2\tau} e^{-w^2\tau}. \quad (\text{A.6})$$

Therefore, the actual depth profile is given by

$$s[u] = g_\tau^{-1}(u) s_\tau[u] = \frac{1}{\sqrt{2\tau}} e^{u^2\tau} s_\tau[u] \quad \left\{u \in \mathbb{Z} | 0 \leq u \leq \frac{M}{2} - 1\right\}. \quad (\text{A.7})$$

In this study the oversampling ratio R and the spreading distance M_{SP} were set to 2 and 4, respectively. Increasing R and M_{SP} would improve the accuracy of the NU-FFT, though this would reduce the processing speed. Therefore, R and M_{SP}

were chosen to satisfy the accuracy requirement of the system and to limit the computational load. It should be noted, that other kernel functions (e.g., Kaiser-Bessel, two term cosine, three term cosine) than the Gaussian one might improve the reconstruction accuracy further (Chan and Tang, 2011). The effect of other kernel functions on the accuracy of the thickness calculation will be subject to further research.

A.2 References

- Chan, K.K.H., Tang, S., 2010. High-speed spectral domain optical coherence tomography using non-uniform fast Fourier transform. *Biomed. Opt. Express* 1, 1309–1319.
- Chan, K.K.H., Tang, S., 2011. Selection of convolution kernel in non-uniform fast Fourier transform for Fourier domain optical coherence tomography. *Opt. Express* 19, 26891–904.
- Greengard, L., Lee, J., 2004. Accelerating the Nonuniform Fast Fourier Transform. *SIAM Rev.* 46, 443–454

Appendix B

Gaussian Optics

B.1 Gaussian Optics

Irradiance distribution of Gaussian beam as a function of the radius distance r from the axis is given by Hecht, 2008

$$I(r) = I_0 \exp \left\{ -\frac{2r^2}{w^2} \right\}. \quad (\text{B.1})$$

w is the radial extent of the beam where the irradiance has dropped to I_0/e^2 with I_0 as the beam irradiance on the beam axis. I_0 can be expressed by the total power carried by the beam:

$$\begin{aligned} P &= \int_0^\infty I(r) 2\pi r \, dr \\ P &= \frac{1}{2} I_0 \pi w^2 \\ I_0 &= \frac{2P}{\pi w^2}. \end{aligned} \quad (\text{B.2})$$

Replacing I_0 in Eq. (B.1) gives

$$I(r) = \frac{2P}{\pi w^2} \exp \left\{ -\frac{2r^2}{w^2} \right\}. \quad (\text{B.3})$$

Under the laws of geometrical optics a beam converging at a certain angle should collapse to a point; this does not occur due to diffraction. However, at the intersection of the asymptotes the beam radius reaches a minimum value of w_0 , i.e., the beam waist radius. w can be expressed from the intensity at w_0 (FWHM) by:

$$\begin{aligned} I(w_0) &= \frac{I_0}{2} = \frac{P}{\pi w^2} = \frac{2P}{\pi w^2} \exp \left\{ -\frac{2r^2}{w^2} \right\} \\ 2 \exp \left\{ -\frac{2r^2}{w^2} \right\} &= 1 \\ \ln(2) - \frac{2w_0^2}{w^2} &= \ln(1) \\ \ln(2) &= \frac{2w_0^2}{w^2} \\ w^2 &= \frac{2w_0^2}{\ln(2)}. \end{aligned} \quad (\text{B.4})$$

Replacing w^2 in Eq. (B.3) gives an adapted irradiance distribution of a Gaussian beam:

$$I(r) = \frac{\ln(2)P}{\pi w_0^2} \exp\left\{-\frac{\ln(2)r^2}{w_0^2}\right\}. \quad (\text{B.5})$$

B.2 References

Hecht, E., 2008. Optics. Pearson Education.

Appendix C

Propagation of Uncertainty for Film-coated Tablets of Different Dimensions and Shapes

C.1 Volume of a Film-coated Tablet

- **Volume of a spherical film-coated tablet**

The volume of a spherical tablet core with a radius r is expressed as

$$V_{\text{core,spherical}} = \frac{4}{3}\pi r^3. \quad (\text{C.1})$$

Assuming a uniform coating layer, the volume of a film-coated tablet with a coating thickness d_c can be denoted as

$$\begin{aligned} V_{\text{tablet,spherical}} &= \frac{4}{3}\pi(r + d_c)^3 \\ &= \underbrace{\frac{4}{3}\pi r^3}_{V_{\text{core,spherical}}} + \underbrace{4\pi d_c \left(r^2 + d_c r + \frac{1}{3}d_c^2 \right)}_{V_{\text{coat,spherical}}}. \end{aligned} \quad (\text{C.2})$$

- **Volume of a round film-coated tablet**

The volume of a round tablet core with a radius r and a height h is expressed as

$$V_{\text{core,round}} = r^2\pi h. \quad (\text{C.3})$$

Assuming a uniform coating layer, the volume of a film-coated tablet with a coating thickness d_c can be denoted as

$$\begin{aligned} V_{\text{tablet,round}} &= (r + d_c)^2\pi(h + d_c) \\ &= \underbrace{r^2\pi h}_{V_{\text{core,round}}} + \underbrace{\pi d_c(2rh + d_c(h + 2r) + d_c^2)}_{V_{\text{coat,round}}}. \end{aligned} \quad (\text{C.4})$$

- **Volume of a bi-convex film-coated tablet**

The volume of a bi-convex tablet core with a radius r , a tablet band height h_b and a cap height h_c is expressed as

$$\begin{aligned}
V_{\text{core,bc}} &= V_{\text{cylinder}} + 2V_{\text{cap}} \\
V_{\text{cylinder}} &= r^2\pi h_b \\
V_{\text{cap}} &= \frac{\pi h_c}{6}(3r^2 + h_c^2) \\
V_{\text{core,bc}} &= r^2\pi h_b + 2\frac{\pi h_{\text{cap}}}{6}(3r^2 + h_c^2) \\
V_{\text{core,bc}} &= \pi \left(r^2 h_b + r^2 h_c + \frac{1}{3} h_c \right) \tag{C.5}
\end{aligned}$$

Assuming a uniform coating layer, the volume of a film-coated tablet with a coating thickness d_c can be denoted as

$$\begin{aligned}
V_{\text{tablet,bc}} &= V_{\text{cylinder,coat}} + 2V_{\text{cap,coat}} \\
V_{\text{cylinder,coat}} &= (r + d_c)^2\pi h_b \\
V_{\text{cap,coat}} &= \frac{\pi(h_c + d_c)}{6}(3(r + d_c)^2 + (h_c + d_c)^2) \\
V_{\text{tablet,bc}} &= (r + d_c)^2\pi h_b + 2\frac{\pi(h_c + d_c)}{6}(3(r + d_c)^2 + (h_c + d_c)^2) \\
V_{\text{tablet,bc}} &= \underbrace{\pi \left[\frac{4}{3}d_c^3 + (h_b + 2h_c + 2r)d_c^2 + (2rh_b + 2rh_c + r^2 + h_c^2)d_c \right]}_{V_{\text{coat,bc}}} \\
&\quad + \underbrace{\pi \left[r^2 h_b + r^2 h_c + \frac{1}{3} h_c^3 \right]}_{V_{\text{core,bc}}} \tag{C.6}
\end{aligned}$$

The mass of a film-coated tablet can be calculated by

$$m_{\text{tablet}} = V_{\text{core}}\rho_{\text{core}} + V_{\text{coating}}\rho_{\text{coat}}. \tag{C.7}$$

C.2 Propagation of Uncertainty

Suppose the coating thickness d_c and the coating mass m_{coat} are related through $d_c = f(m_{\text{coat}})$. In our case we know the uncertainty of the coating mass and want to derive the corresponding uncertainty of the coating thickness. Using $m_{\text{coat}} - \mu_{m,\text{coat}} = \Delta m_{\text{coat}}$ (the deviation of coating mass from the theoretical mean), and similarly $d_c - \mu_{d,c} = \Delta d_c$ (the deviation of coating thickness from the theoretical mean) and taking a Taylor expansion of the function f about the true value gives

$$f(\mu_{m,\text{coat}} + \Delta m_{\text{coat}}) \approx f(\mu_{m,\text{coat}}) + \frac{df}{dm_{\text{coat}}} \mu_{m,\text{coat}} \Delta m_{\text{coat}}. \tag{C.8}$$

The Taylor expansion is truncated after the first correction term to simplify the situation. We further assume that the true values obey the equation $\mu_{d,c} = f(\mu_{m,\text{coat}})$ with $\mu_{d,c}$ and $\mu_{m,\text{coat}}$ as the mean values of coating thickness d_c and

Appendices

coating mass m_{coat} , respectively. Hence, the means and deviations are related by $\mu_{d,c} + \Delta d_c = f(\mu_{m,\text{coat}} + \Delta m_{\text{coat}})$. Using this relations and Eq. (C.8) we can rewrite the Taylor expansion as

$$\mu_{d,c} + \Delta d_c \approx f(\mu_{m,\text{coat}}) + \frac{df(\mu_{m,\text{coat}})}{dm_{\text{coat}}} \Delta m_{\text{coat}}. \quad (\text{C.9})$$

Cancelling the true values gives

$$\Delta d_c \approx \frac{df(\mu_{m,\text{coat}})}{dm_{\text{coat}}} \Delta m_{\text{coat}}, \quad (\text{C.10})$$

which shows how the actual error in coating mass translates to the error in coating thickness. The deviation of coating mass from the theoretical mean can be defined on the basis of Eq. (C.10) using $m_{\text{coat}} = h(d_c)$ as

$$\Delta m_{\text{coat}} \approx \frac{dh(\mu_{d,c})}{dd_c} \Delta d_c. \quad (\text{C.11})$$

In order to determine the maximum allowed deviation of the coating thickness from the concept of content uniformity as described in the US Pharmacopeia (The United States Pharmacopeial Convention, 2011b) we need to rearrange Eq. (C.11). Therefore, we define $\Delta m_{\text{coat}} = m_{\text{coat}} \sigma_{\text{max}}$ with σ_{max} as the standard deviation of the actual coating mass to the label claim (specified as 6.5%). By rearranging Eq. (C.11), we can determine Δd_c using the formulas as stated in section C.1 by

$$\Delta d_c = \frac{m_{\text{coat}}}{\frac{dm_{\text{coat}}}{dd_c}} \sigma_{\text{max}}. \quad (\text{C.12})$$

- **Propagation of uncertainty for a spherical film-coated tablet**

First, we need to evaluate the derivative of $m_{\text{coat,spherical}}$ with respect to d_c :

$$\frac{dm_{\text{coat,spherical}}}{dd_c} = 4\pi(r + d_c)^2 \rho_{\text{coat}}. \quad (\text{C.13})$$

Using Eqs. (C.12) and (C.13), we can write the formula for the error of the coating thickness as

$$\begin{aligned} \Delta d_c &= \frac{4\pi d_c \left(r^2 + 2rd_c + \frac{1}{3}d_c^2 \right) \rho_{\text{coat}}}{4\pi(r + d_c)^2 \rho_{\text{coat}}} \sigma_{\text{max}} \\ \Delta d_c &= \frac{d_c \left(r^2 + 2rd_c + \frac{1}{3}d_c^2 \right)}{(r + d_c)^2} \sigma_{\text{max}} \end{aligned} \quad (\text{C.14})$$

- **Propagation of uncertainty for a round film-coated tablet**

First, we need to evaluate the derivative of $m_{\text{coat,round}}$ with respect to d_c :

$$\frac{dm_{\text{coat,round}}}{dd_c} = \pi(2rh + 2d_c h + 4rd_c + 3d_c^2)\rho_{\text{coat}}. \quad (\text{C.15})$$

Using Eqs. (C.12) and (C.13), we can write the formula for the error of the coating thickness as

$$\begin{aligned} \Delta d_c &= \frac{\pi d_c(2rh + (h + 2r)d_c + 4rd_c + d_c^2)\rho_{\text{coat}}}{\pi(2rh + 2d_c h + 4rd_c + 3d_c^2)\rho_{\text{coat}}} \sigma_{\text{max}} \\ \Delta d_c &= \frac{d_c(2rh + (h + 2r)d_c + 4rd_c + d_c^2)}{2rh + 2d_c h + 4rd_c + 3d_c^2} \sigma_{\text{max}} \end{aligned} \quad (\text{C.16})$$

- **Propagation of uncertainty for a bi-convex film-coated tablet**

First, we need to evaluate the derivative of $m_{\text{coat,bc}}$ with respect to d_c :

$$\begin{aligned} \frac{dm_{\text{coat,bc}}}{dd_c} &= \pi[4d_c^2 + (h_b + 2h_c + 2r)2d_c + 2rh_b + 2rh_c + r^2 \\ &\quad + h_c^2]\rho_{\text{coat}}. \end{aligned} \quad (\text{C.17})$$

Using Eqs. (C.12) and (C.13), we can write the formula for the error of the coating thickness as

$$\begin{aligned} \Delta d_c &= \frac{\pi \left[\frac{4}{3}d_c^3 + (h_b + 2h_c + 2r)d_c^2 + (2rh_b + 2rh_c + r^2 + h_c^2)d_c \right] \rho_{\text{coat}}}{\pi[4d_c^2 + (h_b + 2h_c + 2r)2d_c + 2rh_b + 2rh_c + r^2 + h_c^2]\rho_{\text{coat}}} \sigma_{\text{max}} \\ \Delta d_c &= \frac{\frac{4}{3}d_c^3 + (h_b + 2h_c + 2r)d_c^2 + (2rh_b + 2rh_c + r^2 + h_c^2)d_c}{4d_c^2 + (h_b + 2h_c + 2r)2d_c + 2rh_b + 2rh_c + r^2 + h_c^2} \sigma_{\text{max}} \end{aligned} \quad (\text{C.18})$$

C.3 References

The United States Pharmacopeial Convention, 2011. (905) Uniformity of Dosage Units. Stage 6 Harmonization.